



**Università
degli Studi
di Ferrara**

**DOCTORAL COURSE IN
"CHEMICAL SCIENCES"**

CYCLE XXXV

DIRECTOR Prof. Alberto Cavazzini

**ELECTROREDUCTION OF CARBON DIOXIDE OVER NANOSTRUCTURED METALLIC CATHODES: A
ROUTE TOWARDS ARTIFICIAL PHOTOSYNTHESIS**

Scientific/Disciplinary Sector (SDS) CHIM/03

Candidate

Dott. Niorettini Alessandro

Supervisor

Prof. Caramori Stefano

Years 2019/2022

Acknowledgements

I would like to thank my research group and my supervisor, prof. Stefano Caramori, who made possible for me to start and develop the research activity during my doctoral studies.

I dedicate a special gratitude to the group of prof. Alina Bienko of Wrocław University for allowing me to work in their laboratories and for teaching me many important things about science chemistry and Polish culture. In particular prof. Urszula Komarnicka and Monika Lesiów for tolerating me for over six months in their office.

I also want to say a particular thanks to Sandra Koziel and Daria Wojtala for the enjoyable time I spent in Italy and Poland, I'm really glad to have had the opportunity to work with you.

I finally want to thank all my family that taught me the importance of science, art and culture and the importance of working with commitment and passion and encouraged me to pursue this career.

SUMMARY

PART 1 Experimental methods and copper nanostructuring

1. Introduction	2
1.1 Electrochemical CO ₂ reduction to fuels: techno-economic feasibility	6
1.2 Economic considerations	11
1.3 Catalytic reduction of CO ₂ on different metallic substrates	12
1.4 State of the art	14
1.5 Experimental setup and cell design	18
1.6 Cell making	21
2. Product analysis and interface characterization	25
2.1 Morphological characterization of nanostructured cathodes	25
2.1.1 Scanning electron microscopy (SEM)	25
2.1.2 High resolution transmission electron microscopy (HR-TEM)	26
2.2 Analytical setup for the identification and quantification of CO ₂ reduction products	26
2.2.1 ¹ H-NMR nuclear magnetic resonance spectroscopy	26
2.2.2 Gas chromatography analysis (GC)	29
2.2.3 Reduction efficiency	32
3. Electrochemical CO₂ reduction	33
3.1 OD treatment of copper electrodes: preliminary results	33
3.2 Experimental optimized OD procedure for Cu cathodes	39
3.3 Faradic efficiencies and electrochemical behaviour of Cu_OD cathodes	41

PART 2 Indium functionalized copper cathodes

1. Introduction and state of the art	45
2. Experimental	46
2.1 Preparation of the cathodes	46
2.2 Morphological and structural characterization	46
2.3 Electrochemical characterization	47
3. Results and discussion	48
3.1 Structural and morphological characterization of the samples	48
3.2 CO ₂ R activity	54
3.3 Cathodes stability and lifetime	61
3.4 Final consideration on OD-Cu ₂ In(X) cathodes	65
4. Copper foams	66
5. Carbon based electrodes	69
5.1 OD treatment and Indium functionalization of carbon based cathodes	71
5.2 Electrochemical responses of copper indium cathodes on carbon foam	73
5.3 Faradic efficiencies of carbon based electrodes	74
5.4 Determination of ECSA (electrochemical surface area) by double layer capacitance	78
5.4.1 Experimental	78
5.4.2 ECSA of copper-indium cathodes	78
5.5 Final considerations	81

PART 3 Cerium functionalized copper cathodes

1. Carbon dioxide reduction using cerium functionalized cathodes	83
1.1 Cerium deposition on copper foils	83
1.2 Electrochemical response of copper cerium cathodes	85
1.3 Faradic efficiencies of copper-cerium cathodes	86
1.4 Final considerations	88

PART 4 Gold cathodes

1. Carbon dioxide reduction over gold cathodes	90
1.1 Introduction	90

1.2 Cathode preparation	91
1.3 Synthesis and characterization of the Au nanostructures	93
1.3.1 TEM microscopy	95
1.4 ECSA measurements	97
1.5 Lead underpotential deposition (UPD)	99
1.6 Electrochemical performances of the Au nanostructures	100
1.7 Faradic efficiencies	101
1.8 CO-Bridge and electrode passivation	104
1.9 Final considerations	106

CONCLUSION	107
-------------------	------------

References	108
-------------------	------------

.....

ADDENDUM I Internship at Wrocław University for the synthesis and characterization of metallic complexes with enhanced anticancer properties, article: *“Synthesis, Physicochemical, and Biological Properties of Phosphino Cu(I), Ru(II), Ir(III) Complexes”*

Introduction to the work	114
---------------------------------	------------

Abstract	115
-----------------	------------

1. Introduction	116
------------------------	------------

2. Results and Discussion	118
----------------------------------	------------

2.1 Synthesis	118
---------------	-----

2.2 Structural analysis of Cu(I), Ru(II) and Ir(III) Complexes	120
--	-----

2.3 Oxidative Plasmid DNA Degradation	121
---------------------------------------	-----

2.4 In Vitro Anticancer Investigation	123
---------------------------------------	-----

2.4.1 Determination of IC ₅₀ and partition coefficients (Log P) values	124
---	-----

2.4.2 Cellular Accumulation	125
-----------------------------	-----

2.4.3 Cell Death Mechanisms	125
-----------------------------	-----

2.4.4 Induction of cell cycle arrest	127
--------------------------------------	-----

2.4.5 Anticancer activity in 3D tumor spheroids	128
3. Materials and methods	129
3.1 Reagents	129
3.2 Methods	129
3.3 Synthesis	130
3.3.1. Preparation of $\text{Ph}_2\text{PCH}_2\text{N}(\text{CH}_2\text{CH}_3)_2$	130
3.3.2. Preparation of $\text{Ph}_2\text{PCH}_2\text{N}(\text{CH}_2\text{CH}_2\text{CH}_2\text{CH}_3)_2$	131
3.3.3. Preparation of $\text{Ir}(\eta^5\text{-Cp}^*)\text{Cl}_2\text{Ph}_2\text{PCH}_2\text{N}(\text{CH}_2\text{CH}_3)_2$	131
3.3.4. Preparation of $\text{Ru}(\eta^6\text{-p-cymene})\text{Cl}_2\text{Ph}_2\text{PCH}_2\text{N}(\text{CH}_2\text{CH}_3)_2$	132
3.3.5. Preparation of $[\text{Cu}(\text{NCCH}_3)_2(\text{Ph}_2\text{PCH}_2\text{N}(\text{CH}_2\text{CH}_3)_2)_2]+\text{BF}_4$	132
3.3.6. Preparation of $\text{Ir}(\eta^5\text{-Cp}^*)\text{Cl}_2\text{Ph}_2\text{PCH}_2\text{N}(\text{CH}_2\text{CH}_2\text{CH}_2\text{CH}_3)_2$	133
3.3.7. Preparation of $\text{Ru}(\eta^6\text{-p-cymene})\text{Cl}_2\text{Ph}_2\text{PCH}_2\text{N}(\text{CH}_2\text{CH}_2\text{CH}_2\text{CH}_3)_2$	134
3.3.8. Preparation of $[\text{Cu}(\text{NCCH}_3)_2(\text{Ph}_2\text{PCH}_2\text{N}(\text{CH}_2\text{CH}_2\text{CH}_2\text{CH}_3)_2)_2]+\text{BF}_4$	134
3.4 Electrochemical measurements	135
3.5 DNA Strand Break analysis	135
3.6 Partition coefficient	136
3.7 Cell Cultures	136
3.8 Cytotoxic activity	136
3.9 Intracellular accumulation	137
3.10 Flow Cytometry	137
3.11 Three-Dimensional culturing In Vitro	138
4. Conclusions	138
References	140
Supporting Information	144

ADDENDUM II Internship at Wrocław University for the synthesis and characterization of metallic complexes with enhanced anticancer properties, article: *“Liposomal Binuclear Ir(III)–Cu(II) Coordination Compounds with Phosphino-Fluoroquinolone Conjugates for Human Prostate Carcinoma Treatment”*

Abstract	161
1. Introduction	162
2. Results and Discussion	164

2.1 Synthesis	164
2.2 Structural Features	164
2.3 Characterization of Ir(III)-Cu(II) Inorganic Compounds	167
2.3.1 Infrared spectroscopies	167
2.3.2 Electrospray Ionization Mass Spectroscopy (ESI-MS)	167
2.3.3 EPR Spectroscopy	168
2.3.4 Luminescence properties	168
2.3.5 Magnetic properties	169
2.3.6 Electrochemical behaviour	171
2.3.7 Biological Study	172
2.3.8 Characterization of Liposomes	174
2.3.9 First insight into the cytotoxic action mode	175
3. Conclusions	178
4. Experimental Section	179
References	180
Supporting information	184
List of publications and patents	226

.....

PART 1

Experimental methods and copper nanostructuring

1. Introduction:

The use of fossil fuels, contributing to the large majority of all CO₂ emissions, is the main cause of the greenhouse effect and dramatic climate changes. The ambitious target of zeroing CO₂ emissions by 2050 will not be sufficient to slow down the global warming. In order to reverse this trend, it is now imperative not only to reduce our fossil fuels consumption, but also to develop sustainable technologies to remove CO₂ from the atmosphere (negative emissions). In this context, the capture and conversion of CO₂ into alternative fuels and energy rich raw materials could represent a virtually inexhaustible virtuous cycle of energy storage and conversion (Fig. 1)¹.

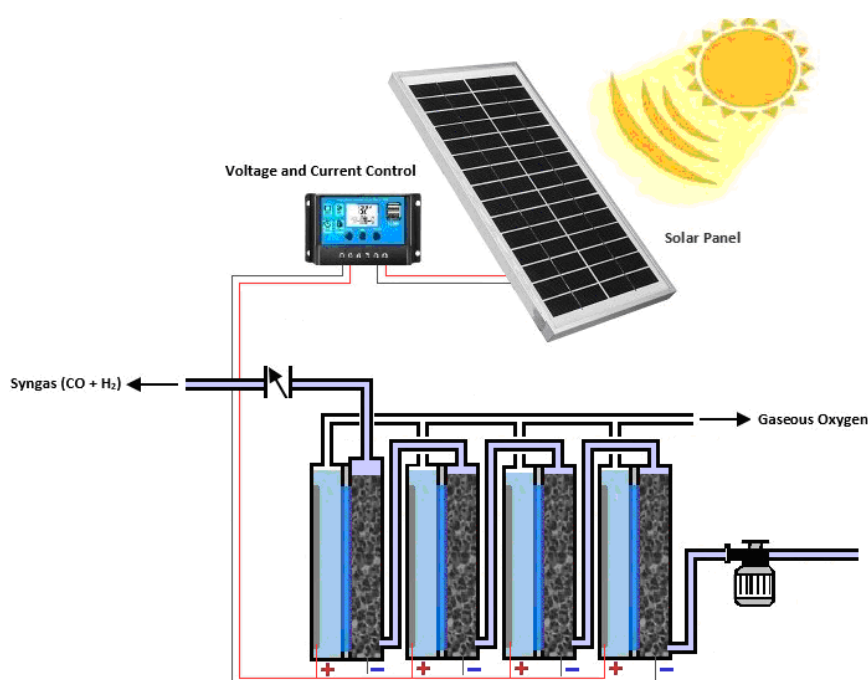


Fig.1 Multiple in-line electrochemical reduction cells associated with a solar generator for CO₂ reduction

The aim of this research project is to investigate about the electrochemical reduction of carbon dioxide mainly into selected value added products, like syngas (a mixture of H₂ and CO), methane and formate, using innovative copper based cathodes able to manifest high current densities and faradaic efficiency. An electrochemical based conversion plant would be able not only to convert into useful chemical species that nowadays are only considered as a waste, but also to overcome the well known discontinuity of renewable energy sources which actually represent the main application limit of solar and wind technology. In fact, storing energy into chemicals represent an interesting solution to avoid the high costs and low efficiencies related to the use of batteries. Multi electron PCET (proton coupled electron transfer) are needed to achieve CO₂ reduction to stable products, therefore the kinetic barriers for these reactions may be substantial, requiring a significant amount of energy in the form of overpotential. The free energy changes associated to various reduction products are summarized in Table 1, where it can be observed that

thermodynamically, the Standard Potentials (E°) vs Normal Hydrogen Electrode (NHE), associated to most of these reactions are quite comparable to those of water reduction except the monoelectronic CO_2 reduction, which is not proton compensated and sets at -1.9 V vs NHE.

Reaction	ΔG° (kJ/mol)	E° (V vs. NHE)
$\text{CO}_2 + 2\text{H}^+ + 2e^- \rightarrow \text{CO} + \text{H}_2\text{O}$	19.9	-0.53
$\text{CO}_2 + 2\text{H}^+ + 2e^- \rightarrow \text{HCOOH}$	38.4	-0.61
$\text{CO}_2 + 4\text{H}^+ + 4e^- \rightarrow \text{H}_2\text{CO} + \text{H}_2\text{O}$	27.5	-0.48
$\text{CO}_2 + 8\text{H}^+ + 8e^- \rightarrow \text{CH}_4 + 2\text{H}_2\text{O}$	-130.8	-0.38
$\text{CO}_2 + 6\text{H}^+ + 6e^- \rightarrow \text{CH}_3\text{OH} + \text{H}_2\text{O}$	-17.3	-0.24
$\text{CO}_2 + e^- \rightarrow \text{CO}_2^{\bullet-}$	183.32	-1.9

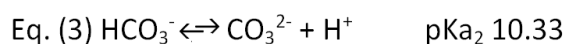
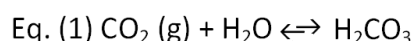
Table. 1 The standard ΔG° (25°C; pH=0) and standard potentials (E°) at 25°C, 1 bar and pH=7.

Thus, from Table 1, none of the most useful CO_2 reductions reactions requires a large potential, except for the formation of $\text{CO}_2^{\bullet-}$ radical, which is defined as a fundamental intermediate for the generation of products, such as CO, formic acid and methane. In order to achieve favorable conditions for the formation of this intermediate, metals with specific catalytic properties were already investigated in literature such as zinc, tin, gold, silver, copper, etc.⁵⁻⁷

However, despite the thermodynamic feasibility of reducing CO_2 , certain kinetic barriers hinder the multi-electron reduction processes, cause high overpotentials and limit the reaction. As a result, the reduction of CO_2 in aqueous solutions is expected to be accompanied, or even replaced, by kinetically more favorable H_2 evolution reaction.

Consequently, to optimize CO_2 reduction in terms of overpotentials and increase the selectivity and faradaic efficiencies, it is necessary to develop suitable electrode substrates with specific morphological characteristics (in terms of crystalline orientation and elemental composition).

Another factor to consider is that in aqueous solution carbon dioxide has a limited solubility, equal to 34 mM². Therefore, the most commonly used electrolyte is potassium bicarbonate (0,5 M solution of KHCO_3 , pH 7.4). The dissolution of gaseous CO_2 (eq. 1, slow process) involves the establishment of the acid/base balance reported in eq. 2, bringing the pH to a value close to neutrality.



According to many studies², the formation of this buffer system is important because it allows to keep the pH value constant even at the cathodic interterface. In fact, a local pH increase, described in eq.2-3,

certainly involves the decrease of the competitive H_2 formation, but at the same time also decreases the CO_2 concentration available at the cathode interface, thus slowing down his electrochemical reduction.

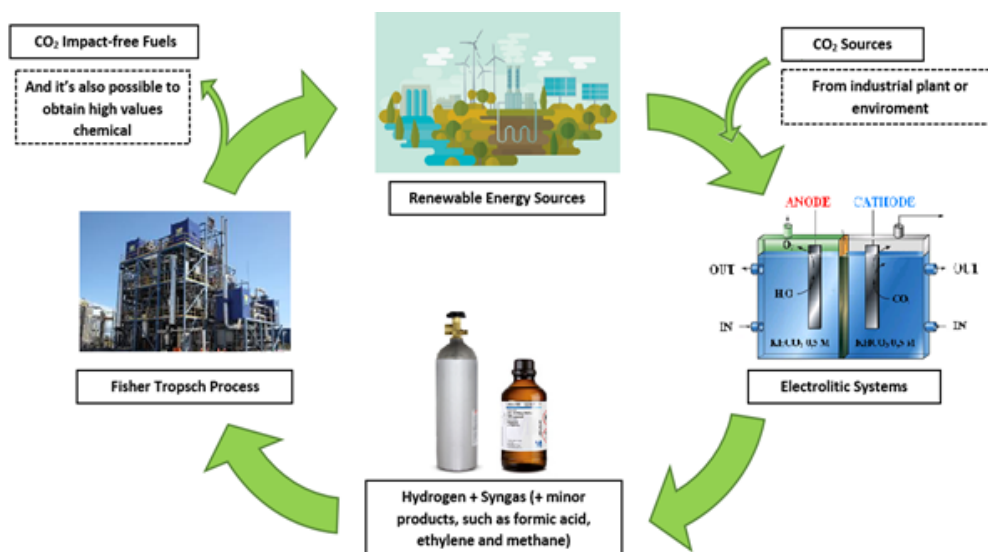


Fig.2 Carbon dioxide cycle coupled to renewable energy conversion

In this work, the electrochemical reduction of CO_2 was studied in aqueous environment, using high-performance cathodes with particular attention to favorable characteristics for scaling up the process for practical applications. Thus low preparation costs, abundant raw materials, and the use of harmless solvents are all significant aspects. A major part of this work is about copper based electrodes, first obtained from simple metal sheet, and later developed into porous electrodes, obtained through the electroplating of conductive carbon foams or the use of commercially available metallic foams. However the electrochemical properties of other nanostructured metal films were explored, like for example gold (see part 3). Copper is a material already known for its catalytic proprieties in terms of CO_2 reduction, in fact it's the only element able to catalyze more than 16 total products containing also two or more carbon atoms. Furthermore, the surface of these cathodes has been modified, via an electrochemical treatment, to emphasize their reactivity towards CO_2 reduction with the aim of selectively produce formic acid, methane and syngas ($CO + H_2$ mixture), a raw material that can be easily converted into high value chemicals via catalytic hydrogenation of CO , through Fischer-Tropsch like processes, providing access to the production of hydrocarbons with a wide range of molecular weights. For example, using this approach it is relatively straightforward to convert syngas in valuable chemicals like methanol, methane or dimethyl ether³, which may have a great impact as green fuels for internal combustion engines or fuel cells. Depending on the CO/H_2 ratio, the synthesis of simple monomers for the polymerization of a wide range of plastic materials is

also achievable, representing an interesting way to fix carbon dioxide into useful materials and close the carbon cycle (see Fig. 3).

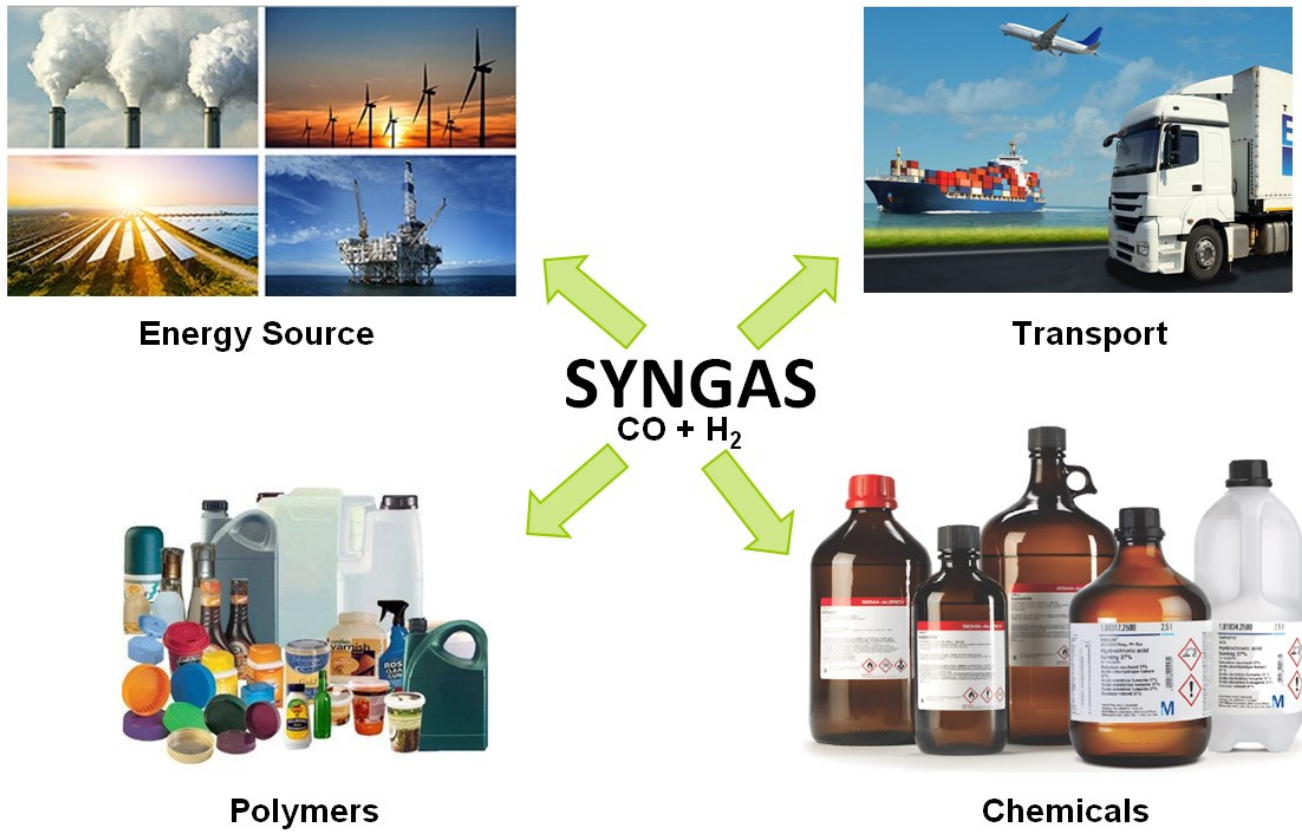


Fig.3 Multiple uses of Syngas

1.1 Electrochemical CO₂ reduction to fuels: techno-economic feasibility

Hydrocarbon fuels provide the majority of all transportation energy, and petroleum is the dominant feedstock from which transportation fuels are produced. Hydrocarbons produced from other feedstocks (fossil and biomass), as well as carbon-free energy carriers (such as hydrogen, batteries and ultracapacitors), are potentially more sustainable alternatives. The benefits of hydrocarbons over carbon-free energy carriers include higher energy density and use of existing infrastructure (fuel distribution and vehicles). Even after a widespread implementation of battery based technologies, hydrocarbons will continue to be needed especially as fuels in aircraft, sea vessels, and haulage vehicles, and they also provide the chemical building blocks for much of the chemical industry. Their widespread use calls for means to produce them sustainably. Using renewable energy (in the form of heat, electricity, and/or sunlight), carbon dioxide and water can be recycled into hydrocarbon fuels (Fig. 4) in a non-biological process. Initially, CO₂ captured from large industrial sources (e.g. aluminum plants) could be utilized. In the long term, the capture of CO₂ from the atmosphere⁸ would enable a closed-loop hydrocarbon fuel cycle (Fig. 2). Finding clever ways to limit/reduce/reuse CO₂ emission will be mandatory in the near future. The EU emissions trading system (EU ETS) is a main EU policy scheme to accomplish the European green deal and to combat climate change, reducing greenhouse gas emissions cost-effectively. The EU ETS works on the 'cap and trade' principle, where the CAP is reduced over time so that total emissions fall. A cap is set on the total amount of certain greenhouse gases that can be emitted by installations covered by the system. Participation in the EU ETS is mandatory for companies active in emission intensive sectors. In the next decades, the EU ETS will increase the price of CO₂ to put EU emissions on a path consistent with international climate targets, so that the most carbon intensive sectors are made unprofitable. At present, CO₂ taxation is 18.50 €/ton⁹, but the goal is to reach 55€ by 2030 and is foreseen 150€ by 2040 and between 200€ and 300€ in 2045-2050.

When solar energy drives the dissociation of CO₂ and H₂O, the fuel cycle is comparable to that of biofuels: an artificial device collects CO₂ and use solar energy to fix it in high energy carbon containing molecules. However, this fuel cycle avoids the biomass intermediate product, which consumes a lot of resources to cultivate (water, fertilizer, etc) and needs to be processed further to produce a fuel. Besides that, natural photosynthesis has a low energy conversion efficiency. For instance, optimized biomass practice with *saccharum officinarum* (sugar cane) currently produces up to 24 tons/ha of sugar and 13 tons/ha of ethanol annually through the direct conversion of atmospheric CO₂ to sucrose. However, once the external energy input (e.g., for fertilizers, mechanical harvesting and transport) is factored in, it turns out that natural photosynthetic solar fuels can produce net energy only in relatively limited geographical contexts. Indeed, the solar to fuel (STF) efficiency is usually not higher than 0.3%¹⁰.

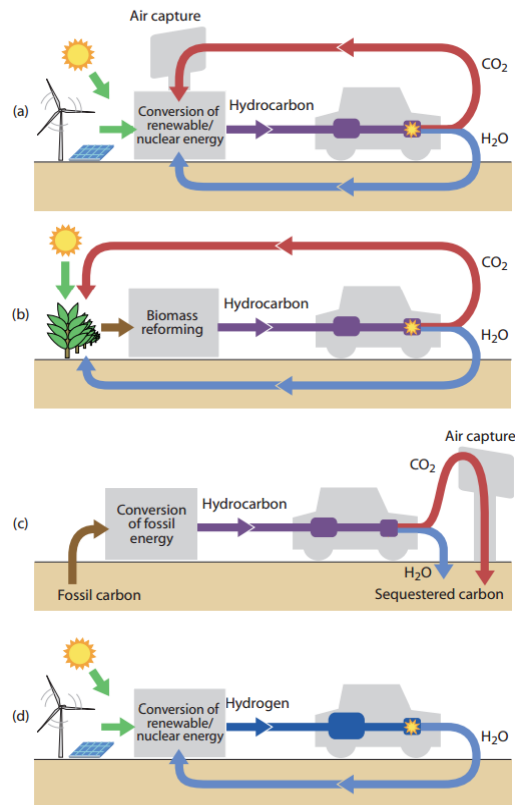


Fig. 4 Comparison of carbon-neutral fuel cycles for hydrocarbons produced using (a) renewable/nuclear energy (shown as solar and wind energy), (b) biomass, (c) fossil fuel. (d) Hydrogen produced by solar/wind energy is also shown for comparison with (a). Whereas the renewable energy based cycles (a, b, and d) are considered materially closed, the fossil fuel based cycle (c) is carbon-neutral but the carbon is stored in an oxidized form.¹¹

This is clearly inferior to the direct photovoltaic (PV) conversion with silicon panels which easily reaches 15-20% maximum solar power conversion efficiency. By considering the coupling with an electrolyser, whose energy efficiency commonly ranges between 50 to 70% (this wide efficiency range is clearly dependent on details about electrode materials, configuration and overall cell engineering)¹²⁻¹³⁻¹⁴⁻¹⁵⁻¹⁶ we observe that the PV+electrolyser system displays an STF >10 %, that is ca. 30 times higher than natural solar energy conversion via bio-mass. In water based electrolyzers, CO₂ can be supplied by bubbling in the aqueous media, or supplied from the gas phase to a gas diffusion electrode. The majority of research in aqueous coelectrolysis of CO₂ and H₂O has focused on improving current efficiency (product selectivity) at a given potential rather than maximizing energy efficiency (for lower operating cost) or current density (for lower capital cost). The CO₂ and H₂O are electrocatalytically reduced to products such as HCOOH, CO, CH₄, C₂H₄, and higher hydrocarbons and alcohols, depending on the cathode composition and cell parameters. Overall, the overpotentials needed to produce for example, H₂/CO are have been relatively high for performing an efficient electrolyzer, as, for example a current of 100 mA/cm² required the application of

about 3 V. We are thus currently working to improve such figures, having already recorded currents close to 500 mA/cm^2 using OD derived copper foam electrodes and 2 A/cm^2 target by using electrode stacks may be within our reach. Selectivity is already very good, with nearly 100% yield of syngas (CO/H_2). High temperature electrolysis with molten carbonate salts as electrolyte could be represent a further strategy to enhance electrolyser efficiency with respect to more conventional (and less energy intensive) water gas/phase electrolysis, as both the high temperature and high conductivity of the molten electrolyte may enhance the rate of product formation via electrochemical reactions. However, heat management is more complicated for these high temperature cells and can more easily lead to energy losses, as well as higher capital costs due to materials and equipment failures.

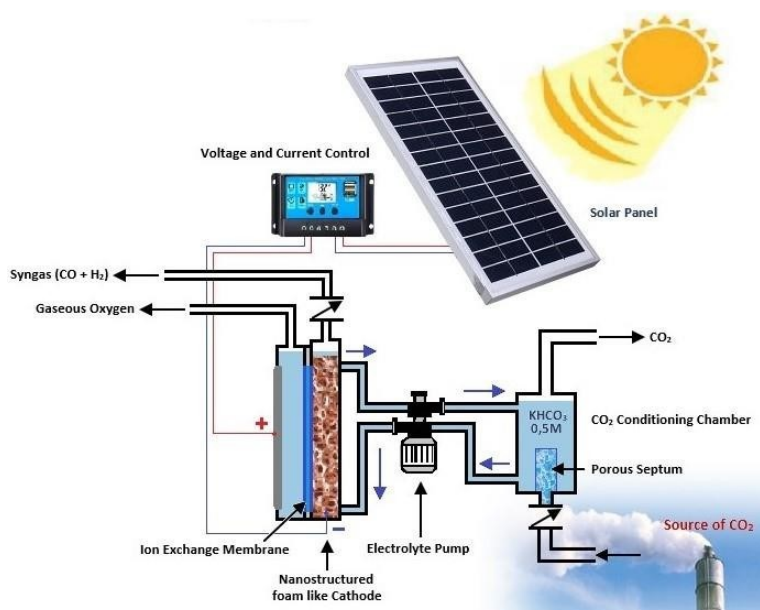
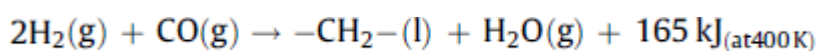
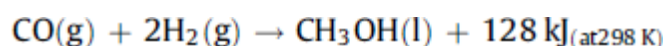


Fig. 5 Schematic example of photoelectrochemical device for CO_2 reduction based on an aqueous electrolyser. CO_2 saturates a carbonate buffer electrolyte which is then supplied to the solar powered electrochemical cell where the separate compartments perform water oxidation and CO_2 reduction. Here, as an example, an OD copper electrode modified with co-catalysts is shown to produce Syngas (CO and H_2 mixture) whereas oxygen is evolved at the anode. The CO_2 depleted electrolyte is circulated back to the saturation chamber where a new cycle begins.

While complex hydrocarbons could be directly obtained from the electrochemical cell (at present in low yields) it is perhaps simpler and often beneficial to produce one or both components (CO/H_2) of syngas and catalyze fuel synthesis from these energy-rich precursors. Fischer–Tropsch synthesis (FTS) was developed in the 1920s and has been used economically as part of coal-to-liquids (CTL) and natural gas-to-liquids (GTL) projects¹⁷. The reaction can be represented by:



where $-\text{CH}_2-$ is part of a hydrocarbon chain. A variety of hydrocarbons can be produced; chain growth depends on the catalyst, syngas composition, and reactor temperature and pressure. High temperature (300–350 °C) yields gasoline and low molecular mass olefins over Fe-based catalysts while low temperature reactors (200–240 °C) yield diesel and high molecular mass linear waxes over Fe or Co-based catalysts. The water-gas shift reaction competes under certain conditions. Synthesis typically yields hydrocarbon chains with a distribution of chain lengths, up to gasoline- or diesel-like fuel distributions. Methanol can be produced in an exoergic Fischer–Tropsch-like reaction. Traditional methanol synthesis is carried out by reforming syngas over a Cu–ZnO/Al₂O₃ catalyst¹⁸ according to:



It is worth observing that in case of a large size industrial plant, an economic analysis¹⁹ evaluated the renewable production of methanol at 2015 industrial electricity cost of Germany, showing that a large size plant could become economically viable at a methanol selling price of 500€/ton with a discounted

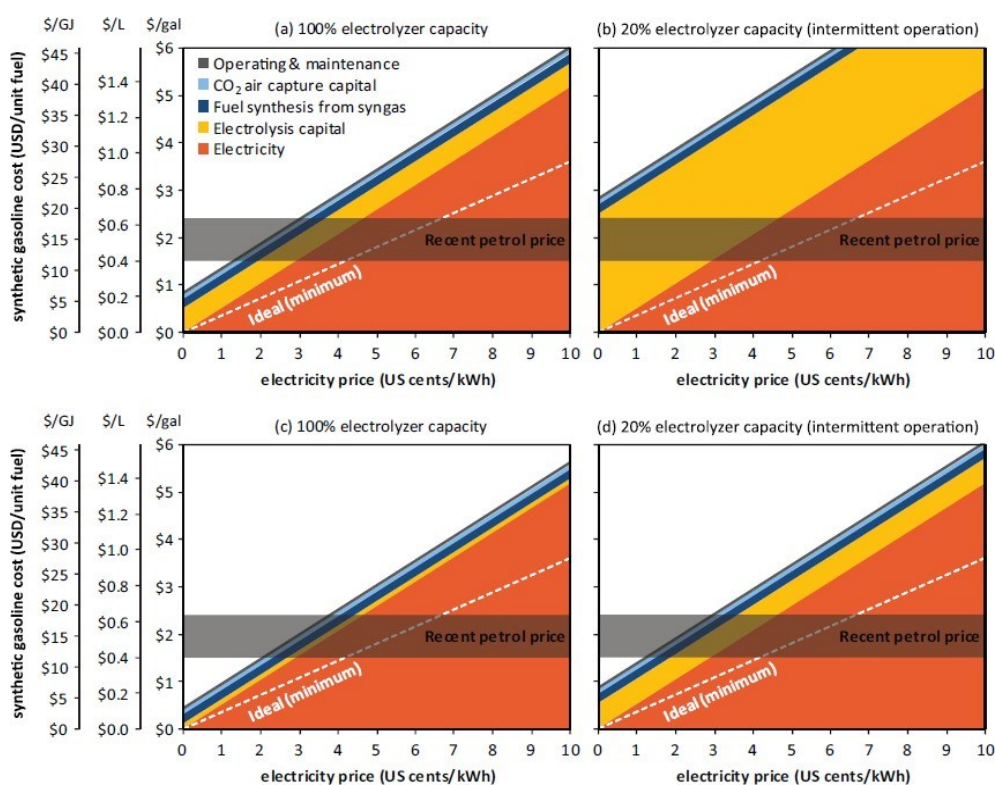


Fig. 6 Estimate of synthetic fuel cost versus electricity price including constant operation (a), (b) the same assumptions but with highly intermittent operation (a 20% capacity factor), and operating the electrolyzer at a higher current density with (c) constant and (d) highly discontinuous operation²².

payback time of ca. 10 years. The analysis assumed the reaction of CO₂ (not of CO) with hydrogen produced in a PEM water electrolyser in a high pressure reactor and that oxygen (produced at the anode) was also to be sold as a chemical product. It turned out that PEM electrolysers are by far the most expensive part of the methanol production plant accounting for more of 75% of the total capital investment (TCI) which makes such technological approach only convenient for methanol selling costs over 600€/ton for small and medium sized plants. A fundamental added benefit of this process is the fact that a considerable amount of CO₂ (71,600 ton/year for a large scale methanol producing plant with a capability of 50000 t/year) is sequestered from fossil plants and used for methanol production, which in turn allows for a reduction in operating plant costs in terms of CO₂ emission taxation. Moreover, comparing this solution with the traditional production by natural gas steam reforming process, a considerable fuel saving of about 30000 ton/year can be obtained²⁰. Overall, by assuming an efficient electrolysis of CO₂/H₂O (ca. 2A/cm²), it has been shown that the limiting cost of the solar fuel produced by electrolysis resides in the electricity cost²¹. It should be noted that, on the long term the cost of non renewable fuels is doomed to increase, while their distribution will become increasingly localized, often in geopolitically unstable areas.

With a constant power supply, synthetic gasoline could be produced at a competitive cost around \$ 2/gal (\$ 0.53/L) at an electricity price of ca. 3 U.S. cents/kW, which could increase to 5-6 U.S. cents/kW at a gasoline price of ca. 3\$/gal. At the moment, this approach is actively pursued by Iceland, which enjoys very favorable conditions of abundant renewable electricity sources from geothermal and hydrothermal sources. For example, Carbon Recycling International²³ is a world pioneer in turning CO₂ emissions into clean fuel and useful products. Founded in 2006 in Reykjavik, Iceland, CRI commercially offers a standard Emissions-to-Liquids (ETL) plant design with nominal 50.000-100.000 ton/yr methanol production capacity system where impurities are removed to produce CO₂ suitable for downstream methanol synthesis. Concentrated CO₂ is available in high concentration in many industrial processes (i.e. aluminum, concrete, ammonia synthesis) and thermal power plants and after purification is combined with hydrogen generated by water electrolysis using MW-scale electrolyser technology, utilizing renewable electricity to produce pressurised high purity H₂ and O₂ gases. With discontinuous sources, the short term economic benefits are lower (longer pay off time of the investment depending on the electrolyzer capacity) but the important advantage of these plants is to offer an ancillary service for national grid stabilization by providing long term energy storage (in chemical form), which is able to absorb the production peaks due to unpredictable Renewable Energy Sources (RES). In this way, these plants can present a potential opportunity to solve a critical aspect of fluctuations in grid power, due to the increased installed capacity of unpredictable RES (in particular solar and wind) installed in most of the EU Countries (i.e Germany, Italy and Spain).

1.2 Economic considerations

The electroreduction of CO₂ represents a unique approach to the valorization of CO₂ as a renewable resource for storing solar energy in energy rich molecules that, differently from pure hydrogen from water electrolysis, relies on the current hydrocarbon related infrastructure and technology grid for their treatment and distribution. If coupled to CO₂ sequestration strategies (see for example Direct Air Capture technologies²⁴) the storage of solar energy can be achieved with the concomitant reduction of the amount of CO₂ greenhouse gas in the atmosphere, thus providing the only means that we have to actively counter climate changes induced by anthropic global warming. As most of the materials that compose our electrolyser are earth abundant (i.e. copper) with very small amounts of co-catalysts, the critical factor that decides on the economic convenience of the process is related to the availability of low cost renewable electricity. This explains the successful example of CO₂ conversion approaches in Iceland, where geothermal power provides virtually cost free electricity. It is believed that with the widespread implementation of intermittent renewable sources, i.e. (solar, wind, and hydro electric plants) the need of long term efficient storing of electrical power will increase, while the cost of electricity will decrease, making the exploitation of solar fuels economically profitable.

1.3 Catalytic reduction of CO₂ on different metallic substrates:

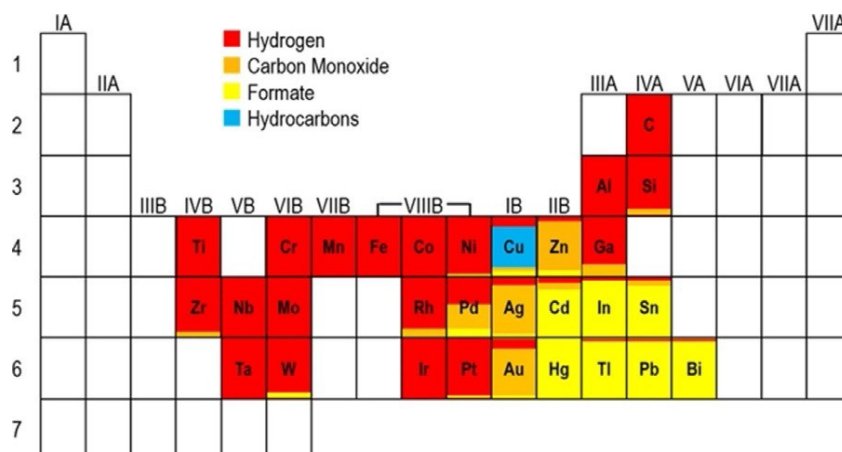


Fig.7 The carbon dioxide reduction periodic table, with all the metals active for the catalysis. (Jaramillo et al. *Energy Environ. Sci.* 2012, 5, 7050)

In this work, the catalytic performances of porous/foil copper-based electrodes were explored for the CO₂ reduction. However, there are many other metals substrates⁵⁻⁷ able to catalyze the CO₂ reduction. Depending on the different reactivity, each metals can be grouped according to the main reduction products it generates under suitable electrochemical polarization. A first group includes metals that selectively produce formate (HCOO⁻ at basic pH), such as Pb, Hg, Sn and In. The mechanism, according to the literature, firstly involves the formation of a radical intermediate, the CO₂^{•-} anion, due to the first monoelectronic CO₂ reduction. This reaction is then followed by a protonation of the radical by water and a second monoelectronic reduction to form HCOO⁻, this mechanism is shown in Figure 8.

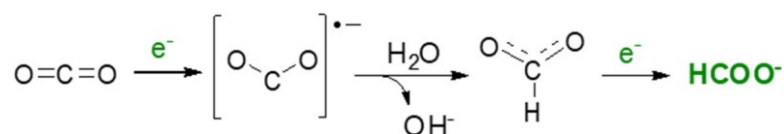


Fig. 8 Generally proposed reaction mechanism for formate generation on metallic substrates.

The second group of electrocatalysts includes metals able to produce carbon monoxide (CO), such as Au, Ag and Zn. These substrates are capable to generate more stable bonds between their surface and the reaction intermediates, which allows the establishment of the staged mechanism shown in Figure 9, with subsequent release of carbon monoxide (CO) and in smaller quantities, formate (HCOO⁻).

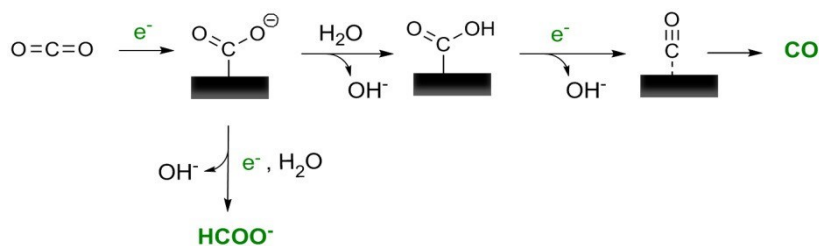


Fig. 9 Carbon monoxide evolution path on metals such as Au, Ag and Zn.

Other metals, such as Co, Ni, Fe and Pt, with both higher O affinity and H affinity, tend to favor the competitive hydrogen evolution reaction (HER), although small amounts of aliphatic alcohols have been detected on these metal surfaces.

Copper (Cu) is a unique metal able to catalyze various products including hydrocarbons and longer chain alcohols (such as methane, ethylene and ethanol). The Figure 10 shows the simplified mechanism proposed for the formation of some of the major CO₂ reduction products observed on copper based cathodes, in particular carbon monoxide, formate, methane, methanol and ethylene.

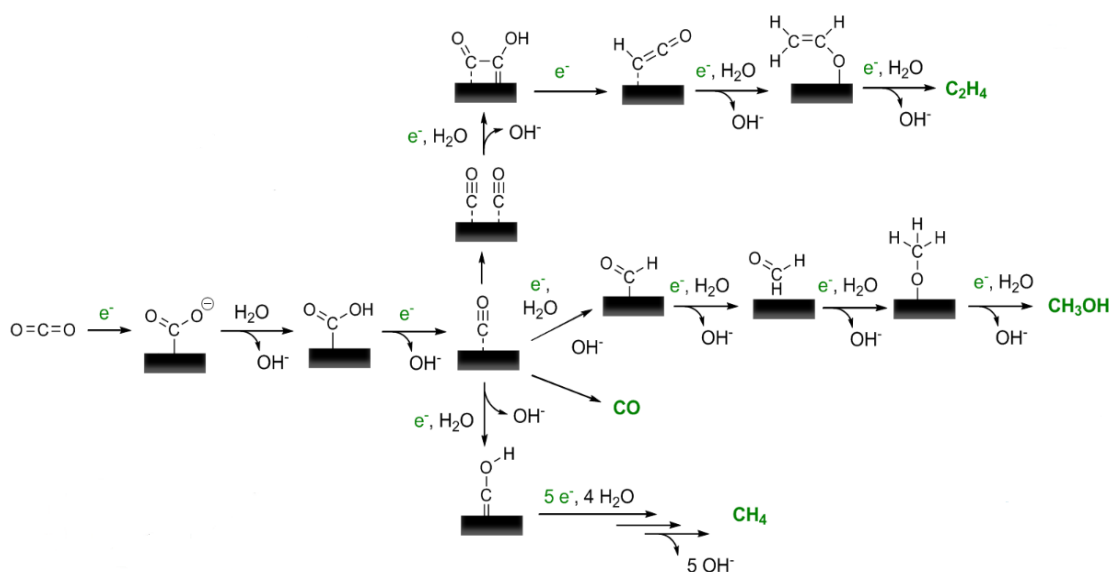


Fig. 10 Reduction mechanisms of CO₂ for some of the major products obtainable on copper cathodes.

At the same time, Cu catalysts were found to suffer the problem of poor selectivity, which results in their rather low faradaic efficiency (FE) which varies according to the complexity of the catalytic path associated with the single product. In order to better direct the activity towards a single CO₂RR product with high efficiencies and current densities we explored the deposition of metal co-catalysts, on top of nanostructured copper electrodes. The co-catalyst is a material that finely tunes the electrode reactivity, helping to emphasize the selectivity towards the CO₂ reduction, usually by suppressing the competitive H₂

evolution which usually occurs when working with protic electrolytes like water or by providing a particular stabilization to selected CO₂ reaction intermediates on the surface.

The enhancement of the performance of these copper based electrodes are particularly interesting both for possibility of electrode tuning, which makes it cheaper than gold and silver. In addition, copper is an environmental benign widespread conductor, cheaper than other excellent conductors like silver and gold, which facilitates its use for industrial applications and reduces the production and disposal costs associated with use of hazardous materials.

1.4 State of the art:

The variety of reduction products obtainable by electrolyzing aqueous CO₂ solutions with copper cathodes was deeply studied by the group of Prof. Jaramillo³ at the Stanford University. In this work they were able to identify up to sixteen different CO₂ reduction products using aqueous electrolyte (0.5 M KHCO₃).

The chemical identification and subsequent quantification of the products was carried out by ¹H-NMR spectroscopy of the electrolytic solution, applying an appropriate suppression of the water signal. In Figure 11 the values of faradic efficiency of the various products characterized in function of the applied bias are shown. These products have been divided into three categories according to their prevalence, that is major (maximum efficiency greater than 10%), intermediate (maximum efficiency between 1 and 10%), minor (maximum efficiency less than 1%).

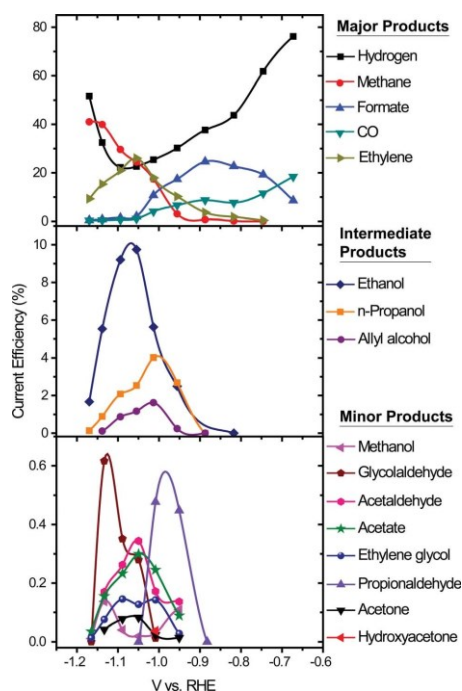


Fig. 11 Current efficiency for each product as a function of potential is shown for major, intermediate range, and minor products.

At low overpotentials (before reaching -0.75 V vs.RHE), only hydrogen, CO, and formate are observed. The lowest overpotentials, reveal a predominance of hydrogen production over both CO and formate, which are formed at relatively fast rates. As the overpotential increases, the percentage of the current going into hydrogen evolution decreases while CO_2 reduction products increase. At -0.75 V vs RHE, ethylene and methane are the first hydrocarbons to be observed, with ethylene favoured over methane. Above -0.9 V vs RHE even more complex molecules begin to be identified, like n-propanol, allyl alcohol and ethanol, the latter with a maximum yield of up to 10% of the total at -1.05 V vs RHE (about -1.7 V vs SCE). This study confirms, therefore, that copper can give rise to many compounds of industrial interest and that, consequently, the development of catalysts based on this metal with an appropriately nanostructured active surface can potentially lead to an increase in performance and selectivity in favour of certain specific products, as will be highlighted below.

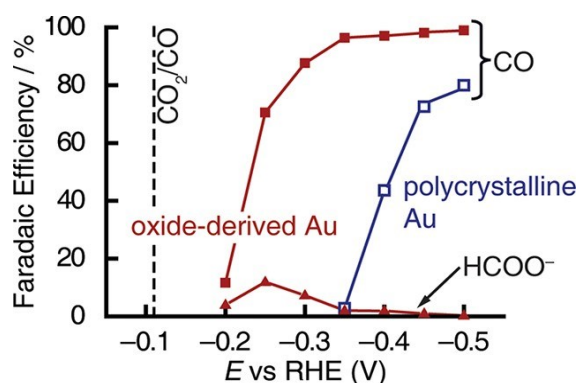


Fig. 12 Faradic efficiencies for CO and HCO_2^- production on oxide-derived Au and polycrystalline Au electrodes at various potentials between -0.2 and -0.5 V in 0.5 M NaHCO_3 , pH 7.2. Dashed line indicates the CO equilibrium potential.

In fact most of the proposed work in this thesis is based on the study and the optimization of novel copper cathodes consisting of a nanostructured cubic surface²⁵, whose preparation was inspired by a methodology reported by Prof. Kanan²⁶ of the University of Stanford. In particular, this work report the nanostructuring of gold surfaces through a pulsed anodizing treatment with the formation of oxides, which are then electrochemically reduced to Au^0 . The catalytic performance of these electrodes, referred to as Oxide Derived Au, are reported in Fig. 12, where increased yield in CO production is extremely evident compared to the simple gold foil (polycrystalline Au) starting from a threshold 150 mV less negative than the unmodified electrode. The high selectivity obtained ($> 98\%$ in CO) was later directly related to the number of grain edges present in OD cathodes, having an incomplete coordination sphere and, therefore, greater catalytic activity, being able to bind and stabilize CO_2 reduction intermediates.

In another work by Prof. Nilsson²⁷ at the University of Stanford, Cu nanocube structures were obtained from oxidation/reduction processes of polycrystalline copper by cyclic voltammetry in the -1.15 V vs RHE (approximately -1.85 V vs SCE) and +0.9 V (approximately +0.2 V vs SCE) range of using 0.1 M KHCO₃ and 0.004 M KCl. The oxidation and the presence of chlorides at pH greater than 4 promotes formation on the surface of CuCl, which has a "templating" effect in the formation of nanocubes. From morphological studies using electron transmission microscopy (TEM) it was possible to identify the exposed crystalline faces of these nanocubes, corresponding to Cu(100).

Measurements of the products formed from CO₂RR were made using an OLEMS system (Online Electrochemical Mass Spectrometry), which allows to measure the variation of the MS signal, relative to the mass spectrum, as a function of the applied potential. The Figure 10 shows that the exposure of the specific face (100) leads to an increase in the catalytic selectivity towards ethylene compared to the non-nanostructured copper foil, as well as allowing the achievement of higher values of current density.

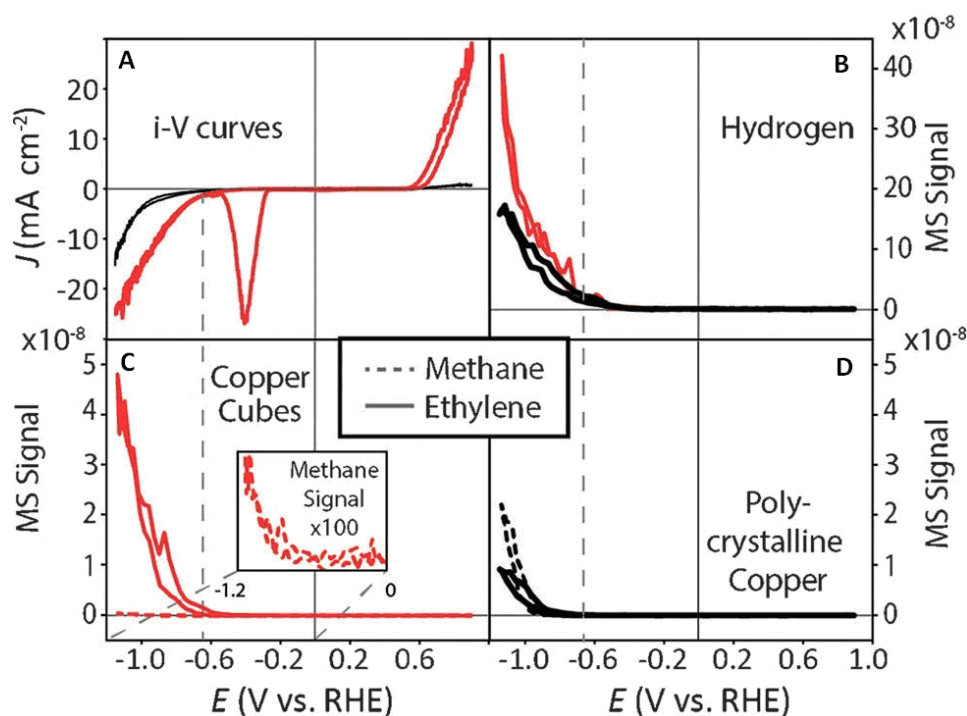


Fig. 13 A) Cyclic voltammograms of Cu nano-cubes (red) and polycrystalline (black) copper surfaces and corresponding hydrogen formation measured by OLEMS shown in (B). Methane (dashed) and ethylene (solid) formation measured by OLEMS on C) the Cu Cube surface and D) polycrystalline copper, showing a dramatic change in electrode selectivity toward Ethylene production.

Cubic surface nanostructures were also obtained by Roldan's group²⁸ at Ruhr University Bochum. In this case, the nanocubes are obtained in aqueous 0.1 M KCl solution through the optimized electrochemical

oxidation on copper foils. Formation of nanocubes is consequent to the electrochemical reduction of the oxidized CuO_xCl_y surface (about 20% of O and 24% of Cl) generating cubes with an approximate side of about 250-300 nm. These modified electrodes underwent a further treatment using H_2 , O_2 or Ar plasmas, which enabled to obtain structures with variable O/Cl content. Fig.14 shows the electrocatalytic performances of these nanostructured cathodes in terms of total current and yield of majority products (CO, ethylene and ethanol).

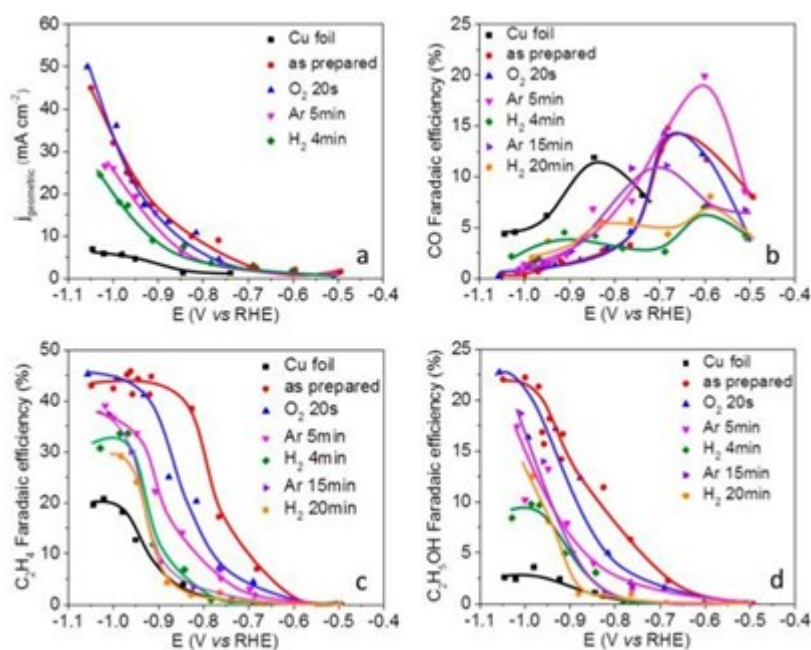


Fig. 14 Potential-dependent geometric current density (a) and Faradic efficiencies of (b) CO, (c) C_2H_4 , and (d) $\text{C}_2\text{H}_5\text{OH}$ after 1 h of electrochemical reaction in a CO_2 -saturated 0.1 M KHCO_3 solution.

According to these reports, all nanostructured electrodes are more performing than simple foils. Another advantage in the preparation of nanostructured and/or porous cathodes is certainly constituted by the increase of the active area exposed to the electrolyte, which results in enhanced current x unit of geometrical area. Furthermore, in the case of nanostructured substrates, the local confinement of the electrolyte due to the morphological roughness of the interface can lead to localized variations of the pH during electrode operation, which may have repercussions on the faradaic efficiencies and the selectivity of CO_2 reduction products. In order to investigate this possibility, during my work the application of an electrochemical treatment finalized to the formation of copper nanocubes on foils and graphite foams was explored, in the frameworks of CO_2 electrolysis.

1.5 Experimental set-up and cell design for CO₂ electrolysis

Whereas for the various phases of cathode preparation single-compartment cells were used, these systems are unsuitable for the reduction of CO₂, as a separation between cathode and anode should be ensured to avoid re-oxidation of products by the unwanted contact with the platinum counter-electrode. A cation exchange membrane consisting of Nafion[®] 117, a polymer based on tetrafluoroethylene sulfonate was used as a compartment separator. As shown schematically in Fig. 15, the membrane separates the cathode compartment from anode, both filled with KHCO₃ 0.5 M solution pre-saturated with CO₂ (pH: 7.4).

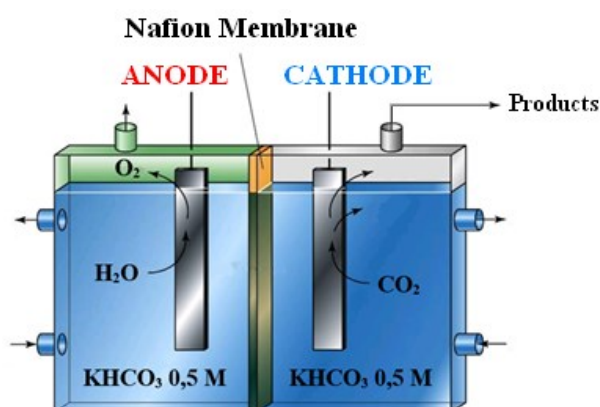


Fig. 15 Scheme of an electrolytic two compartments cell for CO₂ reduction

The cells developed for the evaluation of the faradic efficiencies in a laboratory scale setup were designed in order to minimize the compartments volumes and to continuously recirculate the electrolyte (that is actually contained in a separated storing compartment). The setup allows also a direct and gastight connection to the gas chromatograph that can automatically sample the headspace at preset times.

The cells modules used in this type of measurements are made of Polymethylmethacrylate (PMMA) (Lexar[®] or Corian[®]) which is resistant to the aqueous chemical environment we work in and has good thermal and mechanical properties. These modules can be assembled and interchanged easily, in order to replace the electrolyte or the electrodes, when necessary. Two types of cells were mainly used named as **type 1** and **type 2**.

- **Type 1:** This cell designed for use on small scale and fast experiments (cathodes ca. 1cm²) consists of an anodic and cathodic compartment separated by the Nafion membrane. Each compartment contains an electrolyte volume of 2 ml and allows the cathode and anode to be separated at a maximum distance of 10mm. Using a peristaltic pump it is possible to simultaneously recirculate the gas headspace (approx. 15ml) and the electrolyte contained in the reservoir placed below the cathodic compartment (that allows to store 25ml of CO₂ saturated electrolyte) (see fig. 16). Thanks

to this small flow electrolytic cell it is possible to measure the J/V characteristics of the electrodes as well to quantify their performance in terms of faradic efficiency for reduction products.

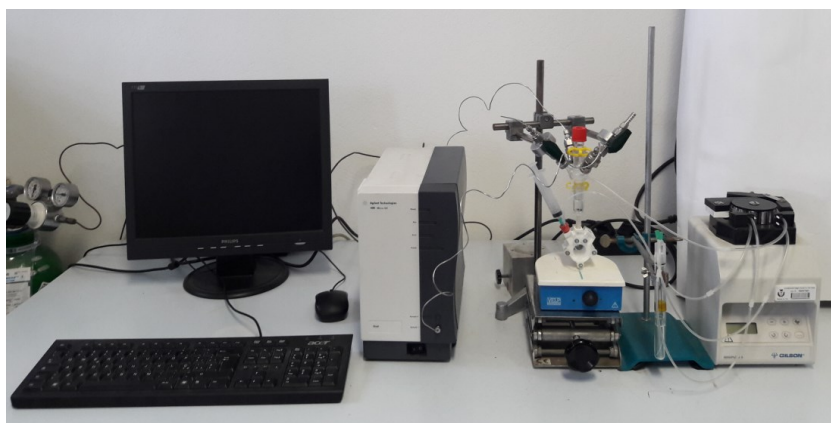


*Fig. 16 Analytical setup equipped with the micro-GC for the gas analysis and quantification and on the right the electrochemical cell and the peristaltic pump for the electrolyte and head space recirculation.
(more details are reported in paragraph 2.2.2)*

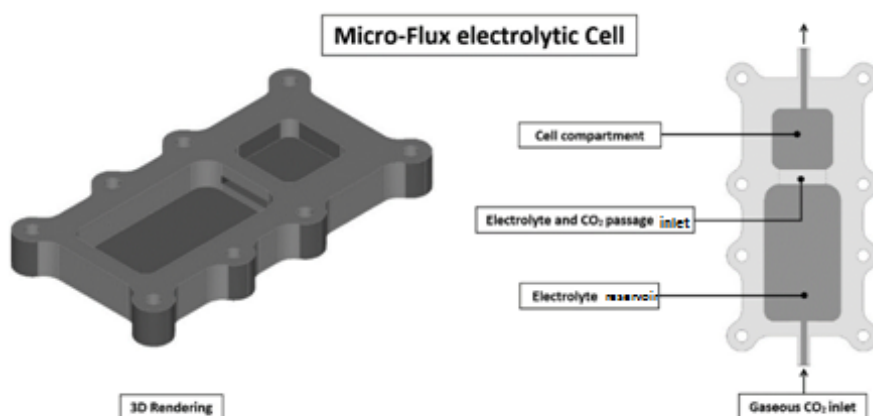


*Fig.17 Scheme of the **type1** flow cell used for our small-scale experiments (the picture on the left shows the 3D rendering of one single compartment, on the right a simple description of the components).*

The figure above (Fig 17) shows some of the details of the Type 1 cell, defined *Type 1 Micro Flux*, used during the experiments for the quantifications of the gaseous product with the gas chromatograph. This particular type of cell is composed by two little compartments that respectively hosts the working and reference electrode and the counter, constituted by a platinum wire. All the system guarantees a continue recirculation of the electrolyte and the gaseous headspace thanks to the use of properly settled peristaltic pumps. On the top of the cell is located a glass six-way connector in which are located respectively the

tube, connected to the cell, the pump connection interface (that direct the gases again through the cell) the two in/out tubes of the gas chromatograph and the two in/out tubes used for the initial carbon dioxide bubbling.

- **Type 2:** This type of cell was appropriately designed for the quantification of soluble CO₂ reduction products collected in the cathodic compartment during a prolonged electrolysis under constant CO₂ flow. (the times depends on the specific efficiencies for the chosen product and the analytical resolution of the used quantification technique). Depending on their (usually lower) faradaic efficiency the detection of water soluble products requires longer electrolysis times in order to accumulate a sufficient analytic concentration to obtain an NMR spectrum with an acceptable S/N ratio. In our case the small cell volume (variable from 2 to 6ml) allows to reach a sufficient concentration of reduction products for analytical purposes with experiments of the duration of few minutes. The cell is constituted by four modules held together with steel screws (M4 thread) and Teflon fastening washers. The compartments are further sealed with Teflon or silicon gaskets, in order to prevent electrolyte leakage. The working electrode is housed in the cathode compartment together with the reference electrode. The counter-electrode (a platinum wire) is inserted on the anodic compartment and is separated from the other electrodes by the usual Nafion® membrane. (see fig 18)



*Fig.18 On the left **type 2** electrochemical cell for the accumulation and analysis of water soluble products (formate and alcohols); on the right is shown a 3D rendering of one of the modular components*

1.6 Cell making

The design and making of these devices was made possible by tooling devices available at external companies. The design in particular was carried out by the use of specific computer aided design (Solid Works and Think Design) software that consent to achieve a high resolution 3D rendering of the final parts, necessary for the subsequent manufacturing with CNC machines

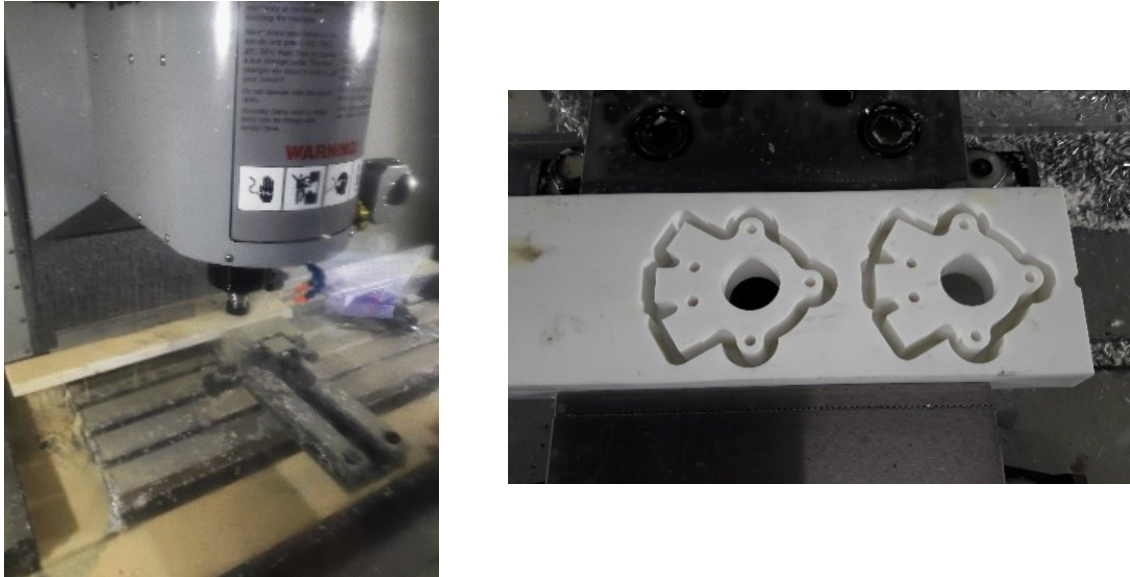
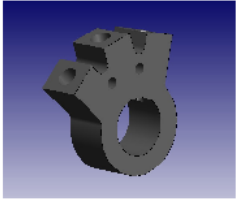
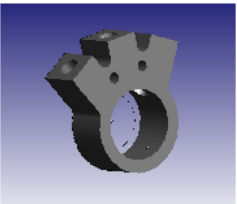
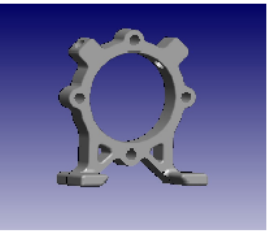
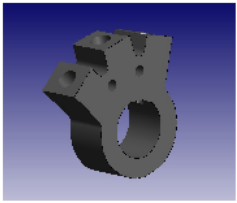


Fig. 19 Milling cutter used for the machining of cell modules and on the left the semi-finished cell components are visible on the right.

In fact the realization of the physical object was made possible by using advanced mechanical machining techniques (in particular the machine codes were made with Mastercam interface), using a three axes HAAS numerical control cutter (VF3-SS) and a custom made pantograph, instruments able to guarantee the highest possible precision (with a machine error of the order of $10^{-4}/10^{-5}$ m) in the carving of the shapes and in the orientation of the pieces (see Fig. 19), an important characteristic for the correct sealing of the final cell.

Milling polymeric materials needs particular attention in the choosing of the right parameters such as the advancement speed of both XY axes as well of the Z. The rpm of the tool can have a huge influence in the final shape of the piece as well. An excessive axes speed can cause the deformation of the surface with a consequent Z error and angular velocity, moreover values higher to 9000 rpm can cause the melting of the surface leading to the same result. In order to avoid thermal deformation a constant flow of refrigerant mixture (at 2.5bar) was maintained during the milling process.

In the table below are reported the main characteristics of the cells made using this technique:

Cell Compartment 3D rendering	Description	Catholyte volume	Main use
	Modular round compartments (20mm ID, 20mm thick) made in Corian + lexan transparent closing walls	6.2ml	Formate analysis
	Modular round compartments (25mm ID, 20mm thick) made in Corian + lexan transparent closing walls	15ml	Formate analysis
	Modular round compartments (60mm ID, 8mm thick) made in Corian + lexan transparent closing walls. each module is equipped with recirculation capillars	20ml	Formate and gaseous products analysis
	Modular round compartments (20mm ID, 20mm thick) and closing walls made in Teflon	6.2ml	For organic electrolytes

Tab. 2 Main characteristics of some of the produced cell prototypes

Particular attention in cell developing was also given to innovative techniques such as the 3D printing that allowed us to built more complex and advanced cells in significantly reduced times, not only in small scale but also for larger scale experiments. This technique is characterized by a really high versatility that allows to create various shapes that cannot be obtained with a common three axes milling. The availability of different typologies of materials permits also to tailor the cell components to our needs in fact, we were able to print prototype cells moving from simple PLA to high resistance ABS and nylon as spacers and membrane support for the internal sealing, using an appropriate SBR rubber filament.

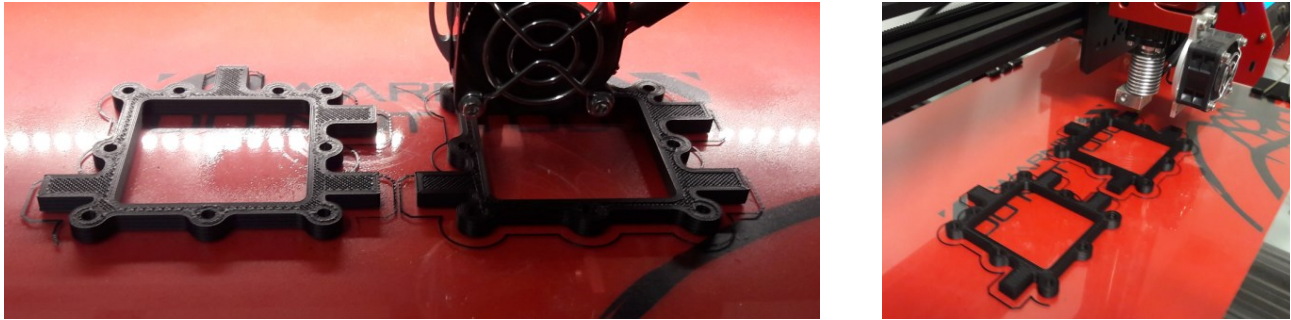


Fig. 20 3D printing of two ABS spacers for a flux cell prototype

The 3D printing used together with the traditional CNC milling was chosen for building of more elaborated devices suitable for larger scale experiments. A first generation of this type of cells collects and combines in the design the optical transparency and the mechanical resistance of the Lexan

CELL SCHEME

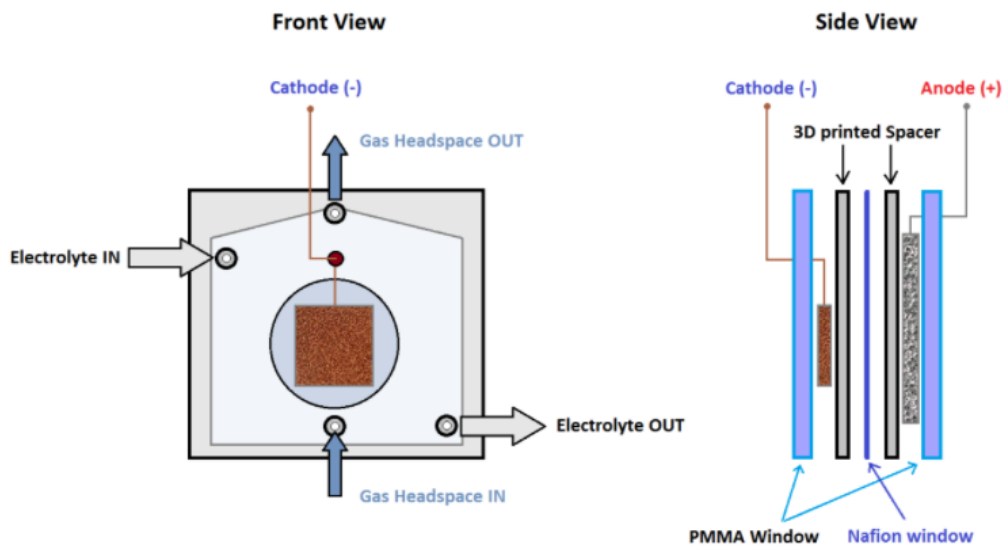


Fig. 21 Scheme of a 3D printed cell

polymer (PMMA) with the flexibility of a 3D printed spacer, permitting in this way to guarantee the perfect sealing for much larger surfaces allowing to develop cells capable to host larger area electrodes (> 25 cm²). On this purpose various models were prepared and customized for cathodes ranging variable dimensions from 5x5 cm up to 20x20cm combined with a proper CO₂ source and a recirculation circuit.

As described in the image above (fig. 21), these electrochemical cells are composed by a large PMMA wall (9mm thick) where inlets and outlets for CO₂ and electrolyte circulation were obtained. A rubber septum is also sealed in place for the electrical contacts.

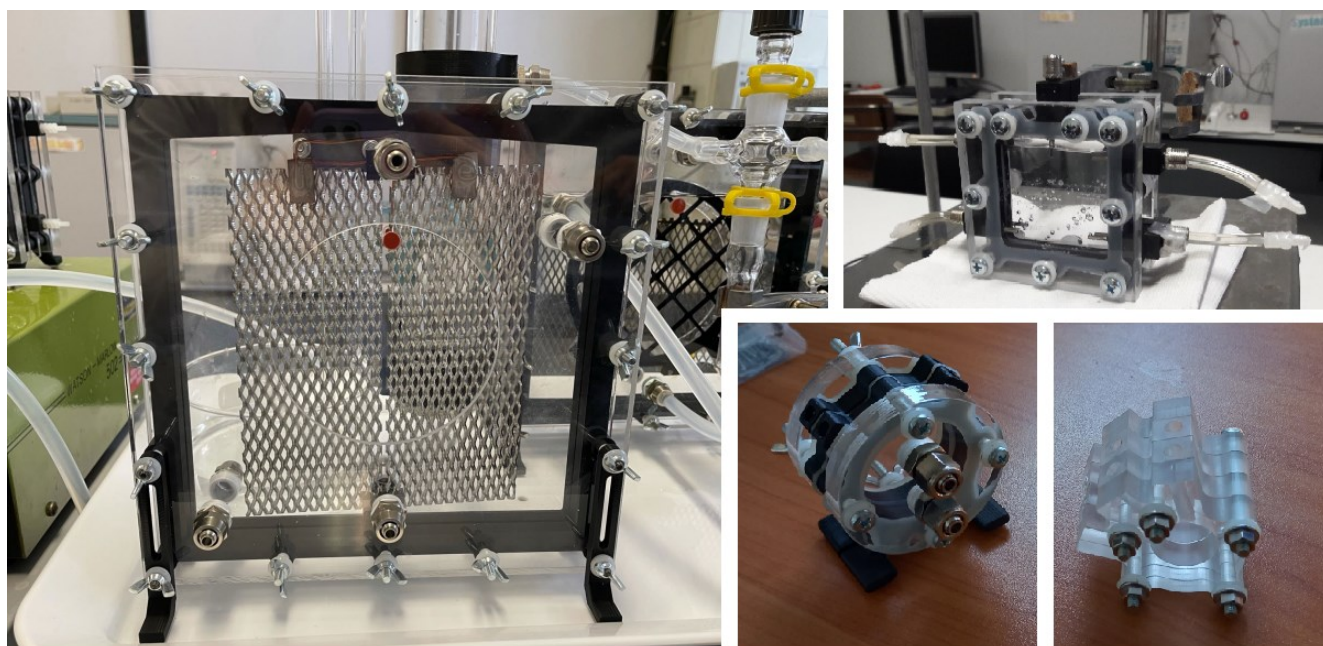


Fig. 22 Images of some of the combined electrochemical cells realized with PMMA and 3D printed parts (see fig 17)

2. Product Analysis and interface characterization

2.1 Morphological characterization of nanostructured cathodes

2.11. Scanning Electronic Microscopy (SEM)

Morphological characterization of nanostructured cathodes described in this thesis was done by scanning electron microscopy or SEM, using a Zeiss EVO 40 at the Electronic Microscopy Center at the University of Ferrara. A scanning electron microscope (SEM) uses a focused electron beam on the sample as a source to produce images of its surface. The electrons are produced by a gun and accelerate using 10-20 keV of potential difference. A set of magnetic lenses transforms the beam emitted by the gun into a spot of some nm that is sent into the sample. The electrons interact with the atoms in the sample, producing the emission of electrons (secondary and back scattered electrons) and photons that contain information about the surface topography and composition. Secondary emitted electrons yield the best-resolved signal and therefore are used for conventional SEM imaging of samples. During the measurements of the samples are stored in a high vacuum (10^{-6} torr) chamber thus the samples must be dry and conductive, or properly treated in order to meet these requirements. This technique allows for the observation of the electrodes surface with magnifications and details superior to simple optical microscopy (which is limited by wavelength of visible light) characteristic that has been fundamental for the investigation of the cathode interface after the various preparation steps, as well as for the correlation with the reported catalytic activity.



Fig.23 On the left the sample holder of the electron scanning microscope is shown; on the right the general set up of the instrument.

A SEM microscopy can also be equipped for EDS spectroscopy (Energy dispersion spectroscopy), this technique is based on the X-ray emission by the elements subjected to the electronic bombardment and allows the identification of the elementary composition of a given surface spot. Usually the top 2 micrometers of sample thickness can be sampled, depending on the energy of the incident electron beam. This technique can also be exploited to build composition maps of elemental distribution, useful to address the homogeneity of the analyzed surface.

2.1.2 High-resolution transmission electron microscope (HR-TEM)

To complete the morphological characterization HRTEM (High-Resolution TEM) investigation was carried out thanks to a collaboration with the Institute of Microelectronics and Microsystems (IMM) of Bologna. High-resolution transmission electron microscope (HRTEM), is a type of electronic microscopy that consists of an electron gun, which produces the electron beam that through a system of magnetic lenses is focused on the object. The electron source, the cathode, is a heated V-shaped tungsten filament or, in high-performance instruments, a pointed rod of a material such as lanthanum hexaboride. Electrons are emitted by the cathode, accelerating toward the anode as they pass through the sample. The electrons interact with the atoms in the sample, which diffract the beam, producing an electronic diffraction pattern which contains important information about the crystallography nature and orientation of the investigated phase. Also X-Ray microanalysis of the elements is possible, as discussed before. The most significant limitation of TEM is the need for very thin samples, usually less than 100 nanometers in order to allow the correct transmission of the electron leading, for example, to the detailed observation of the copper core/shell cuprite that forms on the surface of the cathodes, that we will later discuss.

2.2 Analytical setup for the identification and quantification of CO₂ reduction products

2.2.1 ¹H-NMR nuclear magnetic resonance spectroscopy

Following CO₂ reduction, identification of some of the products dissolved in the catholyte (i.e., the electrolyte present in the cathode) was performed by ¹H-NMR spectroscopy, using the 400 MHz instrument provided by the Department, a Varian Mercury Plus model, shown in Fig. 24. The main compound researched with this technique was the formate anion HCOO⁻. In order to quantify the water soluble products, an internal standard (DMF) was added. A typical standard solution is composed by 500 μl of D₂O + 4 μl of DMF from which a 50 μl aliquot was added to the sample tube, that is filled with 600 μl of electrolytic solution. In the two-compartment type 2 cell, constant potential electrolysis (chronoamperometric experiments) was carried out for a given time. At the end of each electrolysis an aliquot of catholyte was sampled through one of the sealed inlets drilled in the cell walls and immediately transferred to an NMR tube in which the internal standard was also added. The NMR spectrum was acquired with a suitable water signal suppression mode, which, however, obscures a significant portion of

the spectrum around the water resonance peak. This aspect represents the main limitation in the use of this technique, since the identification of products present in traces or with characteristic resonances near the area affected by water is compromised. It was however possible the clear and precise identification of formate, whose signal appears as a singlet at 8.3 ppm due to the single hydrogen atom present in such molecular ion and its quantification was conducted by comparison with the intensity of the aldehydic proton resonance of DMF .

At some potential values it was also possible to observe the formation of other products resulting from the reduction of CO₂ in an aqueous environment, such as acetaldehyde, acetone and ethanol, which however, in our case generated, very weak NMR signals, difficult to quantify with precision. In general these latter products are present with have a < 1 % FE

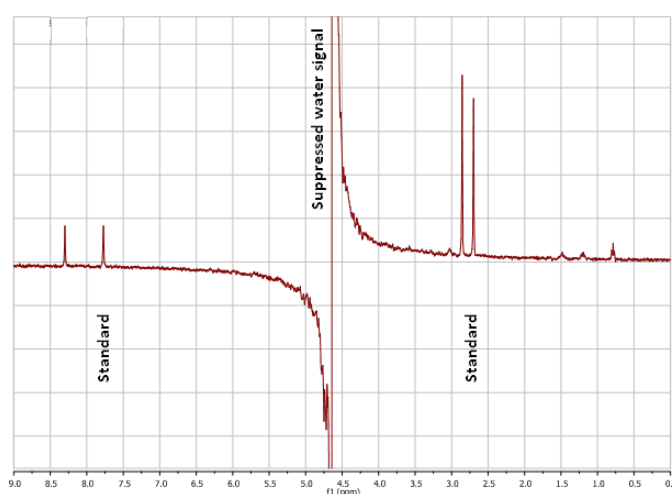


Fig.24 Varian Mercury Plus model at University of Ferrara (on the left) and ¹H 1D NMR spectrum on a sample of 0.5 M KHCO₃ containing a mixture of products (on the right)

As can be observed in the reported above spectrum, typically the peak at chemical shift of 8.33 ppm is related to formate, located near the DMF singlet used as quantification standard at ca. 7.8 ppm (Fig. 24 on the right), moreover the dip in the baseline near the middle of the spectrum corresponds to the location of the suppressed water peak. In addition to these, three chemical shift peaks of 1.87, 1.2 and 0.92 ppm corresponding to acetate, acetaldehyde and propionaldehyde are visible at trace level. The peak assignments are given in Table 3.

CO ₂ Reduction Products						Assignment		Known Standards				
Chemical Shift	¹ H splitting	J coupling	COSY cross peaks	¹³ C (HSQC)	¹³ C (1D)	¹³ C splitting	Probed Nucleus	Product Name	¹ H splitting	Chemical Shift	J coupling	¹³ C (1D)
9.57	s						CH ₃ CH ₂ C H=O	Propionaldehyde	s	9.57		209.6
9.55	q	2.93	2.12				CH ₃ C H=O	Acetaldehyde	q	9.55	2.93	206.9
8.33	s			172.2	171.76	s	HCOO	Formate	s	8.33		171.77
				161.16			Bicarbonate	Electrolyte				162.97
				130.74			Phenol	Internal Standard	t	7.2	7.61	130.7
				121.24			Phenol	Internal Standard	t	6.86	7.61	121.07
				115.92			Phenol	Internal Standard	d	6.8	8.78	116.31

CO ₂ Reduction Products							Assignment		Known Standards			
Chemical Shift	¹ H splitting	J coupling	COSY cross peaks	¹³ C (HSQC)	¹³ C (1D)	¹³ C splitting	Probed Nucleus	Product Name	¹ H splitting	Chemical Shift	J coupling	¹³ C (1D)
5.89	m		5.16, 5.06, 3.99	137.4	137.79	dd	CH ₂ C HCH ₂ OH	Allyl Alcohol	m	5.9		136.86
5.16	d	17.57	5.89, 3.99		116.36	d	CH ₂ CHCH ₂ OH	Allyl Alcohol	d	5.17	17.33	115.74
5.13	q	4.68	1.21		88.67	d	CH ₃ C H(OH) ₂	Acetaldehyde	q	5.13	5.37	88.57
5.06	d	10.54	5.89, 3.99		116.36	d	CH ₂ CHCH ₂ OH	Allyl Alcohol	d	5.07	10.5	115.74
4.94	t	5.27	3.4		90.6	d	(OH) ₂ CHCH ₂ OH	Glycolaldehyde	t	4.94	5.13	90.63
4.843	t	5.27					CH ₂ CH ₂ C H(OH) ₂	Propionaldehyde	t	4.85	5.87	92.77
					91.4	s	(OH) ₂ CHCH(OH) ₂	Glyoxal				91.39
WATER												
4.25	s						CH ₂ C(=O)CH ₂ OH	Hydroxyacetone	s	4.25		68.36
3.99	d	4.68	5.9, 5.15, 5.05	63.5	63.44	d	CH ₂ CHCH ₂ OH	Allyl Alcohol	dt	3.99	5.13, 1.46	62.96
3.545	s			63.65	63.41	s	HOCH ₂ CH ₂ OH	Ethylene Glycol	s	3.54		63.41
3.54	q	7.03	1.06	58.3	58.3	d	CH ₃ CH ₂ OH	Ethanol	q	3.53	7.32	58.3
3.44	t	7.03	1.42	64.35	64.42	d	CH ₂ CH ₂ CH ₂ OH	n-Propanol	t	3.44	6.49	64.43
3.4	d	4.68	4.94	65.6	65.38	d	(OH) ₂ CHCH ₂ OH	Glycolaldehyde	d	3.4	5.13	65.42
3.23	s			49.85	49.76	s	CH ₃ OH	Methanol	s	3.23		49.75
DMSO Internal Standard												
2.44	q	7.03		37.25			CH ₃ C H ₂ CH=O	Propionaldehyde	q	2.44	7.32	37.34
2.12	d	2.93	9.55	30.94	30.8	d	CH ₃ CH=O	Acetaldehyde	d	2.12	2.93	30.89
2.1	s			30.9			CH ₃ C=OCH ₃	Acetone	s	2.1		30.44
2.02	s			25.3			CH ₃ C(=O)CH ₂ OH	Hydroxyacetone	s	2.02		25.63
1.79	s			24	24.19	d	CH ₃ C(=O)O ⁻	Acetate	s	1.87		23.74
1.48	dt	5.85		30.95			CH ₂ CH ₂ CH(OH) ₂	Propionaldehyde	dt	1.47	7.57, 12.94	30.45
1.42	sextet	6.44	3.44, 0.77	25.28	25.37	t	CH ₃ CH ₂ CH ₂ OH	n-Propanol	sextet	1.42	7.32	25.41
1.21	d	5.27	5.13	24	23.82	d	CH ₃ CH(OH) ₂	Acetaldehyde	d	1.2	5.37	23.5
1.06	t	7.03	3.54	17.4	17.62	d	CH ₃ CH ₂ OH	Ethanol	t	1.06	7.08	17.63
0.92	t	7.61		5.74			CH ₃ CH ₂ CH=O	Propionaldehyde	t	0.92	7.32	5.54
0.78	t	7.61					CH ₃ CH ₂ CH(OH) ₂	Propionaldehyde	t	0.78	7.32	8.47
0.77	t	7.61	1.42	10.2	10.34	d	CH ₃ CH ₂ CH ₂ OH	n-Propanol	t	0.77	7.57	10.36

Tab. 3 Product identification based on peak information for CO₂ reduction products compared to peak information for commercial authentic standards³.

2.2.2 Gas chromatography analysis (GC)

The determination of gaseous products required the use of gas chromatographic techniques and in particular of two instruments. The first one is an Agilent Technologies 490 micro-GC, equipped with a column with a molecular sieve stationary phase (5 Å, length = 10 m) and a pre-column connected to a back flush system, indispensable to avoid the introduction of CO₂ into the column and the consequent passivation that can occur to the stationary phase. The used carrier gas is Argon, while the GC detector is a thermal conductivity one (TCD). This set-up allows for the detection of small molecule gaseous products, such as H₂, CO, and CH₄, which can be separated by an isothermal program at 60°C. The micro-GC was directly connected to the custom made electrochemical cell, via gas tight connections (see on this regard the image shown in Fig. 25 and 29). Sampling during the chronoamperometry measurements was carried out automatically at predetermined times before injection into the column, the cell headspace (15 mL) is mixed and "homogenized" thanks to specific recirculation pumps. From this large volume, only 9 µl are actually injected into the column, while the rest is fed back into the cell headspace. Identification and quantification of the products was performed by comparison with properly made calibration curves obtained by introducing, in the same electrochemical cell used for the measurements, known amounts of gaseous standards of H₂, CO and CH₄ in similar volumes to the one expected by the experiments. The calibration curve are also verified periodically in order to guarantee a correct response of the instruments that can vary during the time due to little changes to the stationary phase caused by prolonged usage. A periodic regeneration of the molecular sieve column is also necessary.

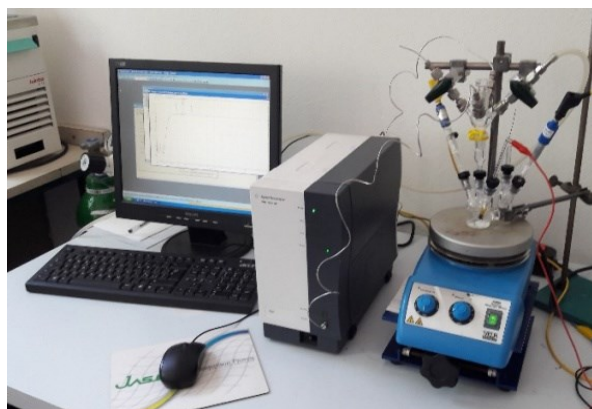


Fig. 25 Experimental setup for gas analysis during CO₂ electrolysis.

The typical chromatogram thus obtained show three peaks at retention times lower than 0.8 min that are related to hydrogen (resulting from water reduction) atmospheric oxygen and nitrogen, respectively (Fig. 26). In contrast, the two peaks corresponding to CH₄ and CO exhibit in normal condition retention times of 0.9 min and 1.8 min, respectively. These peaks are usually very broad and are better visible by zooming the chromatogram as shown in Fig. 27/28.

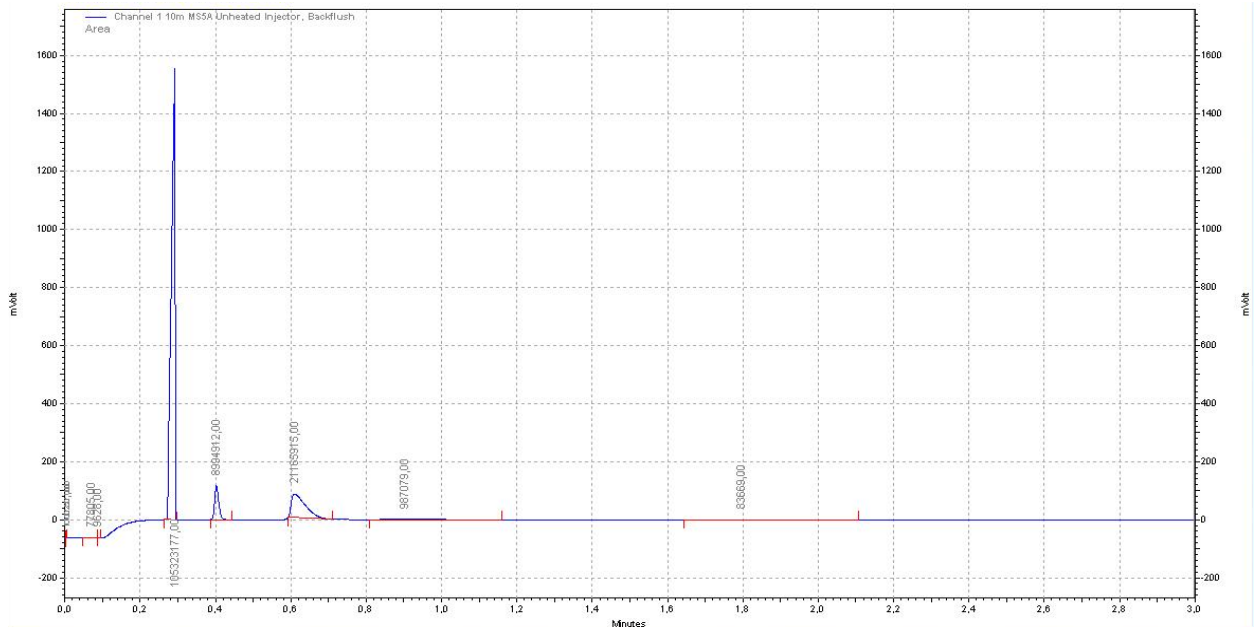


Fig. 26 Headspace chromatogram with clearly visible peaks, in order of retention time, for H₂, O₂, N₂, CH₄ and CO.

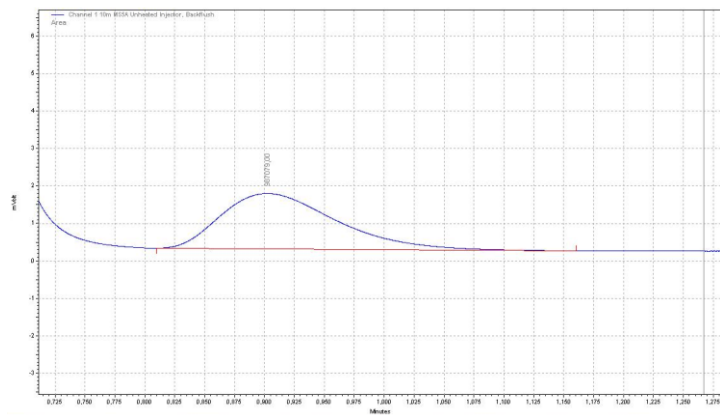


Fig.27 Magnification relative to the CH₄ peak.

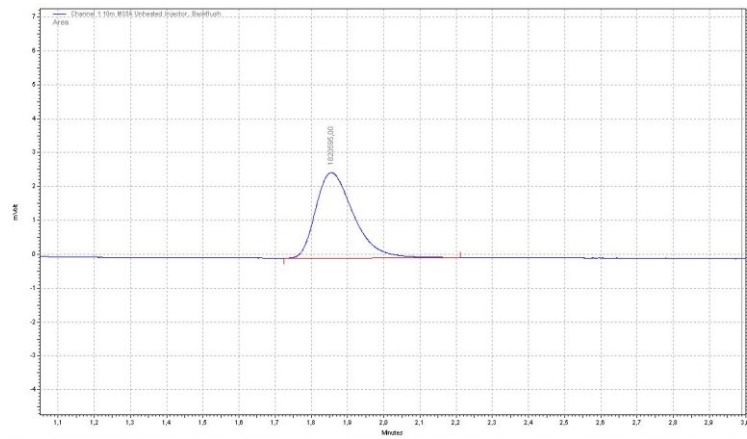


Fig.28 Magnification of the CO peak during electrolysis with copper electrodes.

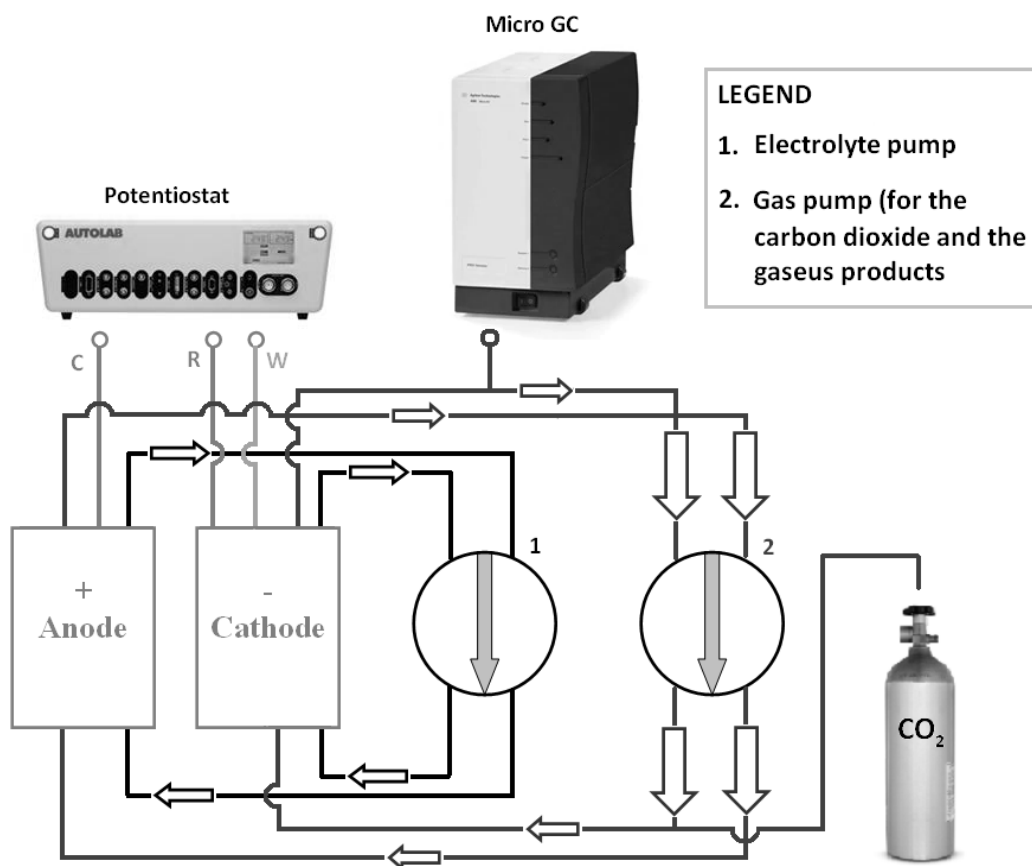


Fig. 29 Scheme of the experimental setup adopted for the analysis of the gaseous CO₂ reduction products



Fig.30 Image of the six-ways connector located on the top of the cell

The fig 29 shows how the headspace and electrolyte are recirculated during a typical electrolysis aimed at the identification of gaseous. Since the duration of the experiments would be limited by the low amount of electrolyte that is contained in the cathode compartment (2ml) of the micro flux cell, a 25ml reservoir is located below the electrode compartment and directly connected to the latter in order to continuously

renew the solution with fresh electrolyte (see chapter 1.3). The cell is designed to manage the electrolyte and gaseous headspace recirculation with only one tube located below the reservoir, in fact the gas flow itself is used to stir the KHCO_3 solution.

2.2.3 Reduction Efficiency (FE)

The faradic efficiency (FE) is a key parameter to evaluate the selectivity of cathodes for CO_2 reduction. In particular, to assess the FE we analyzed at least three electrodes per type. FE expresses how much electric charge has been actually involved in the production of a given compound. By knowing the number of produced moles from the analytical measurements described above, FE was calculated using the following equation:

$$FE = \frac{n \cdot F \cdot \text{moles of product}}{Q_{tot}} \%$$

Where n are the electrons involved in the specific CO_2 reduction path under consideration, F the Faraday constant and Q_{tot} the total charge passed during the electrolysis obtained by integrating the Chronoamperometric curves (current versus time). Ideally, the sum of the FEs of all the products should be 100 %, in order to obtain a Faradic balance assuming the absence of hidden processes or unwanted products migration through the Nafion membrane. The attainment of the Faradic balance is the first fundamental step in the characterization of an electrolytic process.

3. Electrochemical CO₂ reduction

3.1 OD treatment of copper electrodes: preliminary results

In order to develop new copper-based electrodes for the electrochemical reduction of CO₂, we were inspired by the methodology previously reported by the group of prof. Kanan for the treatment of gold cathodes²⁶, as previously mentioned in the state of art section, by properly adapting and optimizing it³³. In particular, the process is based on an electroerosion treatment of the metal adopting a particular pulsed square wave electrolysis between two suitable potentials. This process leads to the initial formation of a thick oxide layer which, following reductive scanning, is further reduced into specific metastable metallic nano/micro structures characterized by a high incidence of grain boundaries, on which the reduction of CO₂ and its catalytic intermediates is hopefully favored³⁰.

Adapting this procedure to copper cathodes implies the optimization of various process parameters including the range and frequency of the square wave potential and the electrolyte composition for the OD treatment. In particular, the manufacture of nano-structured copper cathodes starts from an electropolishing pretreatment of metallic copper foil (99 +% purity) in 85% H₃PO₄ as electrolyte, applying a voltage of +4 V for 300 seconds against a titanium counter electrode³³. This process guarantees the complete cleaning of the metal surface through the effective removal of organic contaminants and metallic oxides respectively derived from the lamination processes of the copper and the air oxidation, resulting in the final formation of an almost smooth surface. Since contact with atmospheric oxygen can restore over time a thin oxide layer in the metal surface, introducing a further degree of variability in the following square wave treatment, care was taken to perform the OD treatment immediately after electropolishing. For this purpose, in the first explorative experiments a slight modification of the Kanan procedure for gold cathodes is applied²⁶, consisting in a square wave electrolysis in 0.1 M K₂SO₄ solution in which the copper electrode is subjected to an alternating potential between +1.1 V and +3.1 V for a total time of 1800 seconds at a frequency of 1000 Hz. In our case, compared to the literature procedure we halved the anodization time, since the original treatment reported for gold (3600 seconds of square wave anodization) caused excessive corrosion of the Cu electrode.

The performances of the electrodes thus obtained were screened by linear voltammetry by recording current-voltage (JV) profiles of the electrodes under carbon dioxide reduction conditions, using a 0.5 M KHCO₃ solution previously saturated with CO₂ for about 15 minutes until the buffer pH of 7.4 is reached.

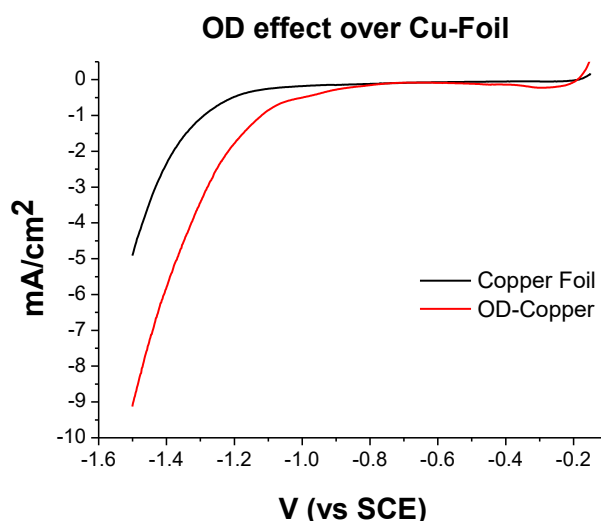


Fig. 31 Comparison between a copper lamina and an OD-Copper realized according to the methodology proposed by Kanan for gold substrates (1000Hz from -1-1 to 3-1V vs SCE in 0.1M K_2SO_4) JV profiles are recorded at 20mV/s in $KHCO_3$ 0.5M with 90% IR-Drop correction.

As shown in figure 31, it can be seen how the JV curve, carried out from the open circuit potential (OCP) down to -1.5 V vs SCE using the OD cathodes (OD-Cu) obtained by the square wave anodization, manifests an approximately doubled cathodic current compared to a reference copper foil, (a Cu lamina subjected to electropolishing, non OD treated nanostructured). In fact, can be easily seen that the faradic current at -1.5 V vs SCE varies from about -5mA/cm² for electropolished copper to about -9 mA/cm² for the OD-Cu, a result which is also associated with an encouraging improvement in the onset potential of the catalytic current (arbitrarily evaluated at -1 mA/cm²), which varies from -1.3 V to a less negative potential of about -1.1 V for OD-Cu.

Justified by the promising results of this preliminary investigation, we further tuned the OD process by considering different square wave cycles and electrolyte composition. The outcome is summarized in table 4.

Electrode	OD Parameters	Electrolyte composition	Onset (V vs SCE)* @ 1 mA/cm ²	J_{max} (mA/cm ²)* @ -1.5 V vs SCE
1 (Foil)	---	---	-1.3	4.9
2	1.1 V ÷ 3.1 V; 1000 Hz; 30 min	K_2SO_4 0.1 M	-1.1	8
3	1.1 V ÷ 3.1 V; 1000 Hz; 5 min	K_2SO_4 0.1 M	-1.1	9.2
4	0.5 V ÷ 0 V; 1000 Hz; 5 min	K_2SO_4 0.1 M	-1.2	8.7

5	1.5 V ÷ 0 V; 1000 Hz; 5 min	K ₂ SO ₄ 0.1 M	-1.2	10.1
6 (OD)	1 V ÷ 0 V; 1000 Hz; 5 min	K₂SO₄ 0.1 M	-1.1	15.6
7	1 V ÷ 0 V; 10000 Hz; 5 min	K ₂ SO ₄ 0.1 M	-1.2	11.9
8	1 V ÷ 0 V; 100 Hz; 5 min	K ₂ SO ₄ 0.1 M	-1.1	15.6
9	1 V ÷ 0 V; 1000 Hz; 5 min	K ₂ SO ₄ 0.1 M + KCl 0.004 M	-1.1	26.0
10	1 V ÷ 0 V; 1000 Hz; 5 min	K ₂ SO ₄ 0.1 M + KCl 0.4 M	-1.1	23.5
11 (Cu_OD)	1 V ÷ 0 V; 1000 Hz; 5 min	K₂SO₄ 0.1 M + KCl 0.04 M	-1.1	54.5

Tab. 4 OD conditions and electrochemical output of various OD treated electrodes

From Table 4 it can be seen that the anodization time can be reduced by 6 times without compromising the maximum recorded current (see lines 2 and 3), indicating that in the first 5 minutes an oxidized layer is already formed. To ensure an efficient nanostructuring a prolonged duration of the process appears to be not recommended and it seems to only lead to the formation of a thicker layer characterized by a greater tendency to detach and dissolve into the anodizing solution.

It has also been shown that it is possible to modify the applied potential values in order to make the process conditions less impacting to the mechanical resistance of the nanostructured layer, by setting cycles between moderately oxidative potentials (from 0.5 to 1.5 V) and the onset potential (characterized by the absence of electrochemical processes) identified at 0 V vs SCE (see lines 4-6). The variations applied led to obtaining significantly better performing electrodes with respect to the first experiments, capable of an almost doubled cathodic current value recorded (up to -18.2 mA/cm² at -1.5 V vs SCE). These electrodes, indicated in line 6 with the wording OD (OD refers to oxide derived-Cu, in analogy with the nomenclature used by Prof. Kanan) are a consequence of a 300s treatment at 1000 Hz between +1 V and 0 V. Figure 32 shows the average performances obtained using this type of electrodes and the respective error bars.

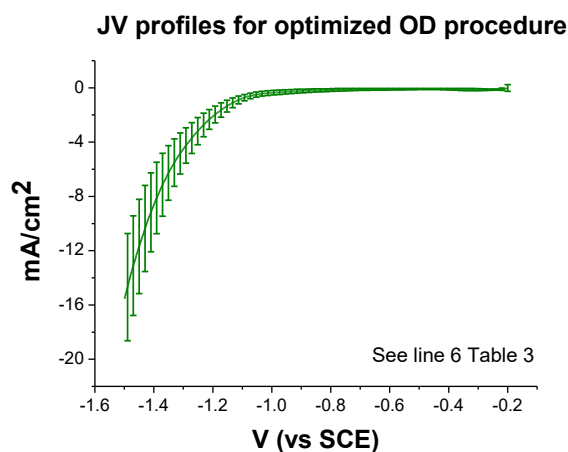


Fig. 32 J/V characteristics of OD-Copper according to the methodology of table 4, line 6 (1000Hz from +1 to 0 V vs SCE in 0.1M K₂SO₄). 20mV/s in KHCO₃ 0.5M with 90% IR-Drop compensation

The variation in the frequency of the square wave did not, however, lead to significant improvements in performance (see lines 6-8 in Table 4).

On the other hand, the setting up of the cell has been proven to have a key role in improving the electrochemical performance in particular, on this regard, the copper foil is placed horizontally on the bottom of the cell compartment during the OD treatment, while the platinum counter is placed at a close distance and centered as much as possible with respect to it in order to obtain a more homogeneous electric field. In this configuration it is important to effectively insulate the connection contacts and the remaining part of copper foil, from the surface that has to be OD treated. In this regard, Kapton adhesive tape was used, a polyimide with excellent resistance performance in the above-mentioned electrolytes, which could be easily removed at the end of the electrolytic process. If necessary also a specific epoxy resin could be used, an appropriate solution especially when we need to define rounded active areas (figure 31) in the case of some cell configuration with circular O-ring. Silver paste was used for wiring the electrodes in the CO₂ reduction experiments.

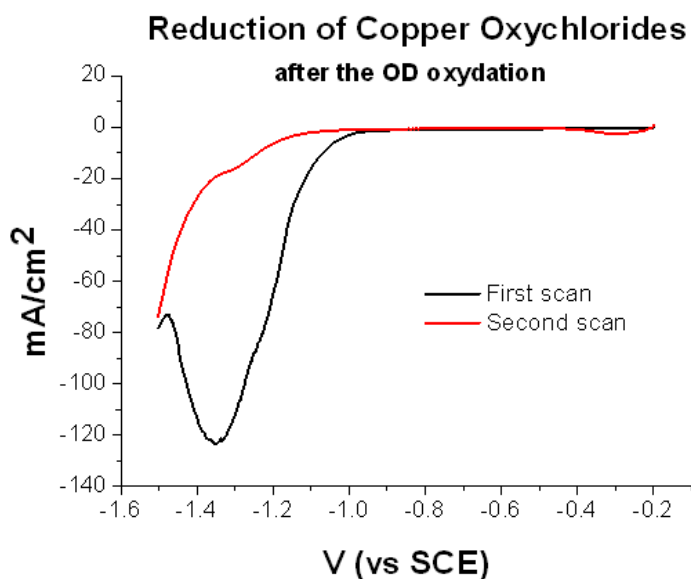


Fig. 33 First and second reduction scans of the copper oxychloride layer obtained after the square wave oxidation, on the right is reported a photo of the final copper interface (the dark circle represents the nanostructured surface)

It is also worth noting that at the end of the pulsed electrolysis procedure the copper foil loses its original shiny metallic surface and shows an opaque pale yellow colour, a clear symptom of the of the drastic changes occurred on its surface. The active form of the electrode is obtained by subjecting the electrodes, immersed in a deaerated 0.5M KHCO_3 (pH: 7.4) to the subsequent metal oxide reduction, by exploiting a sequence of J-V scans from OCP down to -1.5 V vs SCE thus generating the final nanostructured interface of reduced copper. An example of the electrochemical behaviour upon CuO_x is shown in figure 33, where the copper oxide reduction wave is evident at about -1.35 V. The scans are repeated multiple times (usually ca. 20) until the complete disappearance of this characteristic wave. This is also accompanied by the observation of hydrogen evolution on the electrode surface, indicating the restoration of the electrocatalytic properties of the interface.

The copper cathode thus obtained now appears very different from the starting material (Fig. 33 on the right). The surface subjected to the described treatments shows a dark brown/black colour, due to the light trapping in the new ostensibly micro/nanostructured surface feature which can be appreciated, to a good advantage, as a dark oxide circle where the OD treatment was applied. Thanks to electron microscopy analysis (which will be described in more detail in the following chapters), it was possible to note the presence of peculiar cubic structures of cuprite (copper oxide), with an approximate side between about 300 and 400 nm, quite uniformly distributed on the surface. This type of cubic nanostructures, prepared however by a different and innovative technique, have already been reported in multiple literature works

as a promising electrocatalytic morphology for CO₂ conversion, up to ethylene and methane, as previously described²⁷.

Therefore, taking inspiration on these interesting results, it was decided to appropriately modify the OD electrolyte by introducing chloride ions, known in the literature to be favourable templating agents for the growth of copper nanocubes²⁷. In particular, to the initial electrolyte (0.1 M K₂SO₄) a 0.04M concentration of KCl was added, keeping the other already optimized parameters unchanged. As shown Tab.4, line 11, as well as from figure 34, this step allowed the development of the best performing cathodes both in terms of onset potential and current density. In fact, average values of current intensity were recorded up to about -100 mA/cm² at -1.6 V, dramatically increasing the performance of the simple electropolished foil. The further exploration of variable concentrations of chlorides in the OD solution did not, however, lead to significant improvements in the electrochemical performance (see lines 9-11 in Table 4).

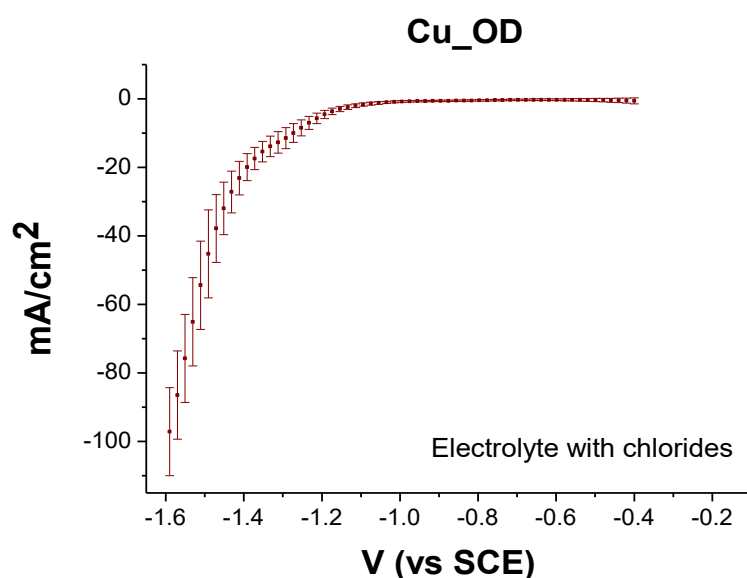


Fig. 34 OD-Copper realized according to the methodology described in table 3, line 11 (1000Hz from +1 to 0 V vs SCE in K₂SO₄ 0.1M + KCl 0.04M) JV profiles are recorded at 20mV/s in CO₂/ KHCO₃ 0.5M buffer with 90% IR-Drop compensation

3.2 Experimental optimized OD procedure for Cu cathodes

Here we present the flow chart relative to Cu-OD electrodes presently prepared

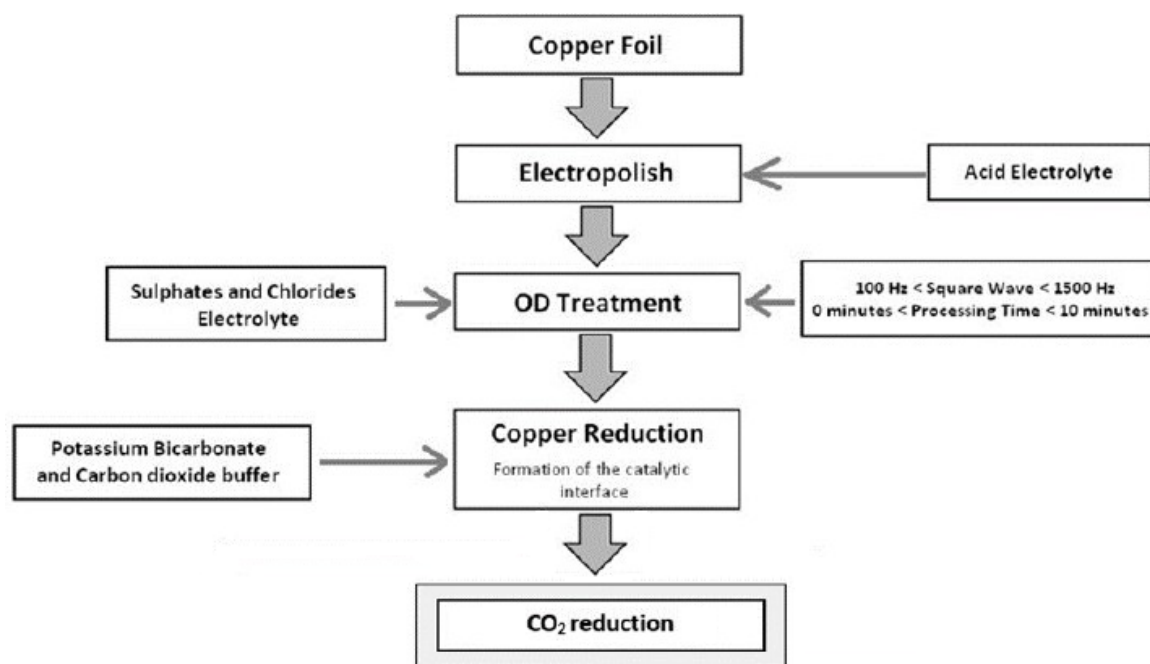


Fig. 35 Scheme of the nanostructuring electrochemical process developed for copper substrates

The copper cathodes used in this work were prepared from different copper based substrates, as it will be described in the following chapters. Regardless of their nature, these were treated with the same OD process schematized above. This treatment, summarized in the scheme in Fig. 35, was optimized with the experience gained from all the previously discussed experiments, aimed to find the right combination of electrolyte composition, frequency and duration of the electrolytic treatment, and cell configuration.

The OD procedure thus developed is described in these three steps:

- 1. Electropolishing:** Necessary step in order to obtain a smooth copper surface, cleaned from all inorganic and organic contaminants and ready for the subsequent square wave anodization. Electro-cleaning is performed in a one-compartment cell (a simple beaker) in which the copper electrode is immersed with a titanium counter-electrode (cathode) in a two electrode configuration. The voltage is held, at +4 V for 300 s (5 min) in 85% H₃PO₄ as electrolyte.
- 2. Pulsed Anodization:** After the surface polishing or copper electrodeposition, the cathode is immersed in a 0.1 M K₂SO₄ / 0.04 M KCl aqueous electrolyte in a single compartment three-electrode cell. The soldered ohmic contact was protected with kapton tape or epoxy resin. A

double jacket saturated calomel electrode (DJ-SCE) was used as a reference, and a platinum wire served as a counter electrode. The square wave anodization (SW) was applied for a duration of 300 seconds, at a frequency of 10^3 Hz according to a wave form, ranging between + 1000 mV and 0 mV vs SCE. An Amel 552 potentiostat and an Amel 568 in-line function generator were used to generate potentials programs. The square wave anodization as previously mentioned leads to the formation of copper oxychlorides, evidenced from developing of a dull white-yellow color. It is important to remember that, to reduce the detachment of these species from the surface, the working electrode is placed horizontally at the bottom of the cell (see Fig. 36).

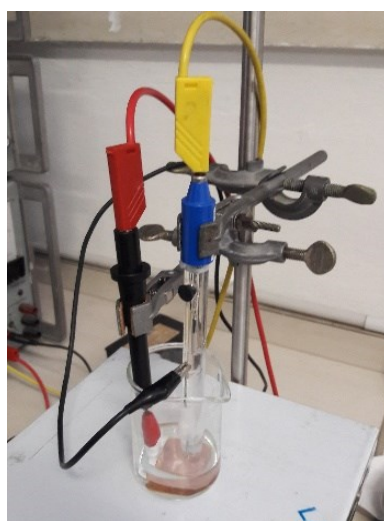


Fig. 36 Experimental setup for the OD procedure, notice the large copper foil placed horizontally on the bottom of the cell

- Reduction Process:** The subsequent process, that allows to the formation of the copper nanocubes, is carried out by potentiodynamic cycling (-0.2/-1.5 V vs SCE at 20 mV/s) the electrode in a single compartment cell in 0.5 M KHCO_3 as electrolyte causing the reduction of the oxidized copper layer and the formation of the catalytic interface constituted by a core shell structure of copper/ Cu_2O . The electrodes thus obtained are generally defined **Cu_OD**.

As previously described this procedure is capable of allowing a precise control on the final morphology of the cathodes, in fact by acting on the duration of the OD treatment, it is possible to obtain a deep impact in the final dimensions and density of the catalytic structures. The figure below well illustrates this aspect, in fact are shown the SEM images of the surface of three different cathodes treated with various OD

timings, in which can be easily seen how the surface density of nanocubes strictly depends on the treatment times.

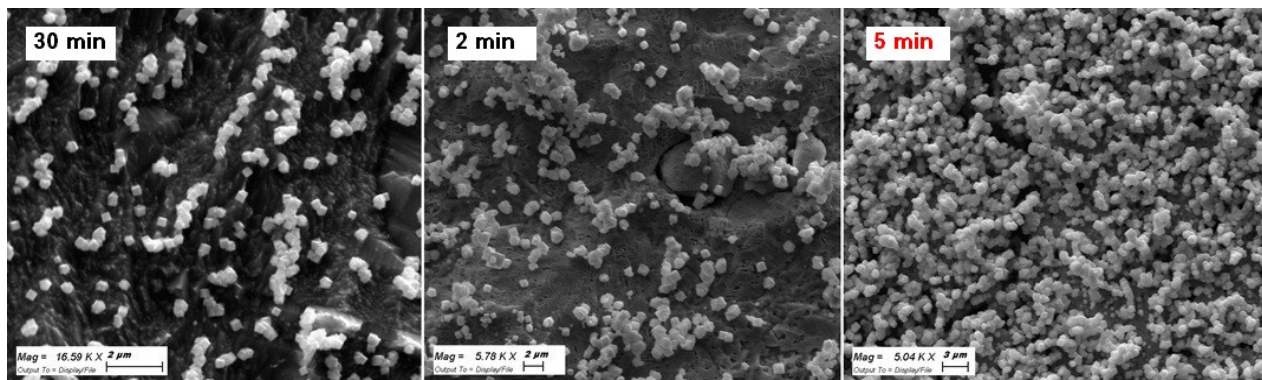


Fig. 37 SEM images of the laminar cathode, treated with different OD times (5 minutes correspond to the optimized time for the highest nanocubes surface density that raises from left to right in the image) .

3.3 Faradic efficiencies and electrochemical behaviour of Cu_OD cathodes

All the CO₂ reduction tests were carried out in aqueous electrolyte, the best in terms of environmental impact, but the most limiting considering the poor solubility of this gas in water (about 33 mmol/l). The aqueous solution used is made of 0.5M potassium bicarbonate conditioned to pH 7.4 by saturation with carbon dioxide. Prior to be used in the catalytic reduction the electrolyte is subjected to a preventive electrochemical purification process carried out in an inert atmosphere of nitrogen using a two titanium electrodes cell on which the potential of + 2V is applied for 54000s (15h). This treatment is necessary for the complete removal of hypothetical contaminants, in particular metal ions, which can interact with the catalytic processes, generating untrustful experimental data^{4,59,85}. From the experiments conducted on the cathodes made according to our methodology it was possible to obtain some encouraging results.

In fact, as shown in the figure 38, extremely high current densities (measured with IR-Drop 90% at 20mV/s) have been reached in aqueous electrolyte (0.5 M KHCO₃ + CO₂, pH:7.4), values substantially higher than what it has been possible to compare from the works then present in literature, widely outperforming the simple metallic lamina, chosen as a reference, in terms of onset potential and current densities. It has also been possible to observe that reasonable catalytic efficiencies have been associated with an excellent electrochemical performance. In fact, the copper cathodes showed a good selectivity for carbon dioxide, mainly towards the conversion into carbon monoxide (with an average maximum of 20% of the total faradic efficiency) and formate (about 10%). Minority products such as methane (3%) and ethylene (about 1%) have also been identified, followed by numerous compounds present in traces such as ethanol, acetaldehyde and acetone mainly. It is interesting to note that in terms of Syngas production (1/3 CO and

2/3 H₂ mixture), the efficiency actually stands at values between 60 and 70% at -1.5V vs SCE, and this figure, coupled with the high current densities, point to a significant amount of products generated during this electrolytic process, at least compared to most literature reports.

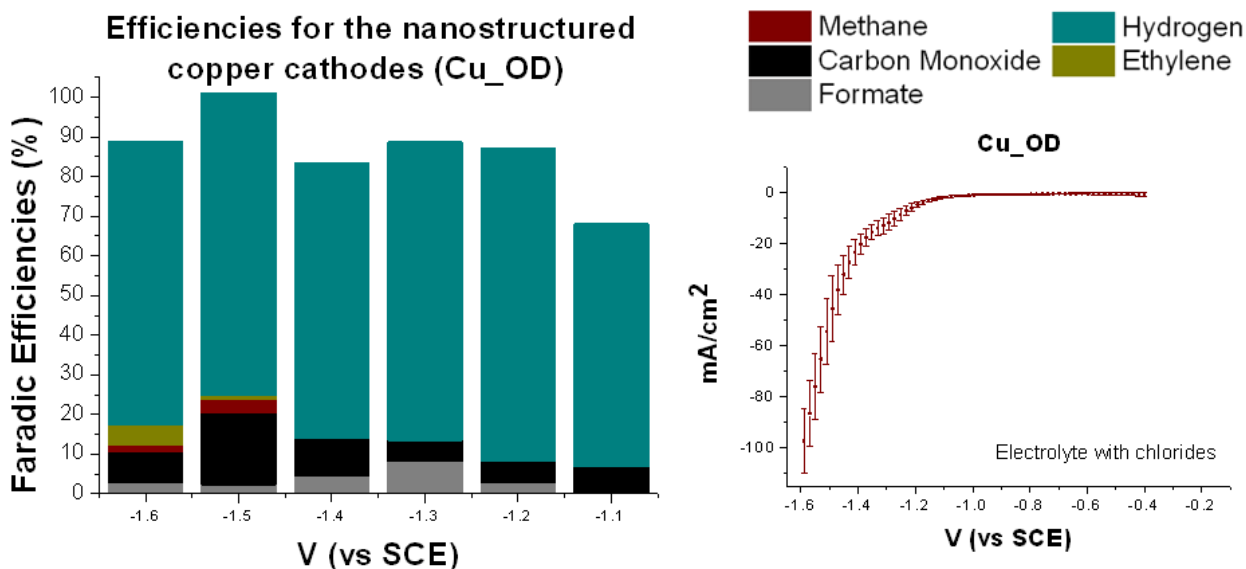


Fig. 38 On the left the obtained Faradic Efficiencies for each applied potential (in KHCO₃ 0.5M pH:7.4) is shown. On the right the average Current/Potential profiles for the Cu_OD electrodes (pH: 7.4, KHCO₃ 0.5M with IR-Drop 90% (scan rate 20mV/s)

The obtained results demonstrate how our catalytic substrate shows good efficiency, but still not ideal selectivity, and in order to approach practical applications it was deemed necessary to improve this aspect toward a single CO₂ reduction product as well as to decrease the competitive hydrogen evolution kinetics. In fact, a varied distribution of products, each one needing separation and purification, it is certainly less attractive under the point of view of the practical application of this electrolytic technology. In particular, we are paying special attention in the generation of Syngas, as it is one of the main products of the oil industry, whose processing, storage and transport techniques have been known and used for a long time also in relation to mixtures of this product with residual carbon dioxide. It is also particularly important in the framework of an ongoing EU project (CONDOR) in which I have been involved and that is focused on the conversion of Syngas generated by a PEC cell, into Dimethyl-ether (DME) in a high pressure catalytic reactor. In order to achieve this goal, we first explored electrode operation in aprotic or less protic solvents: the use of organic solvents with a wide electrochemical stability window, such as propylene carbonate and acetonitrile (both with TBAPF₆ 0.1M as supporting electrolyte) allowed a greater solubility of CO₂ (which reaches about 147mmol/l in propylene carbonate) but at the same time drastically decreased the current densities that can be reached by the system due to an increased electrolyte resistance. Therefore, if on one hand the faradic efficiency towards CO₂ reduction products has increased on the other hand the effective quantity of these is much lower than what is generated by the aqueous environment. Furthermore, even in

the organic solvent we found various low CO₂ reduction products, showing that the electrode still cannot reach the desired selectivity towards Syngas. For this reason we decided to direct our research once again towards the optimization of the catalytic interface, rather than on the electrolyte, acting mainly on the co-functionalization of copper with other metals. In this regard, gold, indium, zinc, tin and cadmium are promising co-catalyst known to selectively produce carbon monoxide (zinc and gold) and formate (the others)³. However the combination of these metals/metal oxides with copper may open to an entirely new electrochemical behaviour, owing to cooperative effects between copper and the co-catalyst acting in a synergistic way.

We thus aimed to explore the co-functionalization of Cu-OD electrodes with various co-catalysts which attracted considerable interest in the current CO₂ electro-reduction literature that is (indium, cerium and gold). As shown in the figure 39, the co-functionalization of copper electrodes by electrodeposition is the last step after the formation of the copper nanocubes by the application of the OD process.

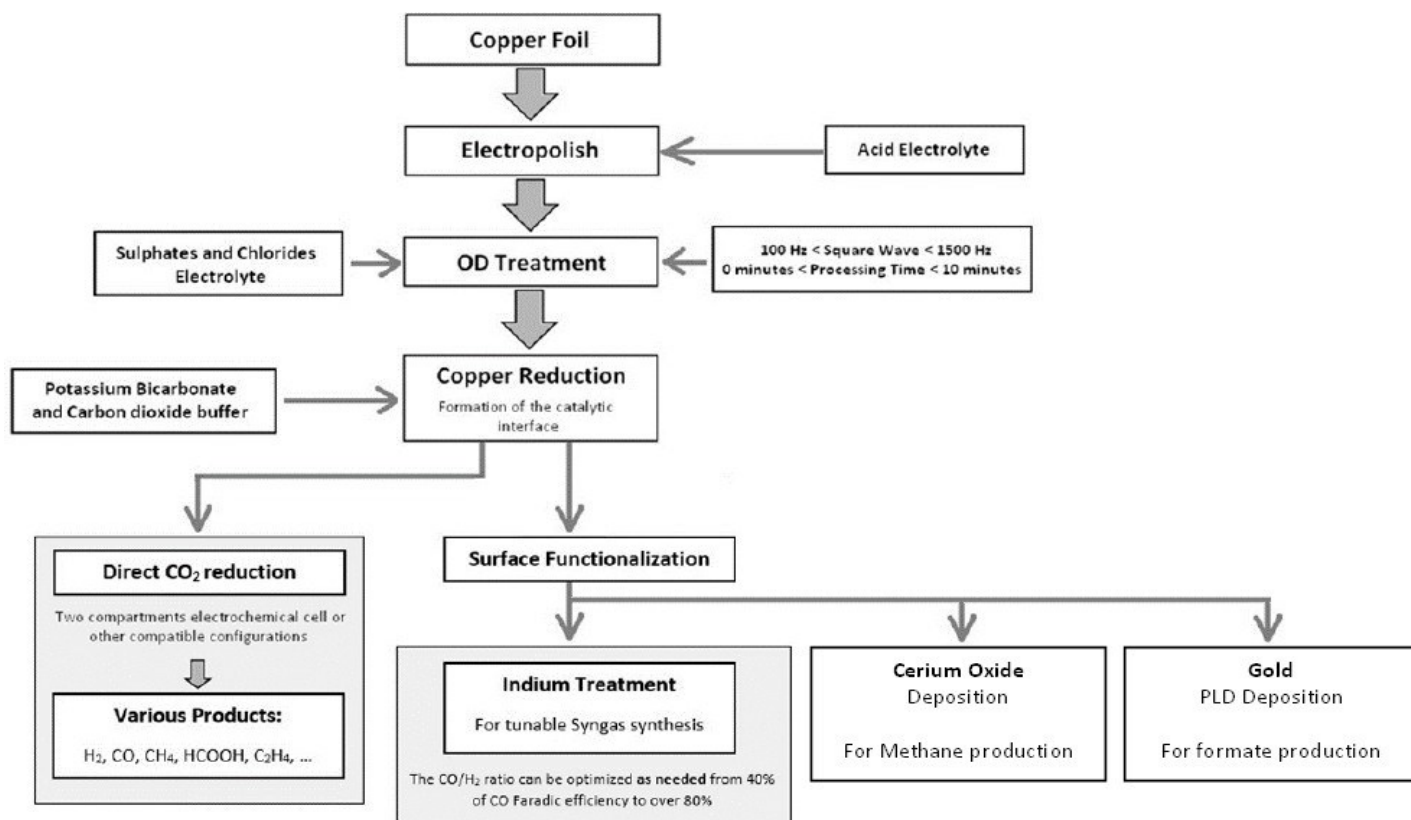


Fig.39 Flow chart describing the process of electrochemical nanostructuring for copper substrates and their co-functionalization for enhancing their catalytic activity towards CO₂ reduction

PART 2

Indium functionalized OD copper cathodes

Introduction and state of the art

Very interesting results have been obtained by introducing an indium functionalization treatment, as will be described in the following paragraphs. Based on what has been found in the literature, it was decided to deposit indium metal using an electrochemical way through a method that allows the formation of small aggregates of this element, isolated on the surface, while maintaining the uniformity of the interface on scales comparable to a few tens of micrometers¹⁴ On this regard literature offers multiple methods as alternative strategies aimed at tuning the CO₂R selectivity of bare Cu entail the formation of alloys. Indeed, several examples of mixing Cu with many other metals have been reported, resulting in either bulk or surface alloys, guest metal modified surfaces, or bimetallic core–shell structures.^{32,96}

Inspired by these works, is here reported a straightforward electrochemical treatments aimed at functionalizing the OD nanostructured Cu foils with indium, in order to yield both improved selectivity for Syngas and high performance in terms of current density. The latter is an important, yet often overlooked, aspect in view of the possible commercialization of CO₂R devices. Indeed, commercial electrolyzers generally operate at 200 mA/cm², with >70% efficiency,⁹⁷ while the typically reported performances of CO₂R electrocatalysts are <3 mA/cm². Literature examples of Cu–In nanostructured catalysts for CO₂R are still limited. For example, Takanabe and coworkers reported the electrochemical reduction of CuInO₂, resulting in the formation of Cu₁₁In₉ and Cu₇In₃ alloys, with high efficiency in CO and formate production (respectively 70% and 20% FE at –1.5 V vs SCE).⁹⁸ The Züttel group reported on a Cu–In interface obtained when a thin layer of In was formed by dipping on top of Cu(OH)₂ nanowires.⁹⁹ When the In content is 20% vs. Cu, best performances in terms of CO evolution are observed, i.e. 93% FE at –1.3 V vs SCE. Zangari and coworkers instead reported on the co-electrodeposition of mixed Cu–In phases with different compositional and dendritic morphologies.¹⁰⁰ The electrodes with 40% In showed high formate production (49% FE), together with Syngas in the optimal ratio H₂/CO = 2.6, while the maximum amount of formate (62% FE) was obtained with 80% In cathodes. An array of Cu–In electrocatalyst coatings with good control of metal stoichiometries was prepared by the Berlinguette group via near-infrared driven decomposition of mixed-metal precursor solutions. Excellent selectivity for CO (ca. 90% FE) was maintained by Cu_xIn_{1-x} alloys, with x being in the range 0.5–0.8.¹⁰¹

Herein we report on the use of nanostructured indium-modified copper cathodes for the selective formation of Syngas via CO₂ electroreduction in aqueous medium. The syngas composition can be tuned by varying the indium content and/or the applied potential. In particular, under –1.3 V vs SCE applied bias, we obtained 1:2 and 1:1 CO/H₂ mixtures, which can be exploited for the synthesis of methanol and hydroformylation reactions, respectively. Even if the medium-term operation under CO₂R conditions results in some structural modifications of our cathodes, their performances can be fully restored upon the addition of an In(III) precursor to the electrolytic solution.

2. Experimental

2.1 Preparation of the cathodes

Before use the already optimized OD procedure was applied, Cu foils in fact were electropolished in 85% H_3PO_4 , holding +4 V voltage vs. a titanium counter electrode for 300 s. After this treatment, some foils were subjected to pulsed anodization, aimed at nanostructuring the surface. Briefly, the electropolished Cu foil was placed horizontally in a single compartment, three-electrode cell and then immersed in a 0.1 M K_2SO_4 /0.04 M KCl aqueous electrolyte (see chapter 3.2, part 1). The soldered ohmic contact was fully protected with epoxy resin. An Amel 552 potentiostat coupled with an Amel 568 in-line function generator was used to apply a square wave (SW) anodization, switching between +1 V and 0 V (vs. a double-jacketed SCE) with a frequency of 10^3 Hz for a total time of 300 s. The resulting electrode was later reduced in a 0.5 M aqueous KHCO_3 solution via 20 successive linear voltammetry scans, sweeping the applied potential in the range of $-0.2/-1.5$ V vs SCE at a scan rate of 20 mVs^{-1} . This procedure allows for the reduction of the oxidized Cu layer resulting from the anodization, leading to the formation of the actual catalytic interface called OD-Cu (for oxide-derived Cu) throughout the text.

Indium was electrodeposited on OD-Cu electrodes in a two- electrode cell configuration, using an indium wire as the counter electrode, following a slightly modified literature procedure.³¹ The deposition was carried out in the galvanostatic mode, while stirring a solution containing 0.04 M indium(III) nitrate and 0.5 M citric acid. The process was carried out until charge densities of 18, 36 and 54 C/cm^2 were transferred, respectively, yielding OD-Cu_In18, OD-Cu_In36 and OD-Cu_In54 cathodes.

2.2 Morphological and structural characterization

Morphological characterization was performed using a Zeiss Leo 1530 Field Emission Scanning Electron Microscope (FE-SEM), operated at 5 kV. Nanoscale structural and compositional analyses were carried out by using a Philips TECNAI F20 ST high resolution transmission electron microscope (HR-TEM) operating at 200 kV. The instrument is equipped with an energy dispersive micro-analysis (EDS) and scanning transmission high angle annular dark field (STEM-HAADF) detector. For TEM observations, the cathode surface was scratched and the powder sonicated in isopropanol for 5 minutes, before being dropcast onto holey carbon-coated Au grids. The samples were dried at room temperature before observation.

X-Ray Diffraction (XRD) patterns were recorded using a Rigaku SmartLab diffractometer equipped with a Cu-rotating anode and Soller slits to obtain a parallel beam with a divergence of 0.1° . Measurements were performed in specular and Grazing Incidence (GI) geometries to probe films at different penetration depths, from a few nanometers to microns. Due to the high film roughness, the incident angle in GI-XRD scans was

varied from 0.5° to 3° in order to detect Bragg peaks from the film surface. Therefore, the exact values of the penetration length could not be estimated. X-ray photoelectron spectra (XPS) were recorded using Mg K α excitation and analysed using a hemispherical analyser (Phoibos 100, Specs). The survey and high-resolution spectra were acquired with energy resolutions of 1.4 eV and 0.9 eV, respectively, on freshly sputtered silver (Ag 3d). A spectrometer was calibrated to the Au 4 f $_{7/2}$ peak at 84.0 eV. Conductive carbon tape was used to fix and electrically ground the sample. No electrostatic charging effects were observed. The spectra were fit using the CasaXPS software after Shirley's background subtraction.

2.3 Electrochemical characterization

Electrolyte purification. The presence of metal cation impurities (especially Fe $^{2+}$, Pb $^{2+}$ and Zn $^{2+}$) in electrolytic solutions used for CO $_2$ electroreduction is known to cause co-deposition of the corresponding metals on the cathodic surface, possibly leading to modification of the catalytic properties.⁴ Although nanostructured electrodes should be less sensitive to this process,⁵⁹ the electrolytic solution was pre-electrolyzed using two titanium foils held at -2 V for 15 h under nitrogen bubbling.⁸⁵ ICP-mass analysis was then performed, confirming the absence of Fe $^{2+}$, Pb $^{2+}$ and Zn $^{2+}$ within the limits of technique sensitivity (<0.5 ppm).

Product accumulation and analysis. CO $_2$ reduction experiments were carried out in a two-compartment, custom-made polymethylmethacrylate cell. The cathodic side hosts both the working (Cu-based cathode) and reference (SCE) electrodes, while the anodic one contains the Pt counter electrode. The two compartments are separated using a Nafion $^{\text{®}}$ 117 membrane. Both the anolyte and the catholyte consisted of a 0.5 M KHCO $_3$ aqueous solution saturated with CO $_2$ (resulting pH = 7.4) and pre-electrolyzed according to the abovementioned procedure. The working electrodes were soldered to Cu wires and then isolated from contact with the electrolyte by using epoxy resin. Pulsed electrolyses were performed in order to accumulate the reduction products.

The cathodic compartment of the cell was connected to a headspace, from which gaseous samples were automatically collected. Their detection and quantification were performed using an Agilent 490 micro GC (Agilent Technologies) equipped with a 5 Å molecular sieve column (10 m) and a thermal conductivity detector, with Ar as the carrier gas. Quantification of formate was performed via $^1\text{H-NMR}$ spectroscopy (Agilent, 300 MHz), using DMF as the external standard and a customized water suppression sequence. As already stated for the copper nanostructured electrodes, for each product, the faradaic efficiency (FE) was calculated as:

$$FE = \frac{n \cdot F \cdot \text{moles of product}}{Q_{\text{tot}}} \%$$

where n is the number of electrons involved in the specific reduction reaction; F is the Faraday constant; and Q_{tot} is the total amount of charge passed at the interface during the pulsed bulk electrolysis experiments.

Determination of electrochemical surface area (ECSA) by double layer capacitance measurements. Experiments were carried out using an Autolab PGSTAT30 potentiostat in a three electrode set-up using a Pt wire as the counter electrode and a saturated calomel electrode (SCE) solution as the reference in 0.5 M aqueous KHCO_3 . CV scans were recorded at scan rates of 5–200 mV/s^{-1} , in a potential range at which no faradaic processes occur. From the resulting traces, the capacitive current was calculated as $(j_a - j_c)/2$, with j_a and j_c being the anodic and cathodic current densities normalized by the geometric area of the electrodes, respectively. When the resulting values were plotted vs. the scan rate, the slope corresponds to the electrode capacitance. The roughness factor (RF) of the nanostructured electrodes was then calculated, attributing $\text{RF} = 1$ to Cu foil (assumed to be featureless).

3. Results and discussion

3.1 Structural and morphological characterization of the samples

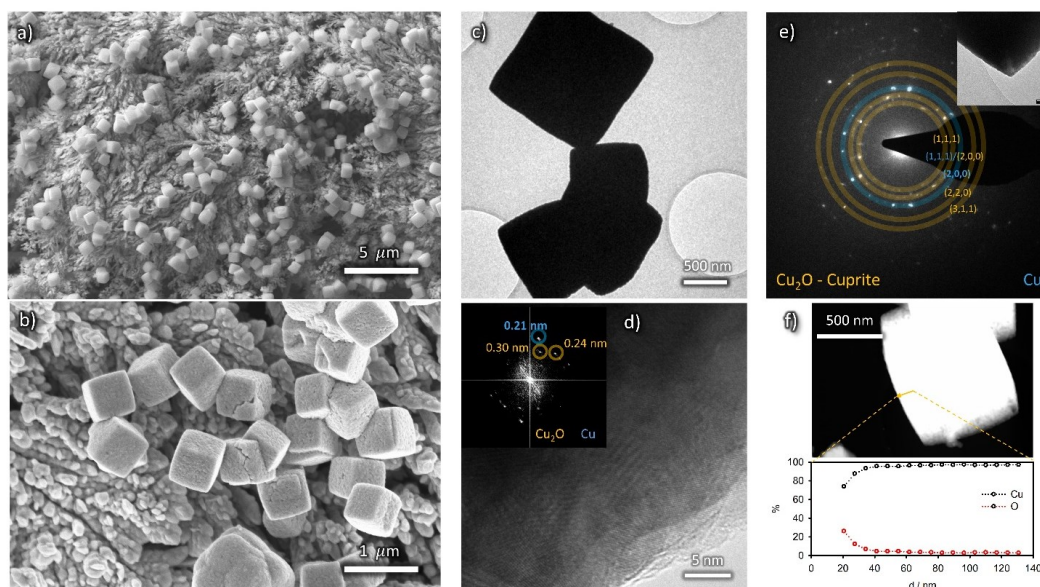


Fig.40 a,b) FE-SEM images of bare OD-Cu; c) Low and d) high magnification HR-TEM micrographs OD-Cu nanocubes displaying reflections compatible with Cu_2O and Cu lattice (FFT in figure d inset); e) Selected area electron diffraction (SAED) of a single nanocube (inset) highlighting concurrent Cuprite and metallic Cu phases; f) STEM-HAADF micrograph of a single cube and Cu/O content obtained by EDS analysis along the highlighted profile.

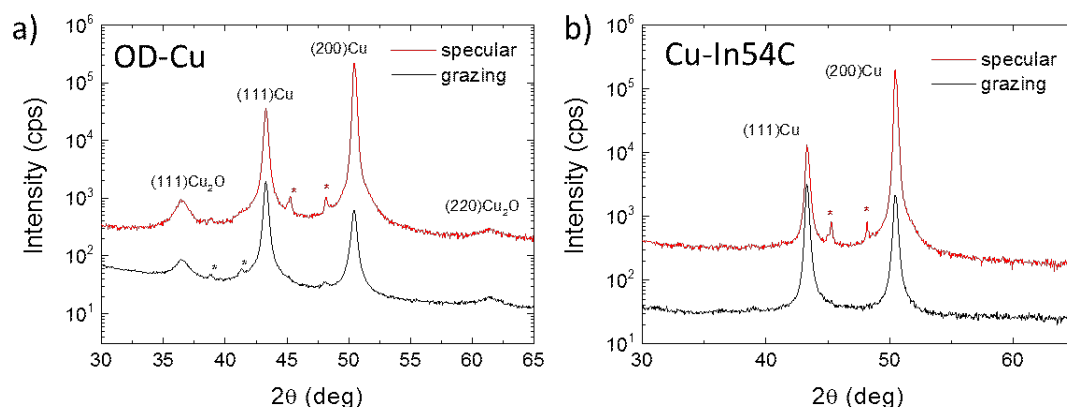


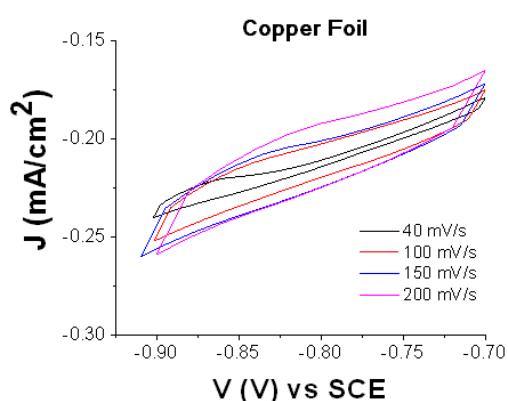
Fig. 41 Specular- and GI-XRD scans on bare OD-Cu (a) and OD-Cu_In54 (b). Stars indicate peaks coming from spurious wavelengths

The synthesis of Cu nanostructures was realized by applying a fast (10^3 Hz) square wave anodization method to an electropolished Cu foil in the presence of chloride ions. The latter are known to act as templates for the formation of cubic Cu structures with a (100) facet orientation.^{25,26} It was reported that for nanostructuring protocols involving oxidative steps (e.g. either thermal,³³ electrochemical^{27,36} or plasma-induced^{35,28}), a Cu_2O phase is firstly produced, which then undergoes reduction during the first steps of CO₂R. The Roldan Cuenya group recently documented this process under in operando conditions, using liquid cell transmission electron microscopy.³⁹ They also evidenced that some dynamical changes in the cubic morphology can occur, resulting in the formation of Cu dendritic structures.³⁹

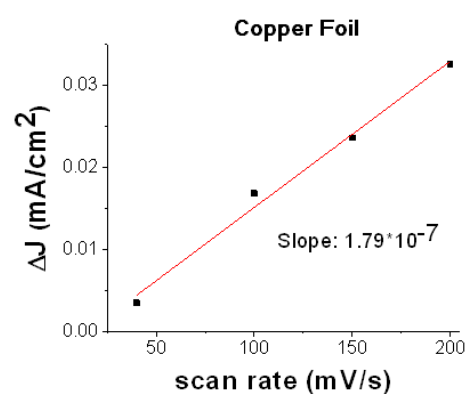
Fig. 40 resumes the morphological and structural characterization of the nanostructured Cu cathodes after pulsed anodization modification. Fig. 40 (a and b) report the SEM images of an OD-Cu sample, showing that this nanostructuring approach results in the deposition of randomly oriented nanocubes with an average size of $<1 \mu\text{m}$, even if some larger nanocubes are also observed. In the background of the SEM images, dendritic structures were also noticed, as previously discussed.

The crystal phase of the nanocubes was investigated by X-ray diffraction. Fig. 41a shows a comparison of the XRD patterns collected on bare OD-Cu in specular and grazing incidence geometries, which probe a thickness of a few μm and a few nm, respectively. The specular scan shows Bragg peaks of metallic face-centered cubic Cu with a partial preferred orientation along the 200 direction and Bragg reflections of the Cuprite (Cu_2O) crystal structure. At grazing incidence, the (111)Cu/(200)Cu intensity peak ratio reflects the polycrystalline nature of the surface. The results indicate that the 200 texturing originates from the underlying Cu foil, while the Cu and Cu_2O nanostructures grown on the top of it are randomly oriented, or,

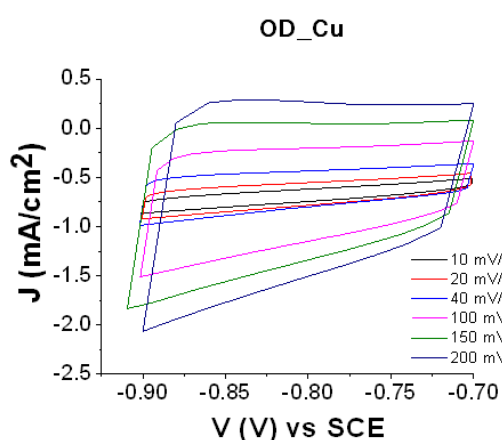
at least, polycrystalline. HR-TEM characterization of the OD-Cu nanocubes also confirms that metallic Cu and cuprite phases are concurrent in the sample (Fig. 40c–e), probably due to the formation of a native oxide layer upon atmosphere exposition. EDS analysis of the sample further proves the presence of an oxide layer on the nanocubes (Fig. 40f), while the complete structural characterization of their core is prevented by their thickness, fully electron-opaque. The enhancement of the electrochemical surface area (ECSA) resulting from surface nanostructuring was measured via cyclic voltammetry experiments (see Fig. 42). By determining the capacitive current with respect to the bare Cu foil, taken as the standard, we were able to estimate the roughness factor (RF) of the OD-Cu cathodes, which resulted to be ca. 50 (see Table 5).



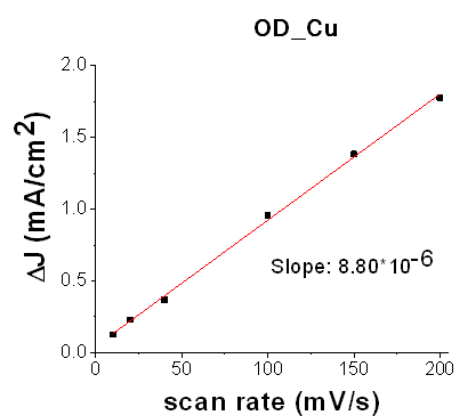
(a)



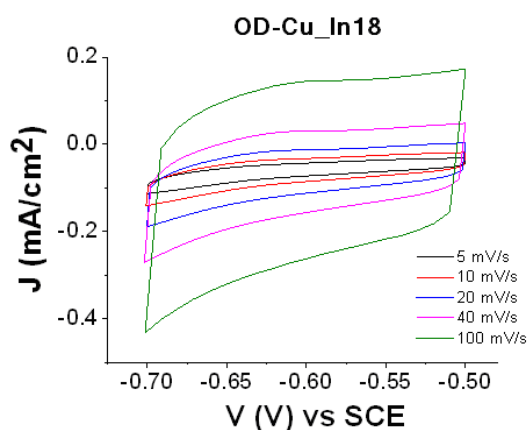
(b)



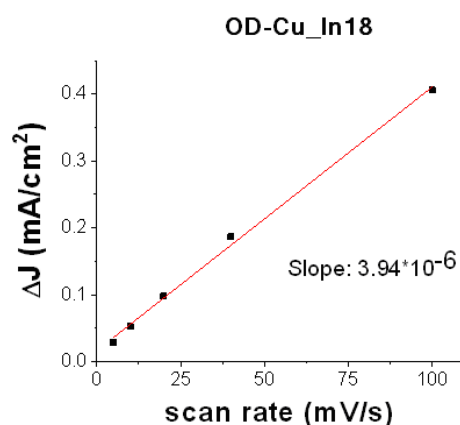
(c)



(d)



(e)



(f)

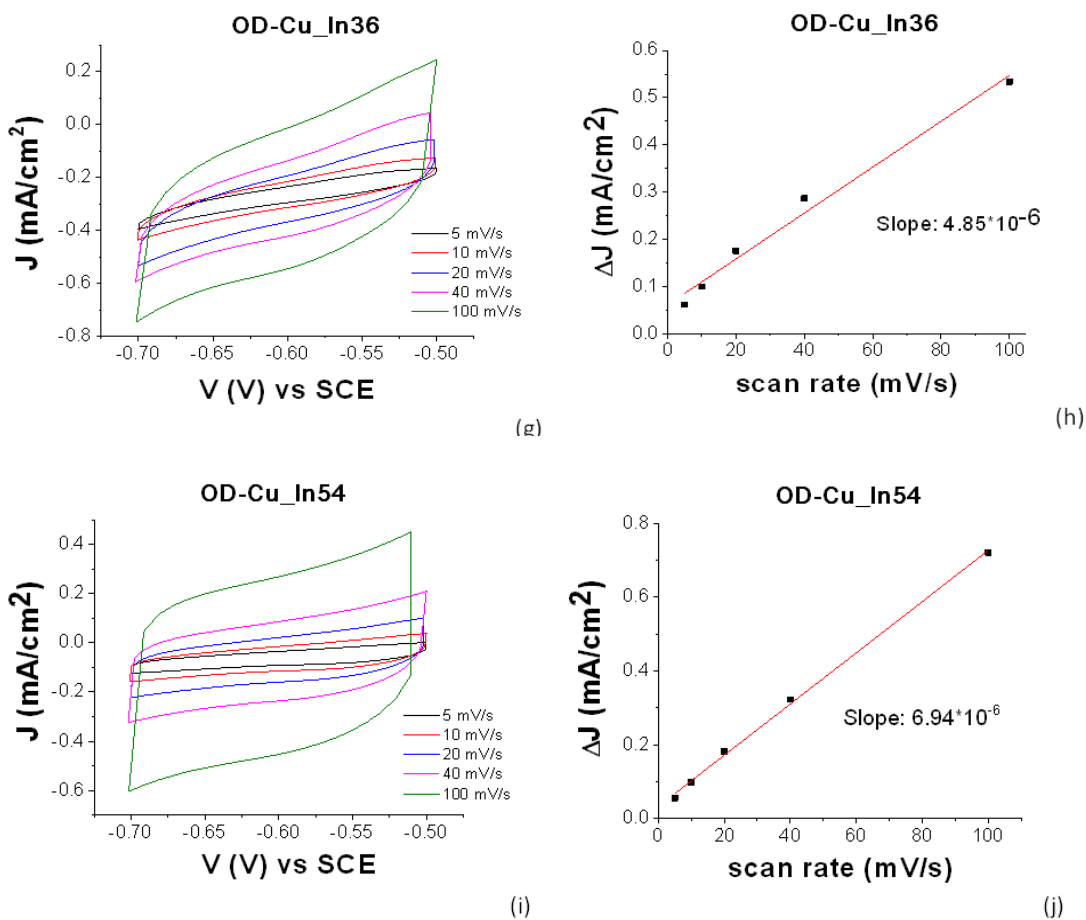


Fig. 42 CV scans for the electrochemical surface area (ECSA) determination for Cu foil (a), OD-Cu (c), OD-Cu_In18 (e), OD-Cu_In36 (g), and OD-Cu_In54 (i) registered in 0.1 M aqueous KHCO_3 . The corresponding linear fits for the determination of electrode capacitance are reported respectively in (b), (d), (f), (h) and (j).

The corresponding roughness factor (RF) values are reported in Table 5.

Electrode	Capacitance (μF)	Roughness Factor
Cu foil	0.179	1
OD-Cu	8.8	50
OD-Cu_In18	3.94	22
OD-Cu_In36	4.85	27
OD-Cu_In54	6.94	39

Tab. 5 Average values of the electrodes capacitance (i.e. the slope of the plots in Figure 42 b, d, f, h and j) and the corresponding roughness factors.

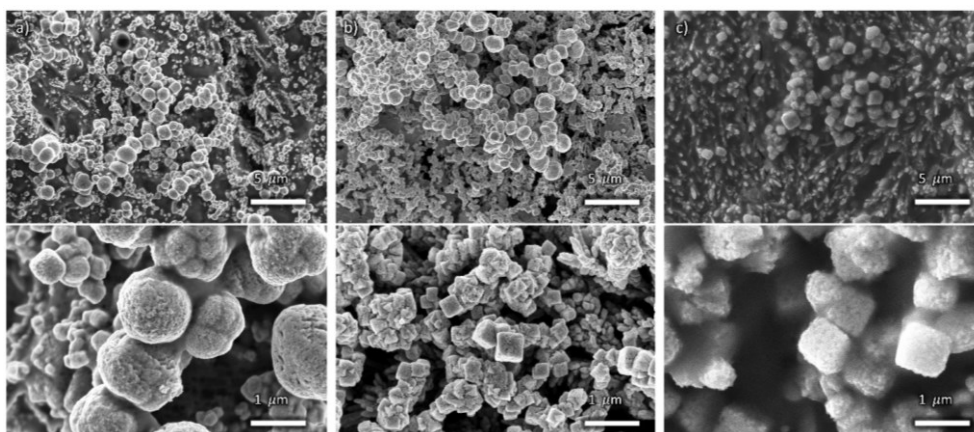


Fig. 43 Low (top) and high (bottom) magnification FE-SEM images of OD-Cu_In18 (a), OD-Cu_In36 (b) and OD-Cu_In54 (c).

Fig. 43 shows the SEM images of In-modified cathodes, displaying a finer texturing and enhanced roughness of the nanocube surface that suggests the presence of an additional coating layer. However, the background areas behind the nanocubes appear smoother than in OD-Cu cathodes without indium, particularly for longer deposition times. This results in a lower ECSA with respect to the OD-Cu cathodes, as evidenced in Fig. 42 e–j and Table 5. Indeed, the OD-Cu_In18, OD-Cu_In36 and OD-Cu_In54 electrodes respectively displayed a roughness factor of 22, 27 and 39. With regard to XRD characterization (Fig. 41b), the specular XRD pattern of OD-Cu_In54 shows Bragg peaks of metallic Cu with the preferential 200 orientation. As already noted for In-free cathodes, the GI-XRD measurements highlight a lower degree of preferential orientation of Cu crystallites, confirming that the produced nanostructures are not epitaxial with respect to the original Cu foil. The Bragg reflections of Cu₂O were not detected in the In-modified cathode, indicating that the indium containing coating protects the underlying Cu from oxidation. No other Bragg reflections were detected, suggesting that the In-containing phases diffract very weakly, probably because of poor crystallinity. The morphology of the nanocubes may be still recognized in the low magnification TEM micrographs (Fig. 47a) but the HR-TEM image reveals the presence of a beam-sensitive amorphous layer around the nanocubes with embedded crystalline nanoparticles (<5 nm diameter, Fig. 47b and c). The d-spacing is compatible with both In₂O₃ and In(OH)₃; an assignment will be done later in the text, based on XPS analysis. Consistently, EDS mapping displays that the described coating layer is rich in In and O (Fig. 47d).

In order to gain more insights into the cathodes' surface composition, their characterization via XPS was also performed. XPS Cu 2p, O 1s, C 1s and K 2p core level transitions were found in the XPS survey signal of OD-Cu (Fig. 48a). From the high resolution spectra of Cu 2p (Fig. 49b) and the corresponding Auger transition of Cu LMM (Fig. 48a), the chemical state of Cu in OD-Cu was identified; the values of the Cu 2p_{3/2}

binding energy (932.5 ± 0.1 eV) and the Auger modified parameter ($AP = 1849.1 \pm 0.2$) were in agreement with Cu(I) in oxidized form (Cu_2O);⁴⁰ nevertheless, the presence of Cu(II) components was below 10%, as deduced from the Cu 2p fit in Fig. 48b. The presence of Cu_2O was further supported by the presence of an O–Cu signal in O 1s at 530.6 eV (Fig. 49 a).^{41,42} From the high resolution C1s signal, apart from aliphatic/adventitious carbon at 285.3 eV, the presence of a carboxyl group or carbonate ions associated with the peak at 289 eV can be observed (Fig. 49b). In the same C 1s region, the K 2p signal was found. Both these features are due to adsorbed ions, residual from the OD-Cu synthesis.

After In deposition, the signal of In $3d_{5/2}$ at 445.2 eV has revealed the presence of In(III) in OD-Cu_In36 (Fig. 48 e).⁴³ One may conclude that the most probable chemical state could be In_2O_3 , but considering that In_2O_3 usually presents a slightly lower chemical shift ($3d_{5/2}$ 444.7 eV), this association is not obvious. A recent paper by Detweiler⁴⁴ reports a systematic study of In oxidation under dry and wet conditions, finding a reliable energy separation between In_2O_3 (444.7 eV) and In (OH)₃ (445.1 eV), compatible with our results. Thus, it is reasonable to claim that the chemical state of In in OD-Cu_In36 is In(OH)₃. The increase in the O 1s signal supported both the formation of In_2O_3 or In(OH)₃, notwithstanding, the signal of O–In is in the same region of O–Cu, being 530.3 eV and 530.7 eV, respectively, but no significant increase was found; while the hydroxyl In-OH signal at 532 eV has contributed to the main peak of O 1s (Fig. 49c), together with oxygen in the carbonate.⁴⁵

After the galvanostatic deposition of indium, the K 2p signal disappeared and the Cu chemical state changed (Fig. 48d) from Cu(I) to Cu(II), as confirmed by the binding energy of Cu $2p_{3/2}$ (934.4 ± 0.1 eV) and AP (1850.2 ± 0.2 eV). From the Cu 2p fit in Fig. 48d, at least 3 components were found: Cu_2O , CuO and $\text{Cu}(\text{OH})_2$. The accurate ratio of Cu(II) was hard to find. Cu(II) is not stable under X-ray irradiation and the evolution of the Cu 2p signal in OD-Cu_In36 (Fig. 51) revealed the photoreduction phenomenon that usually occurs under similar conditions.^{46,47} Thus, Cu(II) was certainly the most abundant prior to the irradiation, while the presence of Cu(I) is mainly ascribed to X-ray irradiation. The O 1s signal of $\text{Cu}(\text{OH})_2$ was found in the 532 eV region, the same region of indium hydroxide (see Fig. 49c).

In summary, XRD showed that the deposition of an In layer prevented the formation of a relatively thick (e.g., detectable by XRD) Cu_2O layer. However, XPS shows that the Cu oxidation state in the near surface layers changes from the prevalently Cu(I) of Cu_2O to the dominant Cu(II) of CuO and $\text{Cu}(\text{OH})_2$ as a consequence of In deposition. Indium itself occurs as oxidized In(III) in In(OH)₃.

3.2 CO₂R activity

The cathodes were tested under electrochemical CO₂R conditions in a two-compartment, three-electrode electrochemical cell in 0.5 M KHCO₃ saturated with CO₂. Fig. 44 shows the current density normalized for the geometrical area (J) vs. the applied bias (V) curves for all the samples. As expected, the output current generated with the nanostructured OD-Cu electrode is higher (ca. 5-fold) than that registered with the Cu foil, reaching up to -53 mA cm^{-2} at -1.6 V vs SCE .

The different performances of these two interfaces are also evident from the quantitative analysis of the CO₂R products, reported in Fig. 45 (see Cu_Foil and OD-Cu) in terms of faradaic efficiency (FE) in the range $-1.3 \text{ V}/-1.6 \text{ V vs SCE}$. It is worth noting that the reductive working potential indicated is applied for 4 cycles of 300 s each, spaced by short (40 s) reconditioning steps at the open circuit potential (see e.g. Fig. 54 for the curves obtained for an OD-Cu_In36 cathode).

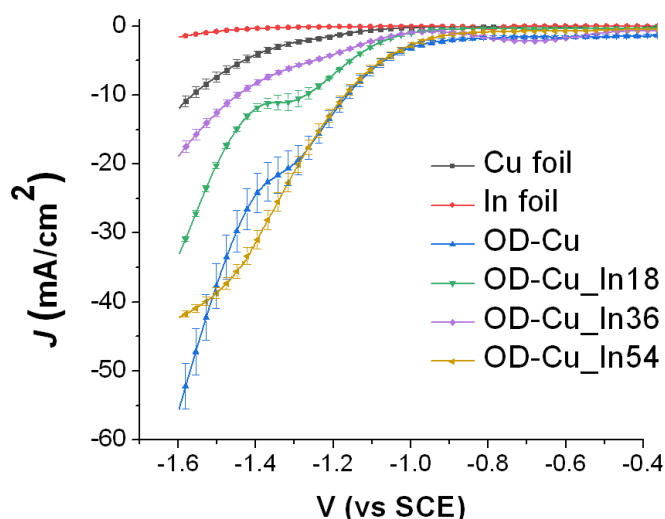
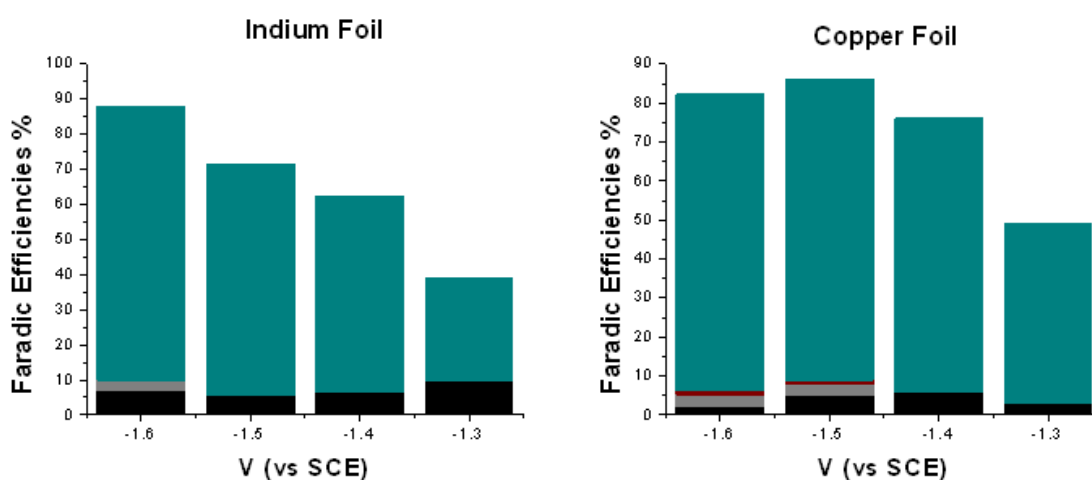


Fig. 44 JV profiles obtained in aqueous electrolyte with Indium treated copper cathodes (respectively 18, 36 and 54 C/cm² in 0.5 M KHCO₃, scan rate 20mV/s) copper, indium foil and OD_Cu as reference



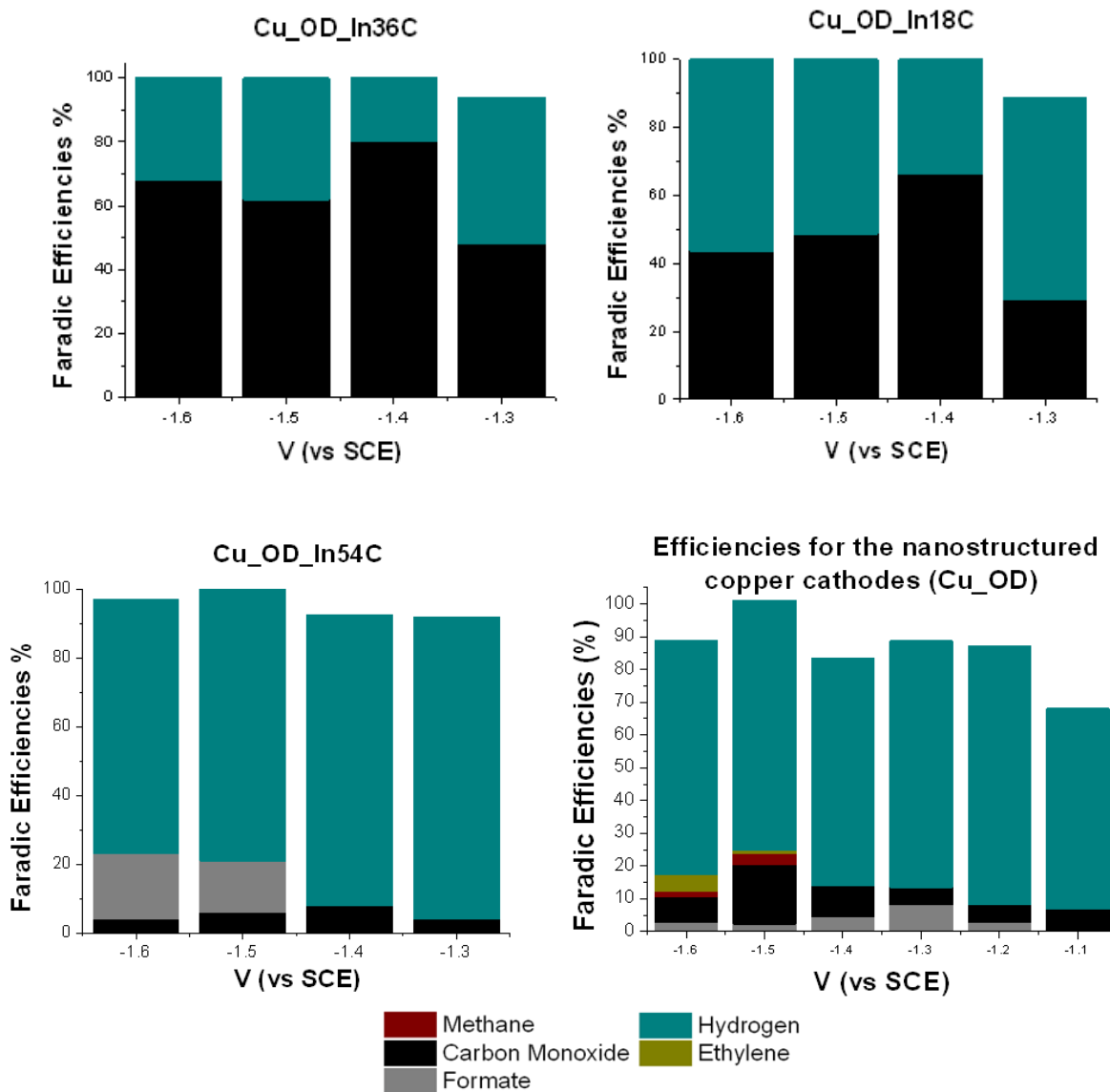


Fig. 45 Faradic efficiencies obtained for the laminar Indium treated cathodes (in 0.5 M KHCO₃ pH:7,4)

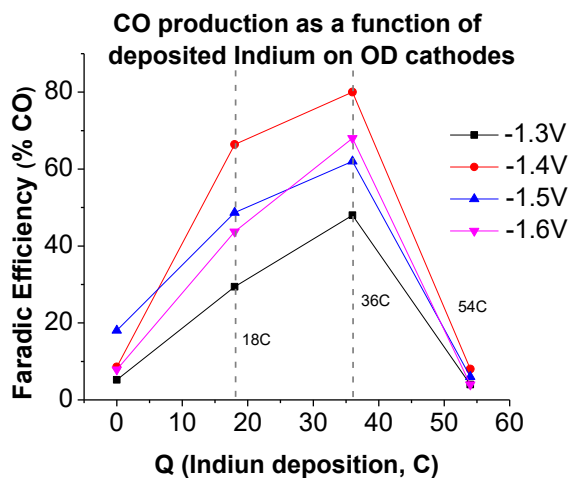


Fig. 46 CO Efficiency as a function of the deposited charge of indium

This procedure was introduced in order to remove adsorbed poisoning species, likely graphitic carbon deposits³⁶ and/or the produced CO itself.^{47,102,103} Anyway, the reconditioning steps only impact the total electrolysis time by less than 10%. At the same time, pulsed CO₂ electroreduction conditions were reported to cause transient changes in local pH and CO₂ concentrations,¹⁰⁴ as well as in the electric field near the catalyst surface.²⁶ This behavior can significantly impact the binding energies of the adsorbed reaction intermediates, which in turn affect the product distribution. Indeed, with regard to the activity of the Cu foil, we observe FE values that differ from those generally reported.^{3,32} In particular, CO evolution starts at -1.3 V, peaks at -1.4 V vs sce (max FE = 6%), and then decreases, while an appreciable production of formate and methane begins at -1.5 V vs SCE (see Fig. 45 “Copper Foil”). Anyway, the total CO₂R products account for ca. 10% of the total current, with H₂ being the main product (FE >46%). On the other hand, the OD-Cu cathodes display higher selectivity for CO, reaching up to 18% FE at -1.4 V vs SCE, while formate starts to be produced at -1.3 V with a maximum FE of 8% (see Fig. 45 “Cu-OD”). At -1.4 V vs SCE applied bias, these cathodes also produce methane (with max FE = 3.5%) and ethylene (max FE = 5% at -1.6 V vs SCE). Even if the total FE due to CO₂R is higher (ca. 25%) with respect to that of the Cu foil, the main product is still H₂.

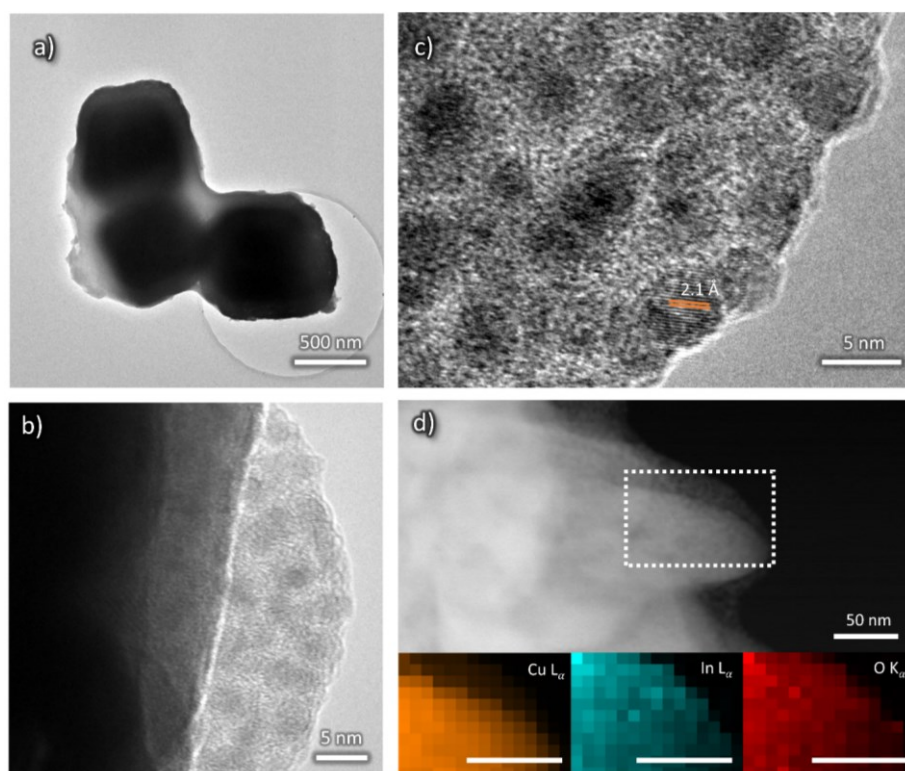


Fig. 47 a) Low and b,c) high magnification HR-TEM micrographs of OD-Cu_In18 sample, displaying the presence of a coating layer embedding crystalline nanoparticles, whose d-spacing is compatible to metallic In or In₂O₃. d) STEM-HAADF micrograph of a OD-Cu_In18 nanocube surface feature and related EDS mapping, displaying higher concentration of In and O in the coating layer.

Indium deposition greatly affects the performances of the mixed-metal cathodes. With regard to the current output (see Fig. 44), the Cu–In cathodes display decreased values at -1.6 V vs SCE with respect to OD-Cu, which can be ascribed (at least partly) to reduced RF. Furthermore, we do not observe a linear dependence of the current density on the In content, with the order being OD-Cu_In36 < OD-Cu_In18 < OD-Cu_In54. Anyway, the selectivity of these composite interfaces towards Syngas production significantly increases with respect to OD-Cu.

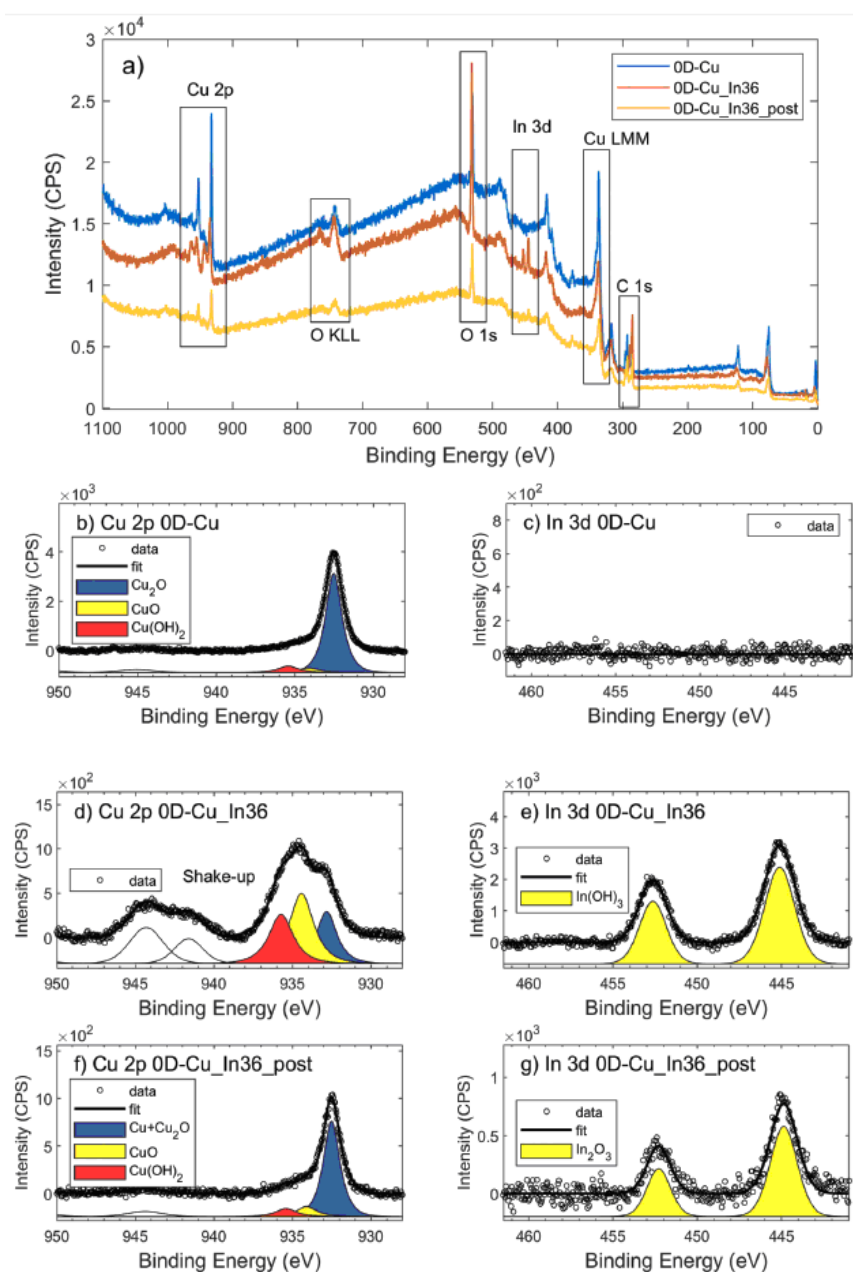


Fig. 48 (a) Survey XPS spectra of OD-Cu (blue), OD-Cu_In36 (red) and OD-Cu_In36_post (orange). XPS signals of Cu 2p, O 1s, In 3d, C 1s and K 2p are present, with Auger signals of O KLL and Cu LMM; (b-d-f) high resolution spectra of Cu 2p_{3/2} in OD-Cu (b), OD-Cu_In36 (d) and OD-Cu_In36_post (f); (c-e-h) high resolution spectra of In 3d in OD-Cu (c), OD-Cu_In36 (e) and OD-Cu_In36_post (g).

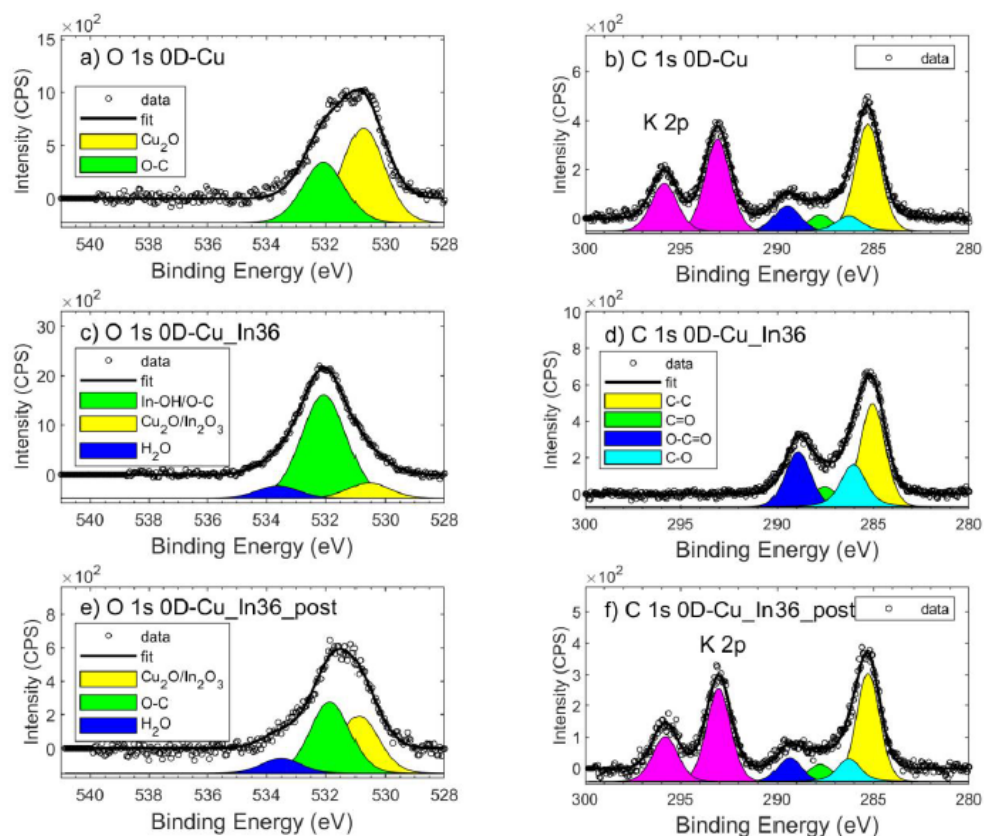


Fig. 49 XPS signals of O 1s (a-c-e) and C 1s (b-d-f). K 2p signal was found only in OD-Cu and OD-Cu_In36_post (doublet in magenta). In (c) the In-OH/O-C peak considers both the contribution of oxygen in carbonate and the hydroxides forms of In (as well as of Cu).

Indeed, as evidenced in Fig. 45, for OD-Cu_In18 and OD-Cu_In36, no other product than Syngas is present in the explored bias range. Appreciable Syngas evolution starts at -1.3 V vs SCE, a relatively low overpotential for the production of the two gases. Under these conditions, the H_2/CO ratio is $\approx 2 : 1$ for OD-Cu_In18 with ca. -5 mA/cm² current density (see Fig. 54 b) and $\approx 1:1$ with ca. -3.5 mA/cm² for OD-Cu_In36 (Fig. 54a). These Syngas compositions are respectively compatible with the production of methanol¹⁰⁵ and with hydroformylation reactions¹⁰⁶. A gaseous mixture with a H_2/CO ratio of $\approx 1:1$ was also obtained for OD-Cu_In18 at -1.5 V vs SCE, sustaining significant current densities in the range $-15/-18$ mA/cm² (Fig. 54b). As far as the production of sole CO versus the applied bias is concerned, a typical volcano trend is observed, with the efficiency peaking at -1.4 V vs SCE for both cathodes, and OD-Cu_In36 yielding a maximum FE of 80%. We also observed the dependence of the FE for CO production on the amount of deposited indium, with OD-Cu_In36 again being the optimized electrode that outperforms the other cathodes in all

the explored potential range (see Fig. 44). A qualitative comparison between the performances of our OD-Cu₁₁In₃₆ cathode and other Cu–In based interfaces reported in the literature is also provided in Table 6:

Synthesis	Morphology	Phase(s)	Products (% FE) ^{a,b}	J _{max}	Ref.
Reductive electrodeposition of In(NO ₃) ₃ on OD-Cu (obtained by fast square wave anodization)	Textured nanocubes (<1 μm)	Cu/Cu ₂ O + In(OH) ₃	@ -1.3V vs SCE ; * For OD-Cu ₁₁ In ₃₆ : <u>syngas</u> (46% H ₂ and 48% CO => H ₂ /CO ratio ≈ 1) * For OD-Cu ₁₁ In ₁₈ : <u>syngas</u> (59% H ₂ and 29% CO => H ₂ /CO ratio ≈ 2)	@ -1.3V vs SCE ; J _{tot} > 3.5 mA/cm ²	This work
Reductive electrodeposition of InSO ₄ on OD-Cu (obtained by thermal oxidation)	Irregular grains (100-500 nm) from agglomeration of 50 nm nanoparticles	Cu ₁₁ In ₉ alloy	@ -1.4V vs SCE : <u>CO</u> (95%) HCOOH (ca. 3%) H ₂ (<2%)	@ -1.4V vs SCE : J _{tot} = -1.7 mA/cm ²	[31]
Cu(OH) ₂ nanowires dipped in an InCl ₃ solution + dehydration	Nanowires (10 μm av. length) with porous structure of Cu nanograins (10-30 nm) covered by a < 5 nm layer of In	Metallic Cu and metallic In	@ -1.3V vs SCE : * For 20% In: <u>CO</u> (93%) H ₂ (ca. 4%) HCOO ⁻ (ca. 3%)	@ -1.3V vs SCE : J _{CO} = -1.5 mA/cm ²	[99]
Electrochemical reduction of CuInO ₂ deposited on carbon paper	Large particle aggregates with some small porosity	Cu ₁₁ In ₉ , Cu ₇ In ₃ and Cu	@ -1.5V vs SCE : <u>CO</u> (70%) HCOO ⁻ (19%) H ₂ (<10%)	@ -1.5V vs SCE : J _{tot} = -2 mA/cm ²	[98]
Near Infrared-driven decomposition of mixed metal precursors on Ti (different compositions obtained)	Nanoparticles (ca. 100 nm average diameter)	* For Cu _{0.75} In _{0.25} : Cu ₂ In phase	@ -1.4V vs SCE ^d ; * For Cu _{0.75} In _{0.25} : <u>CO</u> (80%) H ₂ (20%)	@ -1.4V vs SCE : J _{CO} ≈ -2 mA/cm ²	[101]
In situ reduction of: (a) CuInO ₂ and (b) In ₂ O ₃ /Cu both deposited on carbon black	For both materials: Structural evolution during CO ₂ reduction	Evolved catalyst (for both materials): Cu core + In(OH) ₃ shell	For the evolved cat: @ -1.3V vs SCE : <u>CO</u> (55%) HCOO ⁻ (ca. 5%) H ₂ (ca. 40%)	@ -1.3V vs SCE : J _{CO} ≈ -1 mA/cm ² J _{tot} ≈ -1.8 mA/cm ²	[107]
Electrodeposition from In ₂ (SO ₄) ₃ + CuSO ₄ on Au-sputtered Si. Different deposition potential results in different Cu/In ratios	Dendritic	* If In <25% → Cu(111) * If ca. 38% In → Cu ₉ In ₄ and Cu ₁₁ In ₉	@ -1.7V vs SCE * For 40% In: <u>HCOO⁻</u> (49%) <u>syngas</u> (36% H ₂ and 14% CO => H ₂ /CO ratio = 2.6) * For 80% In: <u>HCOO⁻</u> (62%) CO (ca. 5%) H ₂ (ca. 25%)	@ -1.5/-1.8V vs SCE : J _{HCOO⁻} < -1 mA/cm ²	[100]

Tab. 6. Comparison of CO₂ reduction performance on different Cu-In catalysts. (^a Unless otherwise stated, all data are obtained in CO₂-saturated 0.1 M KHCO₃ aqueous solution; ^b Main product underlined; ^c Data obtained in CO₂-saturated 0.5 M KHCO₃ aqueous solution; ^d Data obtained in CO₂-saturated 0.5 M NaHCO₃ aqueous solution).

At the same time, when the indium content increases, H₂ evolution becomes the dominant reaction (see Fig. 45 “Cu_OD_In54”), with the FE for CO production being <10% . A similar trend for CO and H₂ production was also observed by Züttel and coworkers for the surface modification of Cu(OH)₂ nanowires with metallic In nanoparticles.⁹⁹ Density functional theory studies revealed that the optimized bimetallic interfaces (i.e. those with the highest number of Cu–In interfacial sites, generated by a medium coverage of In on the Cu surface) significantly decrease the free energy barrier for the formation of *COOH (the key intermediate for CO formation) and the strength of the adsorbed *H (thus limiting H₂ production). Also in our case, when the deposited indium exceeds the optimal amount obtained for the OD-Cu_In36 cathode, the interfacial reactivity changes, closely resembling the catalytic outcomes obtained when using a bare In foil (see Fig.45). Indeed, under our conditions, both the latter and the OD-Cu_In54 electrode produce only H₂ and CO in the low applied bias range, but at higher negative bias values formate ions are also produced (up to 19% FE at -1.6 V vs SCE for OD-Cu_In54, see Fig. 45). These results further point out that pulsed electrolysis strongly affects the reactivity of the catalytic metal and the absorption/desorption of key intermediates as CO₂R by indium generally yields HCOO⁻ as the main product.¹⁵

The observed enhanced selectivity for CO₂ reduction to CO can be due also to a synergistic effect between Cu and In(OH)₃, as recently pointed out by Larrazábal et al.¹⁰⁷ Indeed, when the In(OH)₃ layer was etched from an OD-Cu_In36 cathode by means of an acid treatment reported in the literature,¹⁰⁷ the CO₂R performances of the cathode were strongly reduced. As evidenced in Fig. 54c, when comparing the FE for CO production by a pristine OD-Cu_In36 cathode with those of the exact same electrode after two successive etching treatments, under the latter conditions we formed ca. 2/3 and 1/3 of the initial CO amount.

3.3 Cathodes stability and lifetime

While the chronoamperometric experiments for products detection and accumulation gave us a first hint of the good stability of our cathodes in the 20-min timescale, a representative Cu_OD_In36C cathode was also tested in longer-term CO₂R conditions. Indeed, Figure 50 reports the > 2 hour-long electrolysis performed at -1.4V vs SCE, displaying that after the first 0.25 h, the current density sets at a quite stable value of ca. -3.5 mA/cm². However, when sampling the reaction, we observed a decrease of the initial CO amount (accounting for a 70% FE, the sole other product being H₂) down to ca. 10% FE after 1 h. Being the performances in terms of current density essentially unvaried in this time frame, some structural modification in the catalyst should happen, favoring H₂ evolution. In order to shed light on this behavior, we performed microscopic and spectroscopic characterizations of the cathodes after operation

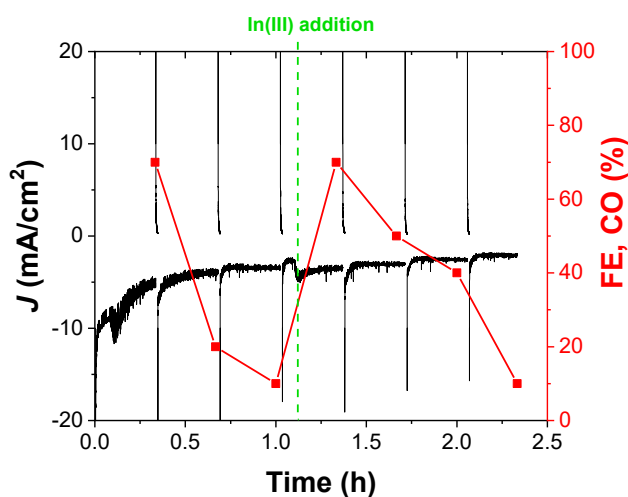


Fig. 50 Chronoamperometric trace of a OD-Cu_In36 cathode stepped between -1.4 Vvs SCE and the open circuit potential, OCP. The Faradaic efficiency for CO production at different sampling times is also reported. The green dashed line marks the addition of 1 mL of a 0.04 M solution of In(NO₃)₃ in 0.5 M citric acid, aimed at restoring the active In-based layer and consequently the previous CO production

In particular, XPS analysis evidenced that after 1 hour of electrochemical CO₂R the Cu_OD_In36C cathode (called Cu_OD_In36_post) presents the same elements of pristine one (except for the appearance of K), but in overall reduced chemical state: Cu is reduced from Cu(II) to Cu(I)+Cu(0) and In change from hydroxide to oxide chemical state. Combining information from the main signal of Cu 2p_{3/2} (932.5 ± 0.1 eV) and the double signal present in Auger Cu LMM signal (AP 1851.1 ± 0.2 eV for Cu(0) and AP 1849.1 ± 0.2 eV for Cu(I)) we can support that the surface after electrochemical test is mostly a mix of metallic Cu and Cu₂O, pointing out that the XPS was performed ex-situ, thus Cu₂O may also rise from atmospheric passivation of metallic Cu. On the other hand, the Indium decreases in relative concentration, from 1.8 to 0.8%, and presents a shift (see Figure 51 c) in binding energy from 445.2 eV to 444.9 eV compatible with chemical

change from hydroxide to oxide, as discussed above. Finally, the O 1s signal presents an increase of purely oxides (Cu_2O and In_2O_3) components in 530.8-530.5 eV region respect to hydroxides and C-O at 532 eV.

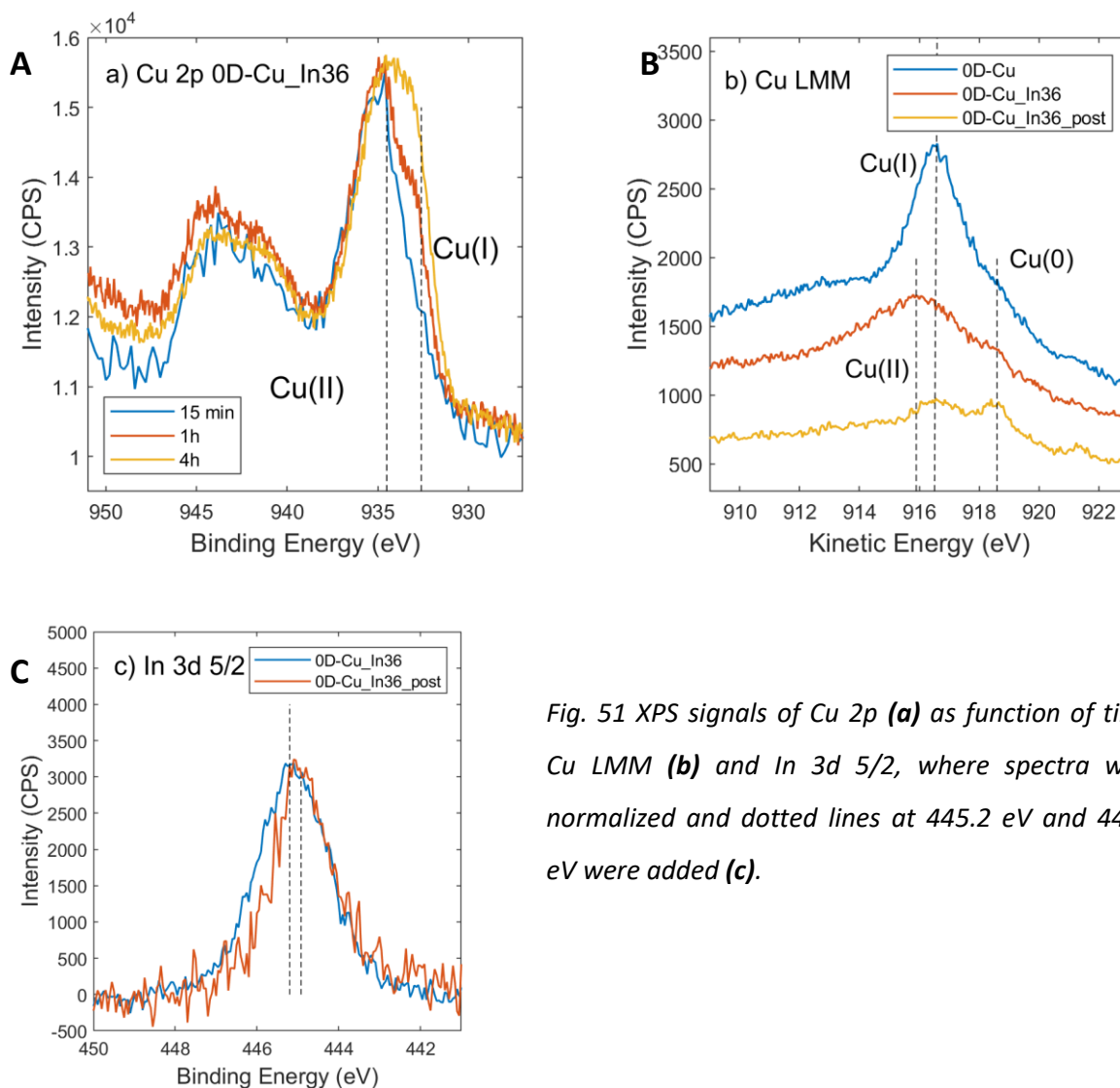


Fig. 51 XPS signals of Cu 2p **(a)** as function of time, Cu LMM **(b)** and In 3d 5/2, where spectra were normalized and dotted lines at 445.2 eV and 444.9 eV were added **(c)**.

The grazing-incidence XRD supports these results, evidencing the appearance of Cuprite phase after CO_2R , as also confirmed by an increased oxygen content in EDS analysis (see Figure 52). A lower Indium content is also observed, probably due to a partial dissolution of the deposited In-based nanostructures, consistent to the drop in the FE for CO production observed over prolonged exposure to the electrolysis conditions. In agreement with that, SEM and TEM micrographs do not exhibit a homogeneous distribution of the In-based coating, in contrast to what observed before the electrolysis experiment (Figure 53).

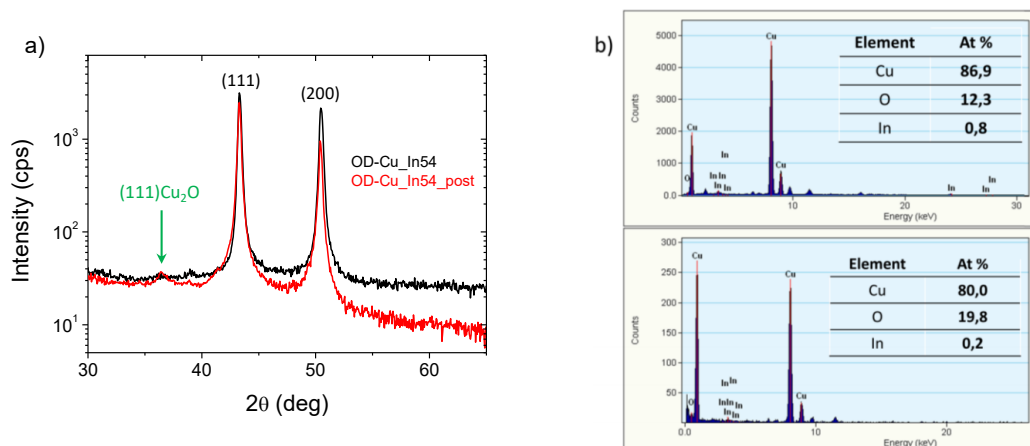


Fig. 52 **(a)** Grazing-incidence X-ray diffractograms of OD-Cu_In54 before (black trace) and after (red trace) CO₂R experiments. **(b)** EDS spectra registered on a wide sample area identified by TEM, reporting relative Cu, O and In atomic content in the inset for OD-Cu_In54 before (top) and after (bottom) CO₂R experiments. Comparison based on OD-Cu_In54 sample to enhance the role of In-deposition on the materials structure upon exposure to CO₂R working conditions.

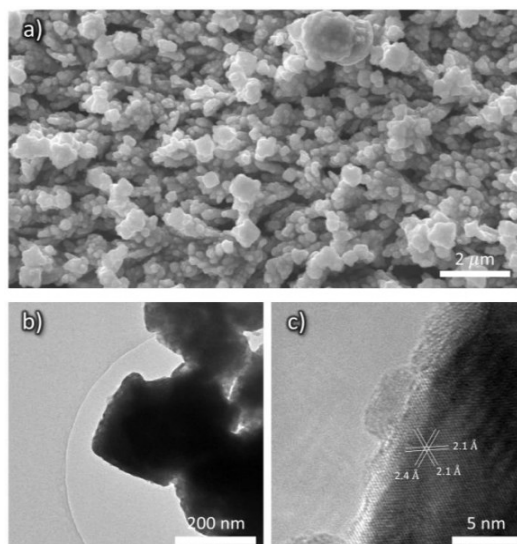


Fig.53 **(a)** SEM micrograph and **(b)** low or **(c)** high magnification HR-TEM micrographs of OD-Cu_In54 after CO₂R experiments. In the inset, d-spacing corresponding to lattice reflections compatible with Cuprite phase.

However, the catalytic activity can be fully restored by performing an additional Indium deposition step in situ. Indeed, as evidenced in Figure 50, after the addition of In(NO₃)₃ to the electrolytic solution, the CO production was fully restored, speaking in favor of a restoration of the active In-based layer.

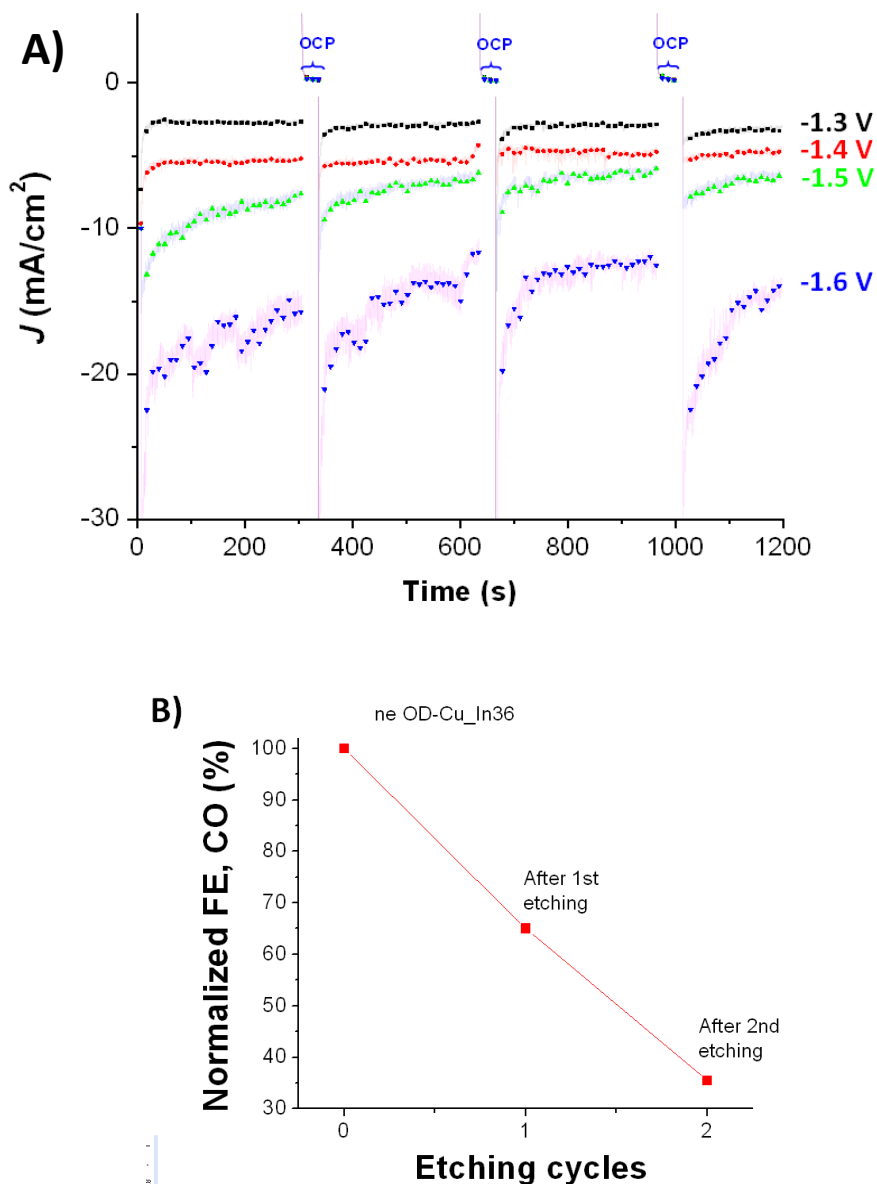


Fig. 54 **(a)** Stepped chronoamperometry experiments performed for the accumulation of the products obtained with OD-Cu₂In₃₆. In particular, the cathode was stepped between the bias reported in the graph (for 300 s) and the open circuit potential, OCP (for 40 s). **(b)** Faradaic efficiency for CO production for a pristine OD-Cu₂In₃₆ compared with those of the same cathode after 1 or 2 etching cycles aimed at removing the In(OH)₃ phase. Each etching cycle consists in 15-min immersion of the cathode in 1 M H₂SO₄ aqueous solution.

3.4 Final considerations on OD-Cu_In(X) cathodes

Nanostructured Cu cathodes with a predominant nanocubic morphology were prepared via straightforward and readily available electrochemical procedures. Their characterization revealed the presence of both metallic Cu and Cuprite (Cu_2O). Further functionalization of these cathodes through In deposition led to the formation of heterointerfaces with enhanced activity towards the selective reduction of the greenhouse gas CO_2 to a valuable product, i.e. Syngas. In particular, in aqueous solution and under low applied bias (i.e. -1.3 V vs SCE), the OD-Cu_In18 and OD-Cu_In36 cathodes produced gaseous mixtures with $\approx 2:1$ and $\approx 1:1$ H_2/CO compositions, which can be exploited respectively for the synthesis of methanol and aldehydes, with current densities >3.5 mA/cm^2 in absolute value. Even if the medium-term stability of the cathodes under CO_2R conditions suffers from the partial leaching of the In-based active phase, their catalytic activity towards Syngas formation can be restored upon further addition of the In(III) precursor to the electrolytic solution.

The development of this work will be directed towards the implementation of the proposed copper nanostructuring/indium functionalization electrochemical techniques to three dimensional substrates, such as Cu foams. The resulting cathodes would provide a porous environment with a highly exposed interfacial area, thus leading to higher currents.

4. Copper foams



Fig. 55 Image of the copper foams used in our laboratories

The OD treatment was observed to be effective also using different substrates from the laminar one, such as copper wires or folded foils apparently without being influenced by the different geometry and the initial crystallographic orientation. Thanks to this peculiar characteristic we decided to use of more morphologically complex substrates like copper foams in the hope of magnifying the electrochemical performance, due to a larger exposed area, while maintaining the catalytic properties of the nanostructured foils. Copper foams are a currently available product on the market commonly designed for various purposes (from heat exchanger to electrodes) and exhibit extremely large effective/geometrical areas in a contained geometric surface. The below reported SEM images (fig. 56) allow to observe the formation of nanocubes even in this particular type of substrate without the application of any significant change in the optimized synthesis procedure described in section 3.2.

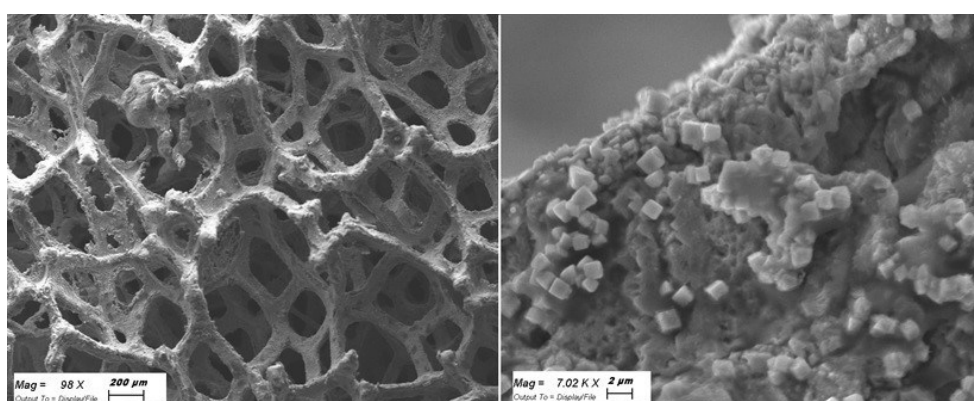


Fig. 56 SEM image of the “foam” electrodes (on the right a particular of the surface)

These 3D electrodes were demonstrated to develop significantly higher currents densities than their similar bi-dimensional counterpart (fig. 57).

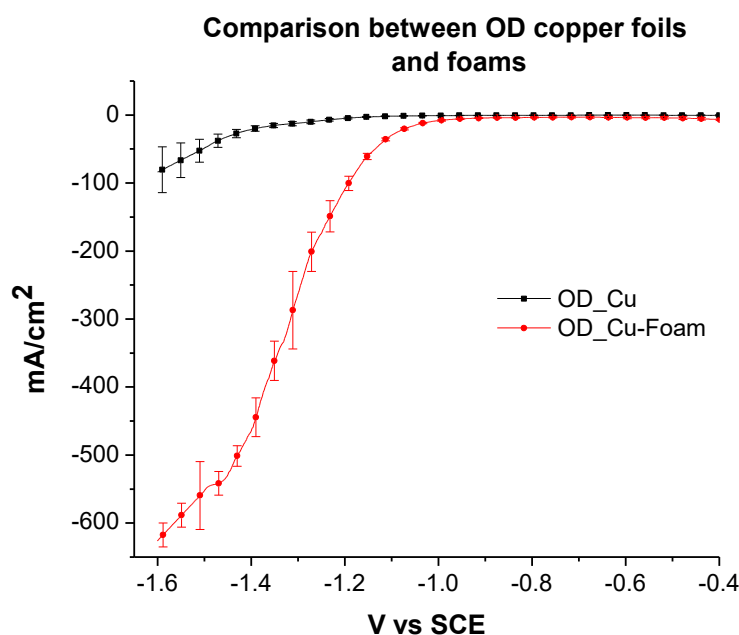


Fig. 57 JV profiles obtained in aqueous electrolyte for OD treated copper foams (OD_Cu_Foam in 0.5 M KHCO_3 , scan rate 20mV/s pH:7.4) compared to the laminar OD_Cu electrodes

As shown in the picture reported above the nanostructured foams (indicated with OD_Cu-Foam) are able to achieve extremely high currents for square centimetre overperforming ten times the Cu_OD foil substrates, reaching at -1.6V vs SCE over 600 mA/cm^2 .

If on one hand the new substrate can be considered a success, surely in terms of electrochemical performance, on the other side the catalytic efficiency is subjected to high variability and in most of the case leads to an insufficient yield in terms of carbon dioxide reduction products. In fact, as showed in the image below (Fig. 58), the carbon monoxide barely reaches the 10% of maximum faradic efficiency leaving a clear catalytic pattern centred on the hydrogen evolution that drives more than 90% of the total current. While the peak in CO synthesis can be observed at the potential of -1.4V vs SCE also a peak in the production of formic acid (present in the form of formate anion) is detect at -1.3V vs SCE, corresponding to an approximate value of 10% FE. Unlike the laminar substrates it was not possible to quantify more complex products such as methane and ethylene suggesting some differences in the catalytic paths from their laminar counterpart even if the OD treatment used is the same. Probably the density of nanocubes in the whole 3D structure is not sufficient to suppress the usual catalytic activity of the conventional randomly oriented copper surface, which is still significantly exposed to the electrolyte.

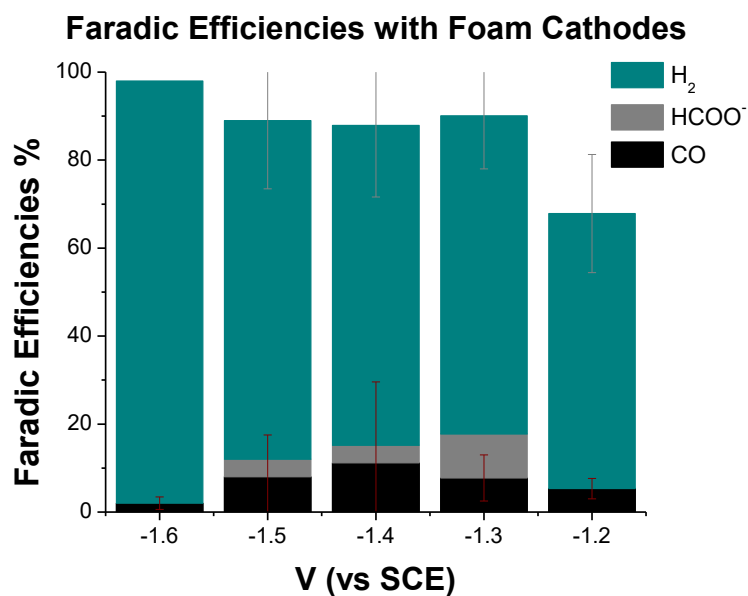


Fig. 58 Faradic efficiencies obtained for OD_Cu-Foam cathodes

Furthermore, while the current density was fairly reproducible, the faradic yields were highly variable from electrode sample to sample, probably due to variations in the cube coverage induced during the OD treatment that were difficult to control. Large error bars reported in the graph (Fig. 58) were the result. Due to these issues and to the related difficulties in achieving a sufficient reproducibility over the FE, we searched for other substrates with a less pronounced catalysis towards H₂ evolution. In that case, the surface that is left uncovered by the cubes will not contribute significantly to proton reduction.

5. Carbon based cathodes

Commercially available carbon foams (CF), are characterized by a high electrochemical area, *per se* poor electrocatalytic properties and good mechanical properties. Carbon foam is endowed with high electrical conductivity while manifesting at the same time a really low activity towards hydrogen evolution in the potential window and electrolytic solution commonly adopted for our experiments. These electrodes are largely inert out to -1.3 V vs SCE and current density of just few mA/cm² at -1.6 V vs SCE could be recorded (Figure 59 on the right).

We also speculated, that, in principle both the Cu electrodeposition and the OD treatment should extend similarly in this type of material, while the carbon fiber which is left unmodified by the copper plating should behave largely as an inert conductor within the potential window of interest.

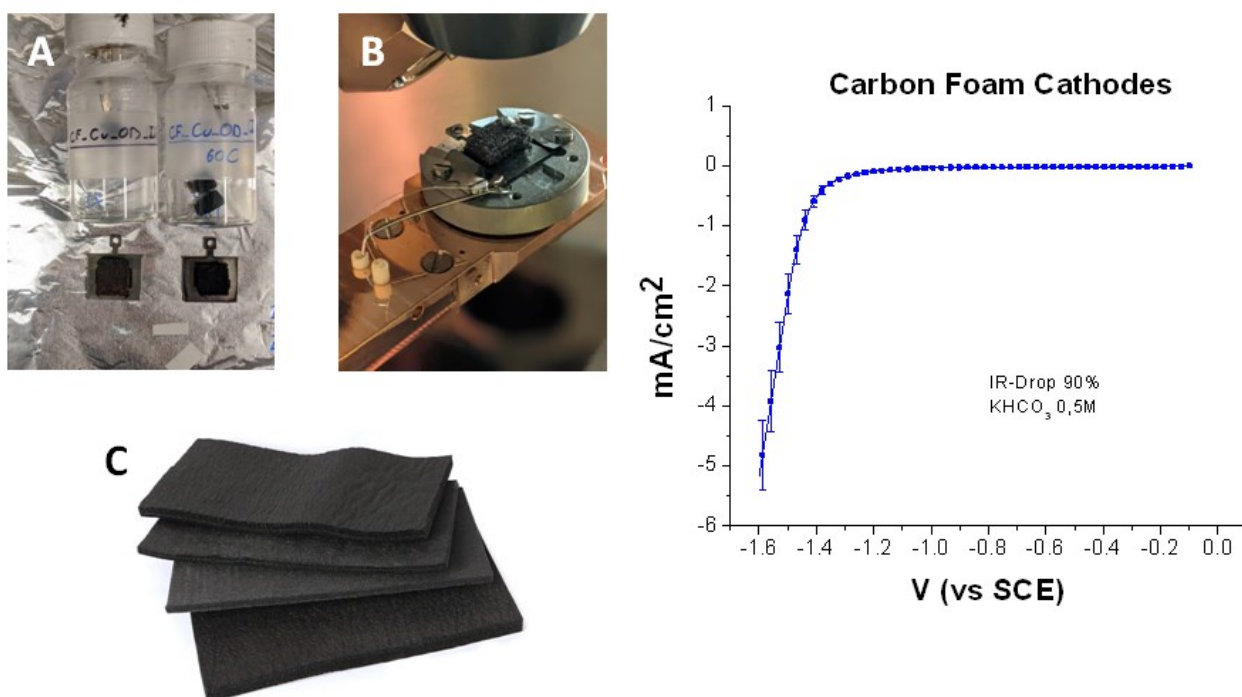


Fig. 59 Pictures of the carbon foam (CF) electrodes (A, B,C) and on the right their JV profiles obtained in aqueous electrolyte for this substrate (0.5 M KHCO₃, scan rate 20mV/s pH:7.4)

As illustrated in the figure 60 carbon foams are constituted by a compact aggregate of carbon fibers that shows, under SEM magnification, a constant diameter in the order of approximately 6-7 μ m. This feature allows them to be the perfect candidates to support copper deposition for the building of the new metallic foam electrodes. On this purpose a common copper plating procedure was chosen, by immersing the contacted foam into an acid solution of copper sulphate 0.5M and sulphuric acid. The process takes place in a one-compartment cell with a copper foil as a counter electrode by potentiodynamic cycling from 0 V to -2

V at a scan rate of 20 mV/s. After an optimized number of 20 scans a clear and uniform copper layer is visible causing the change in the color of the foam from the classical black of carbon to the characteristic red of the copper metal. The positive results of the treatment is confirmed via SEM microscopy by simple imaging of the surface. In fact as described in the figure below (Fig. 60) the copper deposition leads to an increase in the diameter of the fiber of approximately 15 μm reaching a total diameter of 21-22 μm , exposing a compact metallic copper interface.

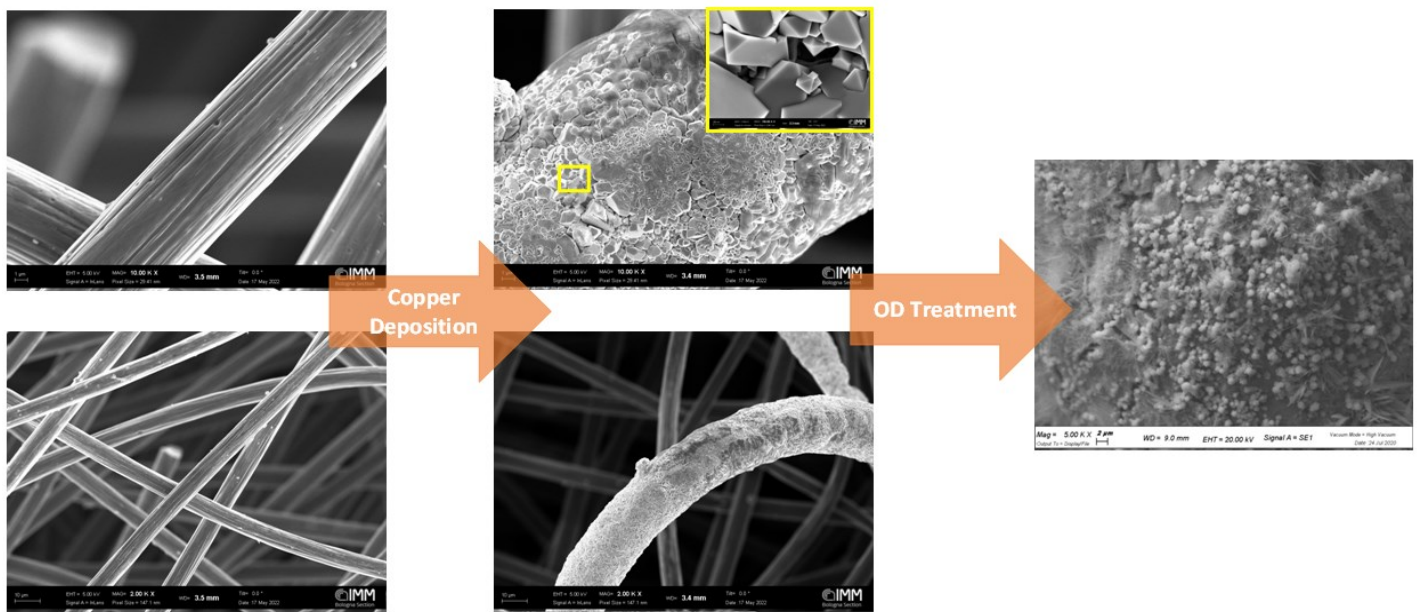


Fig. 60 Different SEM magnifications of a carbon foam copper after each phase of the nanostructuring OD procedure. On the right its possible to appreciate the nanocubes obtained

After the copper deposition it was possible to proceed with the traditional OD treatment of the obtained foam (CF_Cu) since the thickness of the metallic coating is enough to guarantee the complete realization of this procedure. After this step and the subsequent reduction (see chapter 3.2) the foam results decorated with the same nanostructured interface observed for the laminar OD-Cu. In the right side of Fig. 60 are highlighted the details of these structures, where in fact its possible to recordnize the same dendritic copper background decored with the cuprite nanocubes analyzed in details in the previous chapter (see part 2 and 3).

The copper electrodeposition clearly highlights the previously described issues reported for the purely metallic copper foams in fact, thanks to the high visible contrast in the colors between carbon and copper, it is possible do directly visualize by eye the macroscopic regions excluded from a proper metallic coating, in particular the back of the electrode (the side of the electrode not facing the counter electrode) remains largely unmodified by the copper plating, but exposing pristine carbon, being a largely inert substrate, we do not expect it to contribute significantly to the electrolytic process..

5.1 OD treatment and Indium functionalization of carbon based cathodes

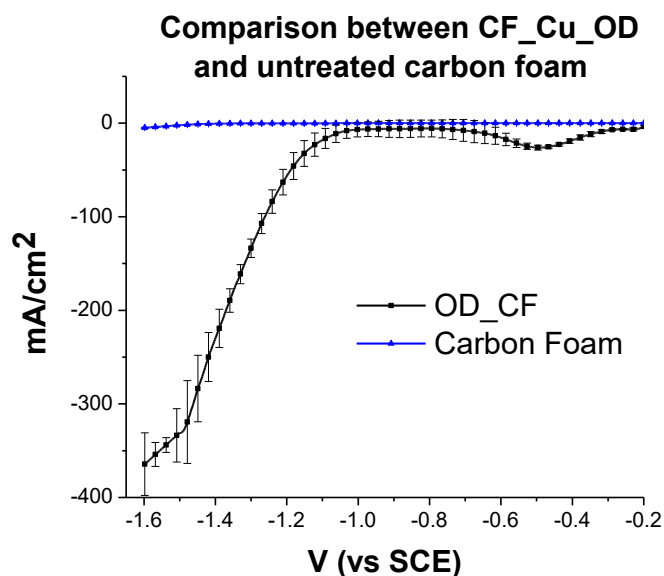


Fig. 61 JV profiles for OD_CF cathodes (in KHCO_3 0.5 M, scan rate 20mV/s pH:7.4) compared to the simple untreated carbon foam reported as reference

The OD treatment takes place following the standard optimized procedure adopted for the laminar cathodes, in particular the CF-copper electrode is immersed in a 0.1 M K_2SO_4 / 0.04 M KCl aqueous electrolyte in a single compartment three-electrode cell. The soldered ohmic contact (in particular on this regard silver paste was used) was protected with epoxy resin. A double jacket saturated calomel electrode (DJ-SCE) was used as a reference, and a platinum wire served as a counter electrode. The square wave anodization (SW) was applied for a duration of 300 seconds, at a frequency of 10^3 Hz according to a wave form, ranging between + 1000 mV and 0 mV vs SCE. The electrodes thus obtained are subsequently subjected to a further reduction in KHCO_3 0.5M to reduce the copper oxide formed in the anodization stage. These electrodes made this way are defined CF-OD.

The current-potential profiles (JV) obtained with these new cathodes (fig 61) shows a dramatic current development almost comparable to the metallic foams. In fact it was possible to reach an average density higher than 350 mA/cm^2 at -1.6V vs SCE outperforming the laminar cathodes. The surface regions that results uncovered and non nanostructured probably leads to the less current observable in comparison to the metal foams, characteristic that can have positive results in the suppression of the hydrogen excess due to the inactivity of the exposed carbon fiber. With a similar behave from the OD_Cu electrocatalysts also these types of electrode shows a comparable onset potential placed at -1.0 V vs SCE (chosen at the arbitrary current of -1 mA/cm^2).

Following the previously discussed results involving the indium modified Cu-OD sheets electrodes, (OD_Cu_In18/36/54) we performed a similar functionalization of the CF-OD electrodes, where however, the amount of deposited indium was tuned to take into account the larger surface area of the CF electrodes. The flow chart below summarizes the electrode preparation procedure

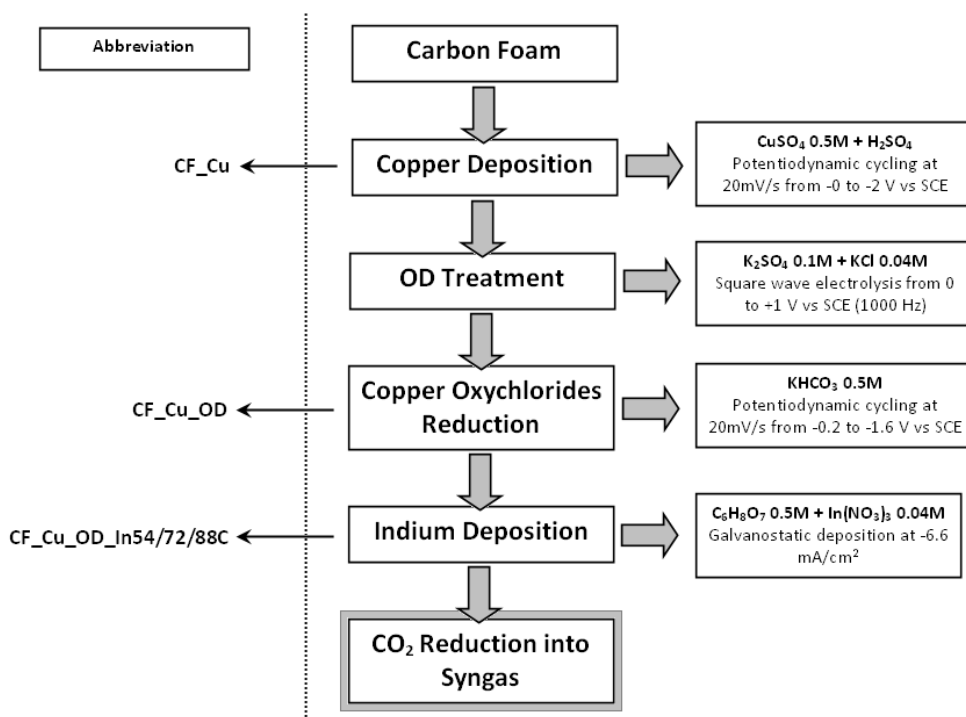


Fig. 62 Electrochemical procedure adopted for the synthesis of indium functionalized carbon based cathodes

The indium electrodeposition proceeds using a two-electrode experimental set-up, with an indium wire as counter electrode as usual. The deposition is carried out under galvanostatic mode (-6.6 mA/cm²) while gently stirring the solution, containing 0.04 M indium citric acid solution (obtained from 0.04 M of indium nitrate + 0.5 M of citric acid). From now on we will call the copper plated carbon foams treated with OD and electrodeposited indium as CF_Cu_OD_InXC where X indicates the amount of charge passed during indium deposition; in particular, the indium deposition was carried out by passing respectively 54, 72 and 88 C/cm² of indium into the cathode.

5.2 Electrochemical responses of copper-indium cathodes on carbon foam

Figure 61 shows the J–V curves of CF-Cu_OD_In(X) electrodes recorded at 20 mV/s (in 0.5 M KHCO₃; pH 7.4) while compensating for the ohmic drop (90%). All the traces correspond to average values of at least five equivalent electrodes and the corresponding standard deviations are also reported as error bars, evidencing the good reproducibility of the outcomes in terms of generated current. The analysis of the J-V curves for porous nanostructured cathodes were made in the standard potential range -0.2 V to -1.6 V (vs SCE). In all cases a pronounced wave is observed at about -1.0 V, related to the reduction of superficial salts/oxides of indium. From the experiments conducted on the cathodes made according to our methodology it was possible to obtain very encouraging results. In particular, the graph shows that the CF_Cu_OD_In72C (blue line) cathode display higher currents than the other two, reaching values close to -150 mA/cm². The other two cathodes, CF_Cu_OD_In54 and CF_Cu_OD_In88, respectively show currents in the order of -100 mA/cm² and -50 mA/cm² at the most negative potentials explored (-1.6 V vs SCE)

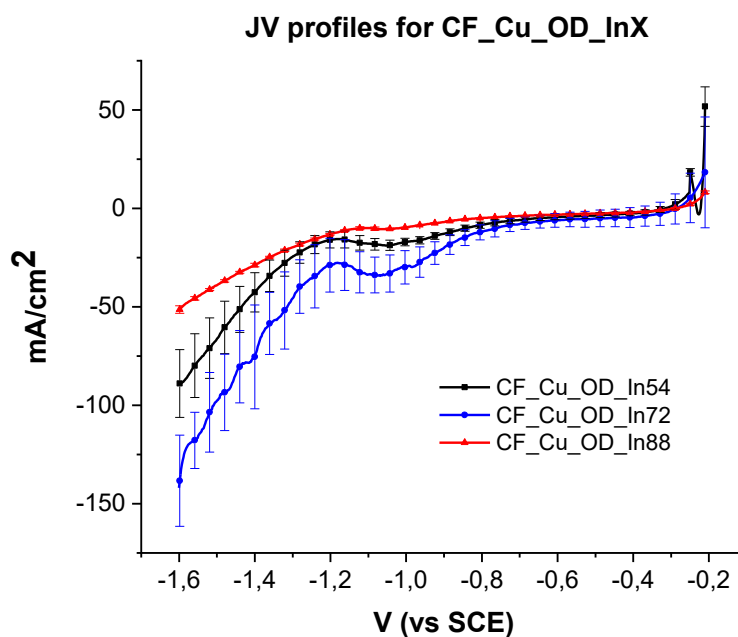


Fig. 63 Averaged J-V curves for CF_Cu_OD_In54C (black); CF_Cu_OD_In72C (blue) and CF_Cu_OD_In88C (red) recorded in 0.5 M KHCO₃ saturated with CO₂ (pH 7.4), normalized for the geometric area and corrected for the iR drop.

As expected, due to the substantial capacitive charging, the current densities reported under potentiodynamic conditions at 20mV/s of scan rate are higher than the currents recorded under steady state conditions (i.e. by potential stepping until a stable steady state current is reached). Nevertheless it is Figure 64 which is most relevant to evaluate the real performance of the electrodes under steady state electrolysis.

The graph below shows the steady state currents of the three electrodes. The analysis is done in a range of -1.3V to -1.6V (vs SCE) and refers to the current values measured after 300s of electrolysis providing useful data related to the Syngas production in time scales in the order of about 2 to 3 hours, that corresponds to the lifetime of these substrates. It can be noted that also in this case cathode CF_Cu_OF_In72 has a higher current density than the others, that is about -60 mA/cm². Concerning the other two cathodes CF_Cu_OD_In54 and CF_Cu_OD_In88 have very similar values, respectively -40 and -45 mA/cm² at -1.6 V but the CF-Cu_OD_In88 is quite superior to CF-Cu_OD_In54 at intermediate voltage.

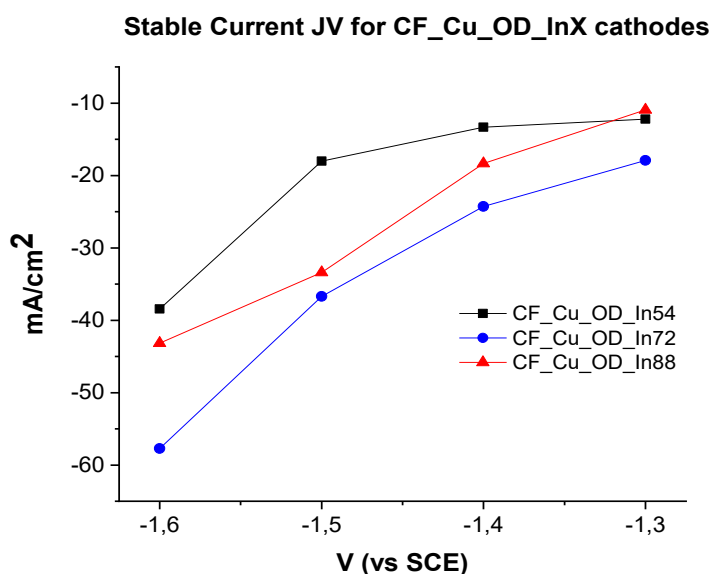


Fig. 64 Steady state current JV for CF_Cu_OD_In54C (black); CF_Cu_OD_In72C (blue) and CF_Cu_OD_In88C (red) recorded in 0.5 M KHCO₃ saturated with CO₂ (pH 7.4).

5.3 Faradic Efficiencies of carbon based electrodes

The catalytic performance of the electrodes developed was evaluated by quantifying the reduction products, using the techniques described in the experimental section. CO₂ electrolysis was accomplished by potentiostatic chronoamperometry by exploring various potentials at which the faradaic activity of the electrode was observed by the previous potentiodynamic JVs. Faradic yield were computed according to Equation reported in chapter 2.2.3. Upon electrolysis of the buffered KHCO₃ solution, we can observe that the CF modified electrodes are substantially selective towards syngas evolution: in Fig. 65 the average faradic efficiencies (FE) of the main products (CO and H₂) are reported for CF_Cu_OD_In54C, CF_Cu_OD_In72C and CF_Cu_OD_In88C as a function of the applied bias vs SCE. Starting from the cathode CF_Cu_OD_In54C, we observe a peak of CO about 35% at -1.3 V and -1.5V (vs SCE), but overall the CO production was quite constant, with fluctuations around 25% within the whole potential interval. For the

CF_Cu_OD_In72C, on the other hand, it was possible to obtain nearly quantitative yield of syngas (H_2+CO in ca. 50% ratio), in the best cases was associated to stable electrode operation for more than 3 hours at high current densities (ca. $-40/-45 \text{ mA/cm}^2$ at ca. -1.5 V vs SCE). A further increase in the surface concentration of indium leading to the CF_Cu_OD_In88C, this type of electrodes shows decreased performance with respect to the previous case, producing a more or less constant trend yield of CO, with a peak up to 40% of CO at -1.4 V .

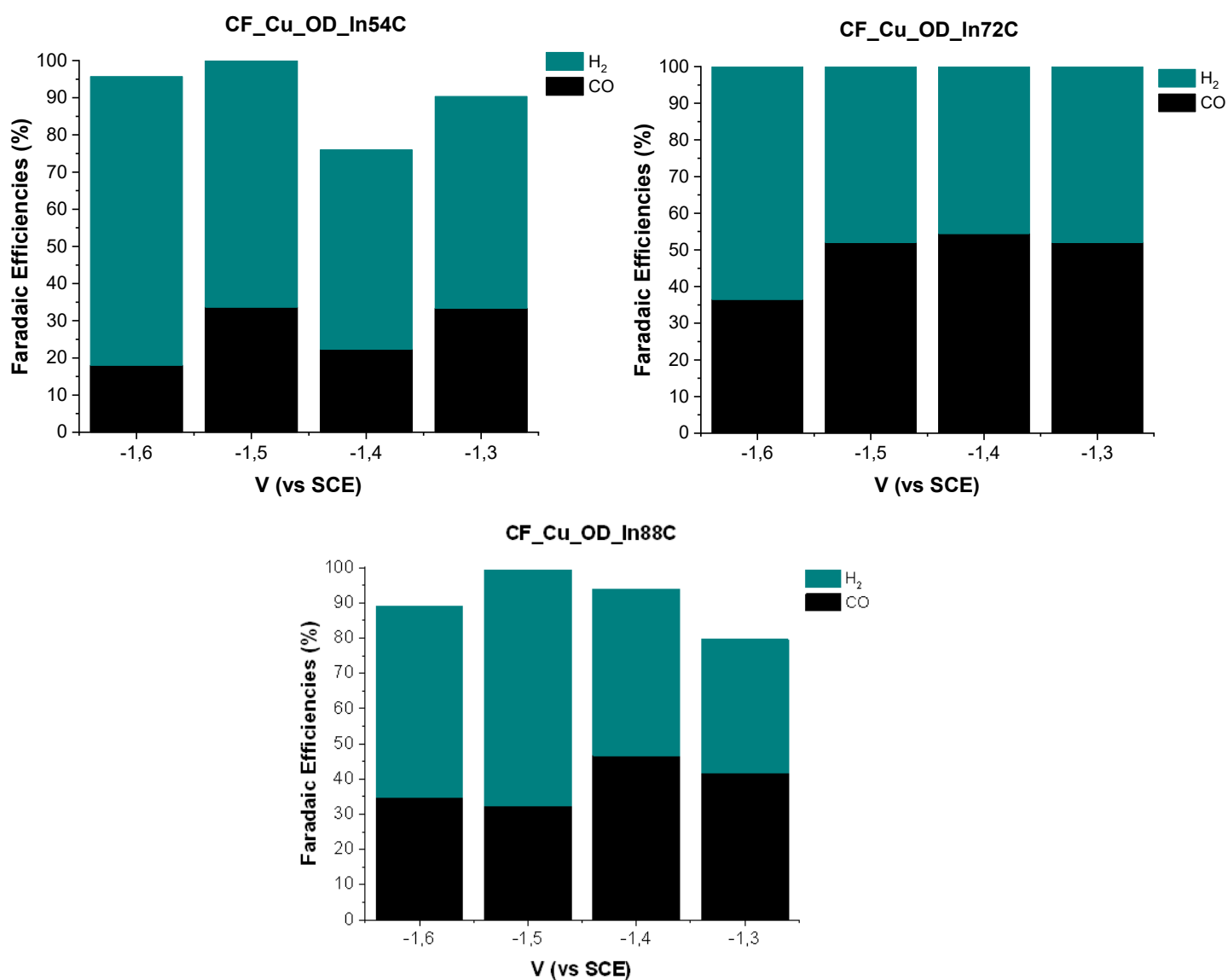


Fig. 65 Faradic efficiencies of syngas evolution (CO and H_2) at CF_Cu_OD_In54C, CF_Cu_OD_In72C and CF_Cu_OD_In88C electrodes in CO_2 saturated 0.5 M KHCO_3 .

Comparing the different Cu/In modified carbon fiber electrodes at different potentials, we note that the electrode CF_Cu_OD_In72C has the best performance. We also observed that CF_Cu_OD_In72C produces a syngas composition which is richer in CO (ca. 50% at $-1.3/-1.5 \text{ V vs SCE}$) than the one desired for methanol production, where, more commonly H_2/CO ratio of 3/1 is used. We note that, in principle, such a mixture

could be obtained by adding H₂ generated from the conventional water electrolysis, or, simply, by performing the electrolysis at a higher voltage, like -1.6 V, where the H₂/ratio is closer to the ideal one, with all the benefit associated by performing the electrolysis at a higher current density.

Another figure of merit for evaluating the performance for the catalytic CO₂ reduction of these electrodes is given by product of the steady state current density (J) times the faradic efficiency (FE) (of CO evolution in the specific shown in Fig.66a), at each applied potential. JxFE yields the number of moles of products produced per unit of time, and represents the rate of CO₂ reduction by the electrochemical cell. From the trends in Fig.67 we confirm that the rate of CO₂ reduction increases with increasing voltage up to -1.6 V vs SCE and that the CF_Cu_OD_In72C is the most efficient within this series.

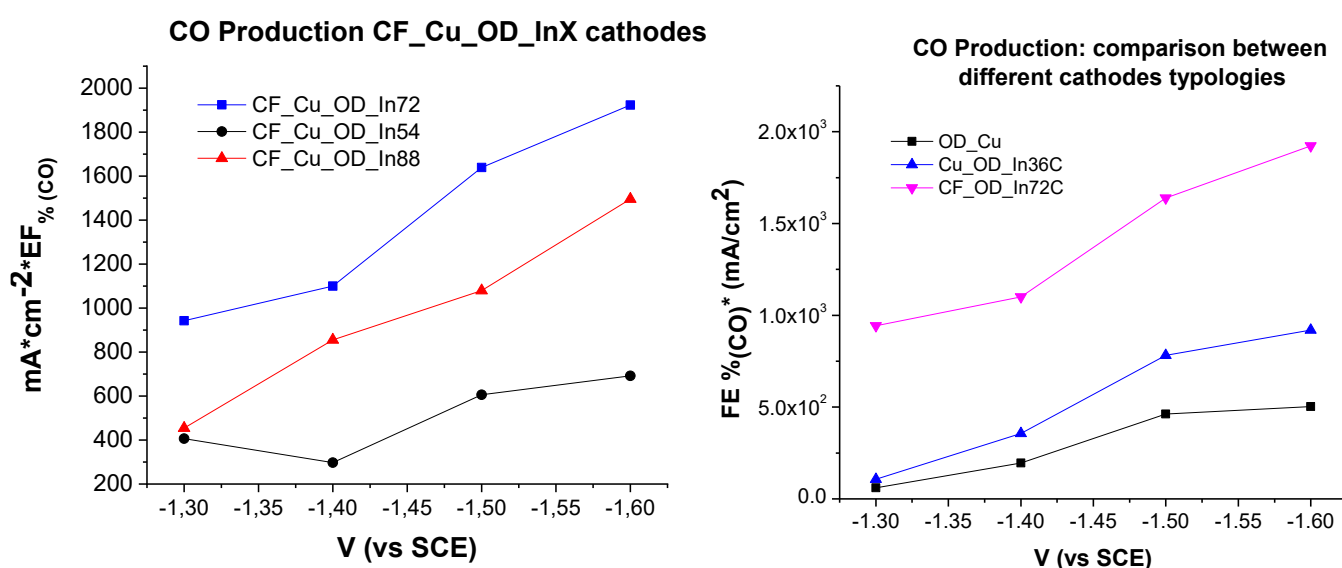


Fig. 66 a) CO production rate of CF_Cu_OD_In54C, CF_Cu_OD_In72C and CF_Cu_OD_In88C at various potentials. c) Carbon monoxide production rate expressed as the product between the stable current (mA/cm²) and the faradic efficiency (%) as a function of the applied bias. The graph describes the data obtained for OD treated copper foil (black line) OD copper foil functionalized with indium (blue line, Cu_OD_In36C) and for the copper deposited carbon foam functionalized with indium (purple line, CF_OD_In72C)

To elucidate the enhanced CO₂RR performance of nanostructured cathodes, we obtained the Tafel plots from slow scan polarization curves of the best In modified one with respect to an un modified CF_Cu_OD type. For the latter, we could not observe a reasonably linear region over approximately two current decades. The polynomial shape of the Tafel plots, suggests a complicated mechanism, where the surface coverage of electrochemical intermediates varies continuously with the potential. Attempts to fit two pseudo linear region afforded values of 90 and 150 mV which cannot be related to a simple rate limiting mechanism of various cathodes. On the another hand CF_Cu_OD_In72C displays a much more linear

behavior, with a slope of 126 mV, which could be indicative of a rate limiting electron transfer process (120 mV at 298K, Figure 67). The slow electron transfer for the competitive H₂ evolution may thus explain the better selectivity of CF_Cu_OD_In72C electrode for CO₂ reduction.

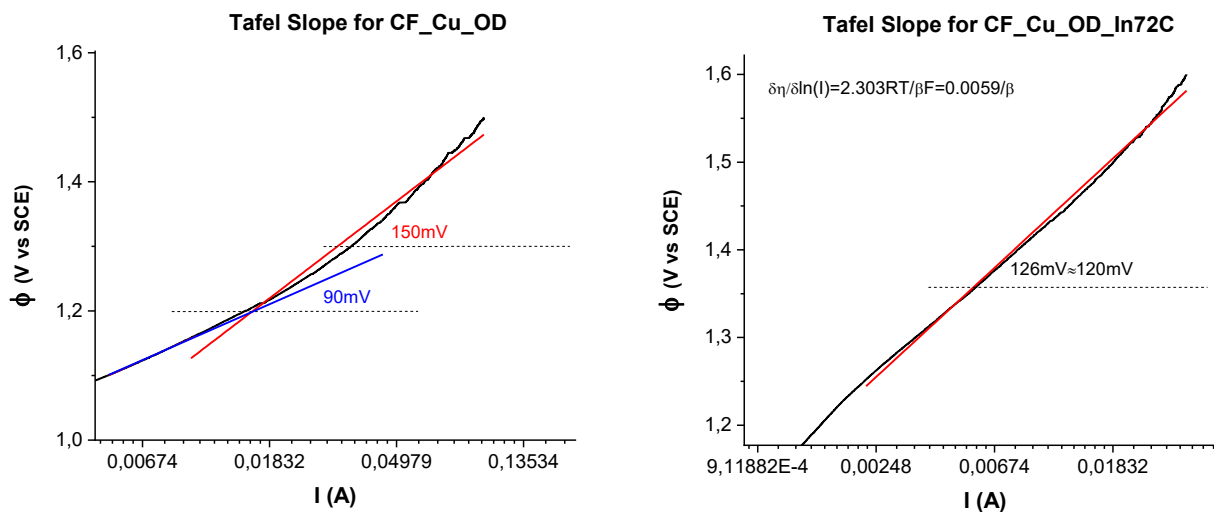


Fig.67 Tafel plots of CF_Cu_OD and CF_Cu_OD_In72C in CO₂ saturated 0.5M KHCO₃ solution.

5.4 Determination of ECSA (Electrochemical Surface area) by Double-Layer Capacitance

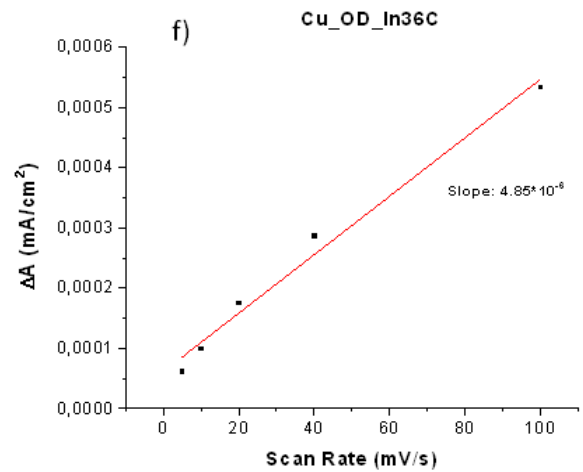
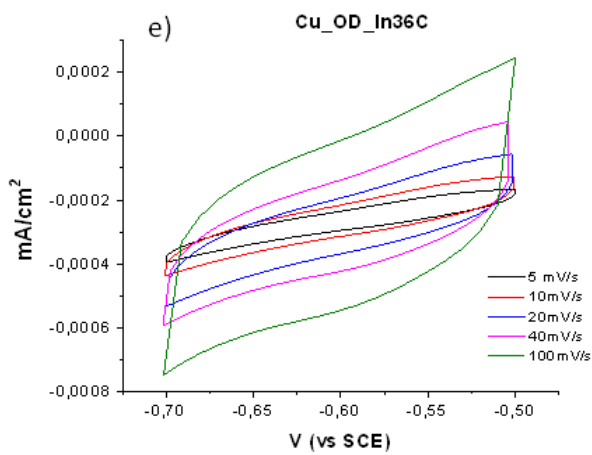
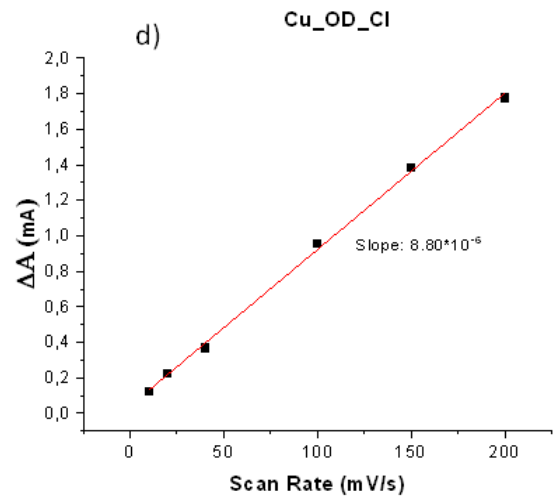
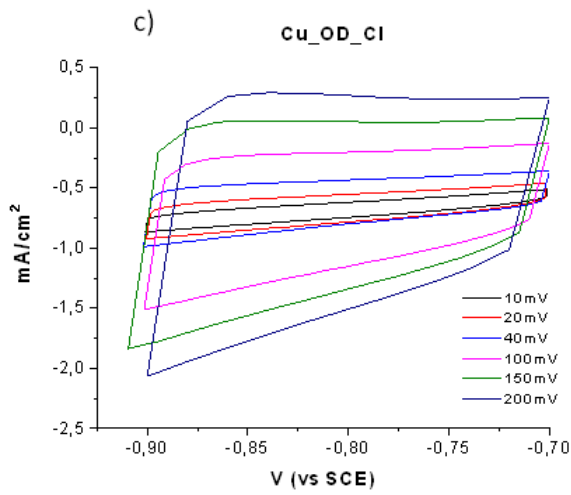
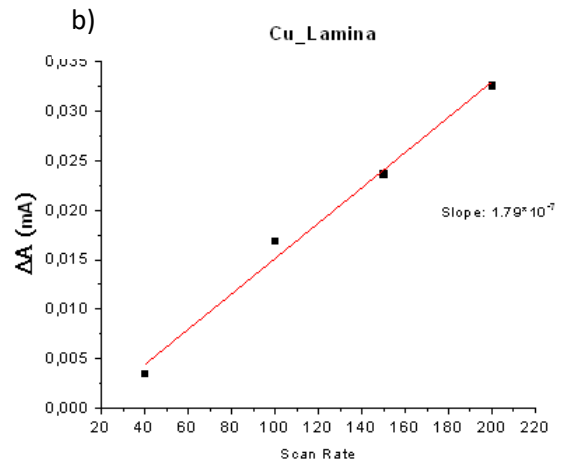
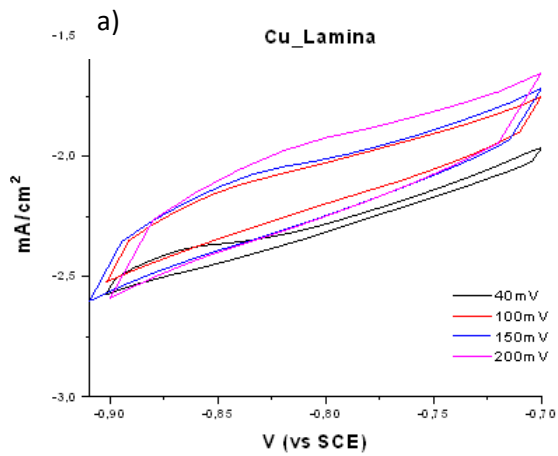
As can be deduced from these experiments changing the starting material for the electrocatalyst has a crucial role in the determination of a subsequent magnification of the electrochemical performance. But if in one hand its possible to detect a clear enhancement in the current densities by using foam substrates instead of a laminar one, the same affirmation regarding the faradic efficiencies cannot be made. In fact appears that treating different substrates with the OD method and the co-functionalization procedure lead to different interfaces with their own catalytic properties. For a better understanding of these phenomena two main ways of analysis are possible, first the attention can be directed to the crystallographic orientation of the copper and its influence on the nanostructuring of both copper and indium (that will be described in details), a second approach can be a detailed definition of the real surface of the cathode in electrochemical terms. The latter was performed using the same procedure and technique already adopted for the laminar copper-Indium substrates (see chapter 2.3).

5.4.1 Experimental

Measures were carried out using an Autolab PGSTAT30 potentiostat in a three-electrode setup using a Pt foil as the counter electrode and a saturated calomel electrode (SCE) as the reference. The electrolyte was prepared by dissolving 0.5 M KHCO_3 . The CV sampling mode was set to “normal linear scan”, thus allowing for a true analog linear sweep instead of the incremental potential steps of typical digitalized potentiostats (staircase mode). CV scans were recorded at scan rates in the range of 5–200 mV/s, spanning ± 50 mV of the OCP, an optimal range where no faradic processes occur. From the CV traces, the capacitive current was then calculated as $(J_a - J_c)/2$, where J_a and J_c are, respectively, the anodic and cathodic current densities at OCP. The resulting values (in mA/cm^2) were plotted against the scan rate of the CV experiments (in mV/s) and the data fitted with a linear equation. The slope of the linear regression, as previously described, gives the capacitance of the electrode (in F/cm^2). For each cathode, the OCP value was directly read on the potentiostat display after connecting all the three electrodes. The OCP values for the different electrodes do not differ significantly in day-to-day use, with maximum variations within 70 mV.

5.4.2 ECSA of copper and copper-indium cathodes:

Double layer capacitance measurements were carried out using all the different cathode typologies developed during our research work with special attention on the best in terms of performance. As expected, carbon fiber electrodes, display an active area which is about one order of magnitude larger than OD treated copper foils.



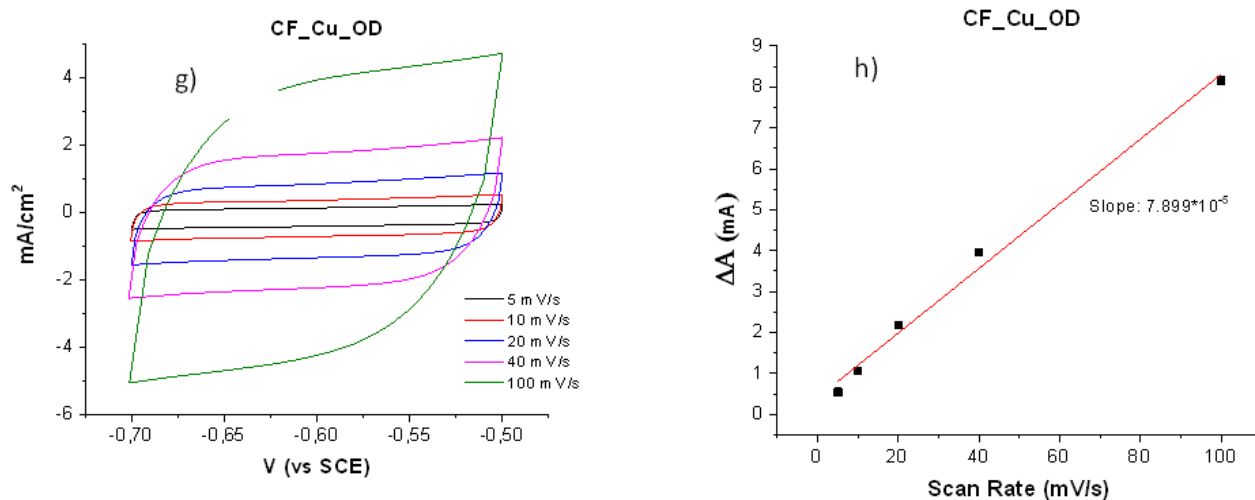


Fig. 68 CV scans around the open circuit potential (OCP) for Cu foil (a), Cu_OD (c), Cu_OD_In36C (e), CF_Cu_OD (g) and CF_Cu_OD_In72C (i) registered in 0.5 M KHCO₃. The corresponding linear fits are reported respectively in (b), (d), (f), (h) and (l). The calculated slopes correspond to double layer capacitances.

Samples	Slope [F]	Roughness factor
Cu foil	1.79×10^{-7}	1
Cu_OD	8.80×10^{-6}	50
Cu_OD_In36C	4.85×10^{-6}	27
CF_Cu_OD	7.90×10^{-5}	440
CF_Cu_OD_In72C	2.05×10^{-5}	114

Tab. 8 Slopes extracted from linear fits of data in Figure 66.

The table 8 shows in fact, the final capacitance results obtained from the ECSA measures of Cu_OD cathodes, Cu_OD_In36C (the best performing laminar electrode functionalized with indium) CF_Cu_OD (the carbon based nanostructured cathode non functionalized) and CF_Cu_OD_In72C (the best indium co-catalyzed carbon foam based cathode). By normalizing all these capacitance values for the one obtained for a simple copper foil, chosen as reference, a more clear *roughness factor* can be estimated that shows the surface improvements reached by every cathode. As can be noticed the OD treatment led in any case to a dramatic increase in the electrochemical surface respectively quantified in 50 and 440 times the copper reference. Moreover the indium deposition seems to partially suppress part of this activity in fact co-functionalized cathodes over perform the reference with a roughness factor of 27 and 114 for laminar and carbon foams substrates. While the reduced electrode surface implies decreased current densities in the indium modified electrodes, as observed by J/V measurements a substantial gain in electrode selectivity towards CO₂ is gained, improving the yield of CO evolution as shown before.

This concept can be explained by observing the reported image (fig. 66 b) that shows the carbon monoxide production rate expressed by the product between the CO efficiency (%) and the stable working current (chosen after 300s of electrolysis). The values regarding the nanostructured foam (CF_Cu_OD) are not reported due to their intrinsic instability in the catalytic performances and their high selectivity towards hydrogen that makes them not an interesting comparison in this context. The CO production increases with the magnitude of the reducing potential applied and appears to be higher (82% more at -1.6V vs SCE) than its non-functionalized counterpart, value that is overperformed of almost four times by using an indium functionalized foam cathode (CF_OD_In72C).

Final considerations

This research work allowed to achieve very interesting results and opened the way for emphasizing the catalytic activity of metallic copper towards CO₂ reduction. The importance of a surface co-functionalization in enhancing the faradic efficiency for Syngas has been also pointed out. In particular the OD treatment, optimized for our electrodes, leads to a surface nanostructuring that is easy to perform, purely electrochemical and achievable with different copper morphologies, regardless the initial crystallographic orientation. The use of harmless and environmentally friendly chemicals is also interesting in view of future industrial application. Furthermore it is worth noting that the electrochemical nanostructuring procedure reported in this thesis consent a fine interface control by the modification of simple parameters such as the frequency of the square wave anodization or the chosen potential window for this step, characteristics that are not possible with the physical methods usually proposed in literature for this kind of copper nanostructures.²⁸ The co-functionalization with metallic indium, finally, positively impacted the catalytic efficiency and the selectivity of this types of cathodes, concretely manifesting an optimal Syngas production in a wide range of potentials, as described in detail in these chapters, for both the laminar and foam substrates.

On the other side further studies and implementations are needed in order to prolong the working life of these electrodes that is still too low for practical applications, on this regard interesting preliminary results have been obtained with in-operando indium treatments as shown by the specific long chronoamperometric measurements performed.

PART 3

Cerium functionalized copper cathodes

1. Carbon dioxide reduction using Cerium functionalized cathodes

1.1 Cerium deposition on copper foils

In order to evaluate the possibility of a cerium oxide co-functionalization of the nanostructured electrodes explorative experiments were carried out using a copper foil first.

A standard electropolishing procedure was first applied to consisting in a 300s two electrode electrolysis using a titanium counter with an applied potential of +4V as previously described. After this pretreatment the deposition of Ceria was chosen by surveying the electrochemical literature describing CeO₂ deposition¹⁰⁸. In particular we focused our attention on reports dealing with the use of Ceria as protecting layer on some steel alloys, since we deemed that these procedures should have been optimized with respect to the deposition of good quality micro layers of ceria. According to these data the following conditions were explored:

Electrolyte	H ₂ O		H ₂ O/Ethanol (1:9)		
CeCl ₃ x 7H ₂ O	0.8mM	0.8mM	0.8mM	1mM	0.8mM
H ₂ O ₂ 30%		25mM			25mM
Deposition Time	10min	10min	10min	10min	10min
	20min	20min	20min		20min
Deposition Current (mA/cm ²)	-0.005	-0.005	-0.01	-0.1	-0.01
		-0.01	-0.01	-0.1	-0.25
		-0.1	-0.1	-0.25	-0.25
			-1		-1
			-5		-5

Tab.9 Deposition parameters commonly used for steel protection (minor changes are possible)

It should be considered that some adaption of these is experimental conditions above to our copper substrate might be necessary, in view of optimizing the catalytic efficiency rather than the interfacial passivation required in the case of steel protection. The preliminary deposition parameter that we selected for copper functionalization are the following:

Electrolyte	H ₂ O	H ₂ O/Ethanol (3:2)
Ce(NH ₄) ₂ (NO ₃) ₆	0.8mM	0.8mM
H ₂ O ₂ 30%	0.25mM	0.25mM
KCl	0.1M	0.1M
Deposition Time	20min	20min
	30min	30min
	60min	60min
Deposition Current (mA/cm ²)	-0.25	-0.25
	-0.5	-0.5
	-1	-1

Tab.10 Adapted parameters for ceria deposition on copper substrates both for pristine metallic foils or foams and for OD nanostructured substrates

Deposition technique	N° scan
JV (linear voltammetric scan) Ce(NH ₄) ₂ (NO ₃) ₆ 0.025M -0.6 V to -2.0 V at 5 mV/sec rate	10
	20
	30

Tab.11 Parameters for the potentiodynamic Ceria deposition

The first goal was to find the proper conditions for an homogenous CeO layer on the copper lamina in order to obtain the maximum adhesion on a flat surface like the metallic foil. Tab 10 shows the most promising parameters adopted for the ceria deposition and in particular (red colour) the best conditions observed in terms of visual uniformity are put in evidence. But if on one hand these parameters allows the creation of an uniform layers on the other the mechanical adhesion of the Ceria in the working conditions seems to be not sufficient for our purposes. In order to enhance the stability of this surface functionalization multiple experiments were carried out with the aim to transfer the good results obtained with the galvanostatic procedure to a mechanically solid interface. This goal was reached with the deposition throughv JV, or linear scan voltammetry, optimized with the parameters shown in table 11. Also in this case three different cerium deposition were studied by changing the number of deposition scans.

1.2 Electrochemical responses of copper-cerium cathodes:

These electrochemical results have to be considered at a preliminary level: we first tuned the amount of ceria by varying the number of potential scans during the potentiodynamic procedure. As previously mentioned the potential scanning deposition was in fact found to be more effective in generating a good adhesion between the ceria and the copper instead of the galvanostatic procedure. We note that the morphological differences obtained in the Ceria layer according to these two different procedures are still under investigation through SEM and TEM analysis. The electrochemical bath for the ceria deposition is composed of 0.025 M ammonium nitrate cerium solution according to the tab 11. The electrodeposition is realized through cyclic 10,20,30 scanning between -0.6 V to -2.0 V at 5 mV/sec rate¹⁰⁹ using a classical three-electrode cell, with the Cu electrode being as the working, a platinum grid as the counter electrode and a saturated calomel electrode (SCE) served as the reference one.

Figure 69 shows reports J–V curves of the cerium oxide modified electrodes recorded at 20 mV/s while compensating for the ohmic drop. All curves were recorded in 0.5 M KHCO₃ buffer at pH 7.4 and were averaged over at least three equivalent electrodes. The corresponding standard deviations are also reported as error bars, evidencing the good reproducibility of the electrochemical response with relative errors < 10%. The graph on the left shows that by increasing the deposition of cerium the faradaic onset shifts progressively to more negative voltage. At the same time, for equivalent voltages, the current decreases by moving from Cu_CeO10scan to Cu_CeO30scan. This is indicative of a slower electron transfer kinetics which may translate in a lower electrochemical reactivity towards hydrogen evolution. In the OD electrodes we find a similar trend to that reported for plain Cu electrodes. The current are just slightly higher than the plain Cu_CeO ones, reaching in the best case (Cu_OD_CeO30scan) about -40 mA/cm² at -2.0 V (vs SCE).

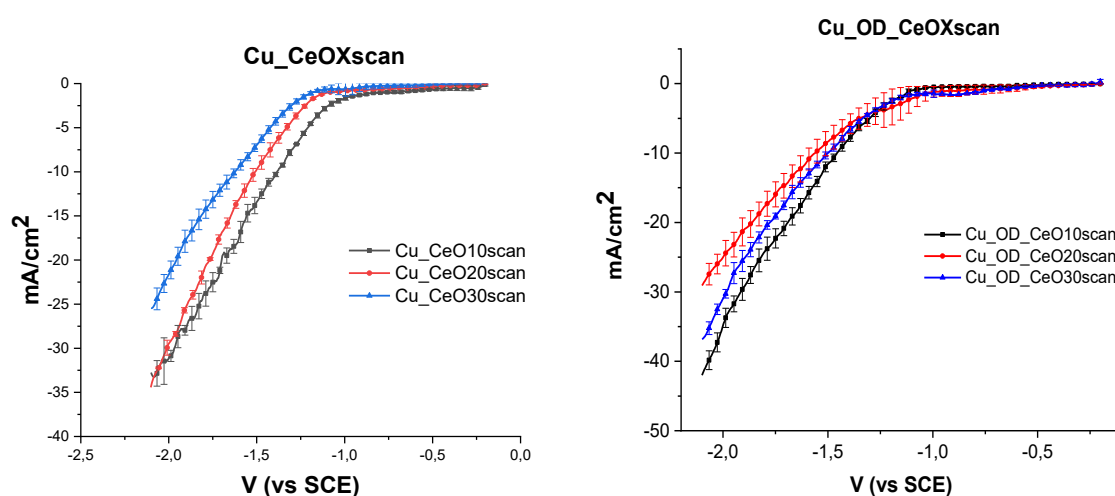


Fig. 69 J/V curves of Cu_CeOXscan (on the left) and Cu_OD_CeOXscan (on the right) cathodes recorded in 0.5 M KHCO₃ at pH 7.4.

1.3 Faradaic efficiencies of copper-cerium cathodes:

In figure 70 the faradaic efficiencies of the Cu_CeOXscan in aqueous carbonate buffer (0.5 M KHCO₃ at pH 7.4) are reported. With the Cu_CeO10scan electrode mostly hydrogen and a minor amount of CO has been observed in the potential range -1.8/2.1 V vs SCE, but Cu_CeO20scan we observe the presence of methane (CH₄), whose production peaks in the -1.9 V/-2.0 region with a maximum 15%. CH₄ FE decreases then by moving to more cathodic potentials where a 5% efficiency at -2.1V vs SCE was observed. Cu_CeO30scan electrode mostly hydrogen and minor amount of CO has been observed in the potential range -1.8/2.1 V, also we observe the presence of methane at -1.9/-2.0 V.

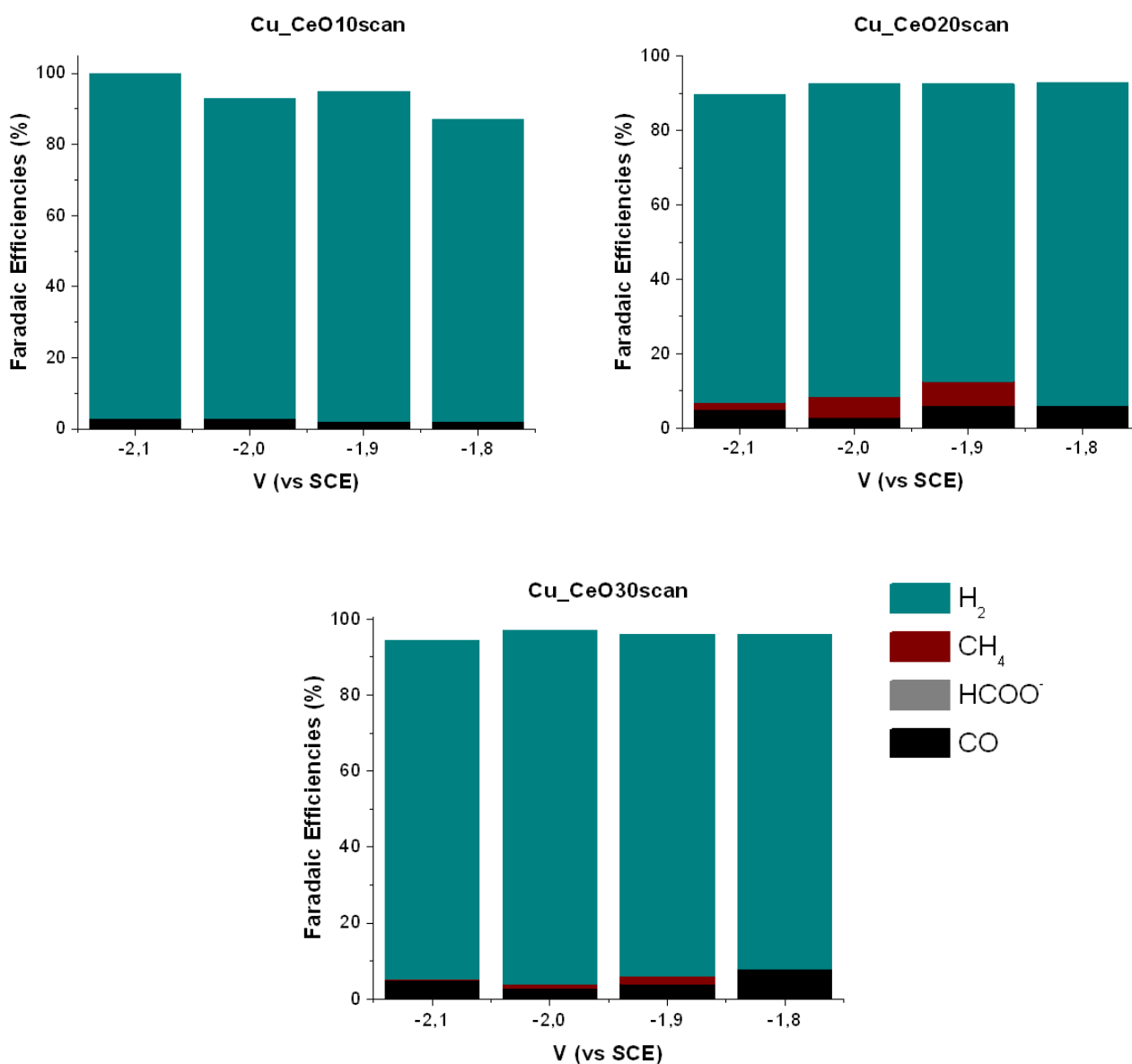


Fig. 70 Faradaic efficiencies of Cu_CeOXscan cathodes for reduction products at various potentials in 0.5 M KHCO₃ at pH 7.4.

With regard to cathodes with OD treatment we have observed a dramatic impact of the OD treatment on the faradaic efficiencies of the ceria modified copper cathodes. Cu_OD_CeO10scan generates as main reduction products: H₂, CO (up to 25% at -1.8V) and CH₄ (which decreases from 20% at -1.9V to 5% at -2.1V). Cu_OD_CeO20scan yields a substantially higher production of methane, quite constant within the explored potential interval and peaking around 40% at -2.1 V. We also observe the formation of a smaller amount of formate, whose FE decreases by moving to more cathodic potentials, going from 10% to 5%. Cu_OD_CeO30scan generates a high percentage of CO and formate which both decreases by increasing the cathodic bias from. The FE of CO decreases from 40% at -1.8 V to 15% at -2.1 V, while the formate goes from 35% at -1.8 V to 5 % at -2.0 V. Hydrogen is the dominating product at high voltage, but also minor evolution of methane was detected (at most 3%) (see fig.71).

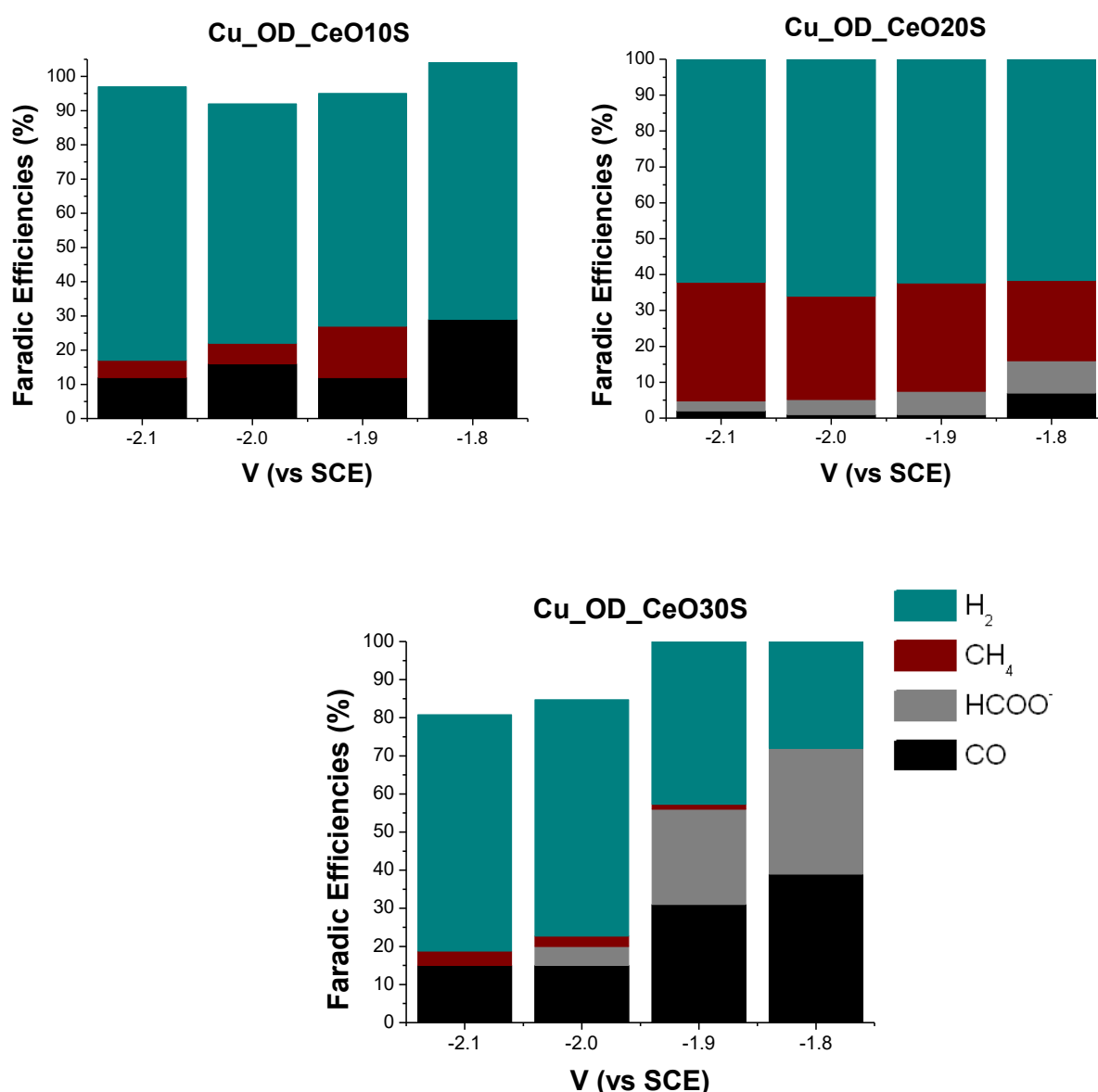


Fig. 71 Faradaic efficiencies of reduction products generated by Cu_OD_CeOXscan cathodes in 0.5 M KHCO₃ at pH 7.4.

In figure 72 the catalytic efficiency (JxFE) for methane production is reported, where we could observe that the best performance is achieved by Cu_OD_CeO20scan electrode. Clearly these results are preliminary and should be confirmed. Moreover additional structural and electrochemical investigations will be required to understand the interfacial reactivity of such electrodes

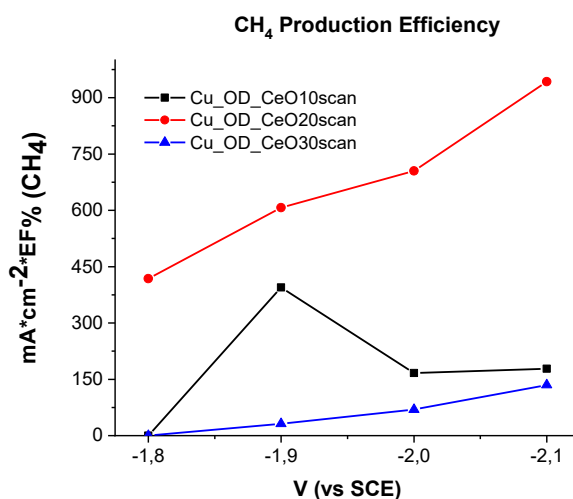


Fig. 72 Comparison between methane production for all Cu_OD_CeOXscan at various potentials.

1.4 Final considerations

Cerium co-functionalization is for sure really appealing, even at this early stage of research in fact, the possibility to directly produce a high value chemical like methane is really interesting for practical applications.

In fact the direct CO₂ reduction into this fuel will allow to avoid the steps represented by the Fisher-Tropsch process, really demanding in terms of energy consumption and costs, with a great impact in the final price of a CO₂ derived product. In this context further improvements in the deposition processes involved and in the reproducibility of these interface will be surely conducted in order to enhance selectivity and the current densities obtainable by these substrates. It is also interesting to note that even at the relatively low faradic efficiency measured during these initial experiments, mixtures of methane and hydrogen are a valuable output as an alternative green source for diesel engines fuels as mentioned in the economic analysis reported in chapters 1.1. and 1.2.

PART 4

Gold cathodes

1. Carbon dioxide reduction over Gold cathodes

1.1 Introduction

From the mechanistic point of view, the first monoelectronic step of CO₂ electroreduction is thermodynamically very demanding (−1.9 V vs the Normal Hydrogen Electrode, NHE), since significant geometric rearrangements are involved in the transformation of the linear substrate in the bent radical anion, CO₂^{•−}. Nevertheless, the coordination of the CO₂ molecule on electrodic surfaces can effectively mitigate this thermodynamic requirement. Indeed, several metals can effectively stabilize not only CO₂^{•−},⁵³ but also other key intermediates for the further (multielectronic) reduction reactions. Among them, *CO, *COOH and *CHO are formed via proton-electron transfer mechanisms⁵⁴ (the asterisk denotes a site on the electrodic surface). On the other hand, an optimal binding strength between the intermediates and the metal surface, *i.e.* not hampering either the coordination or the product release, is crucial in terms of the overall catalytic activity, which is usually assessed through volcano plots (Sabatier principle)⁵⁴. As far as CO binding energy is concerned, the top of the volcano is occupied by gold⁴⁹, which almost selectively forms carbon monoxide as the main CO₂ reduction product⁴. Smaller amounts of formic acid⁴ and methanol^{55,56} have been also detected respectively at low and high overpotentials.

Several reports evidenced the importance of nanostructuring the Au-based cathodic interfaces in order to boost CO formation over the competitive proton reduction in aqueous media. Highly-effective nanostructured Au cathodes typically exhibit: (i) metastable surface structures²⁹; (ii) engineered high-index facets and features^{57,58}; (iii) local changes in the electric double layer near the cathode surface^{39,40}, and/or in the local pH of the electrolyte⁶¹; (iv) under-coordinated sites, including grain boundaries^{30,61,62,63}. The latter has been recently identified as the most relevant feature for an efficient CO formation process by the Chorkendorff group. Through selective poisoning experiments, the authors could indeed prove that surface sites with high coordination numbers are *ca.* one order of magnitude less active for CO evolution than the under-coordinated sites, confirming the structure sensitivity of the CO₂ electroreduction process⁶⁴.

Engineered Au morphologies aimed at maximizing CO selectivity have been prepared through the most various synthetic strategies, including: (i) oxidation/re-reduction of Au foils²⁹, also promoted by O₂ plasma treatments⁶⁵; (ii) electroplating onto host templates⁶⁶; (iii) optimized electrodeposition⁶⁰ or electrocrystallization with MHz potential oscillation⁶⁷; (iv) electron beam deposition^{4,61,62} and (v) deposition of preformed Au nanostructures on conductive electrodes^{58,69,70}. In this context, a straightforward one-step synthesis of porous Au structures with easily tunable morphology (upon appropriately changing the process parameters) and not involving substrate limitations or thermal treatments, appears intriguing. These conditions could be fulfilled by Pulsed Laser Deposition (PLD), a highly versatile technique for the production of nanostructured films⁷¹ or nanoparticles⁷² of virtually any material, including metals⁷³, alloys⁷⁴, semiconductor oxides⁷⁵, and carbon⁷⁶. Highly porous structures are typically achieved by performing the

laser ablation in the presence of a background gas and the resulting morphology can be easily tuned by controlling the gas pressure and/or the target-to-substrate distance^{75,77,78}. Recently, some of us also showed that PLD can be used to produce Au nanoparticles with a precise control of size and substrate coverage, while reporting their integration within nanostructured TiO₂ film by single step deposition^{73,75}.

In this contribution, thanks to a collaboration with the Milan University, it was possible to perform the pulsed laser deposition of two different kinds of porous Au-nanostructured thin films on fluorine-doped tin oxide (FTO) electrodes, and their use as cathodes for CO₂ reduction in aqueous electrolytes. The accurate tuning of the deposition parameters allowed for the one-step synthesis of two nanoscale morphologies, one with a quite regular columnar arrangement, and the other displaying a foamy three-dimensional structure.

1.2 Cathode preparation

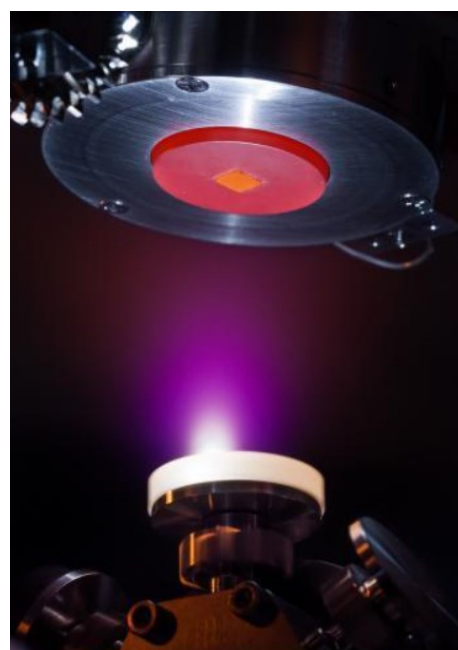
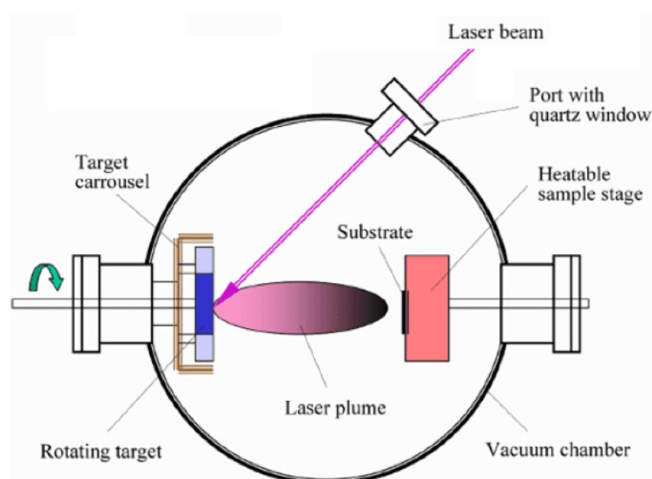


Fig. 73 On the left a simple scheme of the PLD setup, on the right an image of a metallic deposition

The cathodes consist in Au nanoporous films deposited on FTO substrates covered by a Cr adhesion layer, needed to avoid the detaching of the Au deposit during the electrochemical tests. The 5 nm-thick Cr layer was deposited on FTO substrates in an Edwards E306 thermal evaporator, by evaporating pure 99.99% Cr grains, while the equivalent thickness was controlled by means of a quartz microbalance. Au nanoporous films were then deposited on FTO substrates covered by the Cr interlayer via Pulsed Laser Deposition (PLD). An Au (99.99%) target was ablated with a ns-pulsed laser (Nd:YAG, 2nd harmonic, $\lambda=532$ nm, repetition

rate 10 Hz, pulse duration 5-7 ns); the laser fluence on the target was 2.3 J/cm², while the laser pulse energy was 150 mJ. The substrates were mounted on a rotating sample holder at fixed target-to-substrate distance of 5 cm. Depositions were performed at room temperature within a pure Ar background gas at two different pressures, 100 Pa and 1000 Pa, for a duration of 20 minutes (12000 shots). In order to distinguish Au nanoporous cathodes deposited at different Ar pressures, we name the films deposited at 100 and 1000 Pa as **Col-Au** and **Foam-Au**, respectively, as a result of their different morphology. Both films were deposited also on Si(100) substrates added to the sample holder together with FTO substrates, for the purpose of film characterizations.

A field emission scanning electron microscope (FEG-SEM, Zeiss Supra 40) was used to perform morphological characterization on the films deposited on both Si and FTO substrates. In particular, the Si substrates were exploited for cross-sectional and top-view measurements, while the films deposited on FTO were scanned only in top-view. Moreover, the SEM micrographs were analyzed by ImageJ software to extract the substrate coverage and size of morphological features of different Au films.

Structural characterization of deposited Au films was carried out by X-ray diffraction (XRD). XRD patterns were collected using a high-resolution X-ray powder diffractometer (PANalytical X'Pert Pro MPD) using a Cu target (CuK α 1 radiation $\lambda = 1.5406 \text{ \AA}$) at room temperature. The measurements were performed in Bragg-Brentano (θ - θ) geometry with a step-scan technique in 2θ range of 25–85° with a step size of 0.016° and time/step of 40 s. The Bragg-Brentano geometry implies that X-ray diffraction occurs by the crystallographic planes that are parallel to the substrate, thus XRD peak intensities can provide information about the presence of preferential orientation of crystalline domains with respect to the substrate. The size of the Au crystalline domains was determined by using the Scherrer's equation on XRD fitted peaks.

Also transmission electron microscopy (TEM) was performed, obtaining images with a TEM JEOL 2010 with LaB₆ emission gun operating at 160 kV. High-resolution images, energy dispersive X-ray spectroscopy (EDS) and STEM-HAADF (scanning transmission electron microscopy high-angle annular dark-field imaging) analysis were performed with a FEI Titan HRTEM microscope operating at 80 kV. The Au samples were scratched from the Si substrate and deposited on copper TEM grids.

As described for the copper based cathodes, the presence of metal cation impurities (especially Fe²⁺, Pb²⁺ and Zn²⁺) in the electrolytic solutions used for the CO₂ electroreduction can result in unreliable results⁴. Indeed, under the cathodic conditions needed for the reaction to proceed, these metal cations can be reduced to the corresponding metals, and deposited onto the cathodic surface, leading to a significant modification of its catalytic properties. In particular, in the presence of these co-deposited metals, the overpotential for proton reduction is reduced, leading to an enhanced H₂ production over CO₂ reduction. Although nanostructured electrodes are less sensitive to this poisoning⁵⁹, metal impurities were removed also in the case of this new gold electrodes using the same technique previously adopted, in particular a

two electrode electrolysis (Ti vs Ti) was carried out. The applied potential is kept at -2 V under constant nitrogen bubbling for 54000 s (15 h)⁷⁹. The effectiveness of the pre-electrolysis process has been proven also in this context by elemental analysis with ICP-mass, evidencing the clear absence of Fe^{2+} , Pb^{2+} and Zn^{2+} in the limits of the technique sensitivity (<0.5 ppm).

1.3 Synthesis and characterization of the Au nanostructures

The nanostructured Au cathodes were deposited by means of pulsed laser deposition (PLD) on FTO substrates covered with a thin (5 nm) Cr adhesion layer prepared by thermal evaporation. Figure 74 shows the cross-sectional and top-view SEM images of Au films deposited at 100 Pa (Figures 74 a and 74 b) and 1000 Pa of Ar (Figures 74 c and 74 d), which highlight their different morphology as a function of the background deposition pressure. Indeed, the Au film deposited at 100 Pa shows a columnar structure (Figures 74 a-b) for its whole thickness; on the other hand, the Au film deposited at 1000 Pa exhibits a columnar-like structure only for a bottom ~ 80 nm-thick layer in contact with the substrate, while the main structure consists of a non-uniform foam-like morphology up to a few micrometers thick (Figures 74 c and 74 d). For these morphological features, in the following 100 Pa and 1000 Pa-deposited films are called Col-Au and Foam-Au, respectively. In particular, Col-Au film consists of ~ 200 nm thick and ~ 80 nm wide columns (Figure 74 a), on average, separated by voids of the order of 10-15 nm (Figure 74 b). On the other hand, the Foam-Au film shows a column-like bottom layer, sizing about 80 nm thick and 45 nm wide (Figure 74 c), also separated by voids of the order of 10-15 nm (Figure 74 d). Moreover, the foam-like structure on top is up to 3-4 μm thick and appears to be composed of sintered Au nanoparticles with size of a few tens of nm (average size 35 nm). Such foam-like domains cover $\sim 20\%$ of the substrate surface (Figure 74 d).

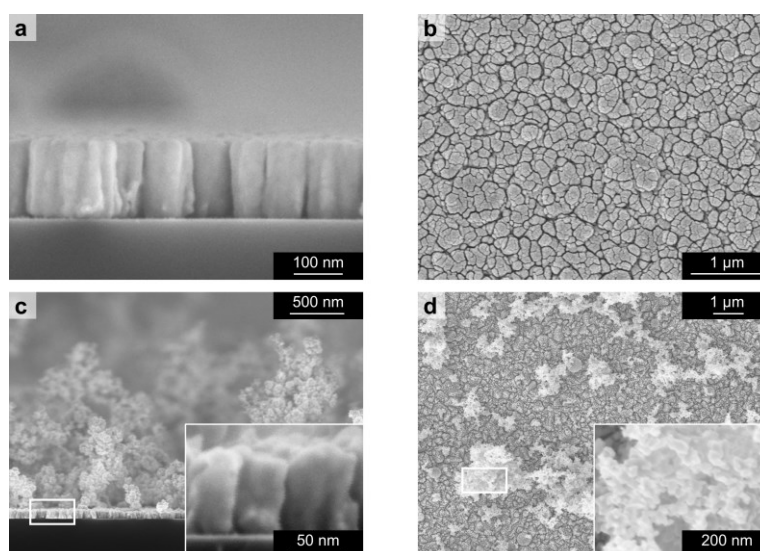


Fig. 74 SEM images (top view and cross-section) of Au films: Col-Au deposited at 100 Pa (a, b) and Foam-Au deposited at 1000 Pa (c, d). Insets in (c, d) show images at higher magnification.

The evident difference in morphology as a function of the background pressure is due to the coexistence of two different mechanisms of film growth during deposition, namely in-plume cluster nucleation and surface diffusion^{81,82}. When other PLD parameters (*e.g.* laser energy and fluence, target-to-substrate distance) are kept constant, the predominance of one mechanism over the other is associated to the pressure level⁷³. Indeed, during the PLD process, the laser-target interaction leads to target vaporization, which results in a plasma plume formation and consequent deposition of ablated species on the substrates^{1,72,77}. The increment of background pressure from 100 to 1000 Pa has the effect of confining more effectively the plasma plume, as well as of slowing down the ablated species. Therefore, in-plume cluster nucleation phenomena are more predominant at 1000 Pa rather than at 100 Pa, resulting in the deposition of a more open and fluffier Au nanoporous film with the different morphologies already described. The presence of the “compact” columnar bottom layer for the Foam-Au cathode deposited at 1000 Pa is probably related to the initial wetting of the substrate by means of the ablated Au. Moreover, the background pressure level also affects the deposition rate, as the higher pressure means stronger scattering and thus a less directional ablation plume, which translates in higher dispersion within the deposition chamber and lower kinetic energy. The amount (mass density per unit surface) of Au deposited at the two pressure conditions was estimated by means of a quartz microbalance, to be $\sim 300 \mu\text{g}/\text{cm}^2$ for Col-Au and $\sim 150 \mu\text{g}/\text{cm}^2$ for Foam-Au. The deposition of such tiny amounts of gold is indeed advantageous for the overall cost of the cathodes.

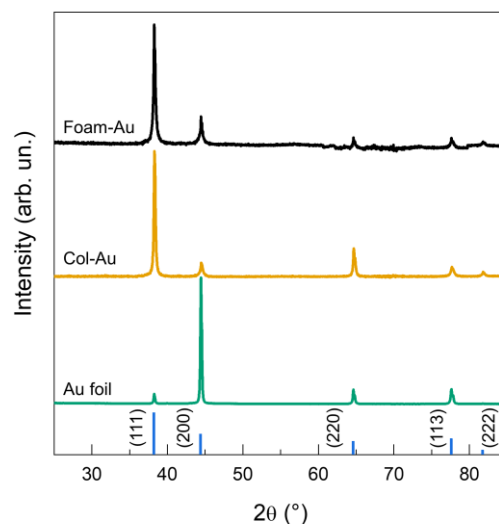


Fig. 75 X-ray diffractograms of Col-Au, Foam-Au and Au foil; intensities have been normalized the (111) reflection (Col-Au and Foam-Au) and (200) reflection (Au foil). The characteristic peaks of the Au fcc structure in a powder system are reported as reference; the height of the reference lines is proportional to the intensity of XRD reflections in reference Au powder.

The structural characterization of Au films was performed by means of X-ray diffraction (Figure 75). Specifically, both the Col-Au and Foam-Au films show peak positions in accordance with Au fcc structure; the higher signal-to-noise ratio of Col-Au indicates a better crystallinity for this film. The relative intensities of XRD peaks differ for both samples from those of reference Au powder with random orientation of crystalline domains. This is a clear indication of preferential crystalline domain growth with respect to the substrate. In detail, both films preferentially grow along the (111) direction; furthermore, for Col-Au, growth along the (220) direction also appears to be preferred with respect to the (200) one. On the other hand, the Au foil exhibits a preferential orientation along the (200) direction. The average size of Au crystalline domains was estimated by applying Scherrer's equation on Au (111) fitted peak, resulting in 37 nm and 29 nm for Col-Au and Foam-Au, respectively.

1.3.1 TEM Microscopy

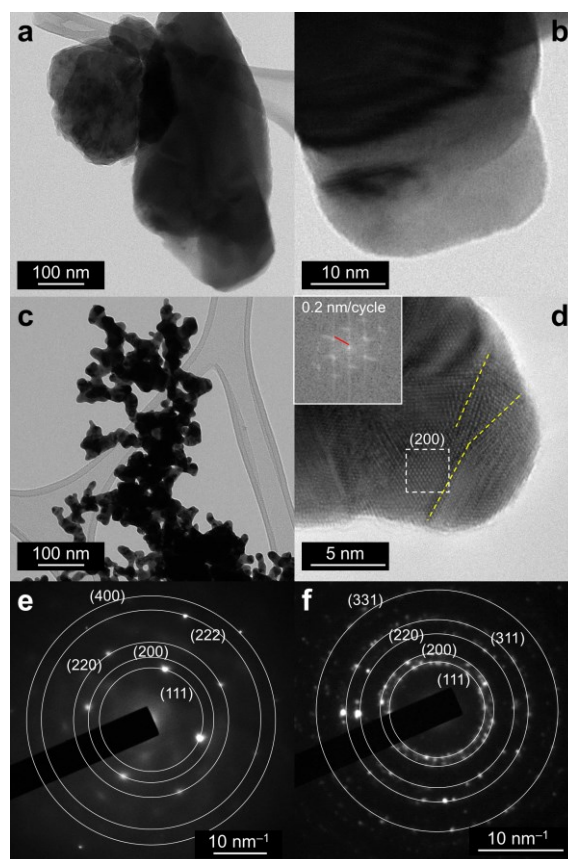


Fig. 76 TEM images of Col-Au (a, b) and Foam-Au (c, d). The inset in (d) shows the Fourier transform of the atomically-resolved area highlighted by a dashed box; the yellow dashed lines mark grain boundaries. (e, f) Selected area electron diffraction (SAED) of the micrograph reported in Figures a and b respectively for Col-Au and Foam-Au, showing diffraction spots corresponding to the lattice planes of pure Au (camera length values of 2.25 and 1.30 were respectively used to correct the interplanar distance values).

TEM analysis, as mentioned in the introduction, was performed to gain more insights on the local structural properties of the nanostructured Au films (Figure 75). Figure 76 a shows a portion of the Col-Au film, which appears dark due to its high density, thus preventing the acquisition of atomically-resolved images (Figure 76 b). Figure 76 c shows the foam-like structures growing on top of the Foam-Au film, while Figure 76 d is a high-resolution TEM image with atomic resolution. In this case, grain boundaries could be discerned (yellow dashed lines in Figure 76 d) as well as (200) planes at the surface. This observation suggests the presence of randomly-oriented grains in the Foam-Au film. It is possible to anticipate that the presence of (200) facets can lead to relevant effects in terms of the Faradic efficiency towards CO₂ reduction to CO (see below)⁶⁴. Indeed, by analyzing larger areas with TEM to acquire SAED patterns (Figures 77 a and 77 c for Col-Au and Figures 77 b and d for Foam-Au) a larger number of diffraction spots was found for the Foam-Au sample, thus confirming the above observation. Finally, the high level of purity of the Au nanostructured films was confirmed by Energy dispersive X-ray spectroscopy (EDS) mapping as illustrated by the STEM-high-angle angular dark-field (HAADF) micrograph reported below in (Fig. 77 c) and the corresponding EDS map reported in Fig 77 d.

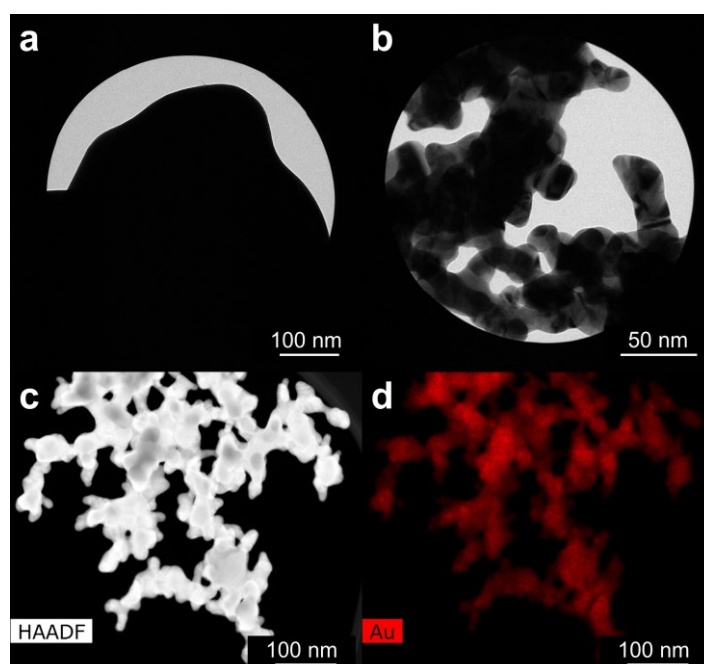
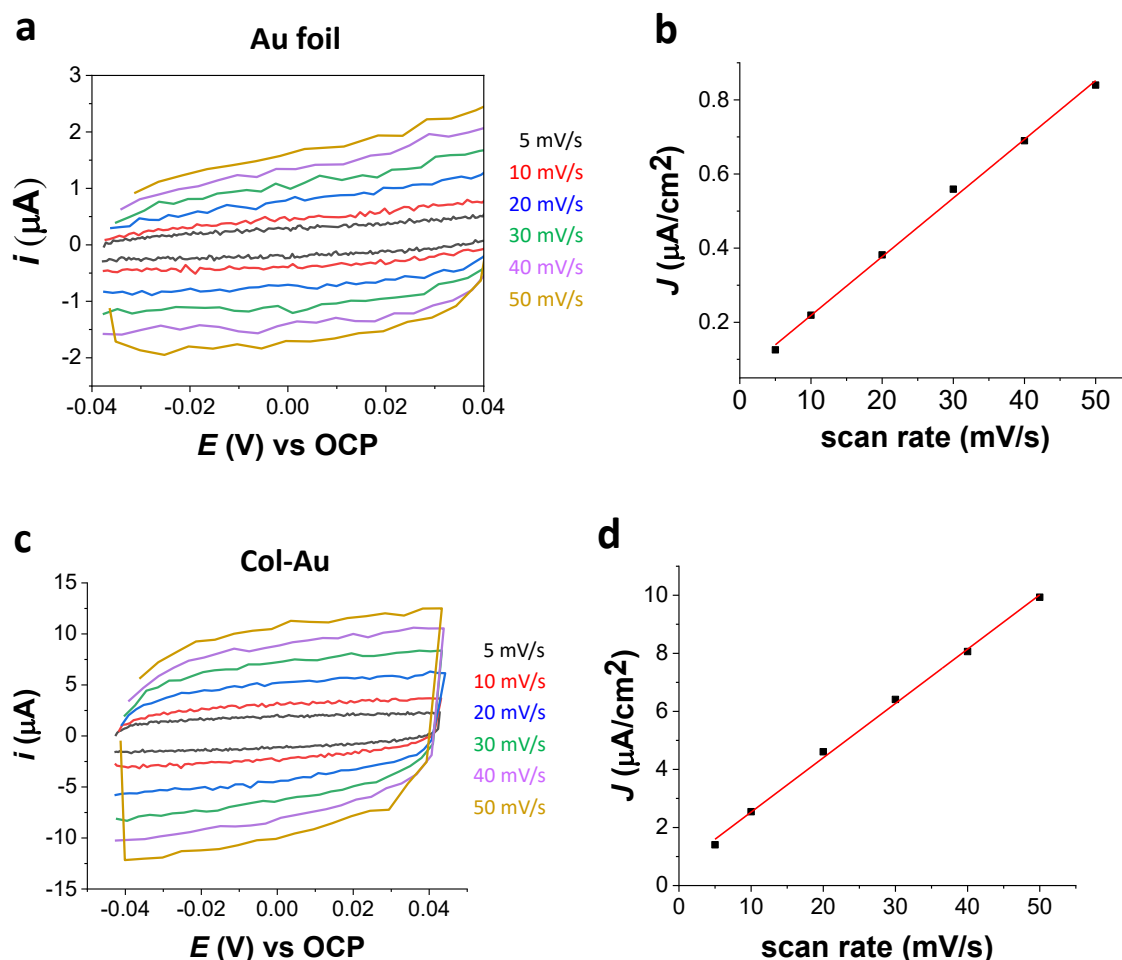


Fig. 77 (a) TEM image of the Col-Au film used for the selected area electron diffraction (SAED) analysis reported in Figure 3e in the main text. (b) TEM image of the Foam-Au film used for the SAED analysis reported in Figure 3f in the main text. (c) STEM-HAADF (high-angle angular dark-field) image of Foam-Au. (d) Energy dispersive X-ray spectroscopy (EDS) mapping of the micrograph reported in (c), showing the pure elemental composition of the Au nanoporous film.

1.4 ECSA measurements

The Col-Au and Foam-Au cathodes were initially characterized through different electrochemical techniques able to provide insights on both their active area and the exposed facets. As regards the first aspect, double layer capacitance (DLC) measurements are widely used^{83,84,85,86}, since they represent a versatile non-destructive technique to estimate the electrochemical surface area (ECSA). However, it is worth noting that several processes involving ion transfer reactions at the interface (*e.g.* intercalation, specific adsorption, or surface proton transfer) can lead to additional contributions altering the actual capacitance values, especially in aqueous media. Thus, we performed the DLC experiments in acetonitrile, a polar aprotic solvent in which more uniform capacitance values for different materials can be obtained, following a recent procedure reported by the Surendranath group⁸⁷. From the analysis of the cyclic voltammograms at different scan rates reported in Figure 78, compared to the ones obtained for a flat Au foil, we could estimate a roughness factor of 12.7 ± 3.1 for Col-Au and 9.1 ± 1.0 for Foam-Au (see also Table 12), most likely reflecting the trade-off between the opposite contributions due to the different morphology of the cathodes and their total gold loading. The values confirmed the high porosity of both the nanostructures, and resulted in line with roughness factors reported for cathodes with comparable morphologies⁶⁸.



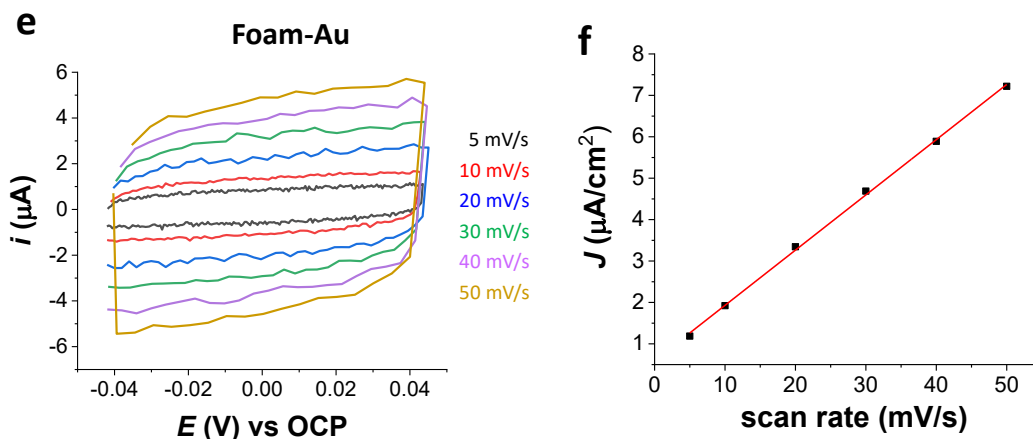


Fig. 78 CV scans around the open circuit potential (OCP) for Au foil (a), Col-Au (c) and Foam-Au (e) registered in 0.1 M KPF_6 in acetonitrile. The corresponding linear fits for the determination of electrode capacitance and RF are reported respectively in (b), (d) and (f). It is worth noting that these Figures are related just to one electrode of each kind, but three of each have been actually tested.

	Au foil	Col-Au	Foam-Au
Average slope (mF/cm^2)	0.0175	0.202	0.145
Roughness factor (RF)	1	12.7	9.1

Tab. 12 Average values of the electrodes capacitance (i.e. the slope of the plots in Figure 74 b, d and f) and the corresponding roughness factors.

1.5 Lead underpotential deposition (UPD)

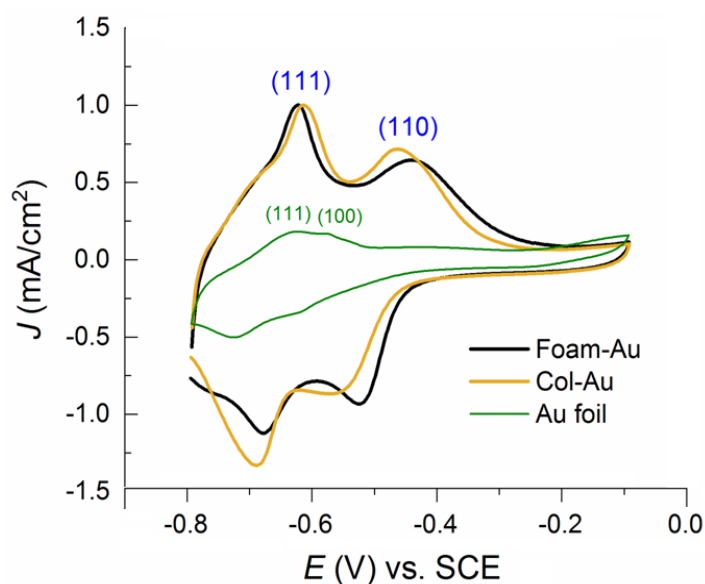


Fig. 79 Pb UPD traces recorded in 1 mM $Pb(NO_3)_2$ + 0.1 M NaOH with 25 mV/s scan rate. (111) and (110) facet orientations are revealed at 0.35 and 0.50 V respectively, while (100) at 0.40 V. The curves for Foam-Au and Col-Au were normalized to match the peak heights of the (111) feature.

In order to gain insights into the distribution of the Au surface terminations of the two nanoporous structures, underpotential deposition (UPD) of Pb was performed. The experiment consist in the acquisition of specific cyclic voltammeteries carried out using a lead enriched electrolyte consisting in a 1mM basic solution of $Pb(NO_3)_2$ (+ 0.1M NaOH). CV were recorded by cycling from -0.8 to -0.1V vs SCE using both the gold morphologies obtained with PLD and also a gold foil chosen as reference. Results are reported in Figure 79, where the two reversible processes at $E_{1/2} = -0.7$ V and -0.50 V vs SCE respectively correspond to Pb deposition and stripping from the (111) and (110) exposed facets of the Au cathodes, in agreement with XRD analyses (the (100) facet could be revealed at 0.40 V only for Au foil, reported as a reference)^{62,66,88,89}. For both Col-Au and Foam-Au, the relative amplitude of each wave was quite similar, suggesting a negligible dependence of the Au surface termination on the morphology of the cathodes. Similar behavior was previously observed in Au-inverse opal thin films⁶⁶, as well as on carbon nanotubes decorated with Au nanoparticles deposited *via* e-beam evaporation⁶². Anyway, in both Col-Au and Foam-Au morphologies the density of the (111) facets is higher with the respect to that of the (110). These results can translate in a reduced selectivity for the CO_2 versus the proton reduction reaction, since the more opened and under-coordinated (110) sites have been recently reported to be *ca.* 6 times more active for CO production than the (111) sites⁶⁴.

1.6 Electrochemical performances of the Au nanostructures

The so-prepared cathodes were tested as working electrodes in a custom-made electrochemical cell (see the corresponding chapter for a detailed description of the cell and the used techniques adopted for their making 1.5 and 1.6) using pre-electrolyzed (Ti vs Ti, as previously mentioned) 0.5 M KHCO_3 saturated with CO_2 as the electrolytic solution. The joined presence of these two species leads to the formation of a buffer system at pH 7.4, instrumental to avoid the build-up of a basic pH (and the consequent decrease of the dissolved CO_2) following the proton consumption during the electroreduction.

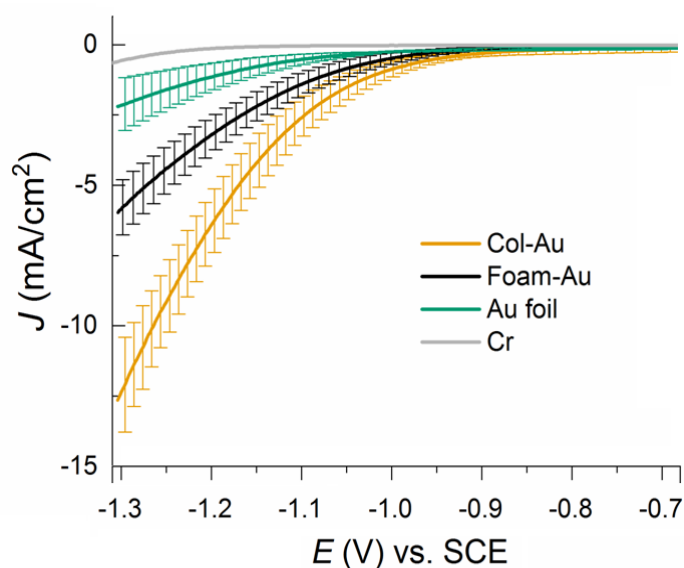


Fig. 80 JV characteristics for Col-Au (dark yellow), Foam-Au (black), Au foil (green) and Cr adhesion layer (gray) recorded in 0.5 M KHCO_3 saturated with CO_2 (pH 7.4) and corrected for the iR -drop.

In this specific context it is interesting to note that the cations of the electrolyte (K^+ in this specific case) are also known to participate in the buffering process, since their hydration shell can be polarized and then undergo hydrolysis under cathodic biases^{59,90,91}. Furthermore, the K^+ adsorbed on the electrodic surface may favor the stabilization of the intermediate anionic species *via* ion pairing^{4,64,92} and, at the same time, decreasing the competitive H_2 evolving reaction due to the build-up of a more positive potential in the Helmholtz layer^{64,93}.

Figure 80 shows the resulting JV curves recorded at 20 mV/s while compensating for the ohmic drop (90%). All the traces correspond to average values of at least 3 equivalent electrodes, and the corresponding standard deviations are also reported as error bars, evidencing the good reproducibility of the outcomes in terms of generated current. The performances of the two nanoporous cathodes were also compared to those of a commercial Au foil as the standard reference, as well as to those of the bare Cr adhesion layer.

The analysis of the JV curves revealed that the onset potential at which a significant cathodic current (in the specific, -0.5 mA/cm^2) starts to flow is -0.97 V for Col-Au, corresponding to an overpotential, η , of 0.16 V

(in absolute mathematical value), being -0.11 V the thermodynamic potential for CO_2 reduction to CO. This onset value is pretty similar to the one registered for the pioneering oxide-derived Au nanostructures reported by the Kanan group²⁹. Less negative onsets (-0.87 V) were however observed for very peculiar Au nanostructures, such as Au needles, for which high local electric fields arise, resulting in a higher local CO_2 concentration⁶⁰.

On the other hand, the onset potential for Foam-Au was observed at -0.32 V ($|\eta| = 0.21$ V), with *ca.* -0.05 V cathodic onset shift with respect to Col-Au. This shift can be due to subtle differences of the reaction kinetics at the two different interfaces, which can translate into different product distribution. At the same time, the two nanoporous morphologies outperformed the Au foil, for which the current onset is observed at -1.1 V ($|\eta| = 0.31$ V), thus speaking in favour of improved kinetics in the nanostructured interfaces when compared to the flat Au surface. The Cr adhesion layer showed, as expected, a very retarded onset potential (at -1.3 V, $|\eta| = 0.5$ V) with the recorded current being essentially due to hydrogen generation⁴.

1.7 Faradic efficiencies

The catalytic activity, in terms of generated current, follows the trend Au foil < Foam-Au < Col-Au, with the latter reaching up to -12.5 mA/cm² at -1.3 V vs SCE. However, the ultimate assessment of the catalytic performances of the nanoporous cathodes must be done after the evaluation and quantification of the reduction products.

To this end, we performed chronoamperometric measurements under different potentials, since the distribution of CO_2 reduction products is known to change upon varying the applied bias. However, while performing these experiments, we noticed a progressive decrease in the cathodic currents, which we attributed to a partial poisoning of the cathodic surfaces. This behavior had been already reported for Au surfaces, and ascribed to different kind of adsorbed species, either potassium and/or carbon deposits⁹⁴, or the produced CO itself⁸⁰. In particular, terminally bonded CO species (CO_{term}) have been reported to be only reversibly absorbed on Au surface (lowering however the fraction of sites available for the catalysis), so they can be easily removed under open circuit potential (OCP) conditions (see on this regard the CO-Bridge section below). Indeed, when the chronoamperometric protocol was modified introducing short reconditioning steps at OCP, the initial current density values for both Foam-Au and Col-Au were restored, allowing for the assessment of the medium term stability of the cathodes, as well as for the accumulation of sufficient amounts of products for their quantification. It is worth noting that even if the reconditioning step can be considered as a “dead time” in the whole process, it accounts only for the 10% of the total electrolysis time (30 s every 270 s) as described in fig 81 below.

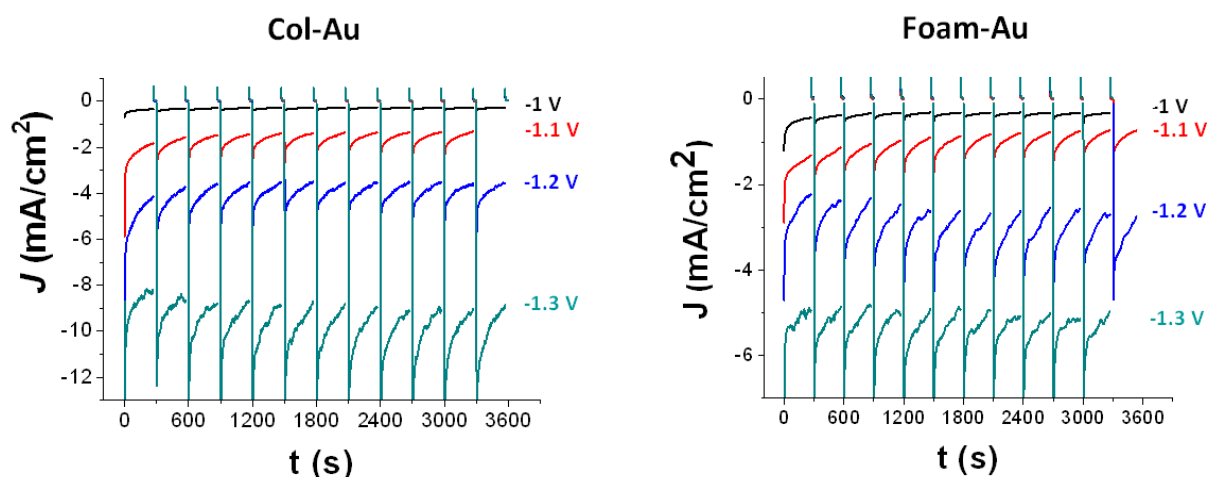


Fig. 81 Stepped chronoamperometry experiments performed for the accumulation of the products obtained with Col-Au (a) and Foam-Au (b) respectively. In particular, the cathodes were stepped between the bias reported in the graphs (for 270 s) and the OCP (for 30 s) the potential are reported vs RHE reference.

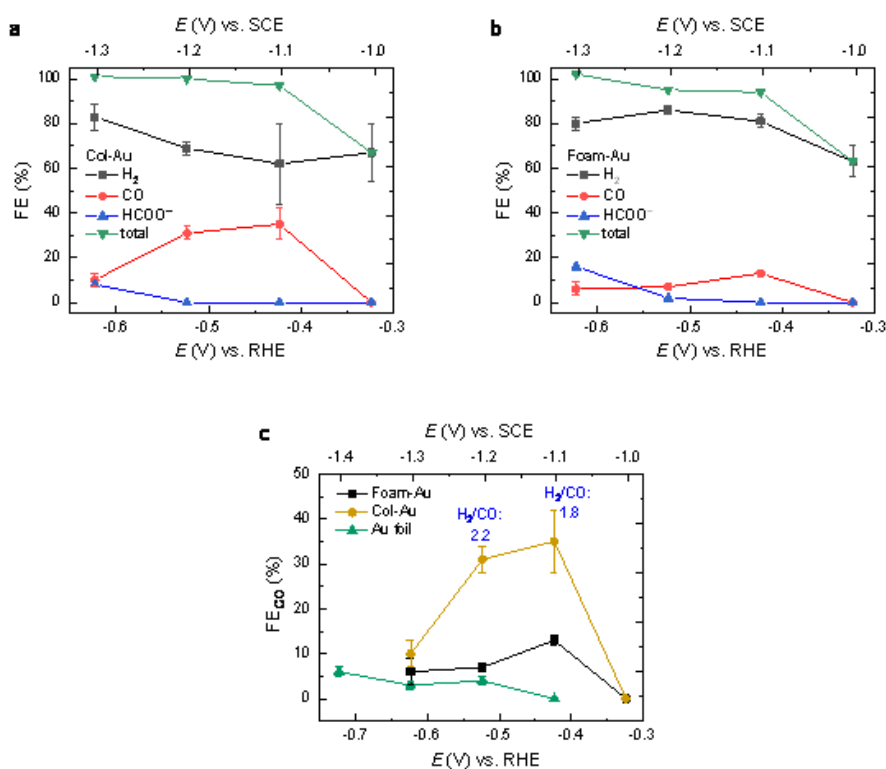


Fig. 82 Faradic efficiency of the different products obtained with Col-Au (a) and Foam-Au (b) cathodes as a function of the applied bias. Each point is an average of at least 3 measurements, and the corresponding standard deviations are reported as error bars. The < 100% total FE observed at -0.32 V (low current, i.e. lower amount of products) can be due to a trapping of the gas products in stagnant corners of the electrochemical cell. (c) Applied bias dependence of the faradic efficiency for the generation of CO for the different cathodes.

The Faradic efficiencies (FE) of the different products as a function of the applied bias are reported in Figure 82 Col-Au electrodes yielded CO as the major CO₂ reduction product (up to 35% FE at the low $|\eta|$ value of -1.0 V), as well as small amounts (< 8%) of formic acid at -1.3 V (Figure 80 a). At the same time, hydrogen also evolved, as a consequence of the competing proton reduction. Anyway, the H₂/CO ratio ~ 2 registered at intermediate bias (-1.1 and -1.2 V) is a particularly appealing gas mixture, being compatible with important industrial processes, such as hydrocarbons or methanol production *via* Fischer-Tropsch syntheses^{50,51,52}.

On the other hand, the Foam-Au surface more markedly favors proton over CO₂ reduction (Figure 82 b). Indeed, the maximum FE value for CO evolution was 13% at -1.1 V ($|\eta| = 0.31$ V), still overcoming the Au foil, for which < 6% of carbon monoxide was observed in the whole investigated potential range (Figure 82c). The H₂/CO ratio for Foam-Au is thus > 2 (see Table 13 for further details), envisaging the use of these gaseous mixtures for the production of short-chain hydrocarbons (*e.g.* methane) *via* Fischer-Tropsch syntheses, being H₂ involved in chain termination processes⁵². Furthermore, the syngas mixtures with higher hydrogen content could be used for biological fermentations, since the specificity of the involved enzymatic reactions makes this kind of processes less dependent on fixed H₂/CO compositions. Indeed, syngas mixtures obtained from the pyrolysis of solid waste and organic residues were recently fed to microorganisms, yielding biodegradable plastics, such as polyhydroxyalkanoates (polyesters)^{17,95}.

Cathode	Applied bias, V vs SCE	FE_{H₂}, %	FE_{CO}, %	H₂/CO ratio
Foam-Au	-1.1	81 ± 3	13 ± 1	6.2
	-1.2	86 ± 2	7 ± 1	12.3
	-1.3	80 ± 3	6 ± 3	14.5
Col-Au	-1.1	62 ± 18	35 ± 7	1.8
	-1.2	69 ± 3	31 ± 3	2.2
	-1.3	83 ± 6	10 ± 3	8.3
Au foil	-1.2	85 ± 5	4 ± 1	23.8
	-1.3	65 ± 6	3 ± 1	19.1
	-1.4	68 ± 5	6 ± 1	10.8

Tab. 13 Faradic efficiency for the two main products (H₂ and CO) obtained with Foam-Au and Col-Au cathodes, as well as with an Au foil, at different applied biases, the H₂/CO ratio is also reported.

1.8 CO-Bridge and electrode passivation

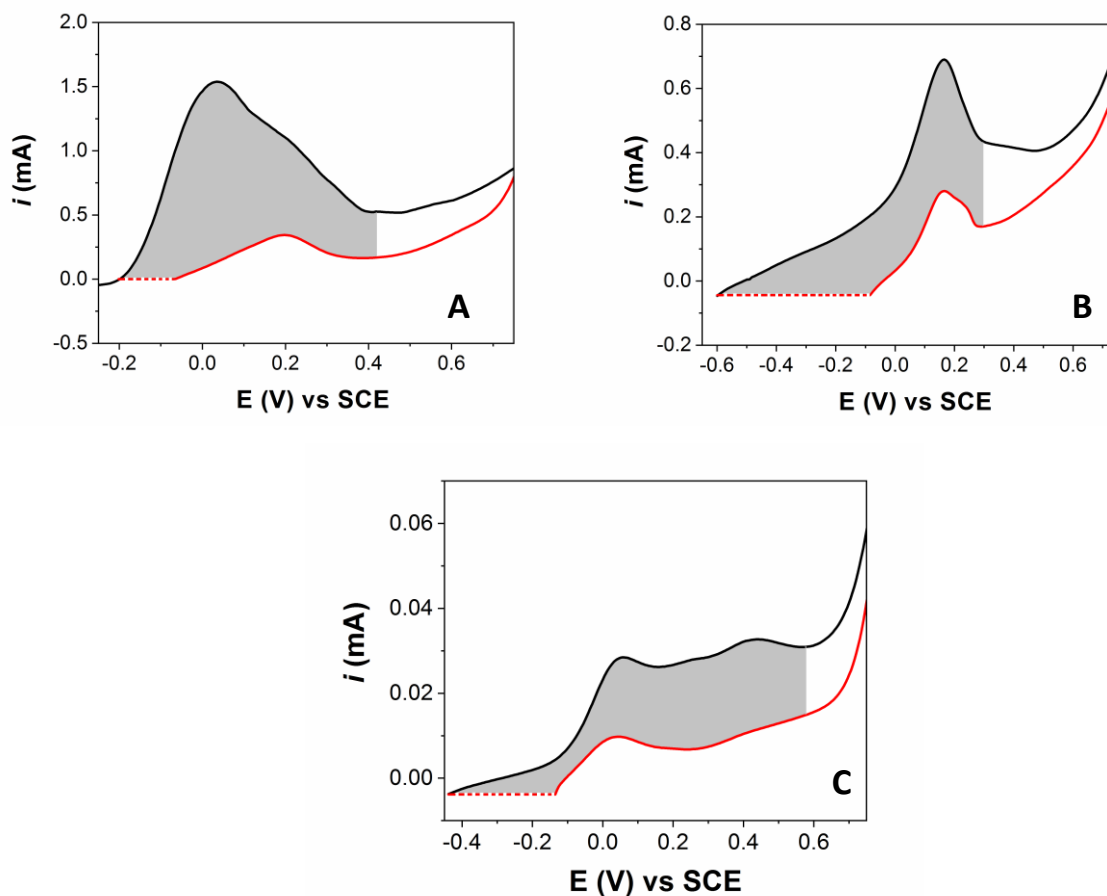


Fig. 83 $\text{CO}_{\text{bridge}}$ stripping analysis for the Col-Au (a), Foam-Au (b) and Au foil (c) cathodes. The first linear scans (black traces) were recorded immediately after the corresponding bulk electrolyses (pulsed between -0.42 V vs RHE and OCP). For all the cathodes, the charge due to the $\text{CO}_{\text{bridge}}$ stripping was calculated by integrating the 1st scan over the potential range indicated with the gray area (i.e. before Au oxidation starts to occur), using the corresponding 3rd scan (red trace) as the baseline, and dividing the obtained value by the scan rate (0.05 V/s).

When compared to other nanoporous structures reported in the literature, which usually show the selective formation of CO in aqueous media (FE > 95%)^{29,41,55,60,66} both our cathodes produced significantly higher amounts of H_2 , speaking in favor of a preferential absorption of $^*\text{H}$ over $^*\text{CO}_2$ (likely as $^*\text{COO}^-$ ⁸⁰ on Col-Au and Foam-Au surfaces. A possible explanation of this behavior could be related to a low amount of grain boundaries in our morphologies, mostly present in the foam-like domains of the Foam-Au film (Figure 76 d) rather than in the vertically-oriented Col-Au (Figure 73 a) and in the bottom layer of the Foam-Au (Figure 74 c). Indeed, the surface density of grain boundaries has been linearly correlated to CO_2 reduction activity⁶². On the other hand, the higher Faradic efficiency in CO production of the Col-Au film with respect

to the Foam-Au film (Figures 82 a-b) could be related to a different relative abundance of under-coordinated facets, such as the (110), with respect to facets with high coordination number, such as (111) and (200). Indeed, XRD results (Figure 70) and TEM analysis (Figure 76) suggest a higher amount of (200) facets for the Foam-Au film. According to recent reports⁶⁴, the equivalent (100) facets exhibit a significantly lower Faradic efficiency towards CO evolution rather than the under-coordinated (211) and (110). Consistently, the Col-Au film, which exhibits a stronger (220) diffraction peak, *i.e.* equivalent to the (110) lattice planes family, produced a higher amount of CO. Moreover, the Au foil, mostly exhibiting the highly-coordinated (200) facets, produced very low amounts of CO (Figure 82 c).

This aspect indirectly translates also in the different amount of irreversibly bridge-bonded CO spectators ($\text{CO}_{\text{bridge}}$) on the surface of the investigated cathodes. Indeed, using the oxidative stripping method described by the Surendranath group⁸⁰, we could estimate the surface coverage of the $\text{CO}_{\text{bridge}}$ spectators (see Figure 79). Table 14 collects the calculated values, increasing in the order Au foil < Foam-Au < Col-Au, thus confirming the preferential coordination of CO on under-coordinated sites.

Cathode	$\text{CO}_{\text{bridge}}$ stripping charge (mC)	$\text{CO}_{\text{bridge}}$ surface concentration, for geometric area (nmol/cm^2)	$\text{CO}_{\text{bridge}}$ surface concentration, for ECSA area (nmol/cm^2)
Col-Au	9.8	42.3	4.0
Foam-Au	3.7	25.6	2.8
Au foil	0.27	1.4	1.4

Tab. 14 $\text{CO}_{\text{bridge}}$ stripping charges calculated from Figures S6a-c for the Col-Au, Foam-Au and Au foil cathodes. The corresponding concentrations of $\text{CO}_{\text{bridge}}$ spectators stripped from the electrodic surfaces are also reported, considering that the stripping process is bielectronic

The table 14 describes the results obtained for the CO-Bridge analysis, performed with the described method, from these data it is possible to note that the higher surface concentration is represented by the columnar nanostructures followed by the foam morphology that appears reduced more than the 50% in terms of simple stripping charge. The subsequent normalization of the characteristic charge for the geometrical area and also for the electrochemical surface (ECSA) further confirm this trend.

1.9 Final considerations

As described in detail in chapters 1.3 and 1.4 among the metals adopted as cathodes, gold has been widely used since it almost selectively forms carbon monoxide as the main CO₂ reduction product. Furthermore, several reports evidenced the importance of nanostructuring the Au-based cathodic interfaces in order to boost CO formation over the competitive proton reduction in aqueous media.

In this contribution, the preparation of two different kind of porous Au-nanostructures was reported, focusing on their use as cathodes for CO₂ reduction in aqueous electrolytes. These cathodic materials were synthesized, thanks to a fruitful collaboration with the Milan University, by pulsed laser deposition, a versatile and easy-to-scale technique, already implemented in industrial processes. The results obtained with the nanoporous catalysts evidenced the formation of an ideal yield in Syngas (CO+H₂), together with smaller amounts of formic acid, outperforming a planar gold foil used as reference. This interesting result is further supported by the advantages offered by the great chemical stability of gold in this environment, avoiding at the same time the problems related to the use of co-functionalized cathodes subjected, as described in the previous parts, to the short working life caused by the gradual co-catalyst detachment.

CONCLUSIONS

Through this work it was possible to explore surface engineered electrodes with the aim of achieving an efficient and selective CO₂ reduction. In particular we mostly focused on copper and gold electrodes. Various types of copper electrodes, including high surface area composite electrodes, were modified by exploiting an unprecedented fast anodization treatment which creates a significant coverage of micro/nanocubes having an higher reactivity towards CO₂ reduction in aqueous media. The use of co-catalyst, including cerium and indium oxides allowed to further tune and enhance the reactivity of these electrodes towards valuable products like CO and methane. With gold, we investigated the dramatic impact of surface nanostructuring over the reactivity and selectivity towards CO₂ reduction. The OD treatment herein developed was deemed of sufficient industrial interest to file first an Italian patent application, later extended to and an European one through the international PCT program. Indeed, the exploitation of easily available electrodes for CO₂ reduction surely represents an appealing solution in the framework of the closure of the carbon cycle, that is needed to counter the climate change induced by greenhouse gases. In addition it may open the route for renewable fuels, which are compatible with the existing industrial and energy infrastructure. In this field, the research will continue towards the stabilization of co-catalysts, by searching surface encapsulation strategies and tuning of the electrolyte composition.

REFERENCES

- [1] S. Hernandez, M.A. Farkhondehfal, F. Sastre, M. Makkee, G. Saracco and N. Russo, *Green Chem.*, 2017.
- [2] A.S. Varela, et al., Controlling the selectivity of CO₂ electroreduction on copper: The effect of the electrolyte concentration and the importance of the local pH, *Catal. Today*, 2015.
- [3] K. P. Kuhl, E. R. Cave, D. N. Abram, T. F. Jaramillo, *Energy Environ. Sci.*, 2012, 5, 7050.
- [4] Y. Hori, in *Modern Aspects of Electrochemistry*, Vol. 42, (Eds.: C. Vayenas, R. White, M. Gamboa-Aldeco), Springer, New York, 2008, pp. 89 – 189.
- [5] W. Paik, T. N. Andersen, H. Eyring, *Electrochim. Acta* 1969, 14, 1217;
- [6] S. Ikeda, T. Takagi, K. Ito, *Bull. Chem. Soc. Jpn.* 1987, 60, 2517;
- [7] Y. Hori, A. Murata, K. Kikuchi, S. Suzuki, *J. Chem. Soc. Chem. Commun.* 1987, 728.
- [8] Lackner KS. Capture of carbon dioxide from ambient air. *The European Physical Journal – Special Topics* 2009;176(1):93–106
- [9] <https://www.carbonbrief.org/qa-will-reformed-eu-emissions-trading-system-raise-carbon-prices>
- [10] E. Williams, A. Sekar, S. Matteson, B. E. Rittmann, *Environ. Sci. Technol.* 2015, 49, 6394–6401
- [11] *Renewable and Sustainable Energy Reviews*, 15, 2011, 1-23
- [12] Graf D, Monnerie N, Roeb M, Schmitz M, Sattler C. *International Journal of Hydrogen Energy* 2008;33(17):4511–9;
- [13] Bailleux C, Damien A, Montet A. *International Journal of Hydrogen Energy* 1983;8(7):529–38;
- [14] Abe I, Fujimaki T, Matsubara M. *International Journal of Hydrogen Energy* 1984;9(9):753–8.
- [15] Janjua MBI, Leroy RL. *International Journal of Hydrogen Energy* 1985;10(1):11–9.
- [16] Ivy J. Summary of electrolytic hydrogen production: milestone completion report. Golden, Colorado: National Renewable Energy Laboratory; 2004 (MP- 560-35948. 28
- [17] Dry ME. The Fischer–Tropsch process: 1950– 2000. *Catalysis Today* 2002;71:227–41
- [18] Mignard D, Pritchard C. Processes for the synthesis of liquid fuels from CO₂ and marine energy. *Chemical Engineering Research and Design* 2006;84, 828– 36
- [19] D. Bellotti, M. Rivarolo, L. Magistri, A.F. Massardo, *Journal of CO₂ utilization* 21, 2017, 132-138
- [20] DOE-NETL, Baseline Analysis of Crude Methanol Production from Coal and Natural Gas, (2014
- [21] C. Graves, S. D. Ebbesen, M. Mogensen, K, S. Lackner *Renewable and Sustainable Energy Reviews*, 15, 2011 1- 23
- [22] *Renewable and Sustainable Energy Reviews*, 15, 2011, 1-23
- [23] CRI, <https://www.carbonrecycling.is/>
- [24] <https://carbonengineering.com/our-technology/>
- [25] Niorettini Alessandro, Bigozzi Carlo Alberto, Caramori Stefano e Bernardi Serena. (2021). Process for forming and regenerating a copper cathode for an electrochemical cell and electrochemical cell for the production of industrial products. (Brevetto italiano e PCT n.WO 028779 A1). World Intellectual Property Organization.
- [26] Y. Chen, C. W. Li, M. W. Kanan, *JACS*, 2012, 134, 19969.
- [27] F. S. Roberts, K. P. Kuhl, A. Nilsson, *Angew. Chem.* 2015, 127, 5268 –5271.

- [28] D. Gao, I. Zegkinoglou, N. J. Divins, F. Scholten, I. Sinev, P. Grosse, B. Roldan Cuenya et al. *ACS Nano*, 2017, 11, 4825–4831.
- [29] Yihong Chen, Christina W. Li, and Matthew W. Kanan *J. Am. Chem. Soc.*, 2012, 134 (49), pp 19969–19972
- [30] Ruperto G. Mariano, Kim McKelvey, Henry S. White, Matthew W. Kanan, *Science* 2017 358 1187
- [31] Dr. Shahid Rasul Dr. Dalaver H. Anjum Dr. Abdesslem Jedidi Dr. Yury Minenkov Prof. Luigi Cavallo Prof. Kazuhiro Takanabe *Angewandte Chemie*, 2015, 54, 2146–2150
- [32] S. Nitopi, E. Bertheussen, S. B. Scott, X. Liu, A. K. Engstfeld, S. Horch, B. Seger, I. E. Stephens, K. Chan, C. Hahn, J. K. Nørskov, T. F. Jaramillo and I. Chorkendorff, *Chem. Rev.*, 2019, 119, 7610–7672.
- [33] C. W. Li and M. W. Kanan, *J. Am. Chem. Soc.*, 2012, 134, 7231–7234.
- [34] H. Mistry, A. S. Varela, C. S. Bonifacio, I. Zegkinoglou, I. Sinev, Y.-W. Choi, K. Kisslinger, E. A. Stach, J. C. Yang, P. Strasser and B. Roldan Cuenya, *Nat. Commun.*, 2016, 7, 1–9.
- [35] D. Gao, I. Zegkinoglou, N. J. Divins, F. Scholten, I. Sinev, P. Grosse and B. Roldan Cuenya, *ACS Nano*, 2017, 11, 4825– 4831.
- [36] B. Kumar, J. P. Brian, V. Atla, S. Kumari, K. A. Bertram, R. T. White and J. M. Spurgeon, *ACS Catal.*, 2016, 6, 4739–4745.
- [37] M. J. Siegfried and K.-S. Choi, *J. Am. Chem. Soc.*, 2006, 128, 10356–10357.
- [38] *Adv. Mater.* 2004, 16, 1743
- [39] R. M. Arán-Ais, R. Rizo, P. Grosse, G. Algara-Siller, K. Dembélé, M. Plodinec, T. Lunkenbein, S. W. Chee and B. Roldan Cuenya, *Nat. Commun.*, 2020, 11, 1–8.
- [40] C. Wagner, *Faraday Discuss. Chem. Soc.*, 1975, 60, 291–300.
- [41] E. Bojestig, Y. Cao and L. Nyborg, *Surf. Interface Anal.*, 2020, 52, 1104–1110.
- [42] I. Platzman, R. Brener, H. Haick and R. Tannenbaum, *J. Phys. Chem. C*, 2008, 112, 1101–1108.
- [43] C. Yan, M. Zharnikov, A. Götzhäuser and M. Grunze, *Langmuir*, 2000, 16, 6208–6215.
- [44] Z. M. Detweiler, S. M. Wulfsberg, M. G. Frith, A. B. Bocarsly and S. L. Bernasek, *Surf. Sci.*, 2016, 648, 188–195.
- [45] D. R. Baer and J. Moulder, *Surf. Sci. Spectra*, 1993, 2, 1–7.
- [46] W. M. Skinner, C. A. Prestidge and R. S. C. Smart, *Surf. Interface Anal.*, 1996, 24, 620–626.
- [47] Y. Hori, A. Murata and R. Takahashi, *J. Chem. Soc., Faraday Trans. 1*, 1989, 85, 2309–2326.
- [48] M. Brust, P. M. Blass and A. J. Bard, *Langmuir* 1997, 13, 5602–5607
- [49] Kuhl, K. P.; Hatsukade, T.; Cave, E. R.; Abram, D. N.; Kibsgaard, J.; Jaramillo, T. F. Electrocatalytic conversion of carbon dioxide to methane and methanol on transition metal surfaces. *J. Am. Chem. Soc.* 2014, 136, 14107–14113.
- [50] Dry, M. E. Practical and theoretical aspects of the catalytic Fischer-Tropsch process. *Appl. Catal. A: Gen.* 1996, 138, 319–344.
- [51] Dry, M. E. The fischer-tropsch process: 1950–2000. *Catal. Today* 2002, 71, 227–241.
- [52] Dry, M. E. High quality diesel via the Fischer-Tropsch process—a review. *J. Chem. Technol. Biotechnol.* 2002, 77, 43–50.
- [53] Hori, Y.; Wakebe, H.; Tsukamoto, T.; Koga, O. Electrocatalytic process of CO selectivity in electrochemical reduction of CO₂ at metal electrodes in aqueous media. *Electrochim. Acta* 1994, 39, 1833–

1839.

- [54] Kortlever, R.; Shen, J.; Schouten, K. J. P.; Calle-Vallejo, F.; Koper, M. T. M. Catalysts and reaction pathways for the electrochemical reduction of carbon dioxide. *J. Phys. Chem. Lett.* 2015, 6, 4073–4082.
- [55] Cave, E. R.; Montoya, J. H.; Kuhl, K. P.; Abram, D. N.; Hatsukade, T.; Shi, C.; Hahn, C.; Nørskov, J. K.; Jaramillo, T. F. Electrochemical CO₂ reduction on Au surfaces: mechanistic aspects regarding the formation of major and minor products. *Phys. Chem. Chem. Phys.* 2017, 19, 15856–15863.
- [56] Narayanaru, S.; Chinnaiiah, J.; Phani, K. L.; Scholz, F. pH dependent CO adsorption and roughness-induced selectivity of CO₂ electroreduction on gold surfaces. *Electrochim. Acta* 2018, 264, 269–274.
- [57] Lee, H.-E.; Yang, K. D.; Yoon, S. M.; Ahn, H.-Y.; Lee, Y. Y.; Chang, H.; Jeong, D. H.; Lee, Y.-S.; Kim, M. Y.; Nam, K. T. Concave rhombic dodecahedral Au nanocatalyst with multiple high-index facets for CO₂ reduction. *ACS Nano* 2015, 9, 8384–8393.
- [58] Zhu, W.; Zhang, Y.-J.; Zhang, H.; Lv, H.; Li, Q.; Michalsky, R.; Peterson, A. A.; Sun, S. Active and selective conversion of CO₂ to CO on ultrathin Au nanowires. *J. Am. Chem. Soc.* 2014, 136, 16132–16135.
- [59] Kim, H.; Park, H. S.; Hwang, Y. J.; Min, B. K. Surfacermorphology- dependent electrolyte effects on gold-catalyzed electrochemical CO₂ reduction. *J. Phys. Chem. C* 2017, 121, 22637–22643.
- [60] [43] Liu, M.; Pang, Y.; Zhang, B.; de Luna, P.; Voznyy, O.; Xu, J.; Zheng, X.; Dinh, C. T.; Fan, F.; Cao, C.; de Arquer, F. P. G.; Safaei, T. S.; Mepham, A.; Klinkova, A.; Kumacheva, E.; Filleter, T.; Sinton, D.; Kelley, S. O.; Sargent, E. H. Enhanced electrocatalytic CO₂ reduction via field-induced reagent concentration. *Nature* 2016, 537, 382.
- [61] Welch, A. J.; DuChene, J. S.; T4gliabue, G.; Davoyan, A.; Cheng, W.-H.; Atwater, H. A. Nanoporous Gold as a Highly Selective and Active Carbon Dioxide Reduction Catalyst. *ACS Appl. Energy Mater.* 2019, 2, 164–170.
- [62] Feng, X.; Jiang, K.; Fan, S.; Kanan, M. W. Grain-boundarydependent CO₂ electroreduction activity. *J. Am. Chem. Soc.* 2015, 137, 4606–4609.
- [63] Zhang, W.; He, J.; Liu, S.; Niu, W.; Liu, P.; Zhao, Y.; Pang, F.; Xi, W.; Chen, M.; Zhang, W.; Pang, S.-S.; Ding, Y. Atomic origins of high electrochemical CO₂ reduction efficiency on nanoporous gold. *Nanoscale* 2018, 10, 8372–8376.
- [64] Mezzavilla, S.; Horch, S.; Stephens, I. E. L.; Seger, B.; Chorkendorff, I. Structure sensitivity in the electrocatalytic reduction of CO₂ with gold catalysts. *Angew. Chem.* 2019, 131, 3814–3818.
- [65] Todoroki, N.; Tei, H.; Tsurumaki, H.; Miyakawa, T.; Inoue, T.; Wadayama, T. Surface atomic arrangement dependence of electrochemical CO₂ reduction on Gold: online electrochemical mass spectrometric study on low-index au (hkl) surfaces. *ACS Catal.* 2019, 9, 1383–1388.
- [66] Koh, J. H.; Jeon, H. S.; Jee, M. S.; Nursanto, E. B.; Lee, H.; Hwang, Y. J.; Min, B. K. Oxygen plasma induced hierarchically structured gold electrocatalyst for selective reduction of carbon dioxide to carbon monoxide. *J. Phys. Chem. C* 2015, 119, 883–889.
- [67] Hall, A. S.; Yoon, Y.; Wuttig, A.; Surendranath, Y. Mesostructure-induced selectivity in CO₂ reduction catalysis. *J. Am. Chem. Soc.* 2015, 137, 14834–14837.
- [68] Nesbitt, N. T.; Ma, M.; Trzeźniewski, B. J.; Jaszewski, S.; Tafti, F.; Burns, M. J.; Smith, W. A.; Naughton, M. J. Au Dendrite Electrocatalysts for CO₂ Electrolysis. *J. Phys. Chem. C* 2018, 122, 10006–10016.
- [69] Kim, J.; Song, J. T.; Ryoo, H.; Kim, J.-G.; Chung, S.-Y.; Oh, J. Morphology-controlled Au nanostructures for efficient and selective electrochemical CO₂ reduction. *J. Mater. Chem. A* 2018, 6, 5119–5128.
- [70] Mistry, H.; Reske, R.; Zeng, Z.; Zhao, Z.-J.; Greeley, J.; Strasser, P.; Cuenya, B. R. Exceptional size-dependent activity enhancement in the electroreduction of CO₂ over Au nanoparticles. *J. Am. Chem. Soc.* 2014, 136, 16473–16476.

- [71] Kauffman, D. R.; Alfonso, D.; Matranga, C.; Qian, H.; Jin, R. Experimental and computational investigation of Au₂₅ clusters and CO₂: a unique interaction and enhanced electrocatalytic activity. *J. Am. Chem. Soc.* 2012, 134, 10237–10243.
- [72] Yang, B.; Mahjouri-Samani, M.; Rouleau, C. M.; Geohegan, D. B.; Xiao, K. Low temperature synthesis of hierarchical TiO₂ nanostructures for high performance perovskite solar cells by pulsed laser deposition. *Phys. Chem. Chem. Phys.* 2016, 18, 27067–27072.
- [73] Geohegan, D. B.; Poretzky, A. A.; Duscher, G.; Pennycook, S. J. Time-resolved imaging of gas phase nanoparticle synthesis by laser ablation. *Appl. Phys. Lett.* 1998, 72, 2987–2989.
- [74] Ghidelli, M.; Mascaretti, L.; Bricchi, B. R.; Zapelli, A.; Russo, V.; Casari, C. S.; Li Bassi, A. Engineering plasmonic nanostructured surfaces by pulsed laser deposition. *Appl. Surf. Sci.* 2018, 434, 1064–1073.
- [75] Canulescu, S.; Döbeli, M.; Yao, X.; Lippert, T.; Amoroso, S.; Schou, J. Nonstoichiometric transfer during laser ablation of metal alloys. *Phys. Rev. Mater.* 2017, 1, No. 073402.
- [76] Bricchi, B. R.; Ghidelli, M.; Mascaretti, L.; Zapelli, A.; Russo, V.; Casari, C. S.; Terraneo, G.; Alessandri, I.; Ducati, C.; Li Bassi, A. Integration of plasmonic Au nanoparticles in TiO₂ hierarchical structures in a single step pulsed laser co-deposition. *Mater. Des.* 2018, 156, 311–319.
- [77] Casari, C. S.; Giannuzzi, C. S.; Russo, V. Carbon-atom wires produced by nanosecond pulsed laser deposition in a background gas. *Carbon* 2016, 104, 190–195.
- [78] Ojeda-G-P, A.; Döbeli, M.; Lippert, T. Influence of plume properties on thin film composition in pulsed laser deposition. *Adv. Mater. Interfaces* 2018, 5, 1701062.
- [79] Gondoni, P.; Ghidelli, M.; Di Fonzo, F.; Russo, V.; Bruno, P.; Martí-Rujas, J.; Bottani, C. E.; Li Bassi, A.; Casari, C. S. Structural and functional properties of Al:ZnO thin films grown by Pulsed Laser Deposition at room temperature. *Thin Solid Films* 2012, 520, 4707–4711.
- [80] Liu, Z.; Masel, R. I.; Chen, Q.; Kutz, R.; Yang, H.; Lewinski, K.; Kaplun, M.; Luopa, S.; Lutz, D. R. Electrochemical generation of syngas from water and carbon dioxide at industrially important rates. *J. CO₂ Util.* 2016, 15, 50–56.
- [81] Fu, Q.; Mabilat, C.; Zahid, M.; Brisse, A.; Gautier, L. Syngas production via high-temperature steam/CO₂ co-electrolysis: an economic assessment. *Energy Environ. Sci.* 2010, 3, 1382–1397.
- [82] Nguyen, V. N.; Blum, L. Syngas and synfuels from H₂O and CO₂: current status. *Chem. Ing. Tech.* 2015, 87, 354–375.
- [83] Sánchez, O. G.; Birdja, Y. Y.; Bulut, M.; Vaes, J.; Breugelmans, T.; Pant, D. Recent advances in industrial CO₂ electroreduction. *Curr. Opin. Green Sustain. Chem.* 2019, 47.
- [84] Wilhelm, D. J.; Simbeck, D. R.; Karp, A. D.; Dickenson, R. L. Syngas production for gas-to-liquids applications: technologies, issues and outlook. *Fuel Process. Technol.* 2001, 71, 139–148.
- [85] Irtem, E.; Andreu, T.; Parra, A.; Hernández-Alonso, M. D.; García-Rodríguez, S.; Riesco-García, J. M.; Penelas-Pérez, G.; Morante, J. R. Low-energy formate production from CO₂ electroreduction using electrodeposited tin on GDE. *J. Mater. Chem. A* 2016, 4, 13582–13588.
- [86] Wuttig, A.; Yaguchi, M.; Motobayashi, K.; Osawa, M.; Surendranath, Y. Inhibited proton transfer enhances Au-catalyzed CO₂-to-fuels selectivity. *Proc. Natl. Acad. Sci.* 2016, 113, E4585–E4593.
- [87] Agarwal, N. R.; Neri, F.; Trusso, S.; Lucotti, A.; Ossi, P. M. Au nanoparticle arrays produced by pulsed laser deposition for surface enhanced Raman spectroscopy. *Appl. Surf. Sci.* 2012, 258, 9148–9152.
- [88] Maffini, A.; Pazzaglia, A.; Dellasega, D.; Russo, V.; Passoni, M. Growth dynamics of pulsed laser deposited nanofoams. *Phys. Rev. Mater.* 2019, 3, No. 083404.

- [89] Marine, W.; Patrone, L.; Luk'yanchuk, B.; Sentis, M. Strategy of nanocluster and nanostructure synthesis by conventional pulsed laser ablation. *Appl. Surf. Sci.* 2000, 154-155, 345–352.
- [90] McCrory, C. C. L.; Jung, S.; Ferrer, I. M.; Chatman, S. M.; Peters, J. C.; Jaramillo, T. F. Benchmarking hydrogen evolving reaction and oxygen evolving reaction electrocatalysts for solar water splitting devices. *J. Am. Chem. Soc.* 2015, 137, 4347–4357.
- [91] Łukaszewski, M.; Soszko, M.; Czerwiński, A. Electrochemical methods of real surface area determination of noble metal electrodes – an overview. *Int. J. Electrochem. Sci.* 2016, 11, 4442–4469.
- [92] Trasatti, S.; Petrii, O. A. Real surface area measurements in electrochemistry. *Pure Appl. Chem.* 1991, 63, 711–734.
- [93] McCrory, C. C. L.; Jung, S.; Peters, J. C.; Jaramillo, T. F. Benchmarking heterogeneous electrocatalysts for the oxygen evolution reaction. *J. Am. Chem. Soc.* 2013, 135, 16977–16987.
- [94] Li, C. W.; Kanan, M. W. CO₂ reduction at low overpotential on Cu electrodes resulting from the reduction of thick Cu₂O films. *J. Am. Chem. Soc.* 2012, 134, 7231–7234.
- [95] Yoon, Y.; Yan, B.; Surendranath, Y. Suppressing ion transfer enables versatile measurements of electrochemical surface area for intrinsic activity comparisons. *J. Am. Chem. Soc.* 2018, 140, 2397–2400.
- [96] J. He, N. J. Johnson, A. Huang and C. P. Berlinguette, *ChemSusChem*, 2018, 11, 48–57
- [97] M. Carmo, D. L. Fritz, J. Mergel and D. Stolten, *Int. J. Hydrogen Energy*, 2013, 38, 4901–4934.
- [98] A. Jedidi, S. Rasul, D. Masih, L. Cavallo and K. Takanabe, *J. Mater. Chem. A*, 2015, 3, 19085–19092.
- [99] W. Luo, W. Xie, R. Mutschler, E. Oveisi, G. L. De Gregorio, R. Buonsanti and A. Züttel, *ACS Catal.*, 2018, 8, 6571–6581.
- [100] Z. B. Hoffman, T. S. Gray, K. B. Moraveck, T. B. Gunnoe and G. Zangari, *ACS Catal.*, 2017, 7, 5381–5390.
- [101] J. He, K. E. Dettelbach, D. A. Salvatore, T. Li and C. P. Berlinguette, *Angew. Chem.*, 2017, 129, 6164–6168.
- [102] Y. Hori, A. Murata and Y. Yoshinami, *J. Chem. Soc., Faraday Trans.*, 1991, 87, 125–128.
- [103] E. L. Clark and A. T. Bell, *J. Am. Chem. Soc.*, 2018, 140, 7012–7020.
- [104] N. Gupta, M. Gattrell and B. MacDougall, *J. Appl. Electrochem.*, 2006, 36, 161–172.
- [105] V. Dieterich, A. Buttler, A. Hanel, H. Spliethoff and S. Fendt, *Energy Environ. Sci.*, 2020, 13, 3207–3252.
- [106] R. Franke, D. Selent and A. Börner, *Chem. Rev.*, 2012, 112, 5675–5732.
- [107] G. n. O. Larrazábal, A. J. Martín, S. Mitchell, R. Hauert and J. Pérez-Ramírez, *ACS Catal.*, 2016, 6, 6265–6274.
- [108] Hamlaoui, Youcef & Pedraza, F. & Remazeilles, Celine & Cohendoz, S. & Rébéré, C. & Tifouti, Lakhdar & Creus, J.. (2009). Cathodic electrodeposition of cerium-based oxides on carbon steel from concentrated cerium nitrate solutions: Part I. Electrochemical and analytical characterisation. *Materials Chemistry and Physics*. 113. 650–657. 10.1016/j.matchemphys.2008.08.027
- [109] Y. Hamlaoui et al. *Materials Chemistry and Physics* 113, 2009, 650–65.

ADDENDUM I

Internship at Wrocław University for the synthesis and characterization of metallic complexes with enhanced anticancer properties, article: *“Synthesis, Physicochemical, and Biological Properties of Phosphino Cu(I), Ru(II), Ir(III) Complexes”*

Introduction to the work

One of the most important challenges nowadays is surely constituted by the search of an efficient and powerful tool against cancer pathologies, tumors in fact are estimated in 2020 to represent the cause of over 10 millions deaths in the world*. Due to this situation, it is imperative to carry out a continuous scientific research in order to highlighting our knowledge of the mechanisms involved in these pathologies and studying new and more effective strategies for definitely fighting these diseases. At the current state of art, one of the most chosen therapeutic path available is surely chemotherapy which, if from one side is certainly accompanied by an acceptable success rate, on the other exposes patients to a wide range of severe side effects. Chemotherapeutic agents in fact not only have to struggle with the cancer itself but have also to interact with an unfriendly environment for their chemistry, in particular limited aqueous solubility of these molecules, poor selectivity and developed resistance are just few of the well known limits encountered by this pharmacological approach.

In the last years the main research goals in cancer therapy is focused into developing strategies to avoid these non-negligible defects, ranging from perfecting the structure and synthesis of these drugs to the growth of new and completely different approaches like thermal or phototherapy.

Thanks to a fruitful cooperation between the University of Ferrara and the Magnetic Materials Group of the University of Wroclaw it was possible to investigate the synthesis of new compounds for cancer treatment with the aim to find novel and more efficient drugs based on ruthenium, iridium and copper complexes. At first my role was centered into giving support to the electrochemical and spectroscopical analysis of these molecules to then concentrate also on the synthetic and biological aspect during my internship in their laboratories. Below is reported in details the result of this collaboration which is currently published in specific scientific journals.

* H. Sung, J. Ferlay, R.I. Siegel, M. Laversanne, I. Soerjomataram, A. Jemal, F. Bray, Global Cancer Statistics 2020: GLOBOCAN Estimates of Incidence and Mortality Worldwide for 36 Cancers in 185 Countries, CA Cancer J Clin., **2021**, 3, 209-249

Synthesis,

Physicochemical, and Biological Properties of Phosphino Cu(I),

Ru(II), Ir(III) Complexes

Urszula K. Komarnicka, Alessandro Nioiretini, Sandra Kozieł, Barbara Pucelik, Agata Barzowska,

Daria Wojtala, Aleksandra Ziółkowska, Monika Lesiów, Agnieszka Kyzioł, Stefano Caramori,

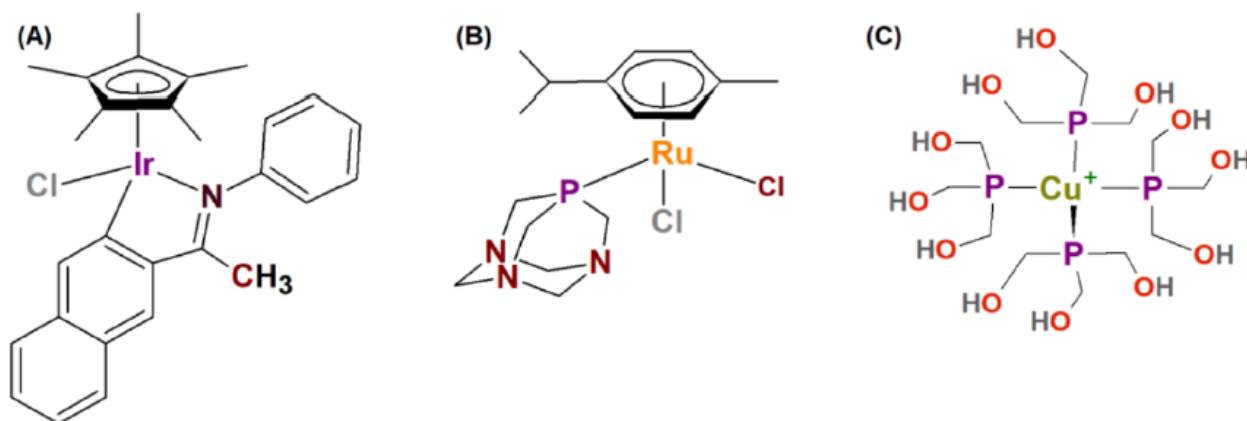
Marina Porchia and Alina Bienko

Abstract: Two novel phosphine ligands, $\text{Ph}_2\text{PCH}_2\text{N}(\text{CH}_2\text{CH}_3)_3$ (**1**) and $\text{Ph}_2\text{PCH}_2\text{N}(\text{CH}_2\text{CH}_2\text{CH}_2\text{CH}_3)_2$ (**2**), and six new metal (Cu(I), Ir(III) and Ru(II)) complexes with those ligands: iridium(III) complexes: $\text{Ir}(\eta^5\text{-Cp}^*)\text{Cl}_2$ (**1**) (**1a**), $\text{Ir}(\eta^5\text{-Cp}^*)\text{Cl}_2$ (**2**) (**2a**) (Cp*: Pentamethylcyclopentadienyl); ruthenium(II) complexes: $\text{Ru}(\eta^6\text{-p-cymene})\text{Cl}_2$ (**1**) (**1b**), $\text{Ru}(\eta^6\text{-p-cymene})\text{Cl}_2$ (**2**) (**2b**) and copper(I) complexes: $[\text{Cu}(\text{CH}_3\text{CN})_2(\mathbf{1})\text{BF}_4]$ (**1c**), $[\text{Cu}(\text{CH}_3\text{CN})_2(\mathbf{2})\text{BF}_4]$ (**2c**) were synthesized and characterized using elemental analysis, NMR spectroscopy, and ESI-MS spectrometry. Copper(I) complexes turned out to be highly unstable in the presence of atmospheric oxygen in contrast to ruthenium(II) and iridium(III) complexes. The studied Ru(II) and Ir(III) complexes exhibited promising cytotoxicity towards cancer cells in vitro with IC50 values significantly lower than that of the reference drug cisplatin. Confocal microscopy analysis showed that Ru(II) and Ir(III) complexes effectively accumulate inside A549 cells with localization in cytoplasm and nuclei. A precise cytometric analysis provided clear evidence for the predominance of apoptosis in induced cell death. Furthermore, the complexes presumably induce the changes in the cell cycle leading to G2/M phase arrest in a dose-dependent manner. Gel electrophoresis experiments revealed that Ru(II) and Ir(III) inorganic compounds showed their unusual low genotoxicity towards plasmid DNA. Additionally, metal complexes were able to generate reactive oxygen species as a result of redox processes, proved by gel electrophoresis and cyclic voltamperometry. In vitro cytotoxicity assays were also carried out within multicellular tumor spheroids and efficient anticancer action on these 3D assemblies was demonstrated. It was proven that the

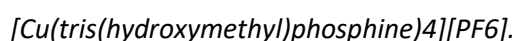
hydrocarbon chain elongation of the phosphine ligand coordinated to the metal ions does not influence the cytotoxic effect of resulting complexes in contrast to metal ions type.

1. Introduction

When it comes to pharmaceutical approaches to anticancer therapy, it is impossible not to mention cisplatin, as for over forty years it has been the active principle of choice in the fight against these diseases¹⁻³. However, on the one hand, medicine has adopted it as one of the pillars of cancer therapy, while on the other hand, its prolonged use has confirmed the numerous limitations and risks, which cannot be ignored, related to the serious immediate and long-term side effects⁴. Cisplatin, in this regard, is also known to develop resistance to prolonged care cycles, a characteristic that makes it particularly ineffective in the event of the manifestation of a relapsed clinical picture⁵. Thanks to the experience gained, alternative strategies have been developed that have led to the synthesis of numerous organometallic platinum-based compounds such as carboplatin and nedaplatin, with the aim of developing selectively toxic molecules towards cancer cells, hoping to generate an efficient bio-distribution and an inability to develop resistance conditions⁶. For this purpose, the correlation between the activity of the metal and its chemical environment is fundamental, in fact, the possibility of using a wide range of ligands paves the way for the study of new and different mechanisms of action, which is capable of limiting the general toxicity associated with these drugs while, in the meantime, maximizing the efficiency of cellular uptake⁷⁻¹¹. In recent years, the research has underlined how a synthetic approach of this type allows great progress in the synthesis and optimization of competitive chemotherapy; however, the intrinsic reactivity and biological characteristics of platinum make it difficult to overcome many important therapeutic obstacles and the consequent achievement of an ideal pharmacology. Due to this fact, the use of alternative metals is becoming a valid possible answer to the problem^{5,12-18}. In relation to this overview, this work aims mainly to explore and understand the synergistic activity of phosphine ligands and copper, ruthenium or iridium ions, complexes with those metal ions are already known for their intrinsic antibacterial¹⁹⁻²⁵, antiviral²⁶⁻²⁹, antifungal³⁰⁻³¹, and anti-inflammatory³²⁻³³ characteristics (Scheme 1). Thanks to a wide range of coordination numbers, redox states, and possible geometries, inorganic compounds seem to possess a remarkable reactivity. In particular, a systematic study on synthesis and characterization of different metallic complexes in association with phosphine ligands was carried out, which are promising candidates for this purpose as their cytotoxicity towards tumor cells is already known^{19,34-43}.



Scheme 1. Schematic view of the (A) half-sandwich Schiff-base Ir(III); (B) RAPTA-C; (C)



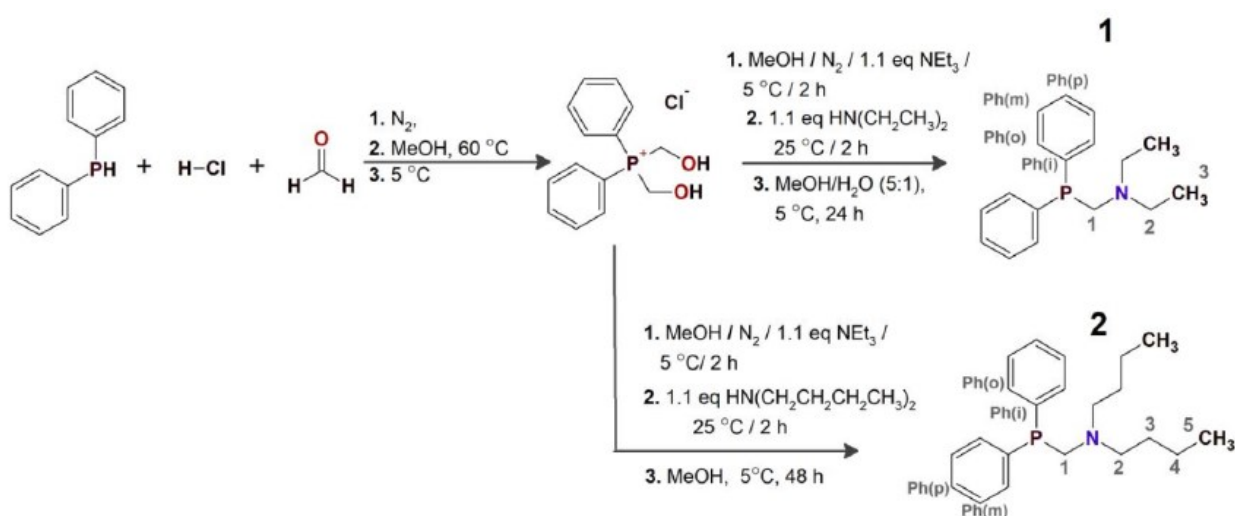
In our work, we have synthesized two new phosphine ligands by attachment diethylamine(HN(CH₂CH₃)₂) or dibutylamine(HN(CH₂CH₂CH₂CH₃)₂) to (hydroxymethyl) diphenylphosphine (Ph₂PCH₂OH). Structures of those ligands differ in the length of hydrocarbon chain. Interestingly, Mashid Kantoury with his team synthesized and studied the biological activity of three organometallic Pt(II) complexes with the general formula [Pt(phen)(L)]NO₃, where phen=phenanthroline, L = methylglycine, amyglycine, and isopentylglycine. The differences between these three complexes are in the length of the hydrocarbon chain in ligands. Based on cytotoxic studies on the human breast cancer cell line (MDA-MB 231), the team managed to prove that, with an abridgment of the hydrocarbon chain in ligands, the cytotoxic activity of the resulting complexes increased⁴⁴. Moreover, Paltan Laha with co-authors came to the same conclusion while investigating several mononuclear cyclometalatediridium(III) complexes towards the human breast cancer cell line (MCF-7)⁴⁵. On the other hand, Swaminathan and her team came to a different conclusion after studying six novel Ru(II)-p-cymene complexes with various acylthiourea ligands against A549 and A549cisR cancer cell lines, as in this case longer hydrocarbon chain improves the cytotoxicity⁴⁶. Furthermore, in the literature, the copper(II) complexes with phen and alkyl chains with different lengths as ligands show the same pattern⁴⁷. Interestingly, Ronald Gust and co-workers showed that cytotoxic activity of resulting compounds not always depend on hydrocarbon chain length. They proved that elongation of the spacer by one methylene group of Zeise's salt derivatives increased their cytotoxicity, but further elongation slightly reduced the activity resulting compounds⁴⁸. The correlation between the role of the metal and its chemical environment has therefore led to the synthesis of compounds with interesting pharmacokinetics; endowed with several biologically active functional structures capable of directing different mechanisms of action. The properties manifested by these compounds and, in particular by ruthenium and iridium, suggest a feasible future applicability. Therefore, this work shall be a useful tool for

understanding the mechanisms of distribution, metabolism, and the role of these molecules in treating cancer pathologies, as a starting point for the optimization of new and more efficient drugs.

2. Results and Discussion

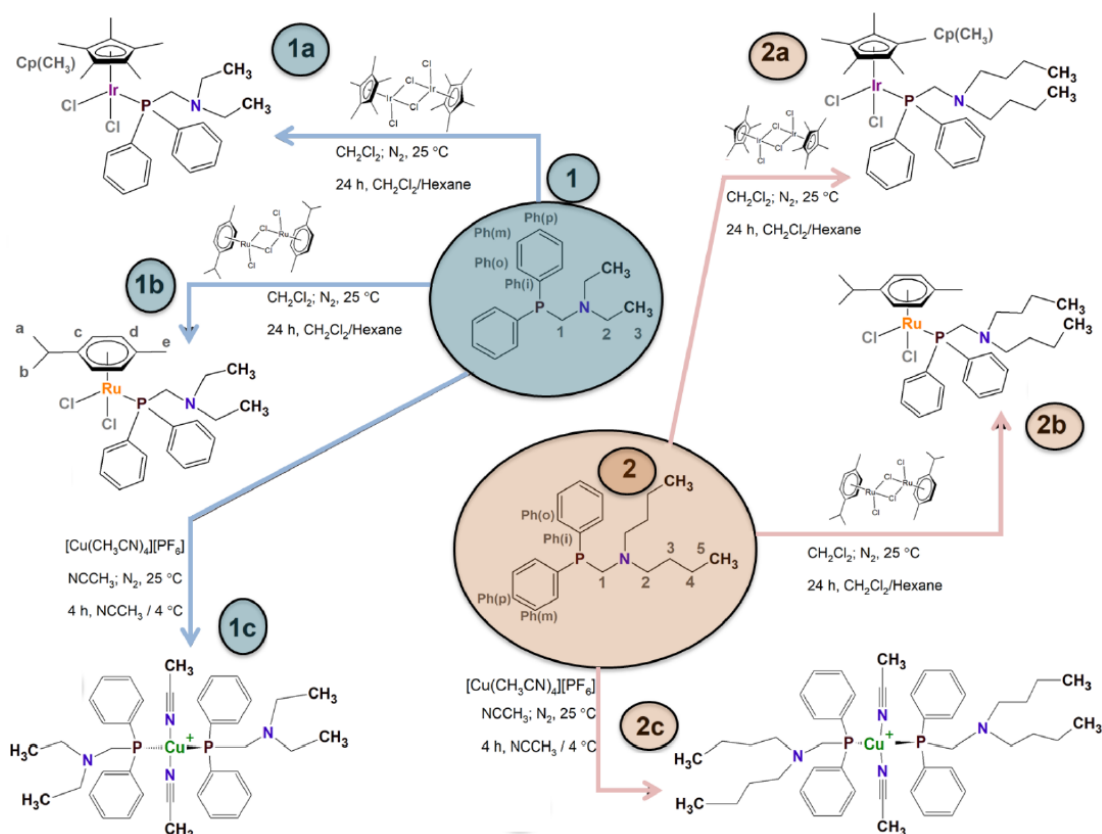
2.1. Synthesis

All syntheses were carried out under an atmosphere of dry oxygen-free dinitrogen, using standard Schlenk techniques or a glove box. The ligands $\text{Ph}_2\text{PCH}_2(\text{CH}_2\text{CH}_3)_2$ (**1**) and $\text{Ph}_2\text{PCH}_2(\text{CH}_2\text{CH}_2\text{CH}_2\text{CH}_3)_2$ (**2**) (Scheme 2) are extremely sensitive and all reaction were performed in nitrogen atmosphere. Synthetic routes of iridium(III) complexes: $\text{Ir}(\eta^5\text{-Cp}^*)\text{Cl}_2\text{Ph}_2\text{PCH}_2(\text{CH}_2\text{CH}_3)_2$ (**1a**), $\text{Ir}(\eta^5\text{-Cp}^*)\text{Cl}_2\text{Ph}_2\text{PCH}_2(\text{CH}_2\text{CH}_2\text{CH}_2\text{CH}_3)_2$ (**2a**) (Cp^* : pentamethylcyclopentadienyl); ruthenium(II) complexes: $\text{Ru}(\eta^6\text{-p-cymene})\text{Cl}_2\text{Ph}_2\text{PCH}_2(\text{CH}_2\text{CH}_3)_2$ (**1b**), $\text{Ru}(\eta^6\text{-p-cymene})\text{Cl}_2\text{Ph}_2\text{PCH}_2(\text{CH}_2\text{CH}_2\text{CH}_2\text{CH}_3)_2$ (**2b**) and copper(I) complexes: $[\text{Cu}(\text{CH}_3\text{CN})_2(\text{Ph}_2\text{PCH}_2(\text{CH}_2\text{CH}_3)_2)_2]$ (**1c**), $[\text{Cu}(\text{CH}_3\text{CN})_2(\text{Ph}_2\text{PCH}_2(\text{CH}_2\text{CH}_2\text{CH}_2\text{CH}_3)_2)_2]$ (**2c**) are presented in Scheme 3.



Scheme 2. Schematic view of the phosphine (**1**, **2**) and synthetic routes.

The copper(I) complexes were found to be non-air stable unlike Ru(II) and Ir(III) complexes. Oxidation of copper(I) to copper(II) was observed within 12 h using UVVis spectroscopy (Figure 1) that was additionally conformed by color of the copper(I) inorganic compound solution changing from transparent to green. Additionally, oxidation of phosphines ligands (**1**, **2**) was observed. It is worth mentioning that copper(I) ions can easily undergo oxidation processes⁴⁹. The instability of copper(I) complexes prevented us from evaluating their biological activity.



Scheme 3. Schematic view of the Ir(III), Ru(II), Cu(I) complexes and synthetic routes.

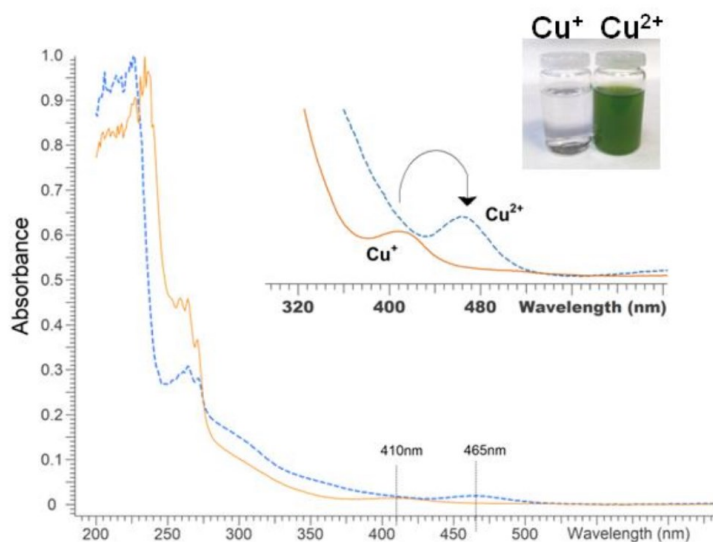


Fig. 1 UV-Vis spectra for copper(I) complex **1c** registered after 0 h (dotted line, transparent colorless solution) and 12 h (solid line, green solution).

All compounds are soluble in polar solvents such as dichloromethane and acetone, but insoluble in non-polar solvents such as pentane and hexane. The analytical data of all the copper(I), ruthenium(II), and iridium(III) complexes are in good agreement with the molecular formula proposed. The target complexes were characterized by NMR spectra, ESI(+)-MS, and elemental analysis. These analytical and spectral data confirmed the stoichiometry of new complexes.

2.2. Structural Analysis of Cu(I), Ru(II), and Ir(III) Complexes

All phosphines $\text{Ph}_2\text{PCH}_2\text{N}(\text{CH}_2\text{CH}_3)_2$ (**1**), $\text{Ph}_2\text{PCH}_2\text{N}(\text{CH}_2\text{CH}_2\text{CH}_2\text{CH}_3)_2$ (**2**), and Ir(III) (**1a**, **2a**); Ru(II) (**1b**, **2b**) and Cu(I) (**1c**, **2c**) complexes were precisely characterized by 1D NMR techniques (^1H NMR, $^{31}\text{P}\{^1\text{H}\}$ NMR) (Figure 2, Table S1, Figures S1–S9, Supplementary Material), and mass spectrometry (Figures S10–S23, Supplementary Material). The application of these techniques allowed determining the structures of the complexes in solution under atmospheric oxygen.

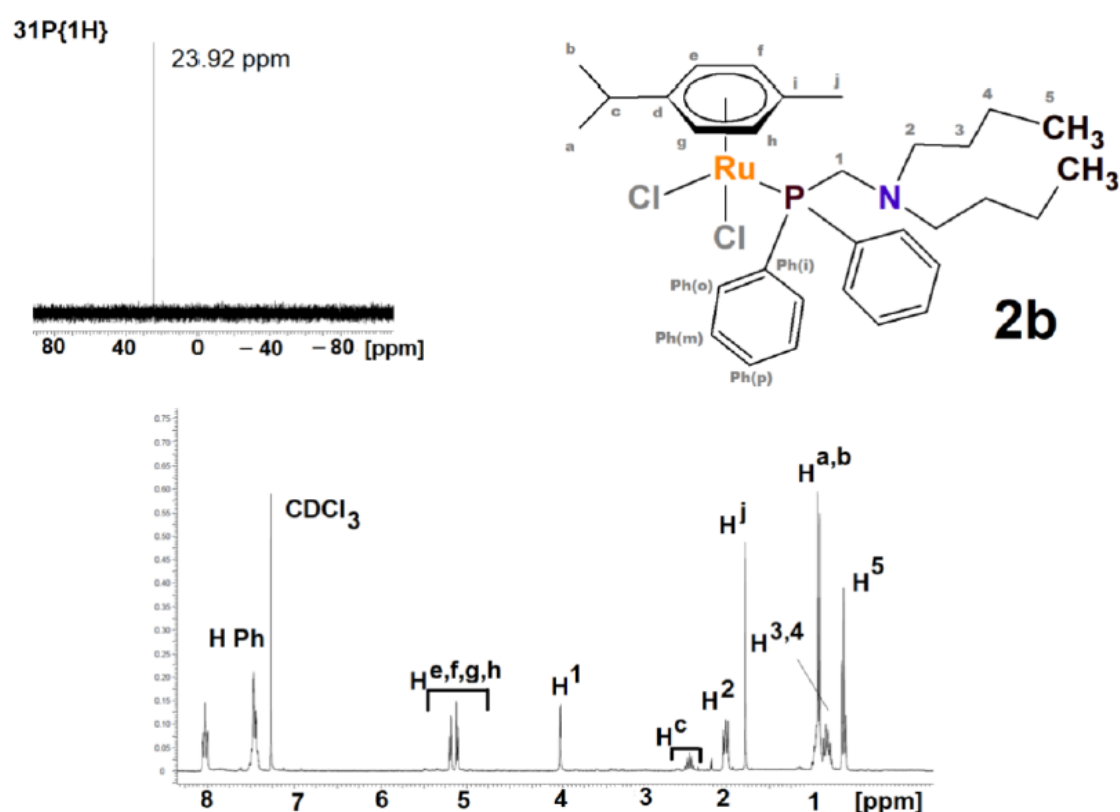


Fig. 2 $^{31}\text{P}\{^1\text{H}\}$ and ^1H NMR spectra (298 K, DMSO) of the **2b**.

The $^{31}\text{P}\{^1\text{H}\}$ NMR analysis is a significant method for preliminary determination of sample purity and it was applied to verify if the product of synthesis is the desired one (Supplementary Materials, Table S1). The signal of uncoordinated phosphines is situated in the negative part of spectrum (**1**: -27.68 ppm and **2**: -

26.72 ppm) and undergoes a downfield shift upon coordination (**1a**: -1.78 ppm; **1b**: 24.32 ppm; **1c**: -14.49 ppm, **2a**: -2.01 ppm, **2b**: 23.92 ppm (Figure 2) and **2c**: -13.07 ppm). Importantly, the absence of other signals in the spectra confirms that coordination compound is the only one product of synthesis, free both from uncoordinated phosphine, or other phosphine derivatives (e.g., phosphane oxides Supplementary Material, Table S1).

As expected, the biggest changes in the ^1H NMR spectra (Supplementary Material, Table S1 and Figures S1–S9) upon the complexation process were observed for the atoms protons undergo an upfield shift (except signals of ^1H for all complex–downfield shift) independently of the type of metal ion (Cu(I), Ir(III), and Ru(II)) and phosphine ligand (**1** or **2**). This might be related to the electron density increase around ligands caused by the formation of complex compounds. It is worth mentioning that after complexation, the variation of the chemical shifts of (PPh₂CH₂-) signals for Ir(III) and Ru(II) complexes compared to the free ligands is larger than those observed for Cu compounds. This means that both phosphine ligands are bounded via phosphorus atom much stronger to iridium and ruthenium ions compared to copper complexes and likely related to their instability. These observations are confirmed by UV-Vis data (described above) showing copper(I) to copper(II) oxidation within a few hours. According to the neutral character of Ir(III) complexes **1a** and **2a**, ESI-MS analysis confirmed the molecular ion peaks $[\text{M} + \text{H}]^+$ in the positive ion modality at m/z 670.20 respectively. Less abundant peaks corresponding to $[\text{M} - \text{Cl}]^+$ and $[\text{M} - \text{Cl} - \text{phosphine}]^+$ ions were also recorded. In addition, loss of phosphine ligand and one chlorine ion gives the product ion at m/z 404.08, which rearranges with addition of an acetonitrile in both mass spectra of the complexes. Ru(II) complexes **1b** and **2b** molecular ion peaks $[\text{M} + \text{H}]^+$ showed almost identical ESI(+) spectra giving the molecular ion peaks $[\text{M} + \text{H}]^+$ at m/z 578.12 and 634.18, respectively. Regarding copper(I) compounds (**1c** and **2c**), the predominant peak in the ESI(+) full spectrum indicates that in solution the metal coordination environment of complexes rearranged due to the addition of ligand phosphine, with the simultaneous loss of the coordinated acetonitrile molecule. These results indicate the formation of mixed-ligand complexes. A peak due to the parent cluster ion of complex **1c** and **2c** was found at m/z 375.11 and 431.17, respectively. This could be identified with fragment ions of the general formula $[\text{Cu-phosphine-CH}_3\text{CN}]^+$.

2.3. Oxidative Plasmid DNA Degradation

The ability of the phosphine ligands (**1**) and (**2**), and of the corresponding iridium(III) complexes (**1a**), (**2a**); ruthenium(II) complexes: (**1b**), (**2b**) as well as of dibutylamine and diethylamine to induce single or double-strand breaks in plasmid DNA was tested in the pBR322 plasmid (C = 0.5 mg/mL) (Supplementary Materials Figures S24–S27). DNA is a common molecular target of anticancer drugs. One of the ways of action of these substances is intercalation into DNA and degradation of its structure⁵⁰. Understanding the mechanism of action of drugs plays a significant role in drug design due to the desire to obtain less toxic

substances with greater potency⁵¹. The ability of studied compounds to induce single- and/or double strand damage to DNA was tested using gel electrophoresis of pBR322 plasmid, which naturally occurs as a covalently closed superhelical form (form I). The process of DNA degradation can lead to the formation of both the relaxed/nicked form (form II) and linear form (form III)⁵². The degree of DNA degradation was determined in a wide range of concentrations (from 2 to 1000 μM). The obtained gel electrophoresis results show that regardless of used concentrations, none of the tested compounds caused DNA degradation. It indicates that studied compounds do not interact with DNA and their mechanism of action is different from cisplatin, the mode of action by interacting with the DNA represents one major reason for the severity of the side effects⁵³. Due to the lack of DNA degradation, tested compounds can probably cause fewer side effects than cisplatin. This probably makes them a safe choice as potential cancer therapeutics. Hydrogen peroxide (H_2O_2) is a source of hydroxyl radicals and a strong DNA oxidant in the presence of transition metal ions and their complexes⁵⁴⁻⁵⁵. Gel electrophoresis can determine the ability of reactive oxygen species (ROS) to cause damage to plasmid DNA. In order to identify a given type of ROS formed by the complexes in the presence of H_2O_2 , gel electrophoresis with the specific quenchers such as: DMSO (effective $\cdot\text{OH}$ scavenger)⁵⁶ and NaN_3 (effective $^1\text{O}_2$ scavenger)⁵⁷ was performed. The studied complexes (**1a**, **1b**, **2b**, **2b**), in the presence of H_2O_2 , are capable of causing DNA single-strand breaks and without causing double-strand breaks. Furthermore, the obtained results indicate that ruthenium complexes in the presence of hydrogen peroxide cause greater changes in the plasmid structure than iridium complexes (Supplementary Materials, Figure S27, lanes 7 and 15 compared to lanes 3 and 11). Partial protection against the formation of the nicked form of DNA was noticed after adding DMSO or NaN_3 to the studied complexes in the presence of H_2O_2 (Supplementary Material, Figure S27.). This means that the tested ruthenium and iridium complexes are able to form moderate amounts of the hydroxyl radical and singlet oxygen. Furthermore, cyclic voltammetry (CV) was studied to precisely understand the redox activity of the studied complexes (i.e., ROS production, vide supra). Both iridium(III) and ruthenium(II) complexes manifest a similar electrochemical behavior, irrespective of the different substituents of the amine group (Figure 3). The cyclic voltammetry of all these mononuclear complexes, independently of the nature of the metal, reveal a main irreversible reductive wave centered at ca. -1.3 V vs. Ag/Ag^+ , which is the envelope of several irreversible processes beginning at ca. -0.8 V vs. Ag/Ag^+ , and are thus assigned to the phosphine ligand electro activity. In the case of the iridium complexes, and differently from the Ru(II) compounds herein considered, a comparatively small irreversible wave centered at about -1.0 V vs. Ag/Ag^+ , (peak 2 in Figure 1, B) separated well from the main peak at -1.3 V vs. Ag/Ag^+ (peak 1 in Figure 1, left) is also observed.

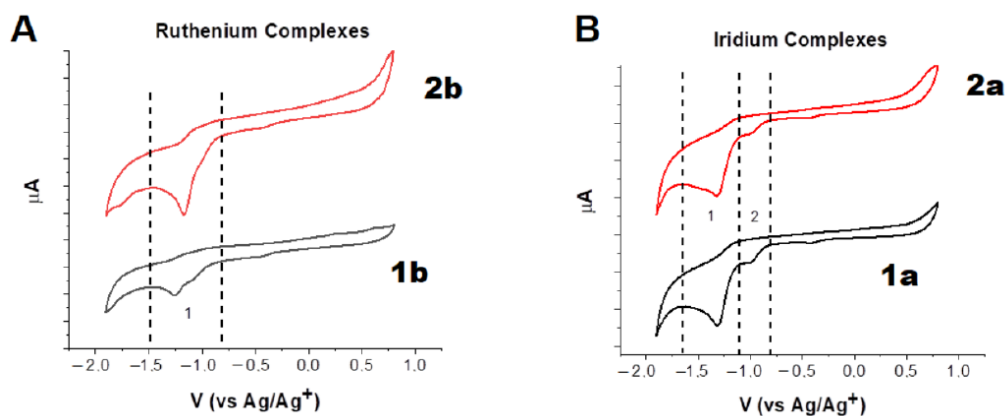


Fig. 3 Cyclic voltammeteries of (A) **2b** and **1b** in DMF + TBACl 0.1 M (vs. Ag/Ag⁺, scan rate 5mV/s) and (B) **2a** and **1a** in DMF + TBACl 0.1 M (vs. Ag/Ag⁺, scan rate 50 mV/s).

2.4. In Vitro Anticancer Investigation

2.4.1. Determination of IC₅₀ and Partition Coefficients (LogP) Values

The lipophilicity of the potential drug has been shown to strongly influence the compounds' efficacy. The logP value (oil/water partition coefficient) is well established to predict the biological activity of drugs and other biologically active compounds. In general, in the increase in lipophilicity, the biological activity of compounds increases because the affinity of substances with biological membranes and permeability is better, leading to better access to the site of action in the body. Nevertheless, this increase has to be controlled because high lipophilicity diminishes aqueous solubility, and consequently, the compound bioavailability. The more lipophilic drug may be may not be ideal for penetration through biological barriers as well as be accumulated in fatty tissue and difficult to excrete, leading to possible systemic toxicity⁵⁸⁻⁵⁹. Thus, the balance between hydrophilicity/lipophilicity of drug candidates is crucial in designing the therapeutic procedure with the selected drug candidate, its application route, and determines the interaction with the potential target^{58,60-61}. With the increase in lipophilicity, the biological activity of compounds increases because the affinity of substances with biological membranes and permeability is better, leading to better access to the site of action in the body. At the same time, a further increase in lipophilicity causes an increase in the affinity for lipids and impedes the transport of molecules of the compound through the water phase, which results in its selective absorption in biological membranes. The logP values for synthesized Ir(III) (**1a** and **2a**) and Ru(II) (**1b** and **2b**) complexes were determined and summarized in Table 1. The logP values of these complexes range between 3 and 4, which confirm their

lipophilic nature. The longer the bicarbonate chain, the higher the logP value for the tested compounds. The effect of logP value on the bioavailability of cytostatic drugs can be seen in the performed biological studies and can diminish their in vitro availability.

	MCF-7	Du-145	A 549	PANC-1	HaCaT	Experimental LogP
dibutylamine	>1000	>1000	>1000	>1000	>1000	nd
diethylamine	>1000	>1000	>1000	>1000	>1000	nd
1	192 ± 20	86 ± 6	183 ± 12	185 ± 12	490 ± 12	nd
2	285 ± 11	57 ± 4	158 ± 11	142 ± 20	448 ± 25	nd
1a	85 ± 8	19 ± 3	12 ± 3	91 ± 13	320 ± 19	3.03
2a	56 ± 6	13 ± 2	16 ± 3	85 ± 16	302 ± 22	4.0
1b	145 ± 15	23 ± 2	10 ± 1	128 ± 14	303 ± 20	3.1
2b	121 ± 20	17 ± 3	14 ± 2	112 ± 18	347 ± 25	3.84
Cisplatin	64 ± 4	50 ± 2	11 ± 3	79 ± 5	102 ± 2	nd.

nd-not determined.

Tab. 1 IC₅₀ (μM) values of the investigated complexes toward the selected cancer cell lines for 72 h and logPo/w. Data are given as mean SD of 3 independent experiments (N = 3).

Moreover, to investigate the activity of synthesized complexes as potential anticancer agents, their cytotoxicity toward a series of human cancer cell lines and a non-cancer cell line (HaCaT) was evaluated using the MTT assay. The IC₅₀ values (the concentration at which 50% of cell growth is inhibited) for these compounds (after 24, 48, and 72 h) against a set of cells are summarized in Table 1 and Supplementary Materials Tables S2 and S3. In addition, we also determined the cytotoxic activity of free ligands toward selected cancer cells. As expected, free ligands show significantly lower cytotoxic activity than prepared metal complexes after all investigated incubation times (24, 48, and 72 h). However, this effect depends on the cell line. The complexes are about ten-fold more active than the phosphine ligands in A549 cells, while the ratio is about three to four in Du-145 cells, about two in MCF-7 cells, less than two in PANC-1 cells and about 0.6 in HaCaT cells. The best values of cytotoxic activity of compounds have been obtained after 72 h of cell incubation. Additionally, synthesized complexes had high sensitivity to A549 cells, so this cell line was selected as the research subject for antitumor activity.

2.4.2. Cellular Accumulation

It has been reported that the cellular uptake efficacy of a compound is affected by many factors, such as lipophilicity⁶²⁻⁶⁴. Synthesized complexes indicate blue fluorescence. Thus, their detection using fluorescence microscopy is possible. For this purpose, A549 (human lung adenocarcinoma epithelial) cells were

incubated with Ir(III) complexes (5 μM) for 24 h and analyzed. Phalloidin was co-incubated with Ir(III) complexes to determine subcellular localization further. The complexes appeared as blue fluorescence, whereas cytoskeleton labeled with Phalloidin-FITC exhibited green fluorescence. As Figure 4 depicts, the blue fluorescence of complexes and the green fluorescence of phalloidin overlapped, indicating that the complexes were mainly accumulated in the nucleus and cytoplasm. Fluorescence microscopic images show that both **1a** (5 μM) and **1b** (5 μM) can penetrate A549 cells (Figure 4). Nevertheless, in the case of **1a** Ir(III) complex, we observe the signal in whole (retain within the cytoplasm) cells with relative higher intensity in the nuclei (Figure 4A). Ru(II) complex **1b** localize mainly in nuclei, and the fluorescence in the cytoplasm is negligible (Figure 4B).

2.4.3. Cell Death Mechanisms

Based on obtained results, it may be concluded that cell death mechanisms after treatment with **1a** differ from those induced by **1b**. Apoptosis induced by Ir(III) or Ru(II) complexes is not very obvious at a relatively lower concentration (1 μM). At a concentration of $>5 \mu\text{M}$, after the treatment with Ir(III) compounds, the percentage of late apoptotic cells increases from up to 60%. For Ru(II) compounds treated cells, the lower toxicity (more live cells) and mainly apoptotic cells are observed (up to 58%). In the case of **1a**, increasing concentration is accompanied by an increase of late apoptosis. The use of 5 and 10 μM induce more apoptosis than **1a** at 1 μM , and more cells remain in the late apoptosis stage than early apoptosis. It may suggest that early apoptotic cells can become late apoptotic cells quickly and the plasma membrane of these cells becomes permeabilized. After the treatment with the highest concentration (50 μM), ca. 15% of stained cells are necrotic cells.

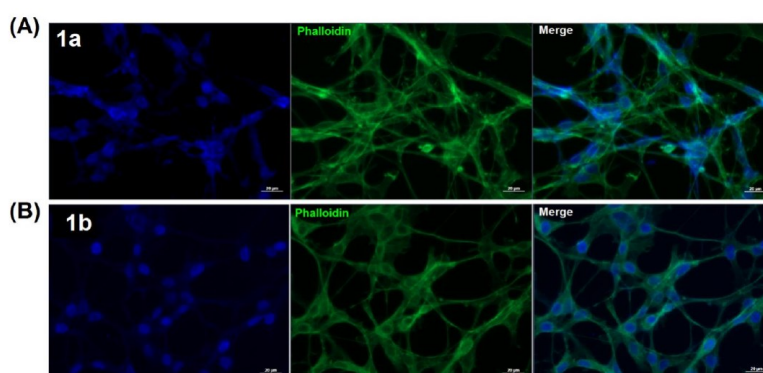
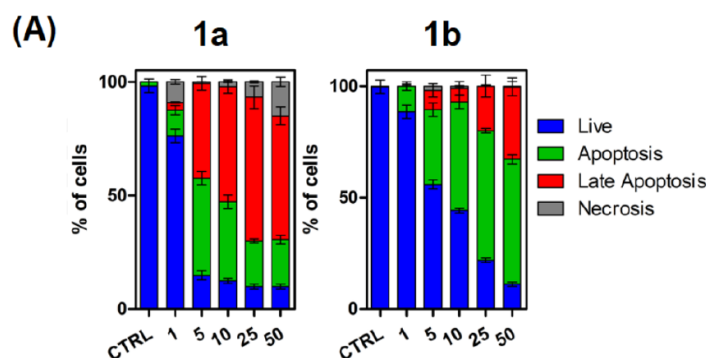


Fig. 4 Accumulation of (A) Ir(III) (**1a**) and (B) Ru(II) (**1b**) in A549 cells. Green fluorescence phalloidin, blue fluorescence-tested compounds.

Analyzing cell death induced by **1b**, it can be seen that the analysis revealed that the treatment with each concentration resulted in more percentages of early apoptotic cells. After the treatment with a high concentration (50 μ M), more late-apoptotic cells can be observed (30%). Nevertheless, there is significantly less population than after treatment with **1a**, where the late apoptosis is a major mechanism of death (up to 55% of AnnexinV-FITC positive and PI-positive cells). Interestingly, almost no cells that died via the necrotic pathway may be detected. The increase in concentration accompanied by the extent of apoptosis seems to be favorable because agents that induce apoptosis directly would overcome many of the problems observed with existing drugs and, as a result, have great therapeutic potential. Apoptosis is preferable to necrosis since it is a particularly efficient mode of cell death that does not produce inflammation and damage to the surrounding normal tissue. Moreover, agents that induce apoptosis directly should be less mutagenic than existing drugs and, because they engage the program further downstream, be less prone to resistance⁶⁵.

The cell death induced by selected Ir(III) and Ru(II) complexes was assessed using Annexin V-FITC/PI double staining. Based on this assay the differentiation of the following cells population was possible: viable cells (Annexin-FITC negative, PI negative), apoptotic cells (Annexin-FITC positive, PI negative), late apoptotic cells (Annexin-FITC positive and PI positive), and necrotic cells (Annexin-FITC negative, PI positive). Treatment of A549 cells with Ir(III) or Ru(II) complexes leads to a dose-dependent increase in the percentage of cells in each phase (Figure 5). Apoptosis induced by Ir(III) or Ru(II) complexes is not very obvious at a relatively lower concentration (1 μ M). At a concentration of >5 μ M, after the treatment with Ir(III) compounds, the percentage of late apoptotic cells increases from up to 60%. For Ru(II) compounds treated cells, the lower toxicity (more live cells) and mainly apoptotic cells are observed (up to 58%). The results reveal that these complexes can induce apoptosis, displaying a similar apoptotic effect, which occurs earlier for Ir(III) compound. Interestingly, the length of the carbon chain does not influence the activity of the resulting complexes.



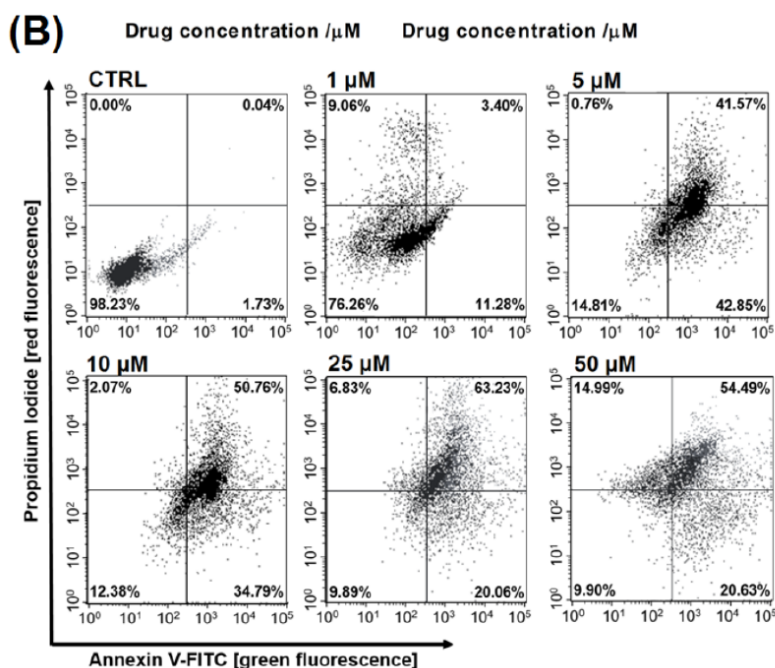


Fig. 5 Cell death mechanisms (A) Annexin V-FITC/PI double staining of A549 cells treated with Ir(III) (**1a**) and Ru(II) (**1b**) at the indicated concentrations for 24 h. (B) Representative histograms showing cell death mechanisms in response to Ir(III) (**1a**) treatment.

2.4.4. Induction of Cell Cycle Arrest

The activity of studied complexes may also be associated with a disturbance of cell cycle progression, proliferation, and development. According to the literature, cell cycle arrest is commonly observed in many metal-based complex antitumor drugs⁶⁶. Meanwhile, the anticancer activity of many anticancer complexes has been associated with cell cycle disturbances⁶⁷. Antitumor drugs induce cell cycle arrest by inhibiting DNA synthesis and enhancing DNA damage, ultimately leading cancer cells to apoptosis. We further studied the influence of Ir(III) and Ru(II) complexes on cell cycle distribution. Synchronized A549 cells were treated with Ir(III) (**1a**, **2a**) or Ru(II) (**1b**, **2b**) at various concentrations for 24 h. Cells were stained with propidium iodide (PI) and analyzed by flow cytometry. The result reveals that both compounds can elicit cell cycle arrest at the S stage at lower concentrations (up to 10 μM), Figure 6. An arrest in S-phase implies that the cell cannot duplicate its DNA. Other authors recently reported a similar effect for iridium(III)polypyridyl complexes⁶⁸⁻⁶⁹. Moreover, the percentage of the G2/M population also increases. However, higher doses (>10 μM) of Ir(III) complexes can enhance G0/G1-phase arrest. These results indicate that **1a** and **1b** elicit concentration-dependent cell cycle perturbations.

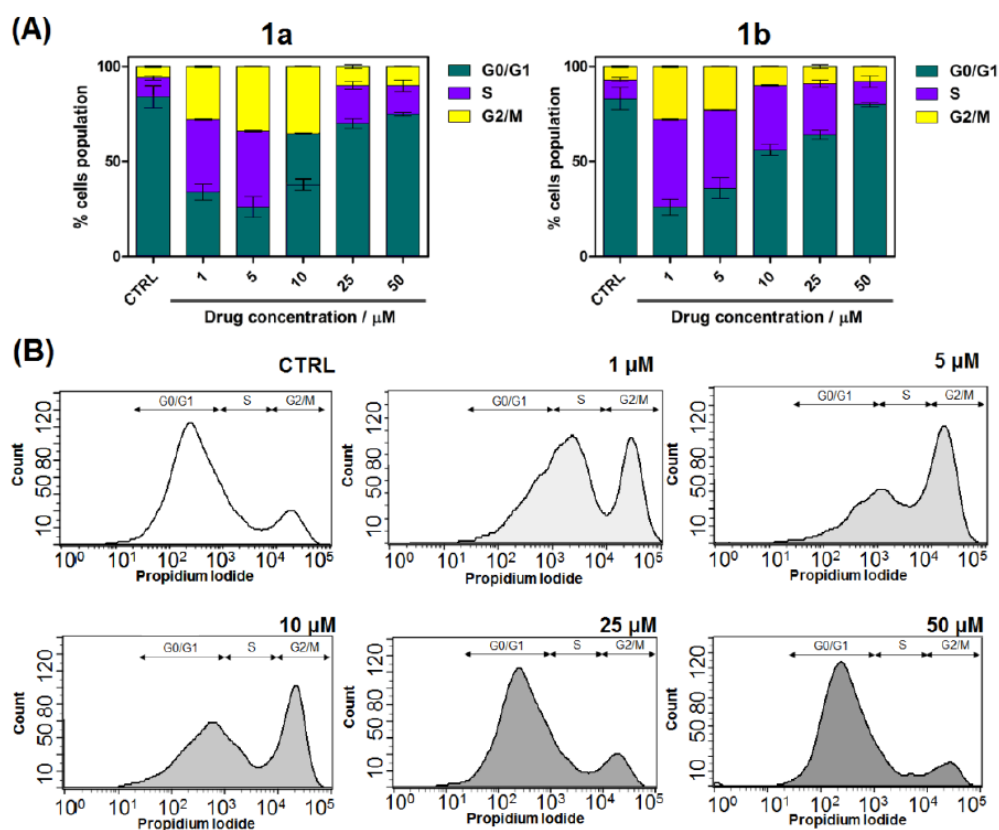


Fig. 6 (A) Cell cycle analysis by PI staining after A549 cells were treated with Ir(III) and Ru(II) at the indicated concentrations for 24 h. (B) Representative histograms showing cell cycle changes in response to Ir(III) treatment.

2.4.5. Anticancer Activity in 3D Tumor Spheroids

Based on the promising results in the 2D cell culture, we also examined the anticancer activity of selected Ir(III) and Ru(II) complexes in the 3D A549 spheroid culture. The use of 3D spheroids culture provides a more accurate model of the in vivo conditions mimicking the solid tumor growth environment⁷⁰. The therapeutic potential of the synthesized Ir(III) and Ru(II) compounds towards 3D spheroids was demonstrated by simultaneous Live/Dead fluorescence staining, providing the distribution of dead cells and cytotoxicity information (Figure 7). It may be seen that Ir(III) more significantly reduces the viability of 3D A549 spheroids, with huge morphology destruction. Nevertheless, the Ru(II) complex is active and leads to the destroyed spheroid structure. In contrast, the untreated spheroids retained their normal morphology and structure and dead cells were not observed.

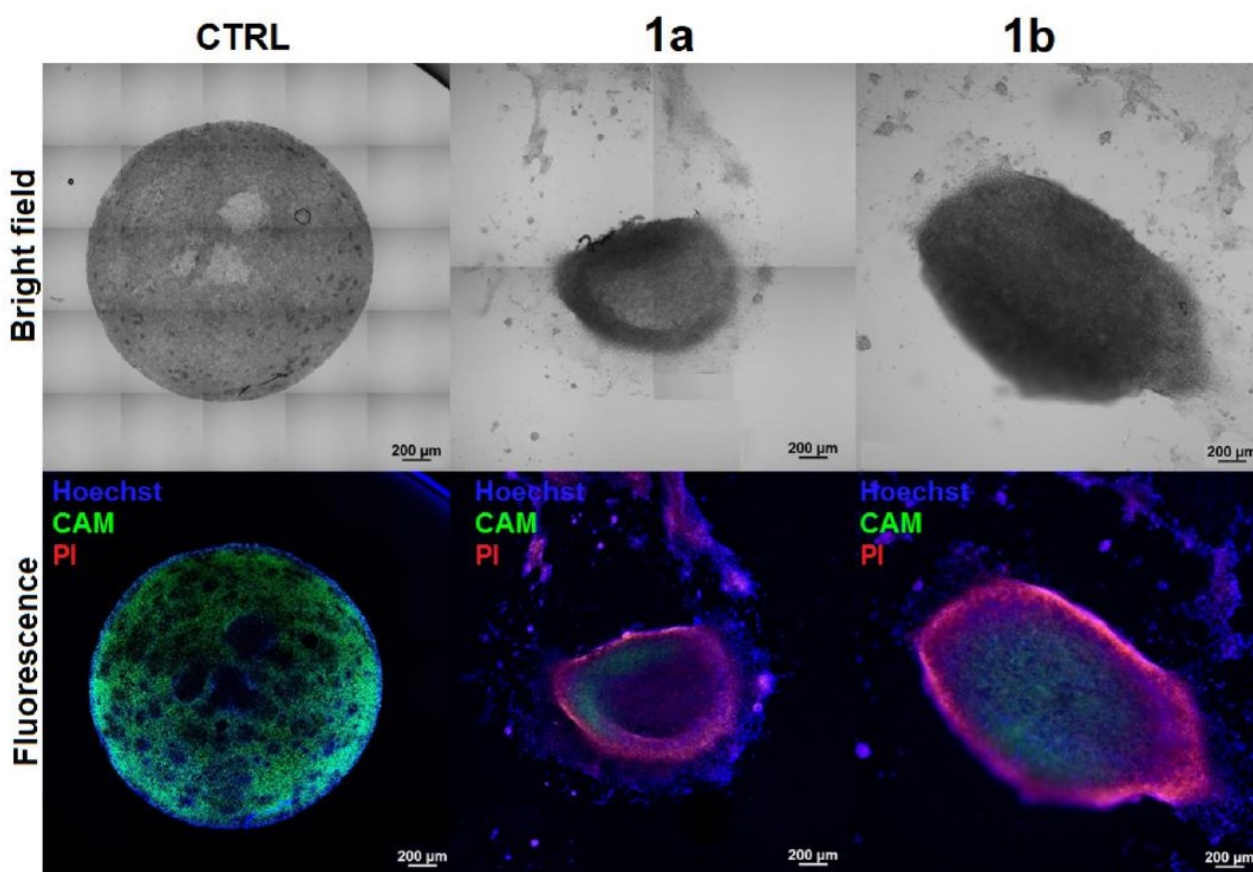


Fig. 7 The cytotoxicity of Ir(III) **1a** and Ru(II) **1b** complexes against A549 efficacy against 3D tumor spheroid model.

3. Materials and Methods

3.1. Reagents

All syntheses and operations were carried out under an atmosphere of dry oxygen-free dinitrogen, using standard Schlenk techniques. Starting phosphine salt $\text{PPh}_2(\text{CH}_2\text{OH})_2^+\text{Cl}^-$ was synthesized according to literature procedures⁵⁴. $[\text{Ir}(\eta^5\text{-Cp}^*)\text{Cl}_2]_2$ (>96%) was purchased from ACROS organics (Fisher Scientific; Geel–Belgium). $[\text{Ru}(\eta^6\text{-p-cymene})\text{Cl}_2]_2$ (¹>98%), $[\text{Cu}(\text{CH}_3\text{CN})_4][\text{BF}_4]$ (99.9%) and other reagents and solvent were purchased from Sigma Aldrich–Merck (Darmstadt–Germany).

3.2. Methods

The NMR spectra were recorded on a Bruker AMX 500 spectrometer (at 25 °C) with traces of solvent as an internal reference for ¹H (CDCl₃: 7.26 ppm) and ¹³C{¹H} spectra (CDCl₃: 77.36 ppm) and 85% H₃PO₄ in H₂O as an external standard for ³¹P{¹H}. The signals in the spectra are defined as: s = singlet (*– strongly broadened

signal), d = doublet, dd = doublet of doublets, t = triplet, and m = multiplet. Chemical shifts are reported in ppm and coupling constants are reported in Hz. Elemental analysis was carried out on a Vario EL3 CHN analyzer for C and H, and they were within 0.3% of the theoretical values. Absorption spectra were recorded on a Cary 50 Bio spectrophotometer (Varian Inc., Palo Alto, CA, USA) in the 800–200 nm range.

Mass spectra were collected using a LCQ Fleet ion trap mass spectrometer (Thermo-Scientific, Waltham, Massachusetts, USA) equipped with an ESI source operating in the positive ion mode. Metal complexes were dissolved in chloroform giving ca. 2×10^{-3} M stock solutions. These solutions were subsequently diluted in methanol to obtain ca. 2×10^{-5} M solutions, which were directly infused into the ESI source via a syringe pump at a flow rate of 10 μ L/min. The ions were produced using a spray voltage of 3.5 kV and the entrance capillary temperature was kept at 280 °C. Other instrumental parameters were automatically adjusted to optimize the signal to noise ratio.

3.3. Synthesis

3.3.1. Preparation of $\text{Ph}_2\text{PCH}_2\text{N}(\text{CH}_2\text{CH}_3)_2$ (**1**)

$\text{PPh}_2(\text{CH}_2\text{OH})_2\text{Cl}$ (0.7434 g, 2.63 mmol) was dissolved in 30 mL of methanol and cooled down using a water bath ($T = 5$ °C). Then, a slight excess of NEt_3 (triethylamine; 2.89 mmol) was added. The mixture was stirred, and with time, reached room temperature (RT). After 90 min, $\text{HN}(\text{CH}_2\text{CH}_3)_2$ (0.1923 g, 2.63 mmol) was added dropwise into the mixture (RT). After 1 h of stirring, a clear solution was observed. The mixture was dried under reduced pressure for 3 h. White, crude product was dissolved in water (30 mL; the milky solution was observed) and extracted four times with CHCl_3 (10 mL) using cannula. Chloroform phase was dried under pressure and white solid of (**1**) was formed. $\text{Ph}_2\text{PCH}_2\text{N}(\text{CH}_2\text{CH}_3)_2$ was dissolved in methanol and kept at -18 °C at least for 24 h. After this time, white crystalline solid was formed. It is well soluble in CHCl_3 , DMSO, CH_2Cl_2 , CH_3CN , EtOH, MeOH, and moderately in H_2O . Phosphine ligand is extremely sensitive to oxidation in solution.

Yield: 88%, **Molar mass:** 271.34 g/mol.

Anal. Calc. for $\text{C}_{17}\text{H}_{22}\text{NP}$: C, 75.25; H, 8.17; N, 5.16%. Found: C, 75.23; H, 8.18; N, 5.14%.

^1H NMR (300 MHz, CDCl_3 , 298 K): δ 3.45 (H1, s), 2.79 (H2, q), 1.01 (H3, t).

$^{31}\text{P}\{^1\text{H}\}$ NMR (121 MHz, CDCl_3 , 298 K): δ -27.68.

ESI(+)-MS in CH_3CN , m/z (%): 288.155 [$\text{M}+\text{H}+\text{OH}$] $^+$; 272.156 [$\text{M}+\text{H}$] $^+$; 199.069

[$\text{M}-\text{N}(\text{CH}_2\text{CH}_3)_2$] $^+$.

3.3.2. Preparation of $\text{Ph}_2\text{PCH}_2\text{N}(\text{CH}_2\text{CH}_2\text{CH}_2\text{CH}_3)_2$ (**2**)

$\text{PPh}_2(\text{CH}_2\text{OH})_2\text{Cl}$ (0.6124 g, 2.17 mmol) was dissolved in 25 mL of methanol and cooled down using water bath ($T = 5\text{ }^\circ\text{C}$). Then, a slight excess of NEt_3 (triethylamine; 2.38 mmol) was added. Mixture was stirred and with time reached room temperature (RT). After 70 min, $\text{HN}(\text{CH}_2\text{CH}_2\text{CH}_2\text{CH}_3)_2$ (0.2800 g, 2.17 mmol) was added drop-wise into the mixture (RT). After 2 h of stirring, clear solution was observed. Mixture was dried under reduced pressure. White, crude product was dissolved in deaerated water (30 mL; milky solution was observed) and extracted four times with deaerated CHCl_3 (10 mL) using cannula. Chloroform phase was dried under pressure and white solid of (**2**) was formed. $\text{Ph}_2\text{PCH}_2\text{N}(\text{CH}_2\text{CH}_2\text{CH}_2\text{CH}_3)_2$ was dissolved in acetonitrile and kept in $-18\text{ }^\circ\text{C}$ at least for 48 h. After this time, white crystalline solid were formed. It is well soluble in CHCl_3 , DMSO, CH_2Cl_2 , CH_3CN , EtOH, MeOH, and moderately in H_2O . Phosphine ligand is extremely sensitive to oxidation in solution.

Yield: 88%, **Molar mass:** 327.44 g/mol.

Anal. Calc. for $\text{C}_{21}\text{H}_{30}\text{NP}$: C, 77.03; H, 9.24; N, 4.28%. Found: C, 77.02; H, 9.25; N,

4.26%.

$^1\text{H NMR}$ (300 MHz, CDCl_3 , 298 K): δ 7.25–7.64 (H^{Ph}), 3.48 (H^1 , s), 2.64 (H^2 , d), 1.34–

1.50 (H^3 , m), 1.34–1.50 (H^4 , m), 0.89 (H^5 , t).

$^{31}\text{P}\{^1\text{H}\}\text{NMR}$ (121 MHz, CDCl_3 , 298 K): δ -26.72.

ESI(+)MS in CH_3CN , m/z (%): 465.346 [$\text{M}+\text{H}+\text{N}(\text{CH}_2\text{CHCH}_2)_2+\text{CH}_3\text{CN}$] $^+$; 423.297

[$\text{M}+\text{N}(\text{CH}_2\text{CHCH}_2)_2$] $^+$; 344.218 [$\text{M}+\text{OH}$] $^+$; 326.206 [$\text{M}-\text{H}$] $^+$; 199.068 [$\text{M}-\text{N}(\text{CH}_2\text{CH}_2\text{CH}_2\text{CH}_3)_2$] $^+$.

3.3.3. Preparation of $\text{Ir}(\eta^5\text{-Cp}^*)\text{Cl}_2\text{Ph}_2\text{PCH}_2\text{N}(\text{CH}_2\text{CH}_3)_2$ (**1a**)

Binuclear iridium complex of $[\text{Ir}(\eta^5\text{-Cp}^*)\text{Cl}_2]_2$ (0.2648 g, 0.332 mmol) was added to a solution of $\text{Ph}_2\text{PCH}_2\text{N}(\text{CH}_2\text{CH}_3)_2$ (0.1802 g, 0.664 mmol) in dichloromethane (25 mL). After a few minutes, the cloudy solution became clean and deep red. The mixture was stirred for 24 h and then the solvent was removed under vacuum. Crude **1a** was dissolved in the mixture of CH_2Cl_2 and hexane (V:V 1:1) and after 72 h in $-5\text{ }^\circ\text{C}$ crystalline red solid showed up. $\text{Ir}(\eta^5\text{-Cp}^*)\text{Cl}_2\text{Ph}_2\text{PCH}_2\text{N}(\text{CH}_2\text{CH}_3)_2$ is well soluble in CHCl_3 , CH_2Cl_2 , methanol, DMSO, and mixture of $\text{H}_2\text{O}:\text{DMSO}$ (100:1).

Yield: 78%, **Molar mass:** 669.69 g/mol.

Anal. Calc. for $\text{IrCl}_2\text{C}_{27}\text{H}_{37}\text{PN}$: C, 48.42; H, 5.57; N, 2.09%. Found: C, 48.41; H, 5.59; N, 2.08%.

^1H NMR (300 MHz, CDCl_3 , 298 K): δ 7.24–7.61 (H^{Ph} , m), 4.01 (H^1 , s*), 2.25 (H^2 , s*), 0.72 (H^3 , s*), 1.47 ($\text{HCp}^*(\text{CH}_3)$, s*).

$^{31}\text{P}\{^1\text{H}\}$ NMR (121 MHz, CDCl_3 , 298 K): δ -1.78.

ESI(+) MS in CH_3CN , m/z (%): 670.196 [$\text{M}+\text{H}$]⁺; 634.206 [$\text{M}-\text{Cl}$]⁺; 404.080 [$\text{M}+\text{CH}_2\text{CNHCl}-\text{Ph}_2\text{PCH}_2\text{N}(\text{CH}_2\text{CH}_3)_2$]⁺; 363.053 [$\text{M}-\text{Cl}-\text{Ph}_2\text{PCH}_2\text{N}(\text{CH}_2\text{CH}_3)_2$]⁺.

3.3.4. Preparation of $\text{Ru}(\eta^6\text{-p-cymene})\text{Cl}_2\text{Ph}_2\text{PCH}_2\text{N}(\text{CH}_2\text{CH}_3)_2$ (**1b**)

Binuclear ruthenium complex of $[\text{Ru}(\eta^6\text{-p-cymene})\text{Cl}_2]_2$ (0.2156 g, 0.3521 mmol) was added to a solution of $\text{Ph}_2\text{PCH}_2\text{N}(\text{CH}_2\text{CH}_3)_2$ (0.1911 g, 0.7042 mmol) in dichloromethane (25 mL). After a few minutes, a cloudy solution became clean and orange. The mixture was stirred for 24 h and then the solvent was removed under vacuum. Crude **1b** was dissolved in mixture of CH_2Cl_2 and hexane (V:V 2:1) and kept in $-18\text{ }^\circ\text{C}$ for 72h. After this time, orange crystalline solid showed up. $\text{Ru}(\eta^6\text{-p-cymene})\text{Cl}_2\text{Ph}_2\text{PCH}_2\text{N}(\text{CH}_2\text{CH}_3)_2$ is well soluble in CHCl_3 , CH_2Cl_2 , methanol, DMSO, and mixture of $\text{H}_2\text{O}:\text{DMSO}$ (100:1).

Yield: 79%, **Molar mass:** 577,53 g/mol.

Anal. Calc. for $\text{RuPNC}_{27}\text{H}_{36}\text{Cl}_2$: C, 56.15; H, 6.29; N, 2.42%. Anal. found: C, 56.12; H, 6.31; N, 2.41%

^1H NMR (300 MHz, CDCl_3 , 298 K): δ 7.31–8.02 (H^{Ph} , m), 3.89 (H^1 , s*), 2.19 (H^2 , s*), 1.31 (H^3 , s*), 0.84 ($\text{H}^{\text{a,b}}$, d), 2.97 (6.80) (H^{c} , spt), 5.37 (36.0; 7.0) ($\text{H}^{\text{e,f,h,i}}$, dd), 1.74 (H^{j} , s).

$^{31}\text{P}\{^1\text{H}\}$ NMR (121 MHz, CDCl_3 , 298 K): δ 24.32.

ESI(+) MS in CH_3CN , m/z (%): 578.116 [$\text{M}+\text{H}$]⁺; 542.132 [$\text{M}-\text{Cl}$]⁺; 312.012 [$\text{M}+\text{CH}_3\text{CNHCl}-\text{Ph}_2\text{PCH}_2\text{N}(\text{CH}_2\text{CH}_2\text{CH}_2\text{CH}_3)_2$]⁺.

3.3.5. Preparation of $[\text{Cu}(\text{NCCH}_3)_2(\text{Ph}_2\text{PCH}_2\text{N}(\text{CH}_2\text{CH}_3)_2)_2]+\text{BF}_4$ (**1c**)

Starting copper(I) complex $[\text{Cu}(\text{CH}_3\text{CN})_4][\text{BF}_4]$ (0.4125 g, 1.1067 mmol) was dissolved in 10 mL of deaerated acetonitrile and added to a solution of $\text{Ph}_2\text{PCH}_2\text{N}(\text{CH}_2\text{CH}_3)_2$ (1.2012 g, 4.4269 mmol; dissolved in deaerated

acetonitrile 10 mL). After a few minutes, a cloudy solution became clean and transparent. The mixture was stirred for 10 h and then solvent was concentrated under vacuum and kept in -18 °C for 48 h. After this time, white crystalline solid formed out. $[\text{Cu}(\text{NCCH}_3)_2(\text{Ph}_2\text{PCH}_2(\text{CH}_2\text{CH}_3)_2)_2] + \text{PF}_6^-$ is well soluble in CHCl_3 , CH_2Cl_2 , methanol, DMSO, and mixture of $\text{H}_2\text{O}:\text{DMSO}$ (100:1).

Yield: 67%, **Molar mass:** 775.129 g/mol.

Anal. Calc. for $\text{CuP}_2\text{N}_4\text{C}_{38}\text{H}_{50}\text{PBF}_4$: C, 58.88; H, 6.50; N, 7.23%. **Anal. found:** C,

58.87; H, 6.52; N, 7.21%

^1H NMR (300 MHz, CDCl_3 , 298 K): δ 7.28–7.49 (H^{Ph}), 3.49 (H^1 , s*), 2.20 (H^2 , s*), 0.89

(H^3 , s*), 2.03 ($\text{H}^{\text{acetonitrile}}$, s).

$^{31}\text{P}\{^1\text{H}\}$ NMR (121 MHz, CDCl_3 , 298 K): δ -14.49.

ESI(+)MS in CH_3CN , m/z (%): 775.275 [M]⁺; 621.233 [$\text{M} + \text{OH} - 2\text{H} - (\text{CH}_3\text{CN})_2 - \text{BF}_4^-$]⁺;

605.240 [$\text{M} - \text{H} - (\text{CH}_3\text{CN})_2 - \text{BF}_4^-$]⁺; 375.109 [$\text{M} - \text{H} - \text{PPh}_2\text{CH}_2\text{N}(\text{CH}_2\text{CH}_3)_2 - \text{CH}_3\text{CN} - \text{BF}_4^-$]⁺; 320.030 [$\text{M} - \text{PPh}_2\text{CH}_2\text{N}(\text{CH}_2\text{CH}_3)_2 - \text{CH}_3 - (\text{CH}_3\text{CN})_2 - \text{BF}_4^-$]⁺.

3.3.6. Preparation of $\text{Ir}(\eta^5\text{-Cp}^*)\text{Cl}_2\text{Ph}_2\text{PCH}_2\text{N}(\text{CH}_2\text{CH}_2\text{CH}_2\text{CH}_3)_2$ (**2a**)

Binuclear iridium complex of $[\text{Ir}(\eta^5\text{-Cp}^*)\text{Cl}_2]_2$ (0.2648 g, 0.332 mmol) was added to a solution of $\text{Ph}_2\text{PCH}_2\text{N}(\text{CH}_2\text{CH}_3)_2$ (0.1802 g, 0.664 mmol) in dichloromethane (25 mL). After a few minutes a cloudy solution became clean and deep red. The mixture was stirred for 24 h and then the solvent was removed under vacuum. Crude **1a** was dissolved in the mixture of CH_2Cl_2 and hexane (V:V 1:1) and after 72 h in -5 °C, crystalline red solid showed up. $\text{Ir}(\eta^5\text{-Cp}^*)\text{Cl}_2\text{Ph}_2\text{PCH}_2\text{N}(\text{CH}_2\text{CH}_3)_2$ is well soluble in CHCl_3 , CH_2Cl_2 , methanol, DMSO, and mixture of $\text{H}_2\text{O}:\text{DMSO}$ (100:1).

Yield: 78%, **Molar mass:** 725.79 g/mol.

Anal. Calc. for $\text{IrCl}_2\text{C}_{31}\text{H}_{45}\text{PN}$: C, 51.30; H, 6.25; N, 1.93%. **Found:** C, 51.29; H, 6.27;

N, 1.91%.

NMR (298 K, CDCl_3): $^{31}\text{P}\{^1\text{H}\}$ (ppm): δ 2.01; ^1H (ppm): H^{Ph} 7.30–8.02; H^1 4.02 s; H^2

2.09 s; H^3 0.72–0.98 m; H^4 0.72–0.98 m; H^5 0.71 t; $\text{HCp}^*(\text{CH}_3)$ 1.37 s.

ESI(+)MS in CH_3CN , m/z (%): 726.255 [M]⁺; 690.269 [$\text{M} - \text{Cl}$]⁺; 404.078 [$\text{M} - \text{HCl} - \text{Ph}_2\text{PCH}_2\text{N}(\text{CH}_2\text{CH}_2\text{CH}_2\text{CH}_3)_2 + \text{CH}_2\text{CN}$]⁺; 363.051 [$\text{M} - \text{HCl} - \text{Ph}_2\text{PCH}_2\text{N}(\text{CH}_2\text{CH}_2\text{CH}_2\text{CH}_3)_2$]⁺.

3.3.7. Preparation of Ru(η 6-p-cymene)Cl₂Ph₂PCH₂N(CH₂CH₂CH₂CH₃)₂ (2b)

Binuclear ruthenium complex of [Ru(η 6-p-cymene)Cl₂]₂ (0.2156 g, 0.3521 mmol) was added to a solution of Ph₂PCH₂N(CH₂CH₃)₂ (0.1911 g, 0.7042 mmol) in dichloromethane (25 mL). After a few minutes, a cloudy solution became clean and orange. The mixture was stirred for 24 h and then the solvent was removed under vacuum. Crude 1b was dissolved in mixture of CH₂Cl₂ and hexane (V:V 2:1) and kept at -18 °C for 72 h. After this time, orange crystalline solid showed up. Ru(η 6-p-cymene)Cl₂Ph₂PNCH₂(CH₂CH₃)₂ is well soluble in CHCl₃, CH₂Cl₂, methanol, DMSO, and mixture of H₂O:DMSO (100:1).

Yield: 84%, **Molar mass:** 633,64 g/mol.

Anal. Calc. for RuPNC₃₁H₄₄Cl₂: C, 58.76; H, 6.99; N, 2.21%. **Anal. found:** C, 58.75;

H, 7.01; N, 2.20%

¹H NMR (300 MHz, CDCl₃, 298 K): δ 7.41–8.04 (H^{Ph}), 4.01 (H¹, s), 1.98 (H², s*),

0.70–0.89 (H³, m), 0.70–0.89 (H⁴, m), 0.68 (H⁵, t), 1.08 (H^{a,b,d}), 2.51 (H^c, spt), 5.15 (H^{e,f,h,i},

^dd), 1.75 (H^j, s).

³¹P{¹H}NMR (121 MHz, CDCl₃, 298 K): δ 23.92.

ESI(+)-MS in CH₃CN, m/z (%): 634.177 [M+H]⁺; 598.195 [M-HCl]⁺; 312.013 [M+CH₃

CN+H-Cl--Ph₂PCH₂N(CH₂CH₂CH₂CH₃)₂]⁺.

3.3.8. Preparation of [Cu(NCCH₃)₂(Ph₂PCH₂N(CH₂CH₂CH₂CH₃)₂)]⁺BF₄⁻ (2c)

Starting copper(I) complex [Cu(CH₃CN)₄][BF₄] (0.4125 g, 1.1067 mmol) was dissolved in 10 mL of deaerated acetonitrile and added to a solution of Ph₂PCH₂N(CH₂CH₃)₂ (1.2012 g, 4.4269 mmol; dissolved in deaerated acetonitrile 10 mL). After a few minutes, a cloudy solution became clean and transparent. The mixture was stirred for 10 h and then solvent was concentrated under vacuum and kept at -18 °C for 48 h. After this time, white crystalline solid formed out. [Cu(NCCH₃)₂(Ph₂PCH₂N(CH₂CH₃)₂)]⁺BF₄⁻ is well soluble in CHCl₃, CH₂Cl₂, methanol, DMSO, and mixture of H₂O:DMSO (100:1).

Yield: 73%, **Molar mass:** 827.203 g/mol.

Anal. Calc. for CuP₂N₄C₄₂H₅₄BF₄: C, 60.98; H, 6.58; N, 6.77%. **Anal. found:** C, 60.97;

H, 6.60; N, 6.75%.

^1H NMR (300 MHz, CDCl_3 , 298 K): δ 7.25–7.32 (H^{Ph}), 3.62 (H^1 , s), 2.08 (H^2 , s), 0.82–1.24

(H^3 , m), 0.82–1.24 (H^4 , m), 0.76 (H^5 , t), 2.02 ($\text{H}^{\text{acetonitrile}}$, s).

$^{31}\text{P}\{^1\text{H}\}$ NMR (121 MHz, CDCl_3 , 298 K): δ -13.07.

ESI(+)MS in CH_3CN , m/z (%): 733.363 [$\text{M}+\text{OH}-2\text{H}-(\text{CH}_3\text{CN})_2-\text{BF}_4^-$] $^+$; 717.368 [$\text{M}-\text{H}-(\text{CH}_3\text{CN})_2-\text{BF}_4^-$] $^+$; 431.173 [$\text{M}-\text{H}-\text{PPh}_2\text{CH}_2\text{N}(\text{CH}_2\text{CH}_2\text{CH}_2\text{CH}_3)_2-\text{CH}_3\text{CN}-\text{BF}_4^-$] $^+$; 328.225 [$\text{M}-\text{Cu}-\text{PPh}_2\text{CH}_2\text{N}(\text{CH}_2\text{CH}_2\text{CH}_2\text{CH}_3)_2(\text{CH}_3\text{CN})_2-\text{BF}_4^-$] $^+$.

3.4. Electrochemical Measurements

The Ru(II) and Ir(III) ($C = 0.5$ mM) complexes synthesized, respectively, with two different phosphinic ligands functionalized with ethylamine and butylamine were characterized by cyclic voltammetry analysis using a PGSTAT302N potentiostat-galvanostat, in order to delineate their characteristic redox profile. The analysis was carried out on a single compartment cell with a classical three electrode configuration, a glassy carbon as working, an Ag/Ag^+ electrode as a reference, and platinum thick wire as counter. An electrolytic solution based on DMF + TBACl 0.1 M was adopted with an analyte concentration of 0.5 mM, previously deoxygenated with nitrogen for 15 min before the start of the experiments and continuously for the entire duration of the measures to maintain a constant slight nitrogen back pressure in the cell headspace. Cyclic voltammeteries were performed by scanning clockwise (oxidation first followed by reduction) the potentials included in the electrolyte stability window (identified from +0.8 to -1.9 V vs. Ag/Ag^+) starting from the OCP, open circuit potential, confirmed at +0.2 V vs. Ag/Ag^+ . Each voltammetric profile was dominated by the presence of an intense broad peak present at negative potentials characteristic of the reduction of the metal, minor peaks often not clearly distinguishable from the main metal process were attributed to the activity of the ligand. Due to the high sensitivity to air and relative instability, it was not possible to carry out tests on the similar copper complexes, $\text{CuPPh}_2\text{CH}_2\text{N}(\text{CH}_2\text{CH}_2\text{CH}_2\text{CH}_3)_2$, and $\text{CuPPh}_2\text{CH}_2\text{N}(\text{CH}_2\text{CH}_3)_2$.

3.5. DNA Strand Break Analysis

The ability of **1**, **1a**, **1b**, **2**, **2a**, **2b**, and starting ligands to induce plasmid DNA damage was tested with the pBR322 plasmid ($C = 0.5$ mg/mL). All compounds were dissolved in DMF with/without hydrogen peroxide (H_2O_2 , $C = 50$ μM), dimethyl sulfoxide (DMSO, $C = 1.4$ mM), or sodium azide (NaN_3 , $C = 40$ mM)⁷¹. After incubation for 1 h at 37 μC , reaction mixtures (16 μL) were mixed with 3 μL of loading buffer (bromophenol blue in 30% glycerol) and loaded on 1% agarose gels, containing EB, in TBE buffer (90 Mm Tris borate, 20

mM EDTA, pH = 8.0). Gel electrophoresis was performed at a constant voltage of 120 V for 120 min. The gel was photographed and processed with a Digital Imaging System (Syngen Biotech, Wroclaw, Poland).

3.6. Partition Coefficient

The partition coefficient was determined by the shake-flask method. A small amount of compound was dissolved in 5 mL PBS-saturated n-octanol. The sample was sonicated until all the compound was dissolved. Next, 5 mL of PBS saturated with n-octanol was added and the experiment proceeded as before. The resulting mixture was vortexed for 30 min in horizontal position. The sample was centrifuged for 2 min at 3700 rpm to obtain a phase separation. Next, 2 mL of each phase was taken. The next steps were a 5 min sonication and measurement of absorption spectra of the obtained solutions. The calibration curve was prepared in order to determine the concentration of the tested compounds in individual solutions. It was made using the absorption intensity of the compounds in series dilution solutions in PBS saturated with octanol or octanol saturated with PBS in the concentration range $c = 1\text{--}100$ nM.

3.7. Cell Cultures

MCF7 cell line (human breast adenocarcinoma, morphology: epithelial-like, ATCC: HTB-22) and A549 cell line (human lung adenocarcinoma, morphology: epithelial, ATCC: CCL-185); HaCaT (human keratinocyte) were cultured in Dulbecco's Modified Eagle's Medium (DMEM, Corning, Poland) with phenol red, supplemented with 10% fetal bovine serum (FBS) and with 1% streptomycin/penicillin. Du-145 cell line (human prostate carcinoma); derived from metastatic site: brain was cultured in minimum essential medium (MEM, Corning) with only 10% fetal bovine serum (FBS). Cultures were incubated at 37 °C under a humidified atmosphere containing 5% CO₂. Cells were passaged using a solution containing 0.05% trypsin and 0.5 mM EDTA. All media and other ingredients were purchased from ALAB, Poland.

3.8. Cytotoxic Activity

Since most of the studied compounds are insoluble in aqueous media (Dulbecco's Modified Eagle's Medium or minimum essential medium (MEM, Corning)), therefore, they needed to be pre-dissolved in DMSO for biological tests. DMSO concentration was kept below 1% in each tested concentration of each compound. Cytotoxicity was assessed by MTT assay performed according to the protocols described previously⁵² in the following experimental approaches: 6 h + 24 h, 24 h + 24 h, and 72 h + 24 h. In brief, 5×10^3 per well (0.2 mL) in the two first approaches, while 1×10^4 cells in the case of longer incubation time were seeded in 96 well flat-bottom microtiter plate, were incubated with the tested complexes at various ranges of

concentrations. After an appropriate incubation time of 6, 24, or 72 h, the cells were washed three times with PBS and fresh medium was applied for a further 24 h in each approach. Various compound concentrations (dilutions in proper medium supplemented with 1% FBS) were tested in five replicates and repeated at least three times. Determined values of IC₅₀ (concentration of a drug required to inhibit the growth of 50% of the cells) are given as mean + S.D. (Standard Deviation). IC₅₀ values were determined from the plots of cell viability in the presence of various concentrations of each compound by matching dose–response curves and using the Origin 9.0 software. Furthermore, post-treatment survival assessment of the treated cells was analyzed under an inverted fluorescence microscope (Olympus IC51, Japan) with an excitation filter 470/20 nm. For this, cells were stained with two versatile fluorescence dyes: fluorescein diacetate (FDA, 5 mg/mL) and propidium iodide (PI, 5 mg/mL) in standard conditions in the dark for 20 min. Before visualization, dyes were removed and cells were washed with PBS twice.

3.9. Intracellular Accumulation

The intracellular accumulation of the compound was assessed in the A549 cell line. Before imaging, cells were seeded on microscopic slides at a density of 1x10⁵ cells and were kept at 37 °C with 5% CO₂ humidified atmosphere for 24 h. After being washed with fresh medium, the cells were incubated with 5 μM solution of tested compound in cell medium for 24 h. Next, after being washed with HBSS, the cells were fixed for 10 min in 3.8% PFA and incubated with specific intracellular organelle probes: 200 nM Mito-Tracker green, 1 μg/mL Quinacrine, and 0.25 nM of PhalloidinAtto 488 (Molecular Probes, Invitrogen Life Technologies; Thermo Fisher Scientific, Waltham, MA, USA), diluted in HBSS buffer. After 30 min incubation, at 37 °C, in the dark, the cells were washed with HBSS two times, and the slide was transferred to the microscope stage and cells were visualized under a fluorescent Zeiss Axio Observer microscope. Registered images were analyzed with the Zeiss ZEN software.

3.10. Flow Cytometry

Cell death was quantified using the AnnexinV-FITC/PI double staining kit (Sigma Aldrich). The cells (1x10⁵ per well) were cultured overnight in 12-well plates. Then, cells were treated with tested compounds for 24 h. After this time, cells were passaged, collected by centrifugation, and washed twice in Hank's Balanced Salt Solution (HBBS). The cells were then re-suspended in 500 μL binding buffer and stained with annexin VFITC and PI according to the manufacturer's instructions (Sigma Aldrich). Stained A549 cells were then examined using a Guava® easyCyte™ flow cytometer equipped with a 488 nm laser. The obtained data were analyzed using InCyte software (MerckMillipore, Burlington, MA, USA). The serum starvation protocol was used to synchronize cell cultures. A549 cells were seeded in a 12-well plate in a growth medium with

20% FBS overnight. Then, the cultures were washed by PBS and changed to a serum-free medium. After serum starvation for 24 h, cells were released into the cell cycle by the addition of serum and tested compounds solution for 24 h. The cells were then detached from the plate using trypsin. Then, after washing, they were incubated with 50 g/mL propidium iodide for 15 min in the dark. Cells were analyzed with the Guava® easyCyte™ flow cytometer equipped with a 488 nm laser. The obtained data were analyzed using InCyte Software (MerckMillipore, Burlington, MA, USA).

3.11. Three-Dimensional Culturing In Vitro

Three-dimensional culturing in vitro: For hanging drop formation, the lid from a tissue culture dish was removed and 5×10^5 CT-26 or A549 cells in 10 μ L drops were placed on the bottom of the lid. In each case, the cell suspension was homogeneous and did not contain aggregates, since it determines the size and uniformity of spheroids. Then, the lid was inverted onto the PBS-filled bottom chamber. The cells were cultured in incubators maintained at 37 °C with 5% CO₂ under fully humidified conditions. Once sheets were formed, they were transferred to 96-well plates coated with Geltrex matrix and incubated with a complete growth medium until spheroids were created. The direct effect of compound toxicity was examined on spheroids derived from both CT-26 and A549 cell lines. Twenty-four hours after treatment, the spheroids were stained with Hoechst33342, calcein AM (CAM), and propidium iodide (PI) to estimate the live/dead cells population for one hour, washed, and visualized under a Zeiss LSM 880 confocal microscope (Carl Zeiss, Jena, Germany) with a 63X immersion objective. Images were analyzed by Zeiss ZEN Software.

4. Conclusions

Herein, we present for the first time two novel phosphine ligands, Ph₂PCH₂N(CH₂CH₃)₃ (**1**) and Ph₂PCH₂N(CH₂CH₂CH₂CH₃)₂ (**2**), and six new metal (Cu(I), Ir(III) and Ru(II)) complexes with those ligands: iridium(III) complexes: Ir(η 5-Cp*)Cl₂(**1**) (**1a**), Ir(η 5-Cp*)Cl₂(**2**) (**2a**); ruthenium(II) complexes: Ru(η 6-p-cymene)Cl₂(**1**) (**1b**), Ru(η 6-p-cymene)Cl₂(**2**) (**2b**) and copper(I) complexes: [Cu(CH₃CN)₂(**1**)BF₄] (**1c**), [Cu(CH₃CN)₂(**2**)BF₄] (**2c**). All compounds were precisely characterized by elemental analysis, selected spectroscopic methods (i.e., absorption and NMR), ESI-MS, and electrochemical techniques. It was proven that copper(I) compounds are not stable in the presence of atmospheric oxygen in contrast to iridium and ruthenium compounds. In addition, we have studied cytotoxic effects of Ru(III) and Ir(III) complexes in vitro towards selected cancer cell lines. We demonstrated in vitro that complexes are characterized by lower IC₅₀ values than that of cisplatin. Furthermore, preliminary investigation on the elucidation of action of the selected compounds towards A549 lung cell line allowed us to formulate the following general conclusions:

(i) Complexes can penetrate into A549 cells. (ii) Ru(II) and Ir(III) complexes can induce apoptosis, displaying the similar apoptotic effect, which occurs earlier for Ir(III) compound. (iii) Compounds can elicit cell cycle arrest at S stage at lower concentrations; however, higher doses (>10 μ M) of Ir(III) complexes can enhance G0/G1-phase arrest. (iv) Redox potentials enable efficient ROS generation that causes plasmid DNA degradation, Finally, the therapeutic potential of the synthesized Ir(III) and Ru(II) compounds towards 3D spheroids was demonstrated by simultaneous in situ Live/Dead fluorescence staining, providing the spatial distribution of dead cells and cytotoxicity information. It was proven that Ir(III) more significantly reduces the viability of 3D A549 spheroids, with huge morphology destruction. Importantly, the length of the hydrocarbon chain of phosphine ligands does not influence the cytotoxic activity of resulting complexes. In vitro anticancer effect mostly depends on metal ion type. In our case, inorganic compounds with iridium seem to be much more effective towards cancer cells than ruthenium ones.

References

- [1] Pan, C.; Kang, J.; Hwang, J.S.; Li, J.; Boese, A.C.; Wang, X.; Yang, L.; Boggon, T.J.; Chen, G.Z.; Saba, N.F.; et al. Cisplatin-mediated activation of glucocorticoid receptor induces platinum resistance via MAST1. *Nat. Commun.* **2021**, *12*, 4960.
- [2] Taber, A.; Christensen, E.; Lamy, P.; Nordentoft, I.; Prip, F.; Lindskrog, S.V.; Birkenkamp-Demtröder, K.; Okholm, T.L.H.; Knudsen, M.; Pedersen, J.S.; et al. Molecular correlates of cisplatin-based chemotherapy response in muscle invasive bladder cancer by integrated multi-omics analysis. *Nat. Commun.* **2020**, *11*, 4858.
- [3] Jingwen, B.; Yaochen, L.; Guojun, Z. Cell cycle regulation and anticancer drug discovery. *Cancer Biol. Med.* **2017**, *14*, 348–362.
- [4] Ghosh, S. Cisplatin: The first metal based anticancer drug. *Bioorg. Chem.* **2019**, *88*, 102925.
- [5] Santini, C.; Pellei, M.; Gandin, V.; Porchia, M.; Tisato, F.; Marzano, C. Advances in Copper Complexes as Anticancer Agents. *Chem. Rev.* **2013**, *114*, 815–862.
- [6] Kozieł, S.A.; Lesiów, M.K.; Wojtala, D.; Dyguda-Kazimierowicz, E.; Bieńko, D.; Komarnicka, U. Interaction between DNA, Albumin and Apo-Transferrin and Iridium(III) Complexes with Phosphines Derived from Fluoroquinolones as a Potent Anticancer Drug. *Pharmaceuticals* **2021**, *14*, 685.
- [7] Scattolin, T.; Voloshkin, V.A.; Visentin, F.; Nolan, S.P. A critical review of palladium organometallic anticancer agents. *Cell Rep. Phys. Sci.* **2021**, *2*, 100446.
- [8] Teixeira, R.G.; Belisario, D.C.; Fontrodona, X.; Romero, I.; Tomaz, A.I.; Garcia, M.H.; Riganti, C.; Valente, A. Unprecedented collateral sensitivity for cisplatin-resistant lung cancer cells presented by new ruthenium organometallic compounds. *Inorg. Chem. Front.* **2021**, *8*, 1983–1996.
- [9] Málíková, K.; Masaryk, L.; Štarha, P. Anticancer Half-Sandwich Rhodium(III) Complexes. *Inorganics* **2021**, *9*, 26.
- [10] De Castro, F.; Stefàno, E.; Migoni, D.; Iaconisi, G.N.; Muscella, A.; Marsigliante, S.; Benedetti, M.; Fanizzi, F.P. Synthesis and Evaluation of the Cytotoxic Activity of Water-Soluble Cationic Organometallic Complexes of the Type $[Pt(\text{C}_2\text{H}_4\text{OMe})(L)(\text{Phen})]^+$ ($L = \text{NH}_3, \text{DMSO}$; $\text{Phen} = 1,10\text{-Phenanthroline}$). *Pharmaceutics* **2021**, *13*, 642.
- [11] Casini, A.; Vessières, A.; Meier-Menches, S.M. *Metal-Based Anticancer Agents*; Royal Society of Chemistry: London, UK, 2019.
- [12] Bykowska, A.; Komarnicka, U.K.; Jeżowska-Bojczuk, M.; Kyzioł, A. CuI and CuII complexes with phosphine derivatives of fluoroquinolone antibiotics—A comparative study on the cytotoxic mode of action. *J. Inorg. Biochem.* **2018**, *181*, 1–10.
- [13] Galvez, L.; Ruz, M.; Schwaiger-Haber, M.; El Abiead, Y.; Hermann, G.; Jungwirth, U.; Berger, W.; Keppler, B.K.; Jakupec, M.A.; Koellensperger, G. Preclinical studies on metal based anticancer drugs as enabled by integrated metallomics and metabolomics. *Metallomics* **2019**, *11*, 1716–1728.
- [14] Ott, I.; Gust, R. Non-Platinum Metal Complexes as Anti-cancer Drugs. *Arch. Pharm. Chem. Life Sci.* **2007**, *340*, 117–126.
- [15] Bouché, M.; Hognon, C.; Grandemange, S.; Monari, A.; Gros, P.C. Recent advances in iron-complexes as drug candidates for cancer therapy: Reactivity, mechanism of action and metabolites. *Dalton Trans.* **2020**, *49*, 11451–11466.
- [16] Lee, S.Y.; Kim, C.Y.; Nam, T.-G. Ruthenium Complexes as Anticancer Agents: A Brief History and Perspectives. *Drug Des. Dev. Ther.* **2020**, *ume 14*, 5375–5392.
- [17] Sharma, S.A.; Sudhindra, P.; Roy, N.; Paira, P. Advances in novel iridium (III) based complexes for anticancer applications: A review. *Inorg. Chim. Acta* **2020**, *513*, 119925.
- [18] Wani, W.A.; Baig, U.; Shreaz, S.; Shiekh, R.A.; Iqbal, P.F.; Jameel, E.; Ahmad, A.; Mohd-Setapar, S.H.; Mushtaque; Hun, L.T. Recent advances in iron complexes as potential anticancer agents. *New J. Chem.* **2015**, *40*, 1063–1090.

- [19] Komarnicka, U.K.; Starosta, R.; Płotek, M.; de Almeida, R.F.M.; Jeżowska-Bojczuk, M.; Kyzioł, A. Copper(I) complexes with phosphine derived from sparfloxacin. Part II: A first insight into the cytotoxic action mode. *Dalton Trans.* **2015**, 45, 5052–5063.
- [20] Appleby, M.V.; Walker, P.G.; Pritchard, D.; van Meurs, S.; Booth, C.M.; Robertson, C. Cu(I) diimine complexes as immobilised antibacterial photosensitisers operating in water under visible light. *Mater. Adv.* **2020**, 1, 3417.
- [21] Gizer, S.G.; Sahiner, N. The effect of sulphur on the antibacterial properties of succinic acid-Cu(II) and mercaptosuccinic acid-Cu(II) MOFs. *Inorganica Chim. Acta* **2021**, 528, 120611.
- [22] Chen, F.; Moat, J.; Mcfeely, D.; Clarkson, G.; Hands-Portman, I.J.; Furner-Pardoe, J.P.; Harrison, F.; Dowson, C.G.; Sadler, P.J. Biguanide Iridium(III) Complexes with Potent Antimicrobial Activity. *J. Med. Chem.* **2018**, 61, 7330–7344.
- [23] Bu, S.; Jiang, G.; Jiang, G.; Liu, J.; Lin, X.; Shen, J.; Xiong, Y.; Duan, X.; Wang, J.; Liao, X. Antibacterial activity of ruthenium polypyridyl complexes against *Staphylococcus aureus* and biofilms. *JBIC J. Biol. Inorg. Chem.* **2020**, 25, 747–757.
- [24] Tian, N.; Feng, Y. Fluorination in enhancing photoactivated antibacterial activity of Ru(II) complexes with photo-labile ligands. *RSC Adv.* **2020**, 10, 25364.
- [25] Selvi, G.; Ozdemir, F.A.; Aykutoglu, G.; Özdemir, N.; Serbetçi, Z.; Dinçer, M.; Dayan, O. Synthesis, catalytic, cytotoxic, and antibacterial properties of new Ru(II) and Pd(II) complexes bearing bidentate Schiff base ligand. *Inorg. Nano-Metal Chem.* **2020**, 1697, 51.
- [26] de Paiva, R.E.F.; Neto, A.M.; Santos, I.A.; Jardim, A.C.G.; Corbi, P.P.; Bergamini, F.R.G. What is holding back the development of antiviral metallodrugs? A literature overview and implications for SARS-CoV-2 therapeutics and future viral outbreaks. *Dalton Trans.* **2020**, 49, 16004–16033.
- [27] Chuong, C.; DuChane, C.; Webb, E.; Rai, P.; Marano, J.; Bernier, C.; Merola, J.; Weger-Lucarelli, J. Noble Metal Organometallic Complexes Display Antiviral Activity against SARS-CoV-2. *Viruses* **2021**, 13, 980.
- [28] Nareetsile, F.; Matshwele, J.T.; Ndlovu, S.; Ngaski, M. Transition Metal Complexes with HIV/AIDS Inhibitory Properties. *Chem. Rev. Lett.* **2020**, 3, 140–160.
- [29] Almalki, S.A.; Bawazeer, T.M.; Asghar, B.; Alharbi, A.; Aljohani, M.M.; Khalifa, M.E.; El-Metwaly, N. Synthesis and characterization of new thiazole-based Co(II) and Cu(II) complexes; therapeutic function of thiazole towards COVID-19 in comparing to current antivirals in treatment protocol. *J. Mol. Struct.* **2021**, 1244, 130961.
- [30] Munteanu, A.-C.; Uivarosi, V. Ruthenium Complexes in the Fight against Pathogenic Microorganisms. An Extensive Review. *Pharmaceutics* **2021**, 13, 874.
- [31] Xu, Z.; Wang, D.S.; Yu, X.; Yang, Y.; Wang, D. Tunable Triazole-Phosphine-Copper Catalysts for the Synthesis of 2-Aryl-1H-benzimidazoles from Benzyl Alcohols and Diamines by Acceptorless Dehydrogenation and Borrowing Hydrogen Reactions. *Adv. Synth. Catal.* **2017**, 19, 3332.
- [32] Paunescu, E.; McArthur, S.; Soudani, M.; Scopelliti, R.; Dyson, P.J. Nonsteroidal Anti-inflammatory—Organometallic Anticancer Compounds. *Inorg. Chem.* **2016**, 55, 1788–1808.
- [33] Leung, C.-H.; Lin, S.; Zhong, H.-J.; Ma, D.-L. Metal complexes as potential modulators of inflammatory and autoimmune responses. *Chem. Sci.* **2015**, 6, 871–884.
- [34] Lima, M.A.; Costa, V.A.; Franco, M.A.; de Oliveira, G.P.; Deflon, V.M.; Rocha, F.V. Palladium(II) complexes bearing thiosemicarbazone and phosphines as inhibitors of DNA-Topoisomerase II enzyme: Synthesis, characterizations and biological studies. *Inorg. Chem. Commun.* **2020**, 112, 107708.
- [35] Jarrett, P.S.; Sadler, P.J. Nickel(II) bis(phosphine) complexes. *Inorg. Chem.* **1991**, 30, 2098.
- [36] Mirzadeh, N.; Reddy, T.S.; Bhargava, S.K. Advances in diphosphine ligand-containing gold complexes as anticancer agents. *Co-ord. Chem. Rev.* **2019**, 388, 343–359.
- [37] Marzano, C.; Tisato, F.; Porchia, M.; Pellei, M.; Gandin, V. Chapter 4—Phosphine Copper(I) Complexes as Anticancer Agents: Biological Characterization, Part II. In *Copper(I) Chemistry of Phosphines, Functionalized*

Phosphines and Phosphorus Heterocycles; Elsevier: Amsterdam, The Netherlands, 2019; p. 83. *Pharmaceuticals* **2022**, *15*, 169–21 of 22

[38] Thomas, J.M.; Madarasi, P.K.; Sivasankar, C.; Samuelson, A.G. Chapter 7—Coordination chemistry of copper(I) complexes with bis(phosphine) ligands. In *Copper(I) Chemistry of Phosphines, Functionalized Phosphines and Phosphorus Heterocycles*; Elsevier: Amsterdam, The Netherlands, 2019; p. 165.

[39] Kuchar, J.; Rust, J.; Lehmann, C.W.; Mohr, F. Silver(I) Complexes with Camphorsulfonate and Phosphine Ligands: Structural Diversity and Antibacterial Activity. *Inorg. Chem.* **2020**, *59*, 10557–10568.

[40] Kim, J.H.; Reeder, E.; Parkin, S.; Awuah, S.G. Gold(I/III)-Phosphine Complexes as Potent Antiproliferative Agents. *Sci. Rep.* **2019**, *9*, 12335.

[41] Engelbrecht, Z.; Meijboom, R.; Cronjé, M.J. The ability of silver(I) thiocyanate 4-methoxyphenyl phosphine to induce apoptotic cell death in esophageal cancer cells is correlated to mitochondrial perturbations. *BioMetals* **2018**, *31*, 189–202.

[42] Needham, R.J.; Prokes, I.; Habtemariam, A.; Romero-Canelón, I.; Clarkson, G.J.; Sadler, P.J. NMR studies of group 8 metallodrugs: 187Os-enriched organo-osmium half-sandwich anticancer complex. *Dalton Trans.* **2021**, *50*, 12970–12981.

[43] Du, Q.; Yang, Y.; Guo, L.; Tian, M.; Ge, X.; Tian, Z.; Zhao, L.; Xu, Z.; Li, J.; Liu, Z. Fluorescent half-sandwich phosphinesulfonate iridium(III) and ruthenium(II) complexes as potential lysosome-targeted anticancer agents. *Dyes Pigments* **2019**, *162*, 821.

[44] Kantoury, M.; Moghadam, M.E.; Tarlani, A.A.; Divsalar, A. Structure Effect of Some New Anticancer Pt(II) Complexes of Amino Acid Derivatives with Small Branched or Linear Hydrocarbon Chains on Their DNA Interaction. *Chem. Biol. Drug Des.* **2016**, *88*, 76–87.

[45] Laha, P.; De, U.; Chandra, F.; Dehury, N.; Khullar, S.; Kim, H.S.; Patra, S. Alkyl chain-modified cyclometalated iridium complexes as tunable anticancer and imaging agents. *Dalton Trans.* **2018**, *47*, 15873–15881.

[46] Swaminathan, S.; Haribabu, J.; Subarkhan, M.K.M.; Gayathri, D.; Balakrishnan, N.; Bhuvanesh, N.; Echeverria, C.; Karvembu, R. Impact of aliphatic acyl and aromatic thioamide substituents on the anticancer activity of Ru(II)-p-cymene complexes with acylthiourea ligands—in vitro and in vivo studies. *Dalton Trans.* **2021**, *50*, 16311–16325.

[47] Shi, X.; Chen, Z.; Wang, Y.; Guo, Z.; Wang, X. Hypotoxic copper complexes with potent anti-metastatic and anti-angiogenic activities against cancer cells. *Dalton Trans.* **2018**, *47*, 5049–5054.

[48] Weninger, A.; Baecker, D.; Obermoser, V.; Egger, D.; Wurst, K.; Gust, R. Synthesis and Biological Evaluation of Zeise's Salt Derivatives with Acetylsalicylic Acid Substructure. *Int. J. Mol. Sci.* **2018**, *19*, 1612.

[49] Małeck, J.G.; Maron, A.M.; Palion, J.; Nycz, J.E.; Szala, M. A copper(I) phosphine complex with 5,7-dinitro-2-methylquinolin-8-ol as co-ligand. *Transit. Met. Chem.* **2014**, *39*, 755–762.

[50] Ralph, R.K.; Marshall, B.; Darkin, S. Anti-cancer drugs which intercalate into DNA: How do they act? *Trends Biochem. Sci.* **1983**, *8*, 212–214.

[51] Mukherjee, A.; Sasikala, W.D. *Drug-DNA Intercalation: From Discovery to the Molecular Mechanism*, 1st ed.; Elsevier: Amsterdam, The Netherlands, 2013; Volume 92.

[52] Komarnicka, U.; Starosta, R.; Kyzioł, A.; Płotek, M.; Puchalska, M.; Jeżowska-Bojczuk, M. New copper(II) complexes bearing lomefloxacin motif: Spectroscopic properties, in vitro cytotoxicity and interactions with DNA and human serum albumin. *J. Inorg. Biochem.* **2016**, *165*, 25–35.

[53] Gou, Y.; Huang, G.; Li, J.; Yang, F.; Liang, H. Versatile delivery systems for non-platinum metal-based anticancer therapeutic agents. *Coord. Chem. Rev.* **2021**, *441*, 213975.

[54] Komarnicka, U.K.; Koziel, S.; Zabierowski, P.; Kruszyński, R.; Lesiów, M.K.; Tisato, F.; Porchia, M.; Kyzioł, A. Copper(I) complexes with phosphines P(p-OCH₃-Ph)₂CH₂OH and P(p-OCH₃-Ph)₂CH₂SarGly. Synthesis, multimodal DNA interactions, and prooxidative and in vitro antiproliferative activity. *J. Inorg. Biochem.* **2020**, *203*, 110926.

- [55] Szczepanik, W.; Czarny, A.; Zaczyńska, E.; Jezowska-Bojczuk, M. Preferences of kanamycin A towards copper(II). Effect of the resulting complexes on immunological mediators production by human leukocytes. *J. Inorg. Biochem.* **2004**, *98*, 245–253.
- [56] Marzano, C.; Pellei, M.; Tisato, F.; Santini, C. Copper Complexes as Anticancer Agents. *Anti-Cancer Agents Med. Chem.* **2009**, *9*, 185–211.
- [57] Bancirova, M. Sodium azide as a specific quencher of singlet oxygen during chemiluminescent detection by luminol and Cypridina luciferin analogues. *Luminescence* **2011**, *26*, 685–688.
- [58] Waring, M.J. Lipophilicity in drug discovery. *Expert Opin. Drug Discov.* **2010**, *5*, 235–248.
- [59] Chmiel, T.; Mieszkowska, A.; Kempieńska-Kupczyk, D.; Kot-Wasik, A.; Namieśnik, J.; Mazerska, Z. The impact of lipophilicity on environmental processes, drug delivery and bioavailability of food components. *Microchem. J.* **2019**, *146*, 393–406.
- [60] Pucelik, B.; Arnaut, L.G.; Dałbrowski, J.M. Lipophilicity of Bacteriochlorin-Based Photosensitizers as a Determinant for PDT Optimization through the Modulation of the Inflammatory Mediators. *J. Clin. Med.* **2019**, *9*, 8.
- [61] Pucelik, B.; Sułek, A.; Drozd, A.; Stochel, G.; Pereira, M.M.; Pinto, S.M.A.; Arnaut, L.G.; Dałbrowski, J.M. Enhanced Cellular Uptake and Photodynamic Effect with Amphiphilic Fluorinated Porphyrins: The Role of Sulfoester Groups and the Nature of Reactive Oxygen Species. *Int. J. Mol. Sci.* **2020**, *21*, 2786.
- [62] Sudhindra, P.; Sharma, S.A.; Roy, N.; Moharana, P.; Paira, P. Recent advances in cytotoxicity, cellular uptake and mechanism of action of ruthenium metallodrugs: A review. *Polyhedron* **2020**, *192*, 114827.
- [63] McKeage, M.J.; Berners-Price, S.J.; Galettis, P.; Bowen, R.J.; Brouwer, W.; Ding, L. Role of lipophilicity in determining cellular uptake and antitumour activity of gold phosphine complexes. *Cancer Chemother. Pharmacol.* **2000**, *46*, 343.
- [64] Bruijninx, P.C.; Sadler, P.J. New trends for metal complexes with anticancer activity. *Curr. Opin. Chem. Biol.* **2008**, *12*, 197.
- [65] Johnstone, R.W.; Ruefli, A.A.; Lowe, S.W. A link between cancer genetics and chemotherapy. *Cell* **2002**, *108*, 153.
- [66] Kozieł, S.; Komarnicka, U.K.; Ziolkowska, A.; Skorska-Stania, A.; Pucelik, B.; Plotek, M.; Sebastian, V.; Bienko, A.; Stochel, G.; Kyzioł, A. Anticancer potency of novel organometallic Ir(III) complexes with phosphine derivatives of fluoroquinolones encapsulated in polymeric micelles. *Inorg. Chem. Front.* **2020**, *7*, 3386.
- [67] Jia, P.; Ouyang, R.; Cao, P.; Tong, X.; Zhou, X.; Lei, T.; Zhao, Y.; Guo, N.; Chang, H.; Miao, Y.; et al. Review: Recent advances and future development of metal complexes as anticancer agents. *J. Coord. Chem.* **2017**, *70*, 2175–2201.
- [68] Zhang, L.-X.; Gu, Y.-Y.; Wang, Y.-J.; Bai, L.; Du, F.; Zhang, W.-Y.; He, M.; Liu, Y.-J.; Chen, Y.-Z. Design, Synthesis, and Anticancer Effect Studies of Iridium(III) Polypyridyl Complexes against SGC-7901 Cells. *Molecules* **2019**, *24*, 3129.
- [69] Wang, F.-X.; Chen, M.-H.; Hu, X.-Y.; Ye, R.-R.; Tan, C.-P.; Ji, L.-N.; Mao, Z.-W. Ester-Modified Cyclometalated Iridium(III) Complexes as Mitochondria-Targeting Anticancer Agents. *Sci. Rep.* **2016**, *6*, 38954.
- [70] Komarnicka, U.K.; Pucelik, B.; Wojtala, D.; Lesiów, M.K.; Stochel, G.; Kyzioł, A. Evaluation of anticancer activity in vitro of a stable copper(I) complex with phosphine-peptide conjugate. *Sci. Rep.* **2021**, *11*, 1–17.
- [71] Lesiów, M.K.; Komarnicka, U.K.; Kyzioł, A.; Bienko, A.; Pietrzyk, P. ROS-mediated lipid peroxidation as a result of Cu(II) interaction with FomA protein fragments of *F. nucleatum*: Relevance to colorectal carcinogenesis. *Metallomics* **2019**, *11*, 2066–2077.

Supporting information

	1	2	[Ir(η^5 -Cp*)Cl ₂] ₂	[Ru(<i>p</i> -cymene)Cl ₂] ₂	1a	1b	1c	2a	2b	2c
³¹ P{ ¹ H}	-27.68	-26.72			-1.78	24.32	-14.49	-2.01	23.92	-13.07
H ^{Ph}		7.25-7.64			7.24-7.61 m	7.31-8.02 m	7.28-7.49	7.30-8.02	7.41-8.04	7.25 – 7.32
H ¹	3.45 s	3.48 s			4.01 s*	3.89 s*	3.49 s*	4.02 s	4.01 s	3.62 s
H ²	2.79 q	2.64 d			2.25 s*	2.19 s*	2.20 s*	2.09 s	1.98 s*	2.08 s
H ³	1.01 t	1.34-1.50 m			0.72 s*	1.31 s*	0.89 s*	0.72 – 0.98 m	0.70-0.89 m	0.82 -1.24 m
H ⁴		1.34-1.50 m						0.72 – 0.98 m	0.70-0.89 m	0.82 -1.24 m
H ⁵		0.89 t						0.71 t	0.68 t	0.76 t
H ^{acetonitrile}							2.03 s			2.02 s
H ^{Cp*(CH3)}			0.96 s		1.47 s*			1.37 s		
H ^{a,b}				1.29 d (6.9)		0.84 d			1.08 d	
H ^c				2.93 spt (7.0)		2.97 (6.80) spt			2.51 spt	
H ^{e,f,h,i}				5.42 dd (19.2; 6.0)		5.37 (36.0; 7.0) dd			5.15 dd	
H ^j				2.16 s		1.74 s			1.75 s	

Tab. S1 Cumulative NMR data for ligands and iridium-complexes.

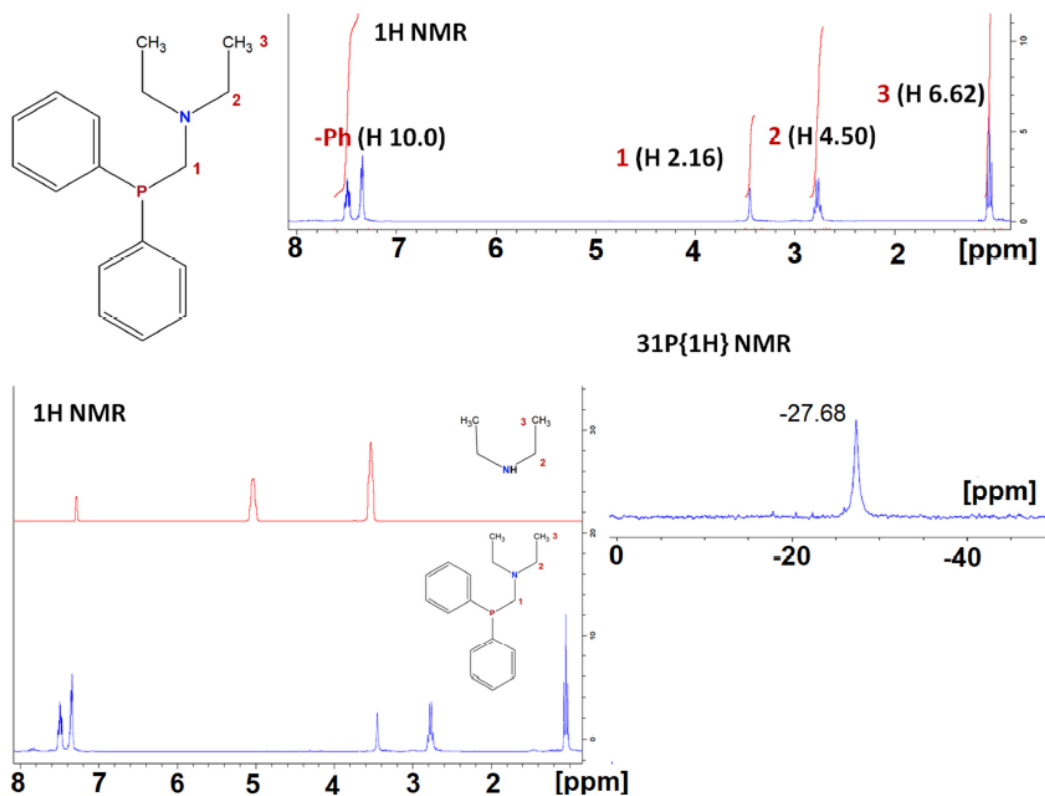


Fig. S1 ¹H and ³¹P{¹H} NMR spectra for **1** (298 K, CHCl₃-d)

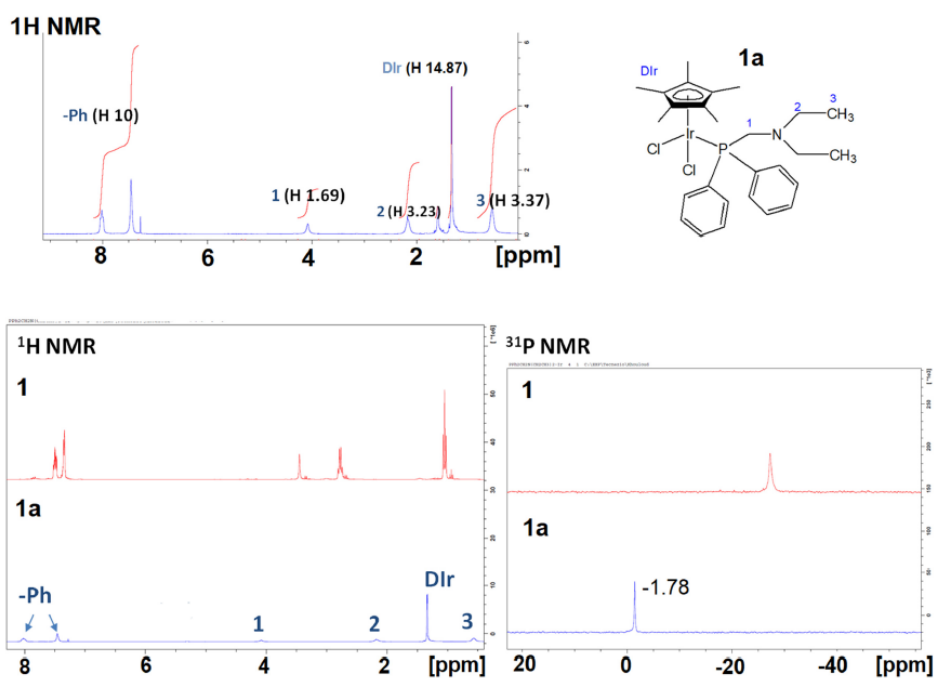


Fig. S2 ¹H and ³¹P{¹H} NMR spectra for **1a** (298 K, CHCl₃-d)

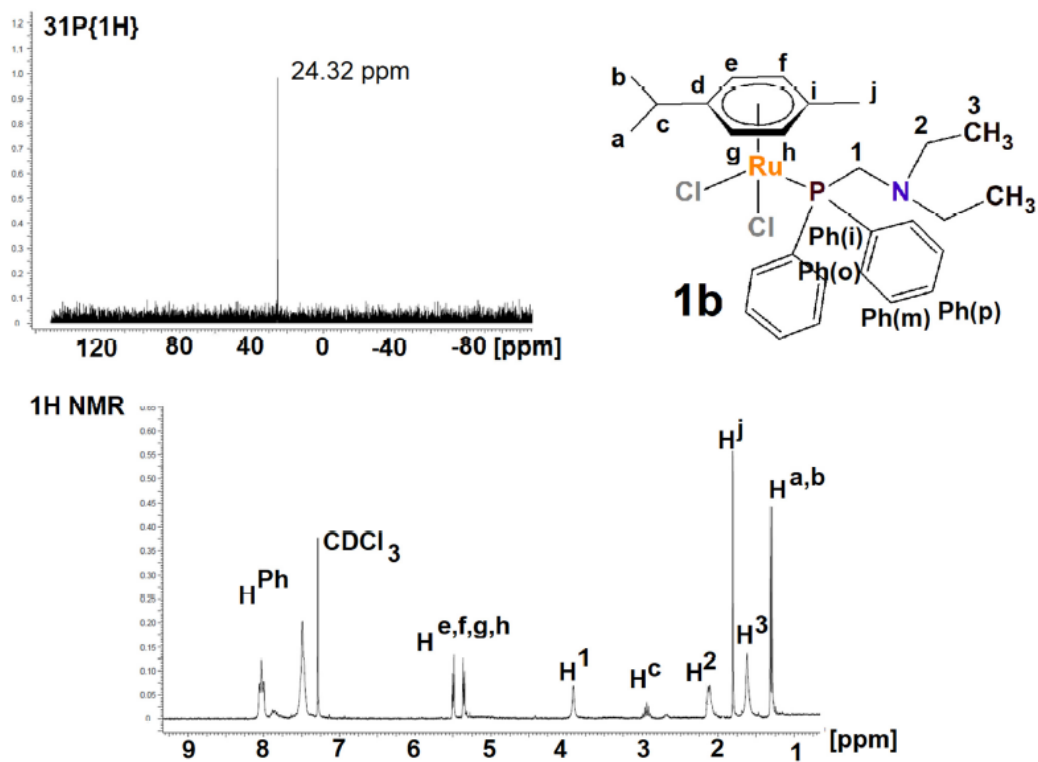


Fig. S3 ¹H and ³¹P{¹H} NMR spectra for **1b** (298 K, CHCl₃-d)

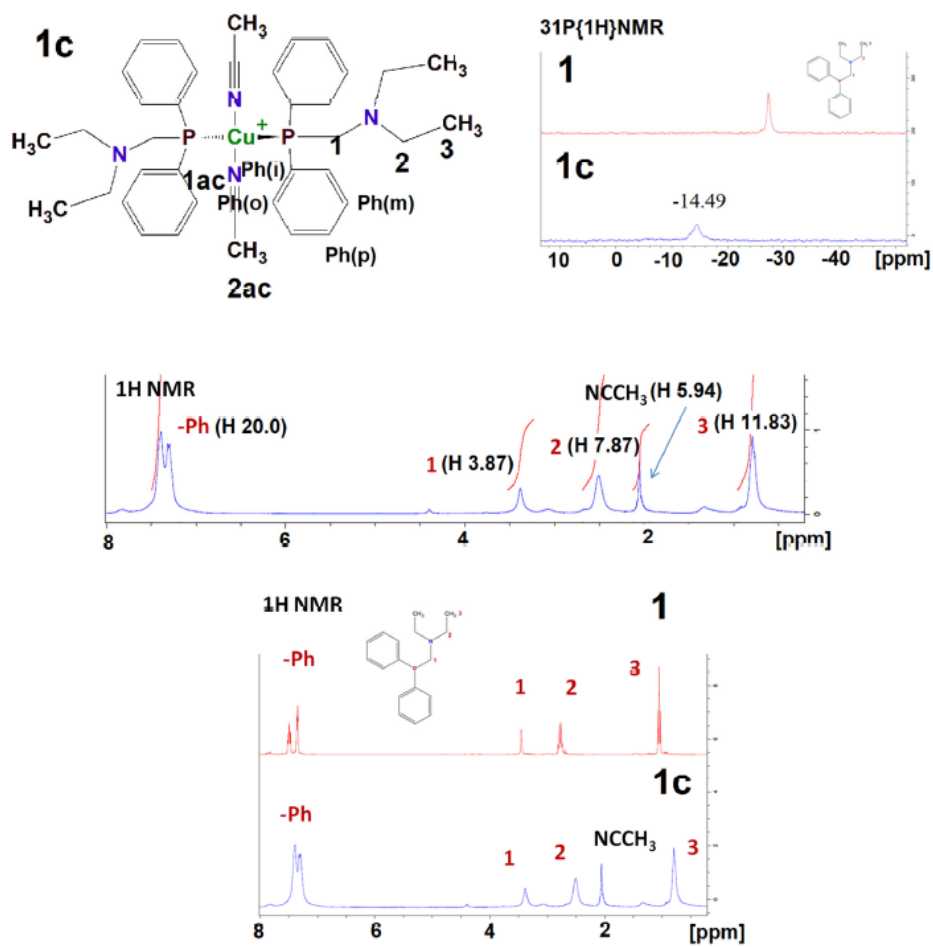


Fig. S4 ¹H and ³¹P{¹H} NMR spectra for **1c** (298 K, CHCl₃-d)

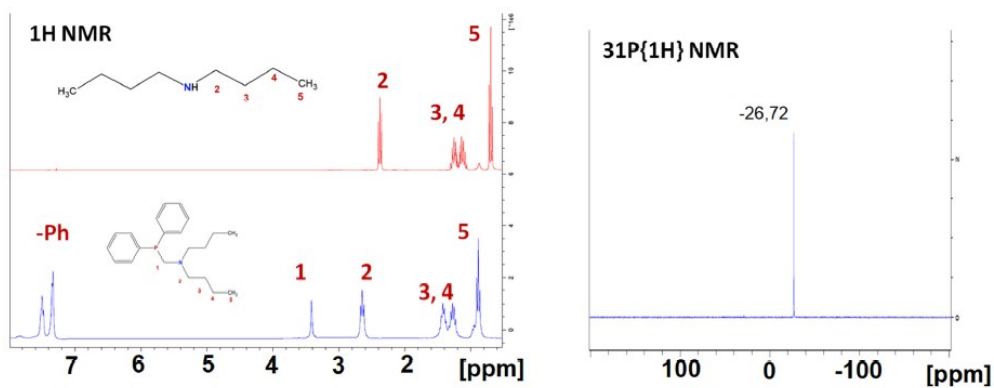
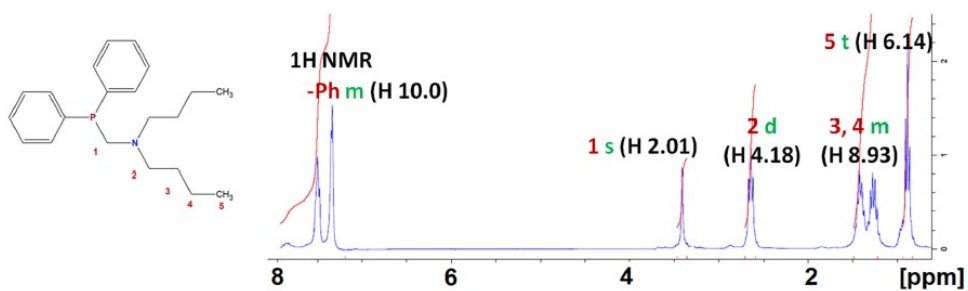


Fig. S5 ^1H and $^{31}\text{P}\{^1\text{H}\}$ NMR spectra for **2** (298 K, $\text{CHCl}_3\text{-d}$)

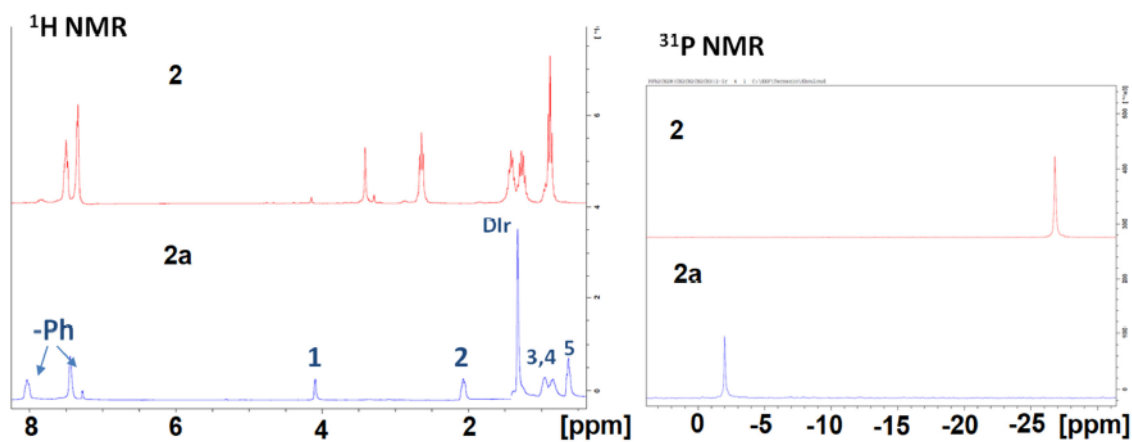
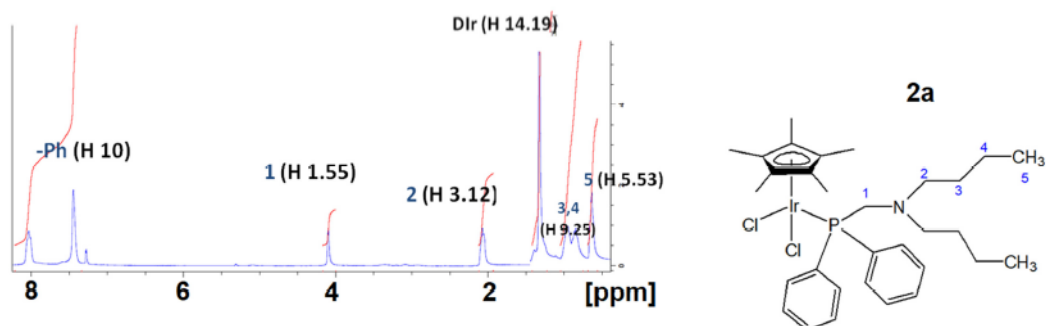


Fig. S6 ^1H and $^{31}\text{P}\{^1\text{H}\}$ NMR spectra for **2a** (298 K, $\text{CHCl}_3\text{-d}$)

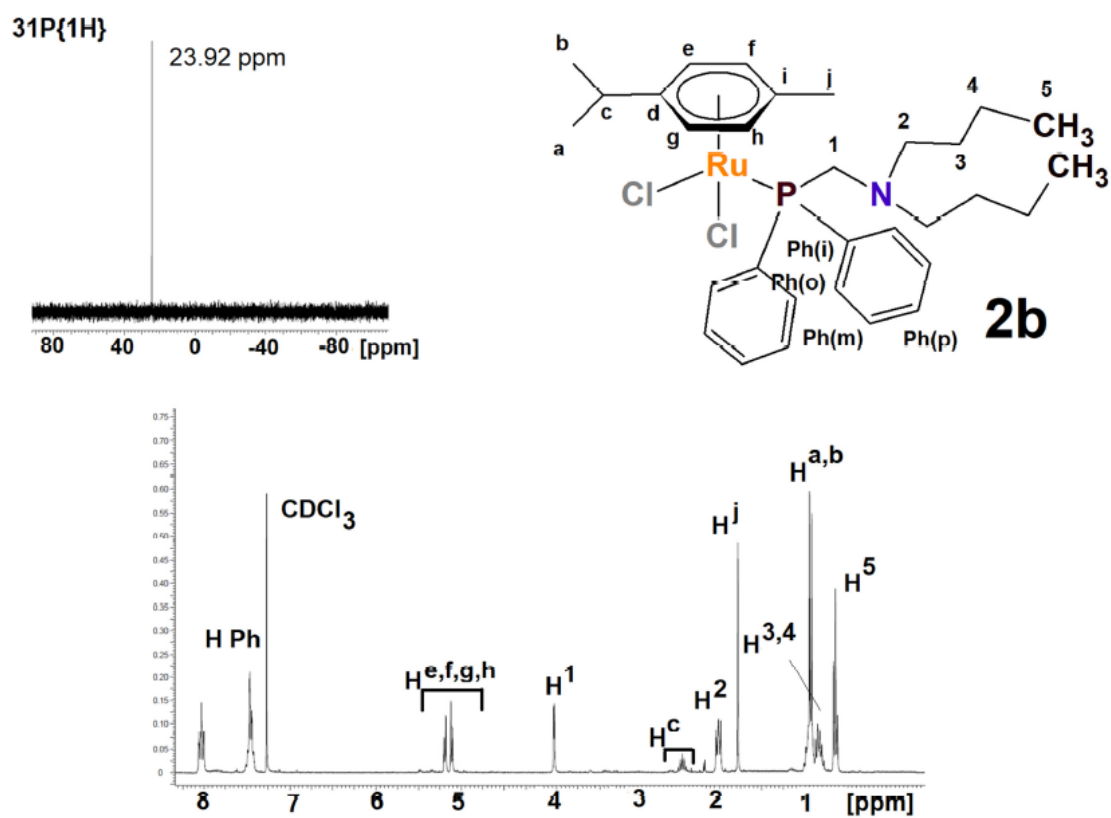


Fig. S8 ^1H and $^{31}\text{P}\{^1\text{H}\}$ NMR spectra for **2b** (298 K, CHCl_3 -d)

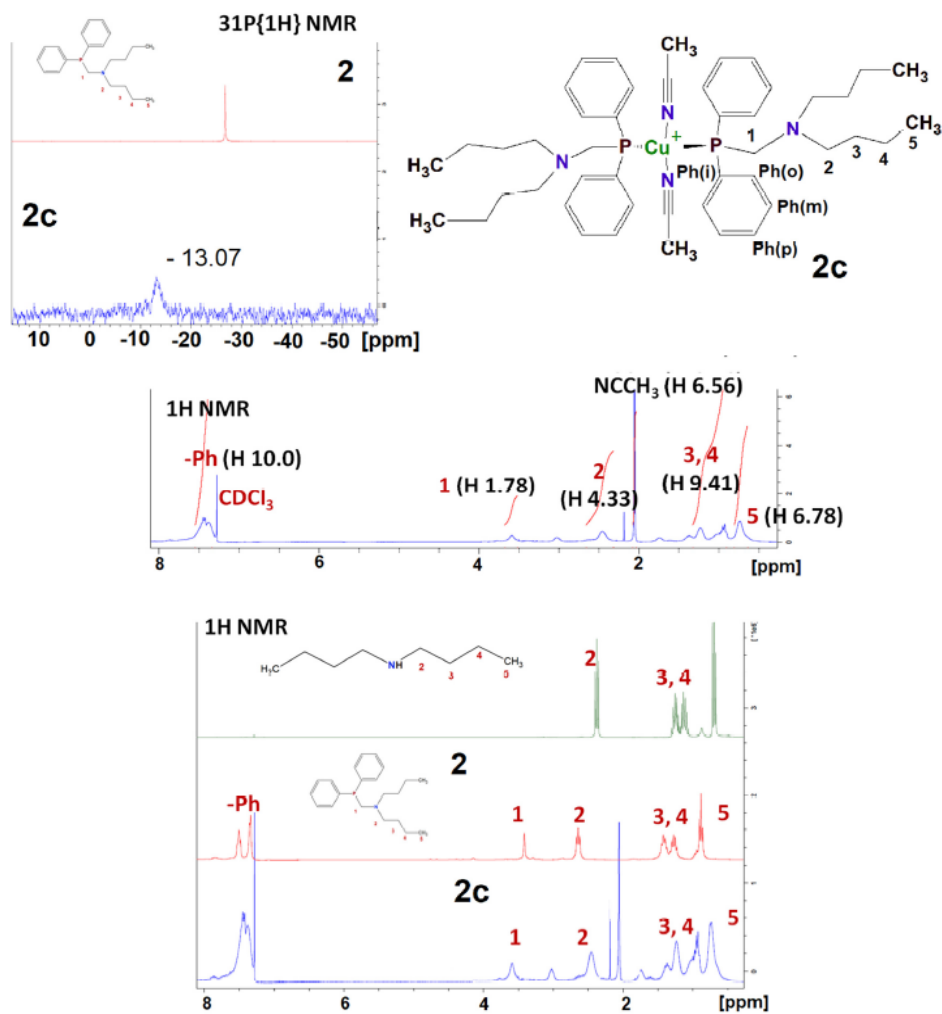


Fig. S9 ¹H and ³¹P{¹H} NMR spectra for **2c** (298 K, CHCl₃-d)

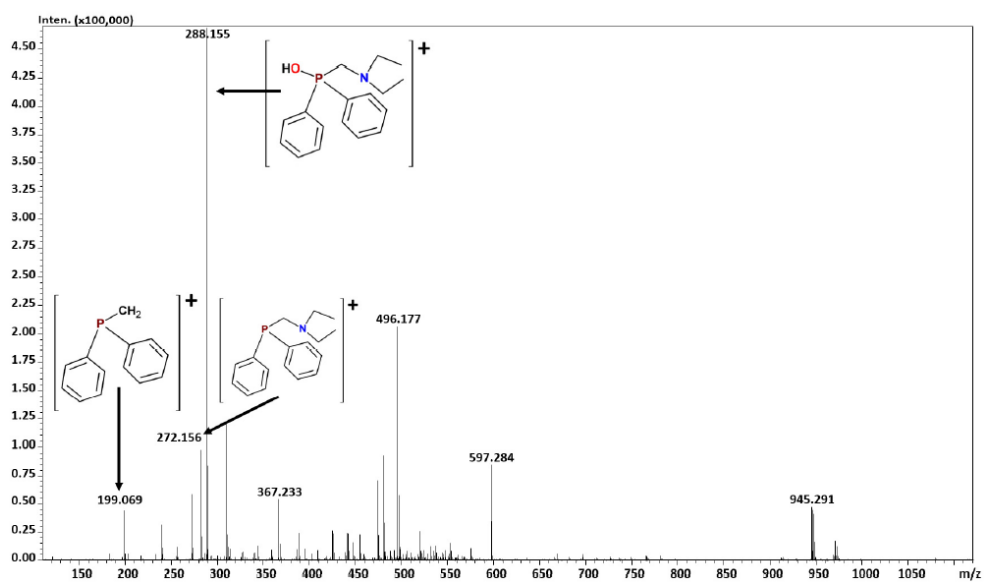


Fig. S10 Full ESI(+)-MS spectrum of **1**.

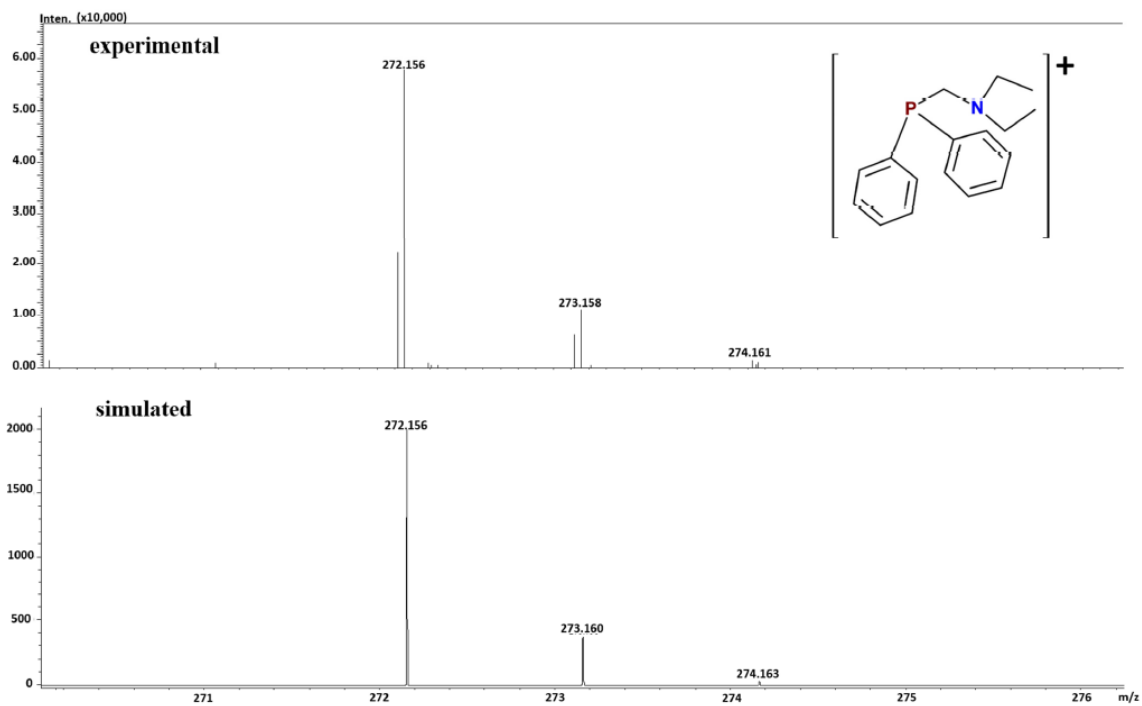


Fig. S11 Experimental and simulated ESI(+)-MS spectrum of 1.

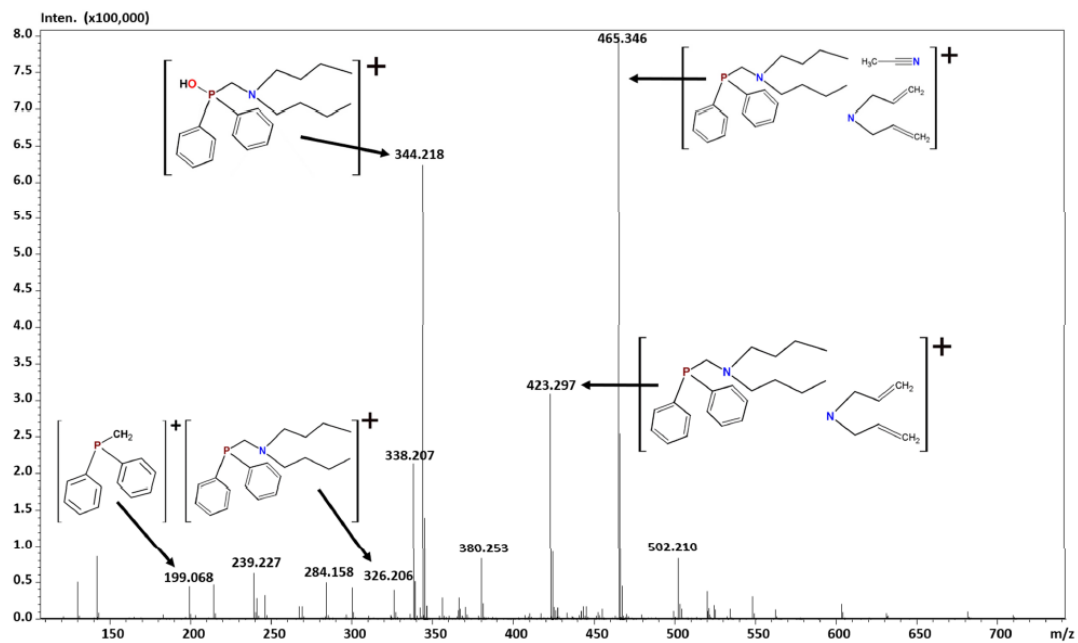


Fig. S12 Full ESI(+)-MS spectrum of 2.

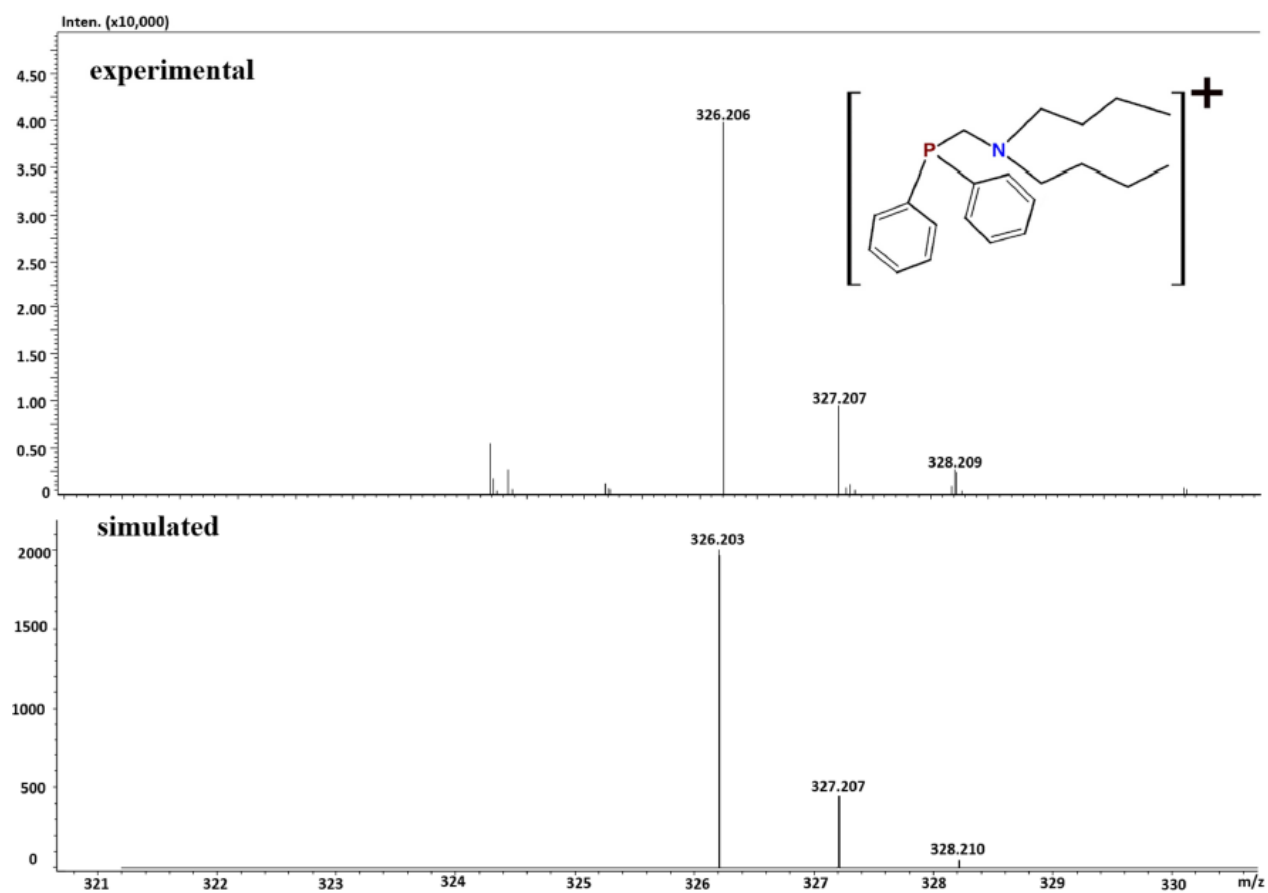


Fig. S13 Experimental and simulated ESI(+)-MS spectrum of **2**.

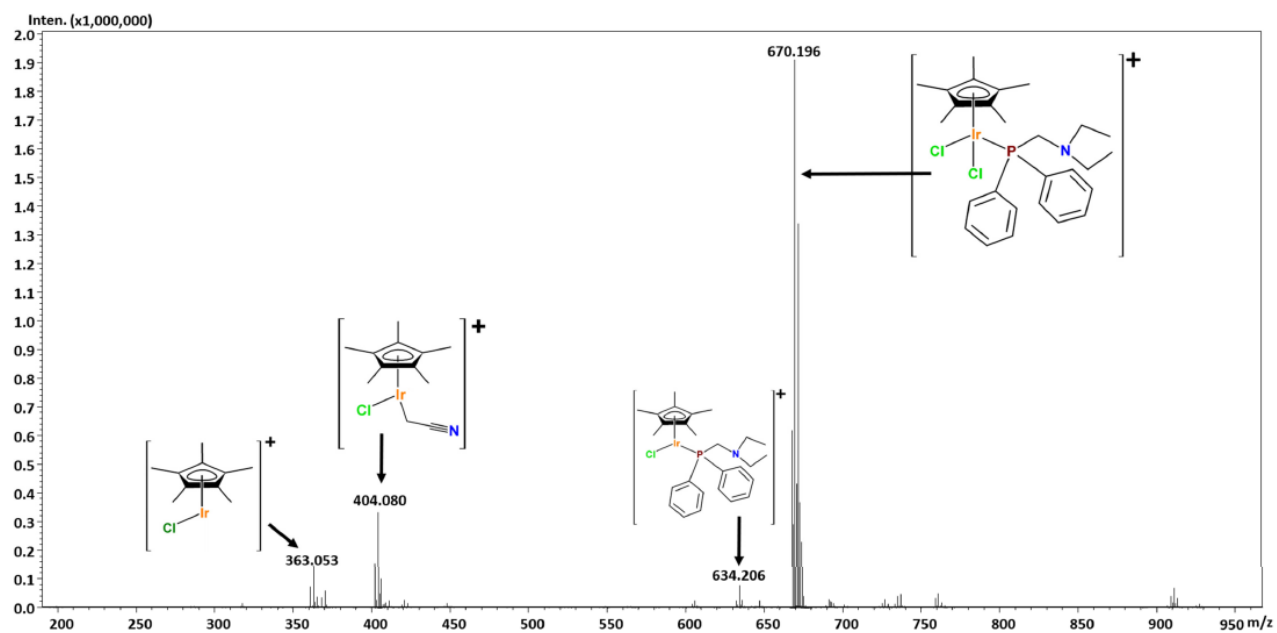


Fig. S14 Full ESI(+)-MS spectrum of **1a**.

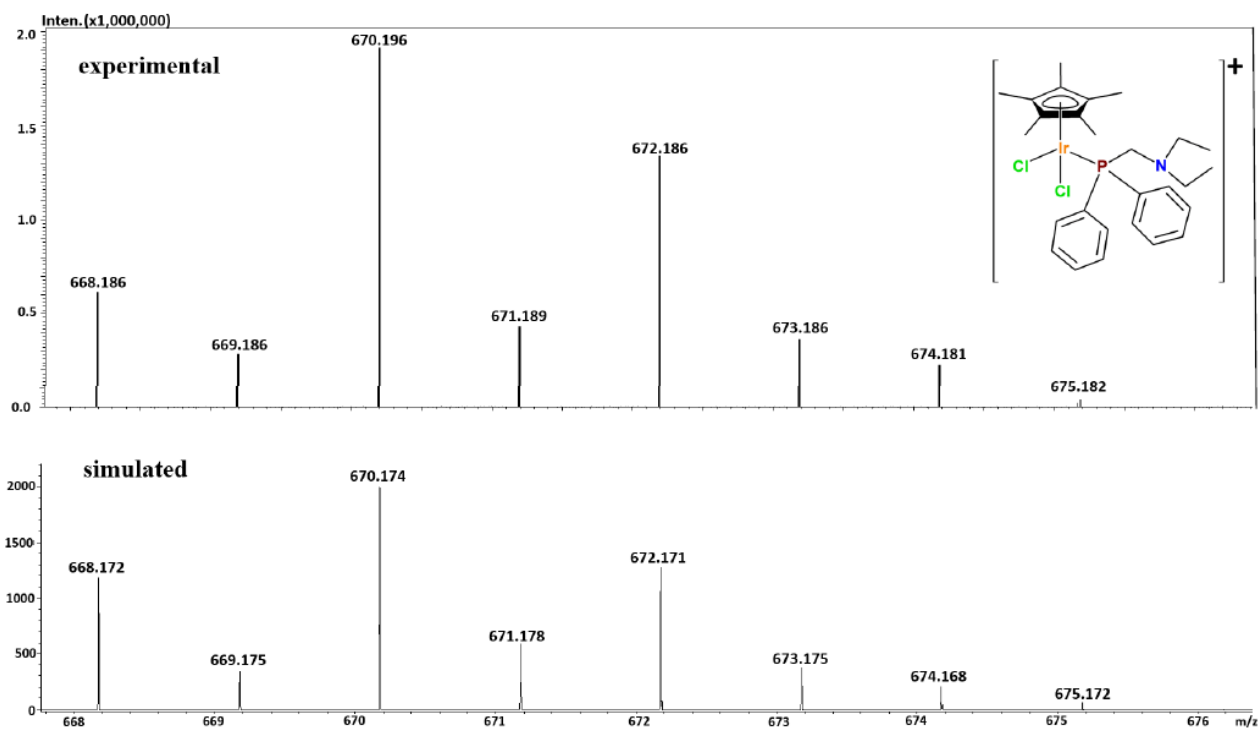


Fig. S15 Experimental and simulated ESI(+)-MS spectrum of **1a**.

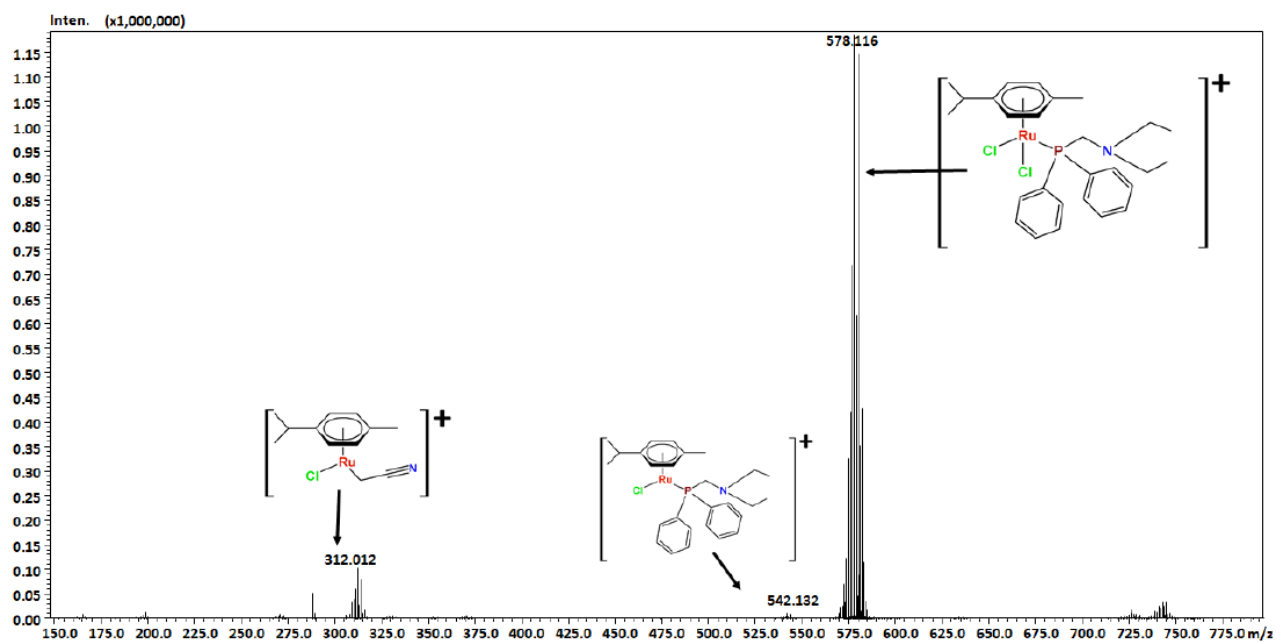


Fig. S16 Full ESI(+)-MS spectrum of **1b**.

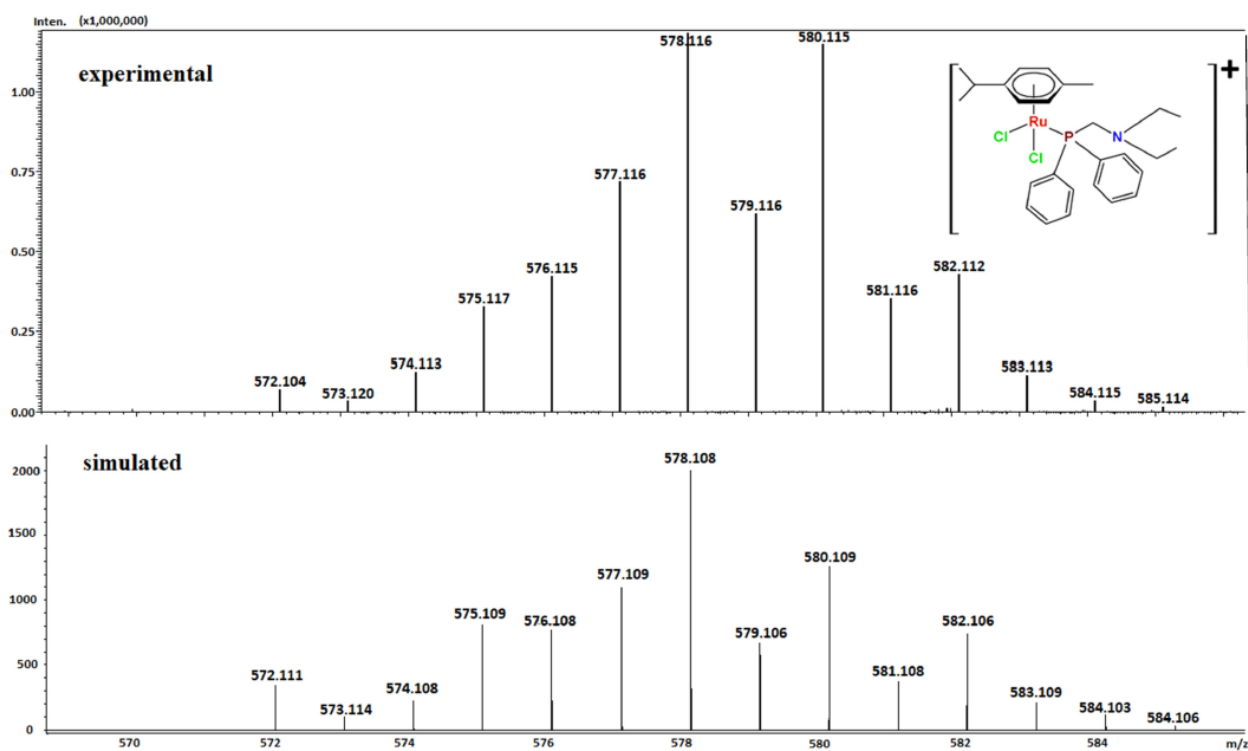


Fig. S17 Experimental and simulated ESI(+)-MS spectrum of **1b**.

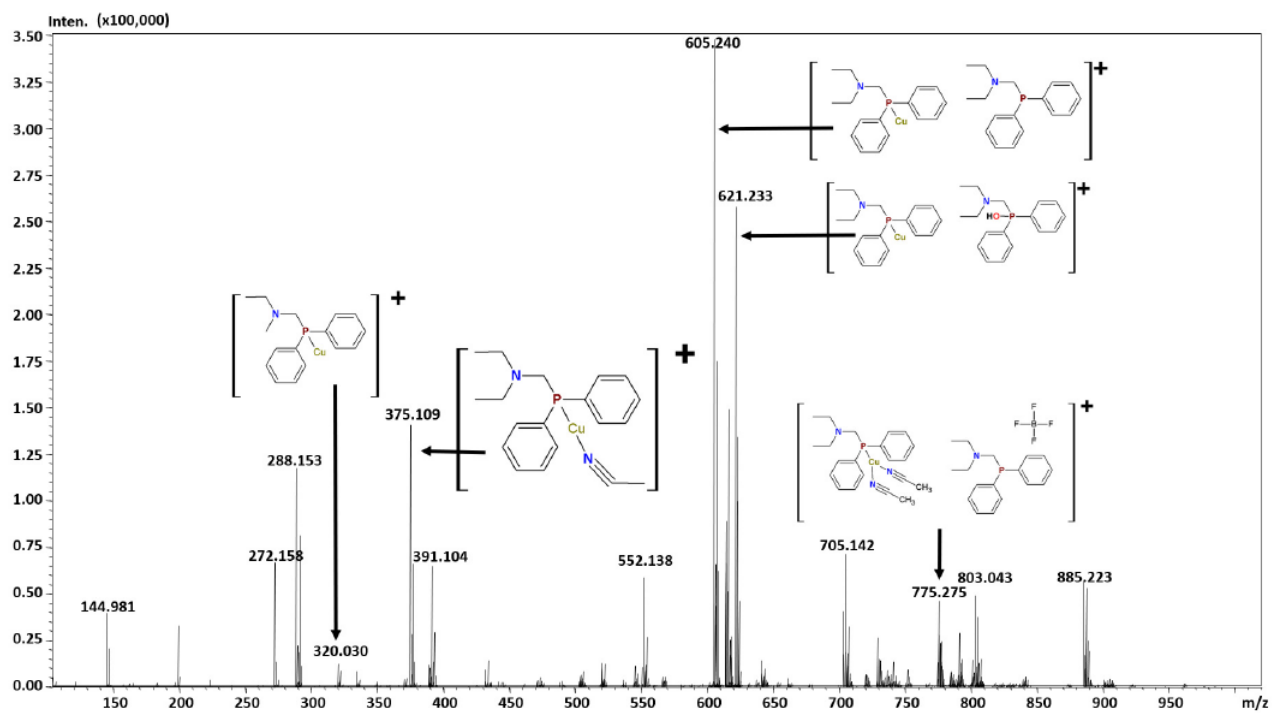


Fig. S18 Full ESI(+)-MS spectrum of **1c**.

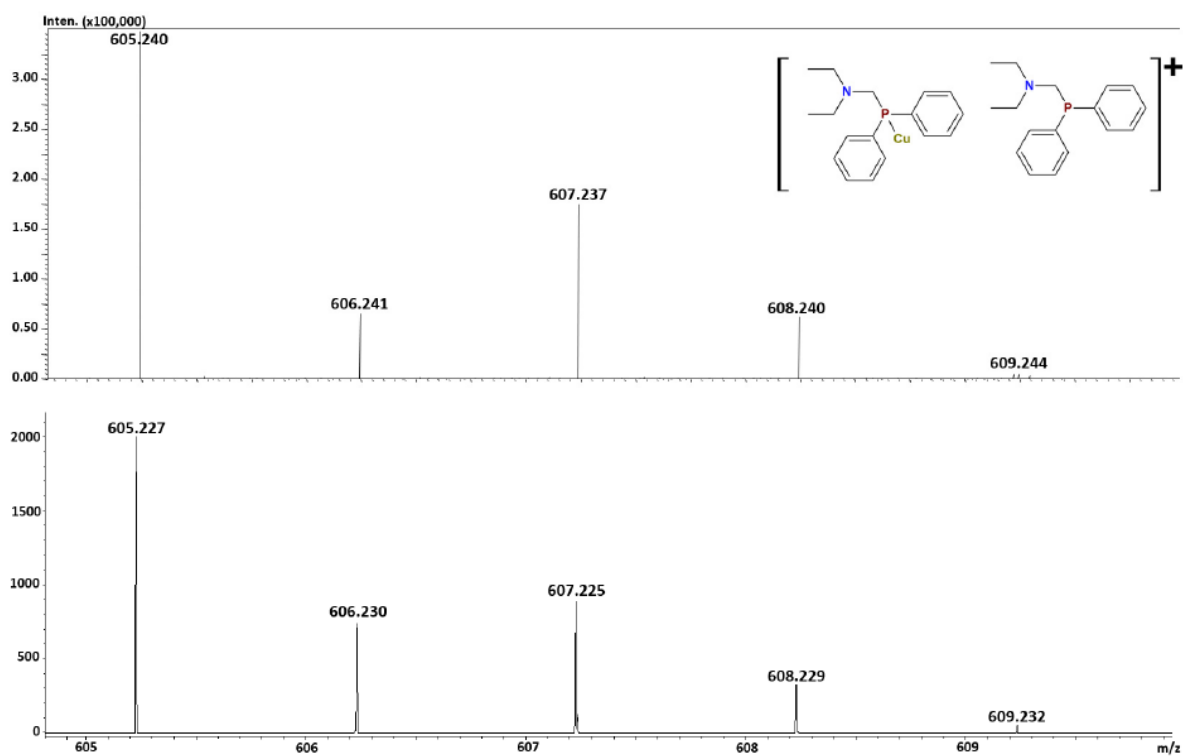


Fig. S19 Experimental and simulated ESI(+)-MS spectrum of **1b**.

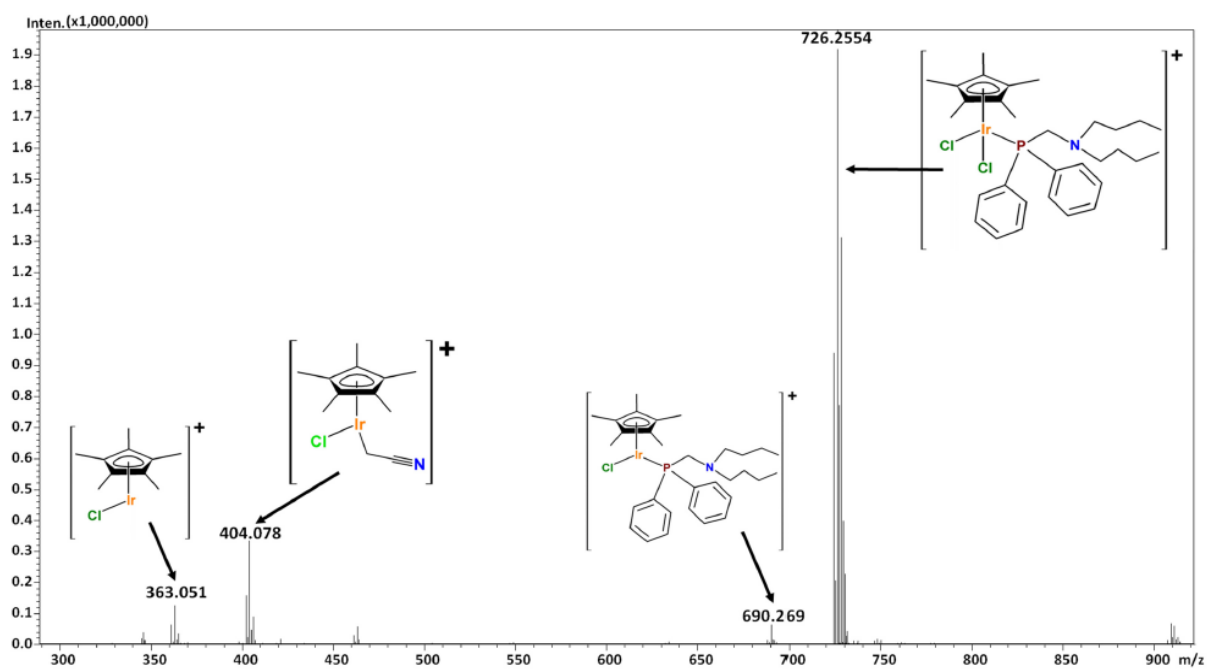
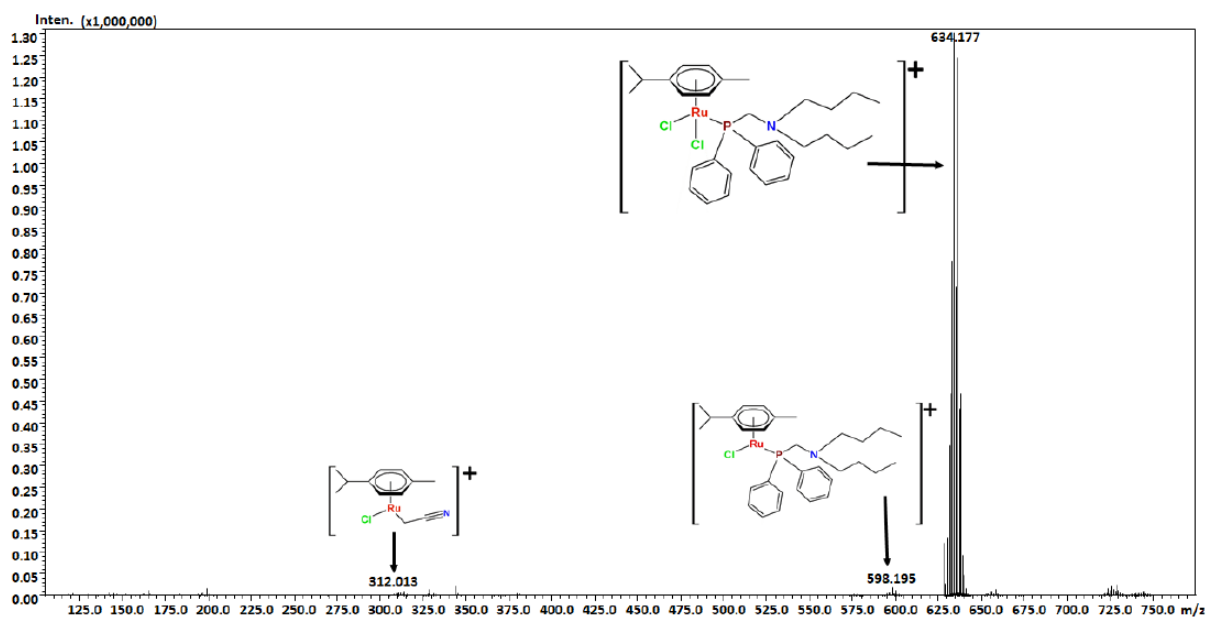
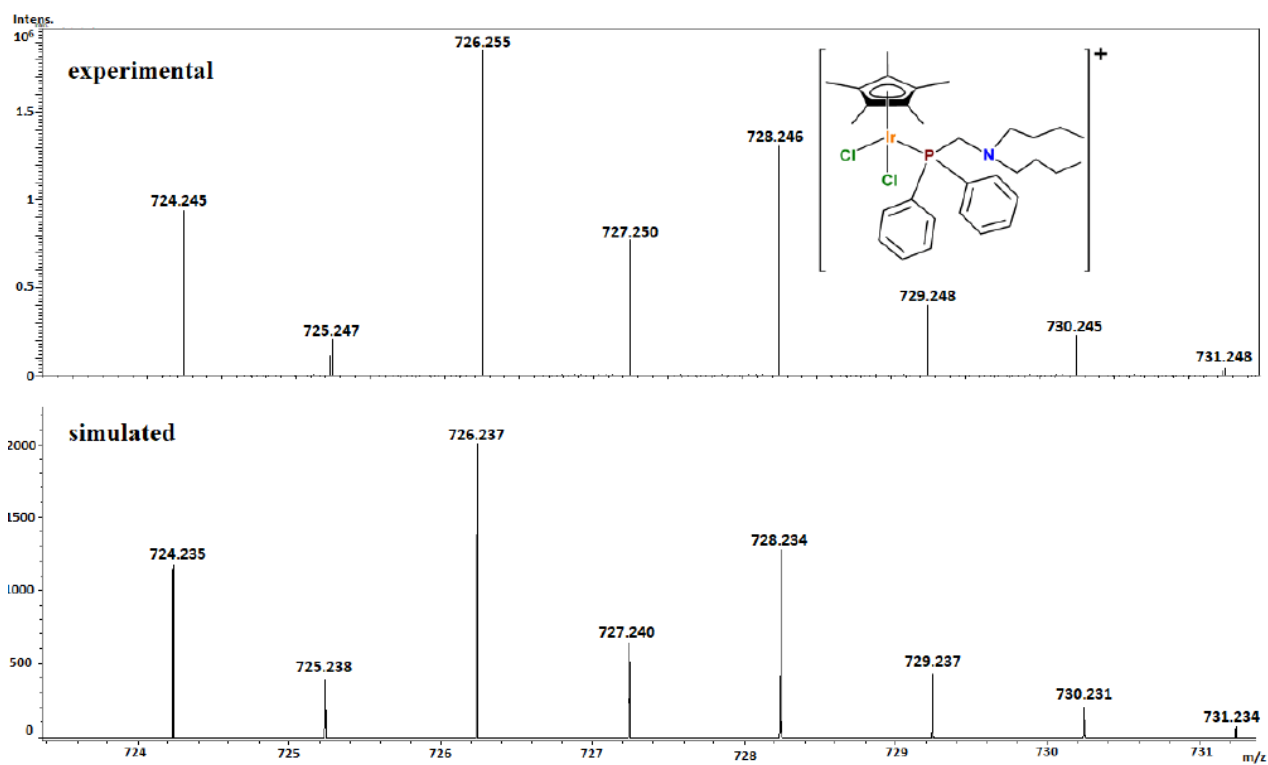


Fig. S20 Full ESI(+)-MS spectrum of **2a**.



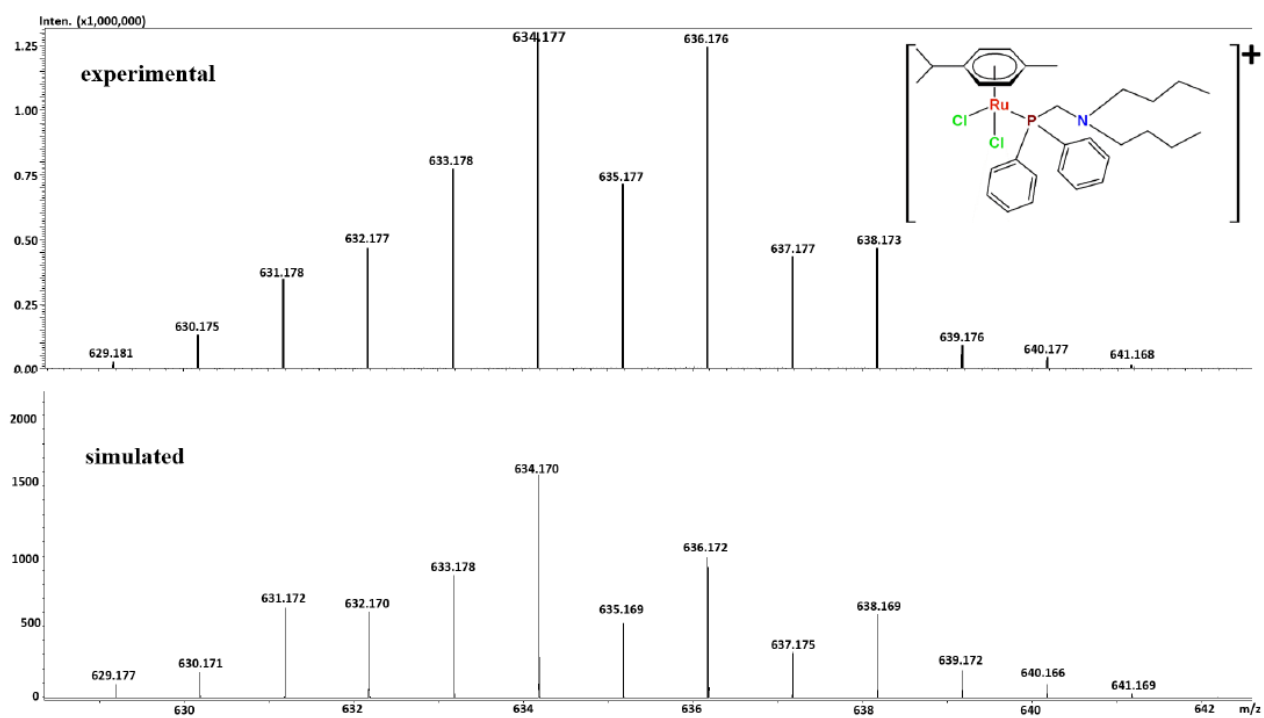


Fig. S21 Experimental and simulated ESI(+)-MS spectrum of **2b**.

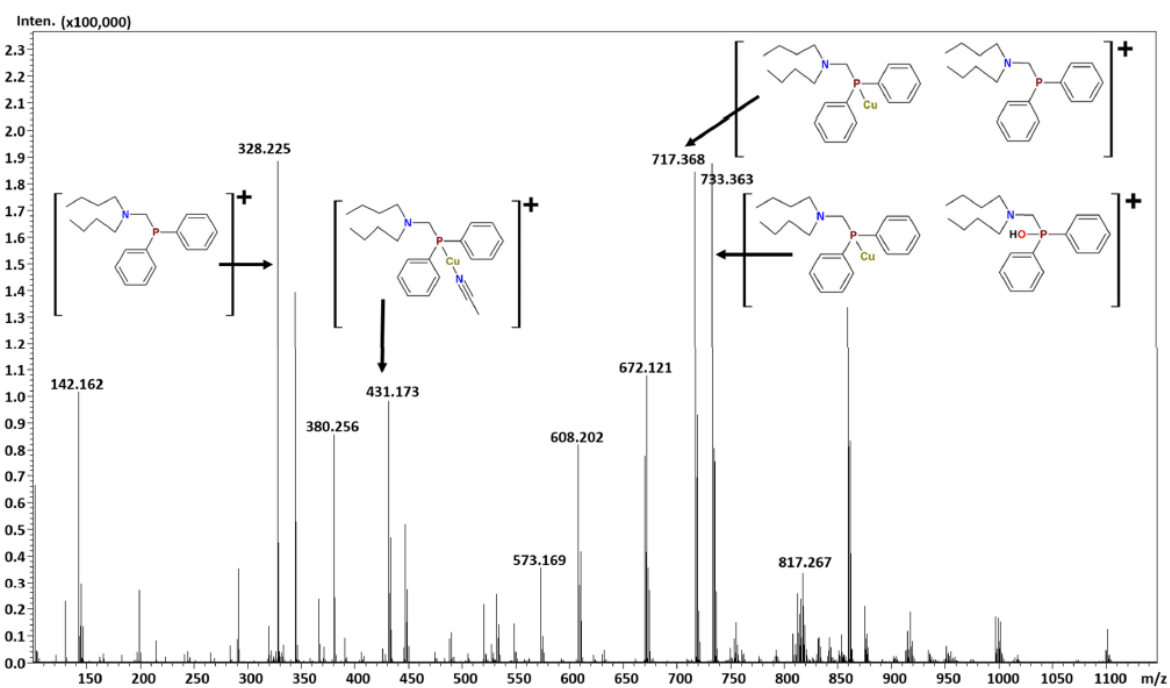


Fig. S22 Full ESI(+)-MS spectrum of **2c**.

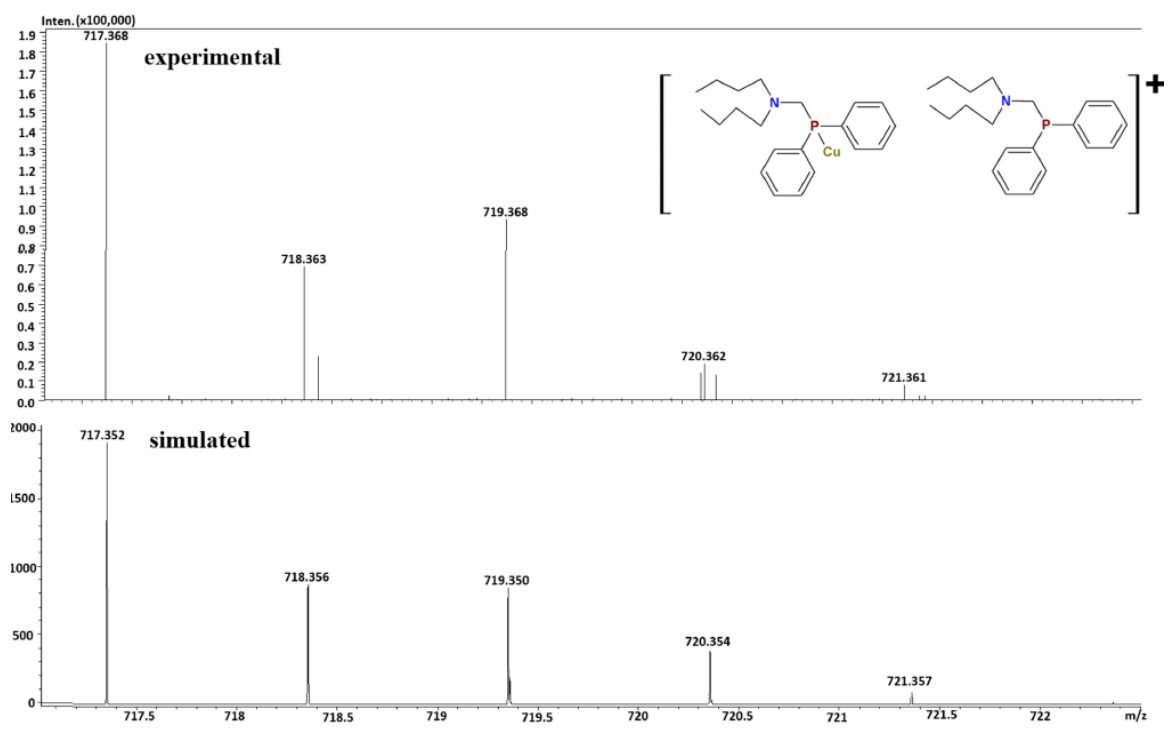


Fig. S23 Experimental and simulated ESI(+)-MS spectrum of **2c**.

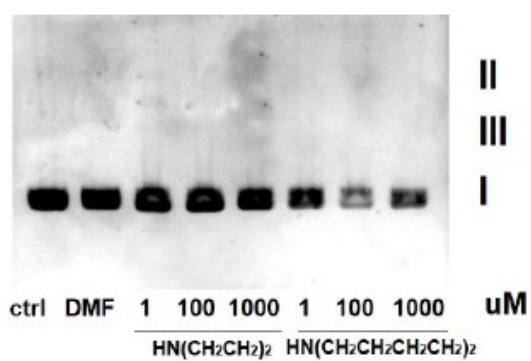


Fig. S24 Agarose gel electrophoresis of pBR322 plasmid cleavage by diethyloamine and dibutyloamine.

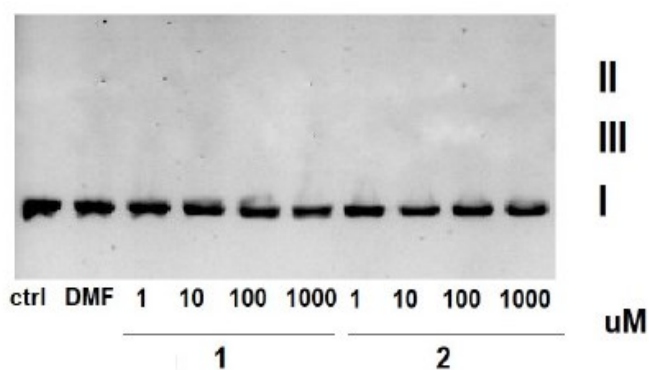


Fig. S25 Agarose gel electrophoresis of pBR322 plasmid cleavage by phosphines

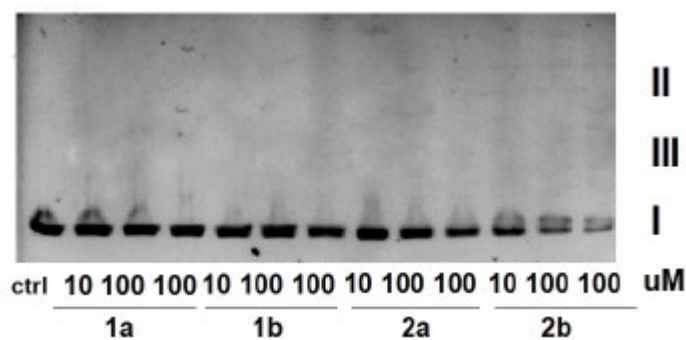


Fig. S26 Agarose gel electrophoresis of pBR322 plasmid cleavage by Cu(I), Ru(II) and Ir(III) complexes.

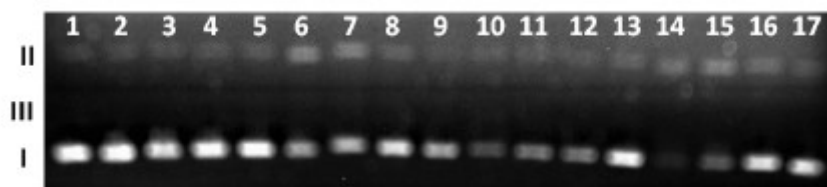


Fig. S27 Agarose gel electrophoresis of pBR322 plasmid cleavage by Ir-ethyl, Ru-ethyl, Ir-but and Ru-but complexes. Lanes: 1, plasmid-control; 2, plasmid + 50 μ M Ir-ethyl; 3, plasmid + 50 μ M Ir-ethyl + 50 μ M H₂O₂; 4, plasmid + 50 μ M Ir-ethyl + 50 μ M H₂O₂ + 1.4 mM DMSO; 5, plasmid + 50 μ M Ir-ethyl + 50 μ M H₂O₂ + 40 mM M NaN₃; 6, plasmid + 50 μ M Ru-ethyl; 7, plasmid + 50 μ M Ruethyl+ 50 μ M H₂O₂; 8, plasmid + 50 μ M Ru ethyl + 50 μ M H₂O₂ + 1.4 mM DMSO; 9, plasmid + 50 μ M Ru-ethyl + 50 μ M H₂O₂ + 40 mM M NaN₃; 10, plasmid + 50 μ M Ir-but; 11, plasmid + 50 μ M Irbut + 50 μ M H₂O₂; 12, plasmid + 50 μ M Ir-but + 50 μ M H₂O₂ + 1.4 mM DMSO; 13, plasmid + 50 μ M Ir-but + 50 μ M H₂O₂ + 40 mM NaN₃; 14, plasmid + 50 μ M Ru-but; 15, plasmid + 50 μ M Ru-but + 50 μ M H₂O₂; 16, plasmid + 50 μ M Ru-but + 50 μ M H₂O₂ + 1.4 mM DMSO; 17, plasmid + 50 μ M Ru-but + 50 μ M H₂O₂ + 40 mM M NaN₃.

	MCF-7	Du-145	A549	PANC-1	HaCaT
dibutylamine	>1000	>1000	>1000	>1000	>1000
diethylamine	>1000	>1000	>1000	>1000	>1000
1	458±11	203±19	620±9	426±7	646±20
2	355±13	185±12	569±11	386±6	556±13
1a	189±9	90±5	68±5	143±3	456±11
2a	125±15	69±6	79±6	106±5	559±25
1b	295±12	122±11	59±3	146±5	446±20
2b	226±20	102±6	81±4	126±6	545±13
Cisplatin	176±5	85±7	70±8	166±20	400±3

Tab. S2. IC₅₀ (μM) values of the investigated complexes toward the selected cancer cell lines for 24 h. Data are given as mean ± SD of 3 independent experiments (N=3).

	MCF-7	Du-145	A549	PANC-1	HaCaT
dibutylamine	226±20	103±7	387±25	258±6	445±25
diethylamine	352±25	126±12	425±38	305±13	545±33
1	149±13	86±6	47±5	185±13	458±20
2	125±20	54±8	72±6	158±23	420±11
1a	184±6	85±9	45±4	204±29	446±26
2a	189±20	69±8	61±3	198±20	420±12
1b	352±25	126±12	425±38	305±13	545±33
2b	226±20	103±7	387±25	258±6	445±25
Cisplatin	151±6	81±8	66±9	131±7	362±4

Tab. S3. IC₅₀ (μM) values of the investigated complexes toward the selected cancer cell lines for 48 h. Data are given as mean ± SD of 3 independent experiments (N=3).

ADDENDUM II

Internship at Wrocław University for the synthesis and characterization of metallic complexes with enhanced anticancer properties, article: *“Liposomal Binuclear Ir(III)–Cu(II) Coordination Compounds with Phosphino-Fluoroquinolone Conjugates for Human Prostate Carcinoma Treatment”*

Liposomal Binuclear Ir(III)–Cu(II) Coordination Compounds with Phosphino-Fluoroquinolone Conjugates for Human Prostate Carcinoma Treatment

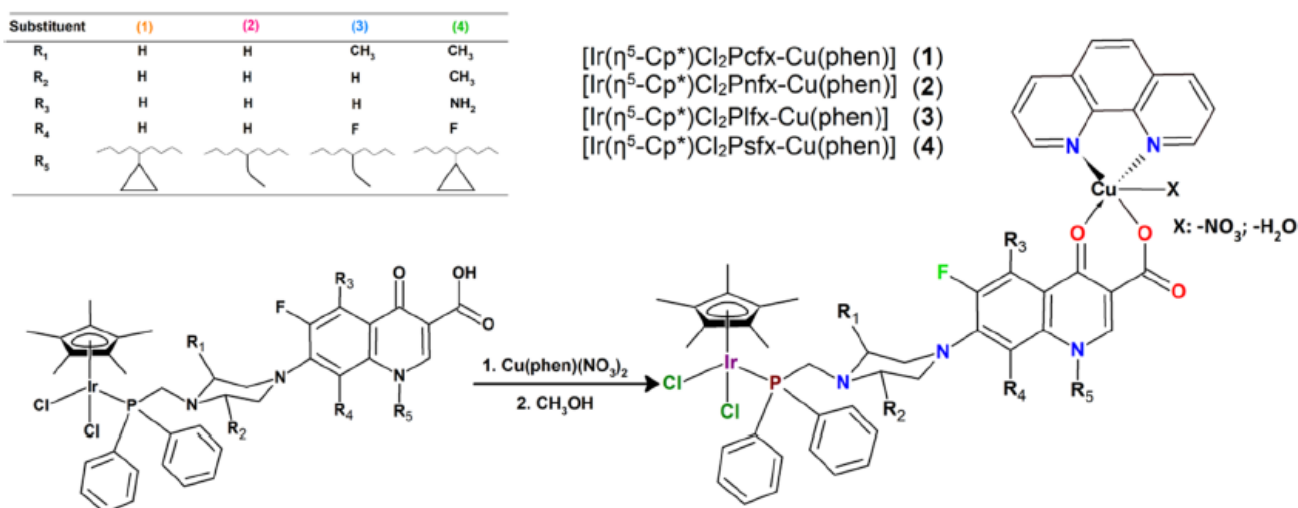
Urszula K. Komarnicka, Sandra Koziół, Barbara Pucelik, Agata Barzowska, Miłosz Siczek, Magdalena Malik, Daria Wojtala, Alessandro Nioiretini, Agnieszka Kyzioł, Victor Sebastian, Pavel Kopel, Stefano Caramori, and Alina Bieńko

Abstract

Novel heteronuclear IrIII–CuII coordination compounds ($[\text{Ir}(\eta^5\text{-Cp}^*)\text{Cl}_2\text{Pcfx-Cu(phen)}](\text{NO}_3)_x \cdot y(\text{CH}_3\text{OH}) \cdot z(\text{H}_2\text{O})$ (1), $[\text{Ir}(\eta^5\text{-Cp}^*)\text{Cl}_2\text{Pnfx-Cu(phen)}](\text{NO}_3)_x \cdot y(\text{CH}_3\text{OH}) \cdot z(\text{H}_2\text{O})$ (2), $[\text{Ir}(\eta^5\text{-Cp}^*)\text{Cl}_2\text{Plfx-Cu(phen)}](\text{NO}_3)_x \cdot y(\text{H}_2\text{O}) \cdot z(\text{CH}_3\text{OH})$ (3), $[\text{Ir}(\eta^5\text{-Cp}^*)\text{Cl}_2\text{Psfx-Cu(phen)}]$ (4)) bearing phosphines derived from fluoroquinolones, namely, sparfloxacin (Hsfx), ciprofloxacin (Hcfx), lomefloxacin (Hlfx), and norfloxacin (Hnfx), have been synthesized and studied as possible anticancer chemotherapeutics. All compounds have been characterized by electrospray ionization mass spectrometry (ESI-MS), a number of spectroscopic methods (*i.e.*, IR, fluorescence, and electron paramagnetic resonance (EPR)), cyclic voltammetry, variable-temperature magnetic susceptibility measurements, and X-ray diffractometry. The coordination geometry of IrIII in all complexes adopts a characteristic piano-stool geometry with the η^5 -coordinated and three additional sites occupied by two chloride and phosphine ligands, while CuII ions in complexes 1 and 2 form a distorted square-pyramidal coordination geometry, and in complex 3, the coordination geometry around CuII ions is a distorted octahedron. Interestingly, the crystal structure of $[\text{Ir}(\eta^5\text{-Cp}^*)\text{Cl}_2\text{Plfx-Cu(phen)}]$ features the one-dimensional (1D) metal–organic polymer. Liposomes loaded with redox-active and fluorescent $[\text{Ir}(\eta^5\text{-Cp}^*)\text{Cl}_2\text{Pcfx-Cu(phen)}]$ (1L) have been prepared to increase water solubility and minimize serious systemic side effects. It has been proven, by confocal microscopy and an inductively coupled plasma mass spectrometry (ICP-MS) analysis, that the liposomal form of compound 1 can be effectively accumulated inside human lung adenocarcinoma and human prostate carcinoma cells with selective localization in nuclei. A cytometric analysis showed dominance of apoptosis over the other cell death types. Furthermore, the investigated nanoformulations induced changes in the cell cycle, leading to S phase arrest in a dose dependent manner. Importantly, *in vitro* anticancer action on three-dimensional (3D) multicellular tumor spheroids has been demonstrated.

1. Introduction

Some of the most life-threatening diseases in the whole world are undeniably cancer diseases.¹ According to the Global Cancer Observatory, over 9 million deaths were caused by cancer diseases in 2020 and around 19 million new cases have been reported.² Currently, the most common metal-based therapeutics



Scheme 1. Schematic illustrations of the inorganic compound structures and synthetic routes (the solvent molecules have been omitted for clarity)

in chemotherapy are those containing Pt(II) ions.³ The effectiveness of drugs is still inhibited by clinical problems, for example, a limited spectrum of activity, high toxicity causing side effects, and acquired or intrinsic resistance.⁴ One of the approaches leading to overcoming these limitations is to find inspiration in the activity of novel heteronuclear complexes.⁵ When we incorporate two various cytotoxic metals into the same molecule, significant improvement in their antitumor activity can be noticed. This phenomenon can be explained by the interaction of different metals with multiple biological targets or by the imprecise chemophysical properties of the resulting heteronuclear complexes. Therefore, in some cases where a specific type of cancer becomes resistant toward one of the metals, the second or third metal might still exhibit some cytotoxic activity. Through the years, several binuclear complexes have been synthesized and tested and some noticeable results have been described: for example, Au(I)–Ag(I), Au(I)–Pt(II), Cu(II)–Na(I), Au(I)–Ti(IV), and Ru(II)–Pt(IV).^{5–10} Patra and coworkers synthesized a heteronuclear complex Ru–Ir with the formula [(ppy)₂Ir(μ-phpy)Ru(p-cym)Cl](PF₆)₂. The study showed that this complex was significantly more active than its mononuclear analogue as well as Cisplatin against cell lines such as MCF7, SKOV3, and PC3. Moreover, the results show that these complexes induce autophagy in cancer cells.¹¹ Zhu and co workers patented a group of platinum–ruthenium inorganic compounds named Ruthplatins with increased or comparable activity to cisplatin toward a number of cell lines (even toward cisplatin-resistant cell lines).

The introduction of the ruthenium center led to increased complex toxicity against healthy MRC-5 lung fibroblast cells compared to the cisplatin control.¹² Consequently, similar to this approach, in our research, we decided to incorporate two metal ions in our research: copper(II) and iridium(III). It was proved that through many processes, such as DNA damage or generation of reactive oxygen species (ROS), Cu(II) complexes could effectively induce cancer cell death. In addition, the superiority of these substances is also represented by the fact that Cu(II) ions are already present in the human body, limiting the possibility of excessive immunological system response.¹³ Additionally, the introduction of a transition metal with unpaired electrons can also endow the obtained complexes with additional magnetic functionality such as SIM, SMM, or superparamagnetic behavior, which show slow relaxation of magnetization.¹⁴⁻²⁴ In the last few years, many scientists around the world have been working on the development of iridium(III) organometallic complexes and have succeeded in proving that iridium(III) inorganic compounds can replace platinum-based drugs.^{3,25-33} These complexes have unique properties such as potential redox activity, a wide range of ligand exchange rates and universal structure, greater cellular uptake efficiency, large Stokes shifts, and lower toxic effect.^{3,25-27,31,32} Various mechanisms are responsible for the antitumor activity of iridium(III) compounds, such as protein activity inhibition, catalysis of cellular redox reactions, and damage of specific subcellular organelles. These amazing properties of iridium(III) complexes make them a rising star among new, potential anticancer agents.^{3,25-33} Additionally, to circumvent the previously mentioned side effects, our potential bioactive molecules will be loaded in liposomes. Liposomal technology has attracted great interest in nanomedicine because of liposomes' low toxicity, biodegradability, and efficient cellular uptake.³⁴⁻³⁶ Liposomes have already been described as great transporters of both hydrophilic and hydrophobic molecules to cancer cells. Additionally, those nanoparticles could also provide (i) protection against the speciation of complexes in the bloodstream as well as (ii) the possibility of targeting in solid tumors.^{36,37} The research described herein on anticancer compounds is a continuation of our ongoing project in which phosphine ligands (Ph₂P-CH₂-FQ, FQ: fluoroquinolone antibiotic) bearing fluoroquinolones, namely, sparfloxacin (Hsfx), ciprofloxacin (Hcfx), lomefloxacin (Hlfx), and norfloxacin (Hnfx), were coordinated to various metal centers: Cu(I), Cu(II), Ru(II), and Ir(III).^{4,38-42} The results described above have confirmed that this mononuclear complex with phosphine is an excellent choice for the design of new biological agents. Therefore, we decided to extend our studies. Here, we investigate the dual nature of the iridium(III)-copper(II) ([Ir(η⁵-Cp*)Cl₂Pcfx-Cu(phen)](NO₃)*1.75(CH₃OH)*0.75(H₂O) (1), [Ir(η⁵-Cp*)Cl₂Pnfx-Cu(phen)](NO₃)*1.75-(CH₃OH)*0.75(H₂O)(2), [Ir(η⁵-Cp*)Cl₂Pifx-Cu(phen)](NO₃)*1.3(H₂O)*1.95(CH₃OH) (3), [Ir(η⁵-Cp*)Cl₂Psfx-Cu(phen)] (4)). The coordination of two different metal ions would significantly broaden the scope of their action mode with cells through different cytotoxic mechanisms. To take the above issues into account, first, their physicochemical properties have been determined using X-ray diffraction, elemental analysis, cyclic voltammetry, mass spectrometry (electrospray ionization mass spectrometry (ESI-MS)), spectroscopic techniques, and variable-temperature magnetic susceptibility measurements. The

cytotoxic effect of the compounds was assessed in vitro toward lung, breast, melanoma, and prostate tumor cell lines and one nontumor human embryonic kidney cell line. Based on the abovementioned findings, in this paper we presented a preclinical investigation into the therapeutic potential of complex IrPcfxCu encapsulated inside liposomes toward three-dimensional (3D) lung and prostate cancer cell cultures. Additionally, a working mechanism for these new inorganic compounds has been proposed and explained.

2. Results and discussion

2.1 Synthesis

The four new heteronuclear complexes Ir(III)/Cu(II) were synthesized (Scheme 1) by stirring [Cu(phen)(NO₃)₂] with 1 equiv of IrFQ ([Ir(η⁵-Cp*)Cl₂PFQ]) at room temperature, previously reported by us in a recent study.²⁷ Binuclear complexes are soluble in CH₃OH, dimethyl sulfoxide (DMSO), and CH₂Cl₂ and insoluble in water.

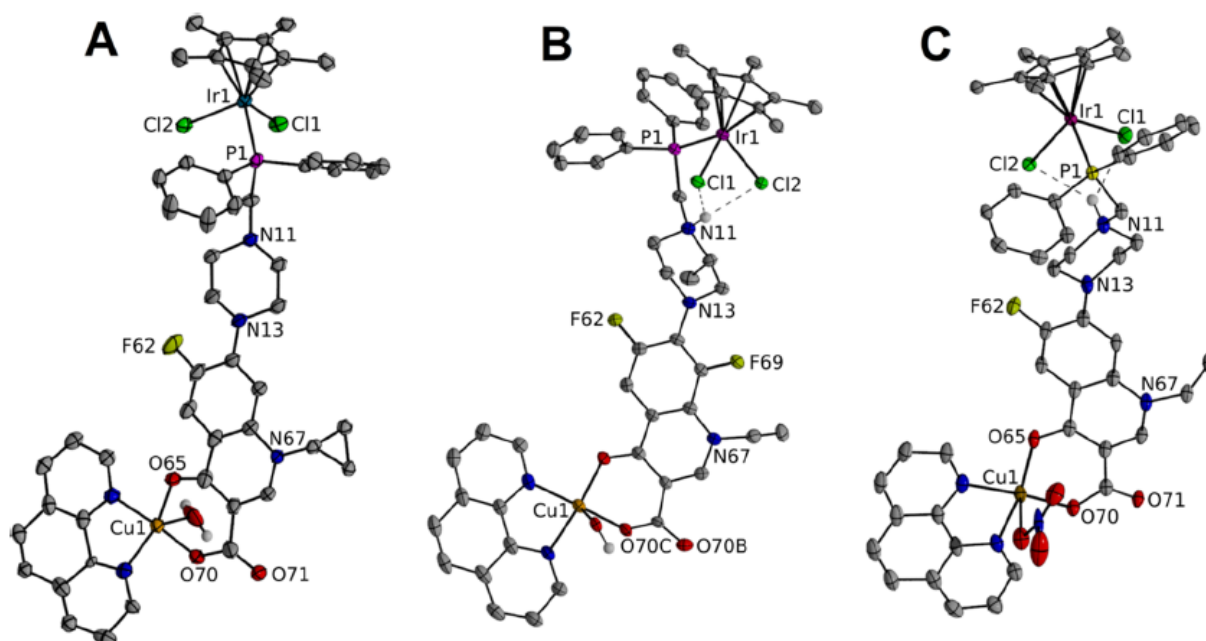


Fig. 1 Crystal structures of the complex molecules IrPcfxCu (1), IrPnfxCu (2), and IrPlfxCu (3). The solvent molecules and protons are omitted for clarity

However, they can be solubilized in water containing 2% DMSO. The synthesis of mononuclear IrFQ complexes (incl.) was carried out under a nitrogen environment using Schlenk techniques. The chemical structures of studied Ir(III)/Cu(II) complexes are presented in Scheme 1.

2.2 Structural Features

The single crystals of [Ir(η⁵-Cp*)Cl₂Pcfx-Cu(phen)](NO₃)·1.75(CH₃OH)·0.75(H₂O) (1), [Ir(η⁵-Cp*)Cl₂PnfxCu(phen)](NO₃)·1.75(CH₃OH)·0.75(H₂O) (2), and [Ir(η⁵-Cp*)Cl₂Plfx

Cu(phen)](NO₃)*1.3(H₂O)*1.95(CH₃OH) (3) were analyzed by the X-ray diffraction technique (Figures 1 and S1–S6; Tables 1, 2, and S1). All obtained iridium(III)–copper(II) complexes (Figure 1) crystallized in two different space groups (1 and 2: crystal system, triclinic; space group, P1; 3: crystal system, orthorhombic; space group, *Pbcn*). Importantly, the crystal structure of 3 features the one-dimensional (1D) metal–organic polymer assembled from Cu(II) centers, Ir(III) complex linkers, 1,10-phenanthroline (phen) molecule, and OH[−] ligands (Figure S1 see the Supporting Information). Every structure also contains solvent molecules and anions (H₂O, NO₃[−], or OH[−]). The coordination geometry of the iridium ion in all of the Ir(III)–Cu(II) complexes adopts the well-known half-sandwich pseudo-octahedral “three-leg pianostool” geometry, where the cyclopentadienyl moiety has served as the top of the stool and the three leg sites have been occupied by phosphorous atom from phosphine ligand and two terminal chloride anions.^{27–30} The bond angle values of P–Ir–Cl and Cl–Ir–Cl, proving the pseudo-octahedral arrangement of atoms around the metal center, are found to be in the range of 86.73–124.2°. They turned out to be higher than the values obtained for mononuclear Ir(III) complexes with the same phosphine ligands previously described by us (the bond angle values for P–Ir–Cl and Cl–Ir–Cl are in the range of 86.04–90.45°).²⁷

	IrPnfxrCu· (NO ₃)· 1.75(CH ₄ O)· 0.75(H ₂ O)	IrPcfxCu· (NO ₃)· 2.75(H ₂ O)	IrPlfxCu· (NO ₃)· 1.3(H ₂ O)· 1.95(CH ₄ O)
C(Cp*ring)–C(Cp*CH ₃)			1.4862
Ir ^I –C ⁶	2.235(6)	2.245(6)	2.19(4)
Ir ^I –C ⁷	2.224(6)	2.237(6)	2.21(3)
Ir ^I –C ⁸	2.198(7)	2.142(6)	2.18(2)
Ir ^I –C ⁹	2.195(6)	2.155(6)	2.19(2)
Ir ^I –C ¹⁰	2.203(6)	2.154(6)	2.21(2)
Ir ^I –C _{Cp*} (average)	2.211(0)	2.186(6)	2.196
Ir ^I –C _{centroid}			1.835
Ir ^I –P ¹	2.312(16)	2.291(15)	2.304(18)
Ir ^I –Cl ¹	2.410(2)	2.411(15)	2.407(18)
Ir ^I –Cl ²	2.427(4)	2.448(17)	2.413(18)
P ¹ –C ¹¹	1.839(5)	1.846(6)	1.859(7)
P ¹ –C ²¹	1.815(5)	1.822(6)	1.814(7)
P ¹ –C ³¹	1.812(5)	1.816(6)	1.819(7)
Cu ^I –O ^{70A}	1.911(4)	1.917(17)	2.057(12)
Cu ^I –O ^{70A'}			2.220(14)
Cu ^I –O ^{65A}	1.917(4)	1.919(17)	1.923(19)
Cu ^I –O ^{65B}			1.959(18)
Cu ^I –N ⁹¹	2.019(5)	1.999(13)	2.004(7)
Cu ^I –N ⁸¹	2.014(5)	2.013(12)	1.991(8)
Cu ^I –O ^{1N}	2.351(6)		
Cu ^I –O ^{1W}		2.32(2)	2.298(3)
FQ _{centroid} –phen _{centroid}			3.743
Centroid—Center of Gravity			
Ir ^I –CCp* (average): average calculated from Ir ^I –C ¹ , Ir ^I –C ² , Ir ^I –C ³ , Ir ^I –C ⁴ , and Ir ^I –C ⁵			
C(Cp*ring)–C(Cp*CH ₃): average calculated from C ¹ –C ^{1A} , C ² –C ^{2A} , C ³ –C ^{3A} , C ⁴ –C ^{4A} , and C ⁵ –C ^{5A}			

Tab. 1 Selected Bond Lengths (Å) for crystallized complexes

The bond distances between iridium metal centers and phosphorus atoms of 1, 2, and 3 complexes have been found to be on average 2.3 Å, whereas the Ir–Cl1 and Ir–Cl2 bond distances of complexes 1, 2, and 3 have been found to be on average 2.4 Å and are comparable to that previously described for mononuclear Ir(III) complexes.^{27–29} CuII ion in all Ir(III)–Cu(II) complexes is coordinated via nitrogen atoms (from phenanthroline ligand) and the IrP(FQ)

	IrPnfxCu·(NO ₃)· 1.75(CH ₄ O)· 0.75(H ₂ O)	IrPcfxCu· (NO ₃)· 2.75(H ₂ O)	IrPlfxCu·(NO ₃)· 1.3(H ₂ O)· 1.95(CH ₄ O)
P ¹ –Ir ¹ –Cl ¹	87.57(1)	86.73(5)	87.93(6)
P ¹ –Ir ¹ –Cl ²	124.2(2)	91.14(6)	90.19
Cl ¹ –Ir ¹ –Cl ²	86.96(13)	88.39(5)	88.28
C _{centroid} –Ir ¹ –P ¹			134.59
C _{centroid} –Ir ¹ –P ¹			121.28
C _{centroid} –Ir ¹ –P ¹			121.68
Ir ¹ –P ¹ –C ¹¹	114.44(18)	112.06(19)	114.0(2)
Ir ¹ –P ¹ –C ²¹	111.4(2)	113.2(2)	118.6(3)
Ir ¹ –P ¹ –C ³¹	118.76(19)	117.1(2)	116.0(2)
C ³¹ –P ¹ –C ²¹	105.5(2)	107.1(3)	103.8(3)
C ³¹ –P ¹ –C ¹¹	104.4(3)	101.2(3)	97.2(3)
C ²¹ –P ¹ –C ¹¹	100.4(2)	104.8(3)	104.4(3)
N ⁹¹ –Cu ¹ –N ⁸¹	82.1(2)	81.6(5)	82.1(3)
O ^{70A} –Cu ¹ –O ^{65A}	94.52(16)	93.7(7)	88.2(6)
O ^{70A} –Cu ¹ –O ^{65B}			95.9(6)
O ^{70A} –Cu ¹ –O ^{70r}			71.69
O ^{65A} –Cu ¹ –N ⁸¹	90.9(2)	88.9(6)	91.0(6)
O ^{65B} –Cu ¹ –N ⁸¹			91.1(6)
O ^{70A} –Cu ¹ –N ⁸¹	172.94(19)	174.5(6)	157.1(5)
O ^{70r} –Cu ¹ –N ⁸¹			108.2(3)
O ^{65A} –Cu ¹ –N ⁹¹	162.68(19)	158.8(7)	167.9(6)
O ^{65B} –Cu ¹ –N ⁹¹			167.5(6)
O ^{70A} –Cu ¹ –N ⁹¹	91.43(18)	94.4(6)	94.4(4)
O ^{70Ar} –Cu ¹ –N ⁹¹			86.2(4)
O ^{1N} –Cu ¹ –N ⁹¹	81.7(2)		
O ^{1N} –Cu ¹ –N ⁸¹	86.88(19)		
O ^{1N} –Cu ¹ –O ^{65A}	113.91(18)		
O ^{1N} –Cu ¹ –O ^{70A}	95.02(18)		
O ^{1W} –Cu ¹ –N ⁹¹		102.9(8)	88.6(3)
O ^{1W} –Cu ¹ –N ⁸¹		93.4(10)	108.2(3)
O ^{1W} –Cu ¹ –O ^{65A}		96.4(9)	103.1(5)
O ^{1W} –Cu ¹ –O ^{65B}			83.6(5)
O ^{1W} –Cu ¹ –O ^{70A}			94.3(4)
O ^{1W} –Cu ¹ –O ^{70Ar}			164.5(4)
Centroid—Center of Gravity			
Ir ¹ –CCp* (average): average calculated from Ir ¹ –C ¹ , Ir ¹ –C ² , Ir ¹ –C ³ , Ir ¹ –C ⁴ , and Ir ¹ –C ⁵			
C(Cp*ring)–C(Cp*CH ₃): average calculated from C ¹ –C ^{1A} , C ² –C ^{2A} , C ³ –C ^{3A} , C ⁴ –C ^{4A} , and C ⁵ –C ^{5A}			

Tab. 2 Selected Angles (deg) for Crystallized Complexes

(where FQ denotes fluoroquinolone) complex via deprotonated carboxylate and pyridone oxygen atoms forming a distorted square-pyramidal coordination geometry (Figures 1 and S1–S6). Average bond lengths for 1 and 2 complexes are as follows: Cu1–N91, 2.002; Cu1–N81, 2.013; Cu1–O65, 1.918; and Cu1–O70, 1.914 Å. Additionally, in the case of 1, the bond length between Cu1 and O1W (from water molecule) is equal to 2.232(1) Å, and for 2, the bond length in Cu1–N (from NO₃⁻ ion) is equal to 2.351(1) Å. Interestingly, the analysis of packing in 3 reveals that the coordination geometry around Cu(II) ions is a distorted octahedron (Figures 1 and S4). The Cu(II) ion is coordinated by four oxygen atoms (two carboxylate, one pyridine oxygen, and one from the OH⁻ group) and two nitrogen atoms from the phenanthroline ring, leading to the formation of 3 polymer. This unit with two bridging OW1 and O70 atoms is formed with a Cu1–Cu1 distance of 4.193(1) Å, similar to that described in the literature for Cu(II) complexes with other quinolone antibiotics and aromatic diimines.^{43–46} Additionally, the conformation of the antibiotic fragment of complexes can be defined in terms of torsion angle, defining the orientation of the piperazine ring and fluoroquinolone moiety (1: C13–N13–C61–C62 –157.56°; 3: C13–N13–C14–C15 –128.45°; 2: C14–N13–C61–C62 –153.29°). Those values differ from the torsion angle of the piperazine ring and antibiotic motif for analogic monometallic Ir(III) complexes with the same phosphine ligands (Ir(η⁵-Cp*)Cl₂Pcfx: C13–N13–C61–C62 –165.92°; Ir(η⁵-Cp*)Cl₂Plfx: C13–N13–C61–C62 –117.48°; Ir(η⁵-Cp*)Cl₂Pnfx: C14–N13–C61–C62 –165.97°).²⁷ The value of the torsion angle for 3 is significantly lower than the values of the torsion angle of both complexes 1 and 2. This phenomenon can be explained by forming a dimer by 3 where many various interactions exist.

2.3 Characterization of Ir(III)–Cu(II) Inorganic Compounds

2.3.1 Infrared Spectroscopies

The Fourier transform infrared (FT-IR) spectra of the four novel iridium(III)–copper(II) complexes together with analysis and discussion have been provided in the Supporting Information.

2.3.2 Electrospray Ionization Mass Spectrometry (ESI-MS)

All inorganic compounds have also been investigated by high resolution mass spectrometry. In almost every case, a molecular ion peak was present and corresponded to isotopic distribution for a protonated parent ion [M+H]⁺. Only complex 1 did not show the corresponding molecular ion peaks, but [IrPCpCu-2Cl-2H + CH₃OH]⁺ ions were detected at m/z 1129.264 (Figures S7–S10). Less abundant peaks corresponding to [M–Cl]⁺ and [M–2Cl + H]⁺ ions have also been analyzed, indicating that chloride ions can be easily displaced. Surprisingly, we can also observe adducts with solvent molecules, either H₂O or CH₃OH. A solvent molecule can occupy the coordination site vacated by chloride ions. Additionally, peaks corresponding to the loss of the phosphine ligands and the arene ring are observed, which indicates poor metal-to-ligand and metal-to-

arene binding. As illustrated in Figures S7–S10 in the Supporting Information, the cluster peaks obtained from the experiments exhibited excellent superimposition compared with those from simulations.

2.3.3 EPR Spectroscopy

The polycrystalline EPR spectra of the synthesized inorganic compounds have been recorded at room temperature and liquid nitrogen temperature (Figures S12 and S13, see the Supporting Information). No changes in the line shape, line width, and resolution as a function of temperature for all complexes have been observed. The anisotropic EPR spectral features can be linked with the axial symmetry having a $d_{x^2-y^2}$ ground state, where the geometry can be assigned to an elongated octahedral, a square-pyramidal, or a square planar geometry. At the X-band, the EPR spectra for 1, 2, and 4 showed an asymmetry in the perpendicular region, with $g_x = 2.091$, $g_y = 2.092$, and $g_z = 2.21$ ($g_{av} = 2.13$) for 1, $g_x = 2.075$, $g_y = 2.151$, and $g_z = 2.11$ ($g_{av} = 2.11$) for 2, and $g_x = 2.091$, $g_y = 2.132$, and $g_z = 2.212$ ($g_{av} = 2.14$) for 4 (see Figure S12, Supporting Information). This range of values is usually observed in the case of compounds with a distorted squarepyramidal geometry. The EPR spectra for 3 are typical of Cu(II) ion coordinated in a distorted octahedron with $g_x = 2.091$, $g_y = 2.131$, and $g_z = 2.291$ ($g_{av} = 2.17$) for 3 in agreement with its structure. The frozen solution EPR spectra of 1 and 2 compounds at 77 K show a well-defined resolution of hyperfine splitting of parallel orientation that is the result of the interaction of an unpaired electron with copper nuclei ($I = 3/2$). The spin Hamiltonian parameters have been calculated by computer simulation (Figure S13, see the Supporting Information) of the experimental spectra with $g_x = g_y = g_{\downarrow} = 2.065$, $g_z = g_k = 2.211$, and $A_k = 164$ G for 1, $g_x = 2.069$, $g_y = 2.073$, $g_z = g_k = 2.215$, and $A_k = 113$ G for 2, $g_x = g_y = g_{\downarrow} = 2.098$, $g_z = g_k = 2.289$, and $A_k = 163$ G for 3, and $g_x = g_y = g_{\downarrow} = 2.068$, $g_z = g_k = 2.301$, and $A_k = 146$ G for 4. Hence, the EPR parameters of all inorganic compounds in frozen solutions are also in agreement with the axial symmetry of the Cu(II) coordination sphere. Furthermore, the changes in parameter values upon dissolving complexes 1, 2, and 4 strongly suggest the replacement of the labile water or NO_3^- ligands with the solvent molecules as has been found in many other already described complexes.^{47,48}

2.3.4 Luminescence Properties

All heteronuclear Ir(III)/Cu(I) complexes emit in fluid solution at room temperature upon photoexcitation in the absorption manifold at 340 nm. The emission was structureless and peaked at 450 nm. A particular case is constituted by complex 4 that manifests an emission peak centered at 540 nm (Figure 2). Moreover, the emission intensity was stronger in dimethylformamide (DMF) compared to DMSO, probably due to stronger solvation interactions in the case of DMSO, which enhances the non-radiative deactivation of these species (see Figure S14, Supporting Information). So, for this reason we decided to conduct all of the spectroscopic measures in DMF. The spectroscopic energy was around 3.2 eV for 1, 2, and 3 complexes and 2.85 eV for 4,

indicating a negligible influence of the solvent in tuning the excited state energy. The coordination of Cu(II) to Ir(III) complexes, which was described by us previously, such as Ir(η^5 -Cp*)Cl₂Pcfx, Ir(η^5 -Cp*)Cl₂Plfx, and Ir(η^5 -Cp*)Cl₂Pnfx, leads to the bathochromic shift of the peak emission maximum wavelength. However, the incorporation of another metallic center to Ir(η^5 -Cp*)Cl₂Psfx causes the red shift of 4 in comparison to Ph₂PCH₂sfx but a blue shift toward the Ir(η^5 -Cp*)Cl₂Psfx. Therefore, 1 ($\lambda_{\text{max}} = 448$ nm), 2 ($\lambda_{\text{max}} = 442$ nm), and 3 ($\lambda_{\text{max}} = 470$ nm) exhibited purple emission, whereas 4 ($\lambda_{\text{max}} = 513$ nm) exhibited green emission (see Figures S15 and S16, Supporting Information).

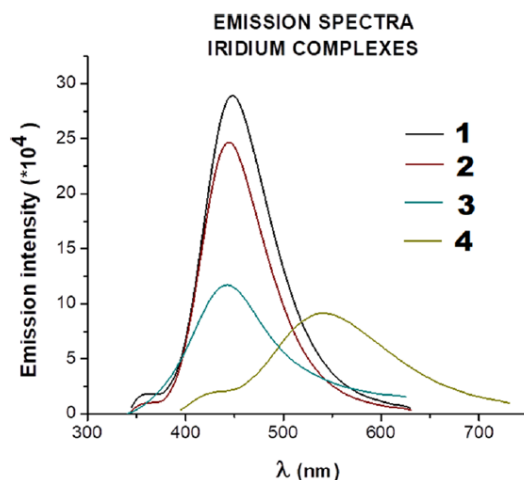


Fig. 2 Emission spectra obtained for heteronuclear Ir(III)/Cu(I) complexes in DMF, $C \approx 0.05$ M.

It could be concluded that the emission wavelength associated with these bimetallic Ir–Cu complexes is strongly related to the nature of the chosen ligand. While 1, 2, and 3 seem to exhibit the same spectroscopic trend, only 4 seems to manifest a different emission pattern.²⁷ The outcome of conducted luminescence experiments corresponds to our previous findings, not only for Ir(III) complexes but also for Ru(II) as well as Cu(I) with the same phosphine ligands.^{13,26,27} Luminescence properties of studied complexes are helpful in detecting their intercellular localization. We were able to localize the complexes inside cancer cells, and the results obtained by us are presented below.

2.3.5 Magnetic Properties

Magnetic data were acquired with the help of the SQUID magnetometer (MPMS, Quantum Design) at an applied field of $B_0 = 0.5$ T, after correction to the underlying diamagnetism, and transformed to the temperature dependence of the $\chi_M T$ product (or effective magnetic moment) (Figure 3, left). The field dependence of the magnetization per formula unit $M_1 = M_{\text{mol}}/N_A \mu_B$ at a constant temperature is shown in Figure 3, right. All examined complexes magnetically behave as a mononuclear unit with $S_{\text{Cu}} = 1/2$ because Ir(III) ions are diamagnetic. Assuming $g = 2.0$, the expected high-temperature value for the $S = 1/2$ spin system is $\mu_{\text{eff}} = g[S(S + 1)]^{1/2} = 1.73 \mu_B$. The experimental data for 1–4 compounds show a value of $\mu_{\text{eff}} = 1.80 \mu_B$ for 1 ($\chi_M T = 0.41 \text{ cm}^3 \text{ K/mol}$), $\mu_{\text{eff}} = 1.75 \mu_B$ for 2 ($\chi_M T = 0.39 \text{ cm}^3 \text{ K/mol}$), $\mu_{\text{eff}} = 1.74 \mu_B$ for 3 ($\chi_M T = 0.38 \text{ cm}^3 \text{ K/mol}$), and $\mu_{\text{eff}} = 1.73 \mu_B$ for 4 ($\chi_M T = 0.38 \text{ cm}^3 \text{ K/mol}$) at $T = 300$ K. The $\chi_M T$ (and/or the effective

magnetic moment) (Figure 3 left) for 1 and 3 decreases slowly with decreasing the temperature down to $T=25$ K. Below 50 K, a rapid decrease of the $\chi_{\text{M}}T$ was observed, reaching an $\chi_{\text{M}}T$ value of $0.33 \text{ cm}^3 \text{ K/mol}$ ($1.62 \mu_{\text{B}}$) for 1 and an $\chi_{\text{M}}T$ of $0.29 \text{ cm}^3 \text{ K/mol}$ ($1.51 \mu_{\text{B}}$) for 3 at 1.8 K. This feature indicates the antiferromagnetic nature of intramolecular exchange interactions mediated through carboxylate groups of phosphino-fluoroquinolone ligands and OH^- linkers in 3 or intermolecular interaction between the nearest copper ion in the supramolecular architecture. Compounds 2 and 4 exhibit weak intermolecular ferromagnetic coupling (systematic increase of $\chi_{\text{M}}T$ value with the temperature) with similar strength (Figure 3, left), which can be seen from almost the same position of the maximum of χT . The magnetization data at $T = 2.0$ and $B_{\text{DC}} = 5.0$ T saturates to $M1 = M_{\text{mol}}/(N_{\text{A}}\mu_{\text{B}}) = 0.86 \mu_{\text{B}}$ (1, 3) and 1.00 (2, 4), which confirms the presence of some weak antiferromagnetic interactions in the case of 1 and 3. A significant contribution of the temperature-independent paramagnetism (TIP) is reflected in the slopes of the $\chi_{\text{M}}T$ dependencies at higher temperatures. A more detailed discussion about the pathways of magnetic exchange interactions together with theoretical analysis based on proper Hamiltonian is presented in the Supporting Information. Additionally, unexpected information was obtained from the AC susceptibility measurements for complex 2. The in-phase (χ_{M}') and out-of-phase (χ_{M}'') components exhibit small frequency dependence with the application of an external field of 0.2 T, indicating the possibility of a slow relaxation of magnetization typical for SMM or SIM behavior (Figures S17 and S18, see the Supporting Information). This phenomenon for Cu(II) ions is very rare due to the absence of a barrier to spin reversal: the axial zero-field splitting parameter D is undefined. More details on the AC measurement procedure and an explanation of the presence of the relaxation process are provided in the Supporting Information.

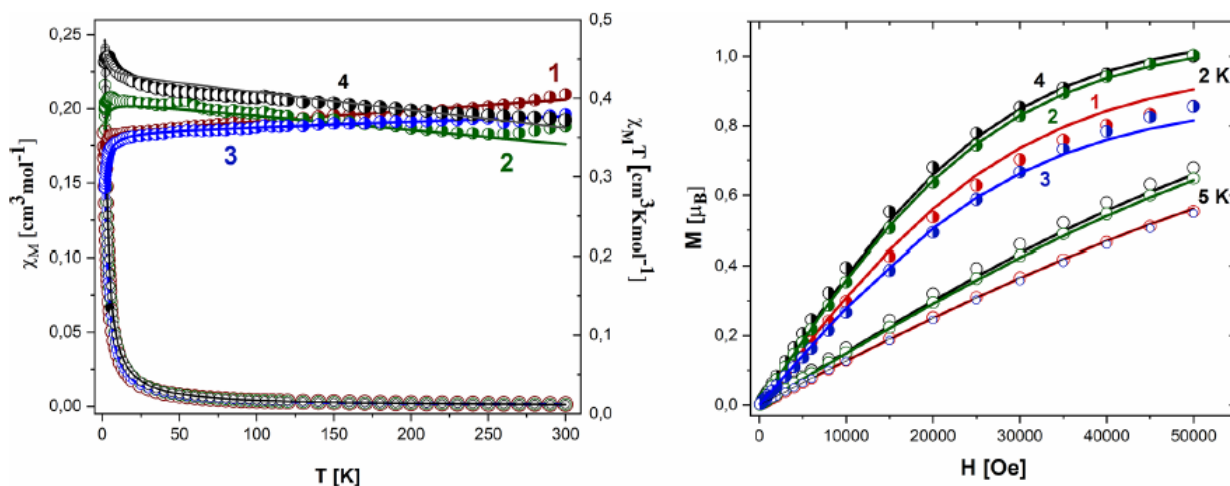


Fig. 3 Left: thermal dependence of $\chi_{\text{M}}T$ (half-open circles) and χ_{M} (open circles) for 1, $[\text{Ir}(\eta^5\text{-Cp}^*)\text{Cl}_2\text{Pcfx-Cu}(\text{phen})]$; 2, $[\text{Ir}(\eta^5\text{-Cp}^*)\text{Cl}_2\text{PnfxCu}(\text{phen})]$; 3, $[\text{Ir}(\eta^5\text{-Cp}^*)\text{Cl}_2\text{Plfx-Cu}(\text{phen})]$; and 4, $[\text{Ir}(\eta^5\text{-Cp}^*)\text{Cl}_2\text{Psfxcu}(\text{phen})]$. Right: magnetization as a function of the magnetic field at 2.00 K (half-open circles) and 5.00 K (open circles) for 1, IrPcfxCu ; 2, IrPnfxCu ; 3, IrPlfxCu ; and 4, IrPsfxcu . The solid lines (on all graphs) are calculated using the Heisenberg–Dirac–van Vleck (HDVV) spin Hamiltonian and PHI.⁴⁹

2.3.6 Electrochemical behaviour

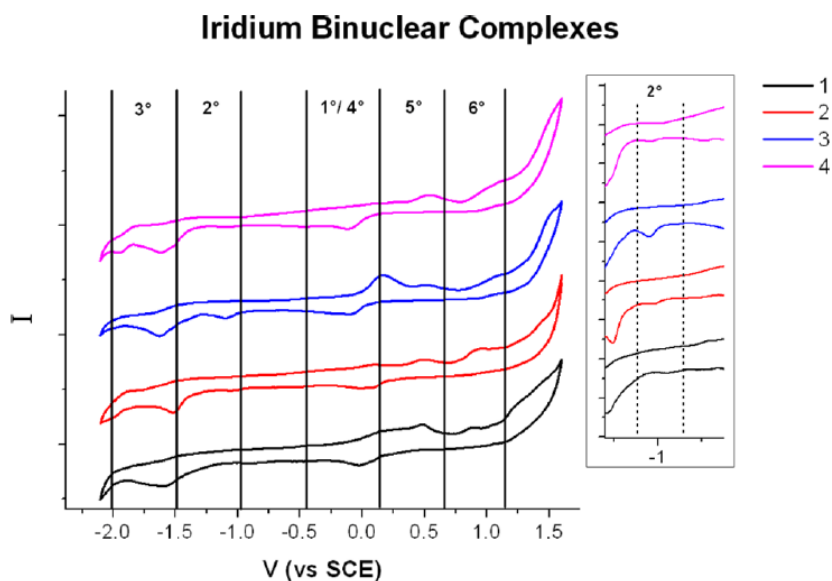


Fig. 4 Cyclic voltammetry of binuclear complexes of Ir(III)/Cu(II) in DMF (50 mV/s from -2.1 to $+1.6$ vs SCE, $TBAPF_6$ 0.1M as a supporting electrolyte).

We decided to investigate the electrochemical properties of the Ir(III)–Cu(II) complex to understand its role in cellular signaling through redox chemistry. Any disruptions of intracellular redox processes can significantly affect a plethora of cellular processes such as proliferation. This may, in turn, result in serious consequences (*e.g.*, cell death).⁴ Cyclic voltammetry of iridium binuclear complexes at 50 mV/s in purged DMF is reported in Figure 4. The scans were recorded by scanning first in the cathodic direction (toward negative voltage) and then moving back to positive values. At a negative voltage, we observed two major irreversible reductive waves, the first at *ca.* -1.1 V vs saturated calomel electrode (SCE) for all heteronuclear complexes Ir(III)/Cu(II) (wave 2°), followed by another more intense reduction wave centered at *ca.* -1.6 V vs SCE (wave 3°) that, upon back scanning, results in a first anodic feature at $+0.2$ V (wave no. 4), followed by a convolved response spanning the voltage range $+0.4$, $+1.3$ V (wave nos. 5, 6) (see Figure S19 in the Supporting Information). In contrast, the restriction of the voltage scan to $-0.3/+0.3$ V vs SCE only makes evident the clean quasireversible process of Cu(II)/(I) with $E_{1/2}$ of *ca.* 0 V (peaks 1 and 4). The complex appearance of the voltammetric waves in the $0/+1.3$ V range of the full scan mostly originates from the oxidation of decomposition products generated during the cathodic scan at potentials more negative than -0.9 V vs SCE.

2.3.7 Biological Study

	IC ₅₀ [μ M] \pm SD; 24 h				
	A549	MCF7	DU145	WM2664	HEK293T
IrPcfcCu (1)	35.5 \pm 5.6 $\times 10^{-3}$	35.3 \pm 6.5	12.8 \pm 2.7 $\times 10^{-7}$	5.2 \pm 4.1 $\times 10^{-3}$	786.8 \pm 11.2
IrPnfcCu (2)	11.2 \pm 7.8 $\times 10^{-3}$	30.0 \pm 0.7	10.8 \pm 1.9 $\times 10^{-4}$	9.9 \pm 3.8 $\times 10^{-3}$	756.8 \pm 5.7
IrPlfcCu (3)	31.6 \pm 7.6 $\times 10^{-3}$	24.2 \pm 7.2	14.2 \pm 2.4 $\times 10^{-3}$	10.1 \pm 2.2 $\times 10^{-3}$	775.8 \pm 15.7
IrPsfCu (4)	18.1 \pm 1.3 $\times 10^{-3}$	10.5 \pm 0.8	10.1 \pm 2.9 $\times 10^{-3}$	6.2 \pm 2.4 $\times 10^{-3}$	676.8 \pm 9.2
cisplatin (CDDP)	57.0 \pm 1.3 $\times 10^{-3}$	51.9 \pm 4.6	68.3 \pm 1.3 $\times 10^{-3}$	2.6 \pm 0.6	21.0 \pm 1.8
Cu(phen)(NO ₃) ₂	536.8 \pm 13.2	317.8 \pm 12.2	412.4 \pm 10.9	933.1 \pm 13.6	81.8 \pm 8.2
	IC ₅₀ [μ M] \pm SD; 72 h (24 + 48 h)				
	A549	MCF7	DU145	WM2664	HEK293T
IrPcfcCu (1)	42.4 \pm 7.3 $\times 10^{-5}$	>1000	125.7 \pm 3.4	137.1 \pm 2.2	886.8 \pm 12.7
IrPnfcCu (2)	36.6 \pm 2.8 $\times 10^{-3}$	>1000	122.7 \pm 5.4	155.1 \pm 3.2	856.8 \pm 15.9
IrPlfcCu (3)	36.0 \pm 2.2 $\times 10^{-2}$	>1000	126.2 \pm 4.4	229.3 \pm 25.9	822.8 \pm 12.3
IrPsfCu (4)	0.6 \pm 2.9 $\times 10^{-4}$	>1000	53.6 \pm 0.40	212.2 \pm 10.5	776.8 \pm 15.3
cisplatin (CDDP)	71.7 \pm 3.7	17.7 \pm 8.6	65.5 \pm 3.6	8.3 \pm 0.4	10.3 \pm 2.1
Cu(phen)(NO ₃) ₂	721.2 \pm 15.1	425.5 \pm 9.9	658.9 \pm 14.5	1106.5 \pm 18.5	42.4 \pm 9.1

Tab. 3 Values of IC₅₀ [μ M] (Concentration of a Drug Required to Inhibit the Growth of 50% of the Cells) for WM2661, A549, MCF7, DU145, and HEK293T Cells after 24 and 24 + 48 h treatment with the studied compounds and Cisplatin as reference

The cytotoxic potency of a drug is generally associated to its cellular uptake, which is in turn connected to its lipophilicity. In general, hydrophobicity plays a critical role in structure–activity correlations and in determining the biological properties of the drug.²⁷ The octanol–water partition coefficients (log *P*) for all complexes were determined and are listed in Table S3 in the Supporting Information (log *P* values have been calculated using programs ACD/log *P* and ALOGPS 2.150). The complexes containing Cu(phen) ligands show substantially lower lipophilicity than mononuclear complexes, which is in accordance with the hydrophilic nature of the diimine ligands.⁵⁰ The cytotoxicity of the four novel heteronuclear Ir(III)–Cu(II) complexes was assessed against four selected cancer cell lines: A549, MCF7, DU145, WM2664, and one normal HEK293T

cell line *in vitro* (Table 3). IC₅₀ values (concentration of a drug required to inhibit the growth of 50% of the cells) were assessed in two different approaches, *i.e.*, after 24 or 24 + 48 h, using the 3-(4,5-dimethylthiazole)-2,5-diphenyltetrazolium bromide (MTT) method. Cancerous and noncancerous diseases have also been treated with the well-known drug Cisplatin in the same concentration range as investigated complexes and are considered as a control. IC₅₀ values have been determined from the plots of cell viability at various concentrations of each compound by matching appropriate dose–response curves and are presented in Table 3. Notably, all of the heteronuclear Ir(III)/Cu(II) complexes showed higher cytotoxicity (after 24 h of incubation) than Cisplatin against all studied cell lines except the WM2664 cells. Interestingly, lung carcinoma cancer cells (A549) were the most sensitive cell line to heteronuclear Ir(III)–Cu(II) complexes even in the case of both incubation times (24 and 24 + 48 h). Among all investigated inorganic compounds, complex 4 exhibited the most significant antiproliferative activity *in vitro* with an IC₅₀ value of 0.6 μ M against the A549 cell line, which was more than 100 times more effective than the reference drug Cisplatin.

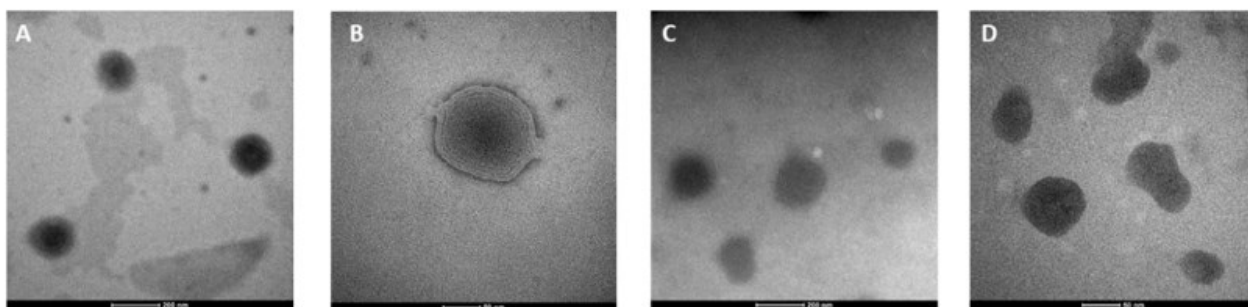


Fig. 5 TEM images of empty liposomes (A, B) and liposomes loaded with the Ir(III)/Cu(II) complex (1a; C, D)

Cytotoxic activity of complex 4 toward A549 cells was higher after 24 and 48 h of recovery time (24+48 h), compared to the experimental approach where cytotoxicity was evaluated after 24 h. This indicates that intercellular biochemical changes initiated during the 24 h of incubation cannot be repaired by the cells. Repair systems responsible for minimizing toxicity are almost not sufficient and may result in breaking down the resistance. In addition, compound 4 elicited a moderate cytotoxic effect against other tumor cell lines (except MCF7 after 72 h). Therefore, this suggests that the introduction of the third-generation fluoroquinolone ($\text{Ph}_2\text{PCH}_2\text{sfx}$) causes a significant increase in cytotoxicity to A549 cells compared to the complexes containing the second-generation fluoroquinolones ($\text{Ph}_2\text{PCH}_2\text{nfx}$, $\text{Ph}_2\text{PCH}_2\text{cfx}$, $\text{Ph}_2\text{PCH}_2\text{lfx}$). This is consistent with our previous observations about the cytotoxicity of mononuclear Ir(III) complexes with then same phosphine ligands.²⁷ The described results show that the activity of all complexes against WM2664 is in the same range as for Cisplatin after 24 h. Such good cytotoxicity *in vitro* was achieved simultaneously with very low toxicity toward normal cell lines. A comparison of the IC_{50} values shown by heteronuclear ($[\text{Ir}(\eta^5\text{-Cp}^*)\text{Cl}_2\text{Psfx-Cu}(\text{phen})]$ (4), $[\text{Ir}(\eta^5\text{-Cp}^*)\text{Cl}_2\text{Plfx-Cu}(\text{phen})]$ (3), $[\text{Ir}(\eta^5\text{-Cp}^*)\text{Cl}_2\text{PcfxCu}(\text{phen})]$ (1), $[\text{Ir}(\eta^5\text{-Cp}^*)\text{Cl}_2\text{PnfxCu}(\text{phen})]$ (2)) vs mononuclear complexes ($[\text{Ir}(\eta^5\text{-Cp}^*)\text{Cl}_2\text{Psfx}]$, $[\text{Ir}(\eta^5\text{-Cp}^*)\text{Cl}_2\text{Plfx}]$, $[\text{Ir}(\eta^5\text{-Cp}^*)\text{Cl}_2\text{Pcfx}]$, $[\text{Ir}(\eta^5\text{-Cp}^*)\text{Cl}_2\text{Pnfx}]$) indicated that the presence of second metal caused a significant decrease in the toxicity against the HEK293T cell line.²⁷ In the A549 cell line, the selectivity index (SI – IC_{50} (normal cell line)/ IC_{50} (cancer cell line)) was found to be approximately 1290 for complex 4. Remarkably, such a high value was achieved despite the addition of a second metal with phenanthroline, which is known to be toxic.⁵¹ This suggests that the introduction of a second metal is an effective method of minimizing toxicity to healthy cells and may bring into play different properties of the resulting compound.

2.3.8 Characterization of Liposomes

To overcome toxicity and low water solubility, complex $[\text{Ir}(\eta^5\text{-Cp}^*)\text{Cl}_2\text{Pcfx-Cu(phen)}]$ (1) has been encapsulated inside liposomes (1L) in two different concentrations (1La: 0.25 mg/mL and 1Lb: 0.5 mg/mL). Negative staining transmission electron microscopy (TEM) images exhibited a spherical shape with a smooth surface and laminar character of homogeneous liposomal dispersion (Figure 5). Statistical analysis of liposome size obtained from TEM analysis (ImageJ) is in agreement with dynamic light scattering (DLS) data (Table S4, see the Supporting Information). Although the size differences between TEM and DLS can be clarified by the technique differences, in TEM, the nanoparticles are dried and the size should be smaller after shrinking than in the case of DLS.⁵² The average size of empty liposomes was *ca.* 135 nm, while that of liposomes loaded with the Ir(III)/Cu(II) complex was *ca.* 110 nm, with the polydispersity index indicating a quite narrow size distribution. The ζ -potential (the electrostatic repulsion of the particle surface) was examined in phosphate-buffered saline (PBS) (pH = 7.4), resulting in negative values for empty and loaded liposomes (*ca.* -30 and -42 mV, respectively) and indicating a stable dispersion.

	HaCaT	A549	Du145
L	180.47 ± 0.108 µg/mL	21.18 ± 0.143 µg/mL	12.56 ± 0.175 µg/mL
1La	260.92 ± 0.172 µg/mL	12.31 ± 0.130 µg/mL	1.74 ± 0.132 µg/mL
	200.68 ± 2.081 µM	9.47 ± 0.261 µM	1.34 ± 0.051 µM
1Lb	200.20 ± 0.118 µg/mL	7.26 ± 0.124 µg/mL	1.56 ± 0.128 µg/mL
	154.14 ± 1.051 µM	5.58 ± 0.121 µM	1.20 ± 0.071 µM
CDPP	9.69 ± 0.206 µg/mL	17.16 ± 0.181 µg/mL	20.56 ± 0.219 µg/mL
	32.20 ± 0.881 µM	56.99 ± 0.481 µM	68.28 ± 2.081 µM

Tab. 4 IC_{50} (µg/mL and µM) Values of the Investigated Compounds toward the Selected Cancer (A549, DU145) and Noncancer (HaCaT) Cell Lines for 24 h (1La: 0.25 mg/mL and 1Lb: 0.5 mg/mL)

The anticancer activity of the tested iridium liposomes was evaluated by their cytotoxicity, determined by the MTT assay against cancer (A549, DU145) and noncancer (HaCaT) cells. The IC_{50} values (concentration at which 50% of the cells are not able to grow any longer) for the tested compounds after 24 h are summarized in Table 4. The cytotoxic activity of the used carriers (liposome, L), the reference compound cisplatin (CDPP), and complex $[\text{Ir}(\eta^5\text{-Cp}^*)\text{Cl}_2\text{Pcfx-Cu(phen)}]$ (1L) encapsulated inside liposomes in two different concentrations (1La: 0.25 mg/mL and 1Lb: 0.5 mg/mL) were also determined. It was observed that the empty liposome exhibited no cytotoxicity, while IC_{50} values for liposomes loaded with the Ir/Cu compounds (1La and 1Lb) were lower than that for CDDP. In the case of the DU145 line, a 10-fold decrease was observed for complex accumulated inside the liposome. Moreover, the compounds exhibited relatively lower cytotoxic activity against normal cells, human keratinocytes.

2.3.9 First Insight into the cytotoxic action mode

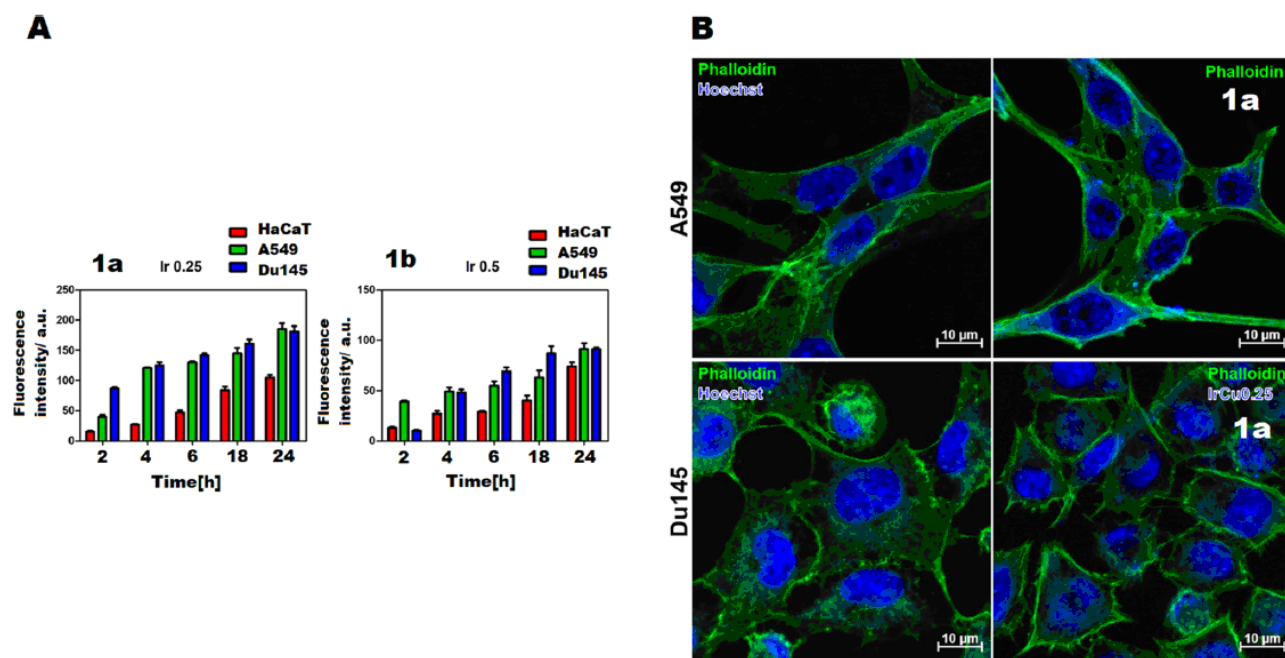


Fig. 6 Cellular uptake. (A) Accumulation of compounds (1La, IrPcfxCu_L0.25; 1Lb, IrPcfxCu_L0.5) in cells as a function of incubation time. (B) Accumulation of 1a in A549 and DU145 cells. Green fluorescence, phalloidin; blue fluorescence, tested compounds.

To investigate the mechanism underlying the activity of liposomes loaded with the Ir(III)/Cu(II) complex in selected cell lines (HaCat, A549, and DU145) and to locate their possible targets in the cell, total cellular uptake and confocal microscopy tests were first performed. Cellular accumulation of 1 in liposomes has been determined by the inductively coupled plasma mass spectrometry (ICP-MS) technique. The time-dependent cellular uptake of 1L compounds is given in Figure 6A. The results obtained confirm that a higher accumulation of liposomes in cells is observed with the increase of time. The highest accumulation of the compound was observed after 24 h. The compound 1L accumulated to a greater extent because a smaller amount of the compound was encapsulated in the liposomes, making them smaller in size. Moreover, we indicated the main accumulation of 1L in nuclei (Figure 6B). It is noteworthy that the accumulation of 1L differed significantly between cancer and normal cells, showing lower accumulation in the noncancer HaCaT cell line. These results fully corroborate the differences between the cytotoxicity of loaded nanoformulations against the cancer lines and the normal cell line. The activity of the tested compounds is certainly associated with cell cycle disruption (Figure 7). Previously published studies confirm that cell cycle arrest is a characteristic of many compounds with anticancer properties. The cell cycle is divided into three main phases: the G0/G1 phase, the S phase, and the G2/M phase.⁵³ DNA content was measured using propidium iodide (PI) and analyzed by flow cytometry (Figure 7A). Before the experiment, the cells were synchronized and then the test compounds were added at different concentrations. Iridium liposomes

Induction of apoptotic death in response to anticancer drugs is one of the most important mechanisms for cancer cell death. Most tumor cells exhibit sensitivity to certain apoptotic stimuli from chemotherapeutic agents.⁴¹ The obtained results confirm that the cell death mechanisms are very similar for the iridium liposomes tested. Interestingly, compounds with lower iridium concentrations (1La) induce a high percentage of cells in late apoptosis (Figure 7B). In the case of the DU145 line, less toxicity of the compounds is observed, particularly for the liposomes with higher iridium concentrations (1Lb), for which the percentage of apoptotic cells is also the highest. Analyzing the cell death mechanisms induced by iridium liposomes, it can be observed that compounds with lower iridium concentration were more effective, and the percentage of living cells was 7% for the A549 cell line and 18% for the DU145 cell line, respectively. Compared to Cisplatin, a significantly higher percentage of late-apoptotic cells than necrotic cells was observed after treatment with the tested CTRL compounds. Apoptosis is a more desirable cell death process because it does not lead to the inflammatory process that occurs with necrosis.

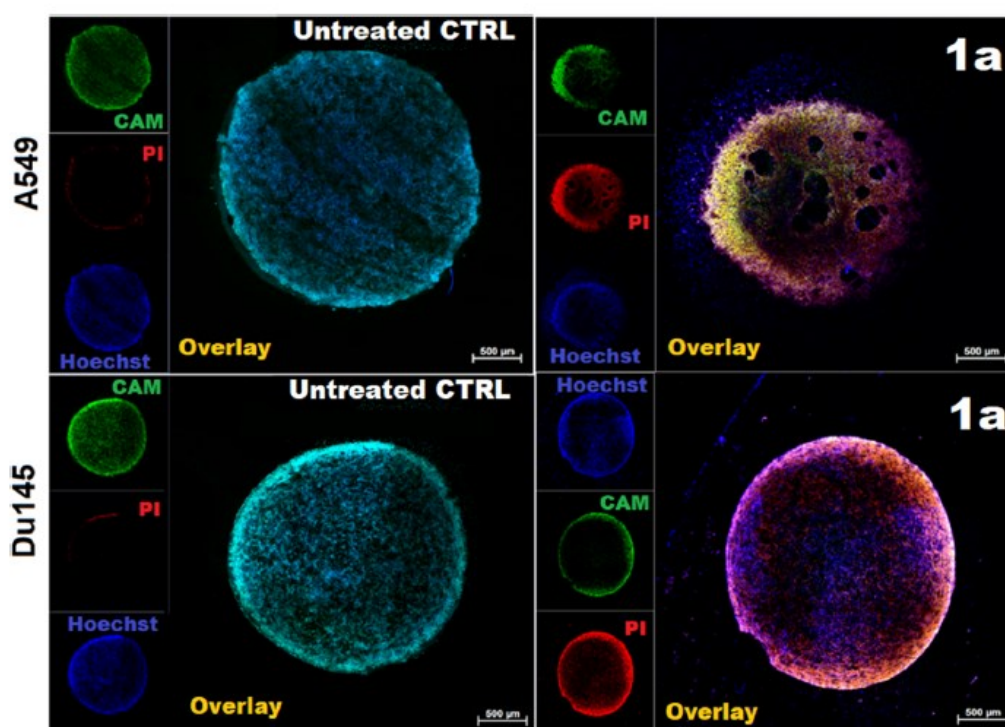


Fig. 9 A549 (on top) and DU145 (on bottom) spheroids: representative live/death fluorescence images of spheroids subjected to 1a and corresponding control untreated spheroids grown in the same culturing conditions.

Several studies have demonstrated that cancerous damage by metal complexes leads to the overproduction of reactive oxygen species (ROS). An increased ROS level can cause a cell cycle arrest or lead to apoptotic cancer cell death.¹³ Therefore, it was important to check whether the cellular damage induced by the liposomal Ir(III)–Cu(II) complex (1L) would lead to increased ROS production. Cellular ROS

generation in A549 and DU145 cells upon 30 min and 4, 12, and 24 h treatment with empty liposome (L), 1L, and cisplatin (CDPP) was monitored by a fluorescent H2DCF-DA ROS probe ($\lambda_{\text{ex}} = 495 \text{ nm}$, $\lambda_{\text{em}} = 530 \text{ nm}$). H_2O_2 was used as a positive control in the first and second cases, respectively. The fluorescence intensity-ROS dependence over time is presented in Figure 8A,B. It was proved that the investigated complex 1L encapsulated inside liposomes in two different concentrations (1La, 1b) induced ROS production inside the treated DU145 and A549 cancer cells. It was proven that ROS generation in both cancerous lines treated with liposomal complex caused a significant increase over time in a concentration-dependent manner. The results obtained on two-dimensional (2D) cell culture encouraged us to investigate the antitumor activity of the selected Ir(III)–Cu(II) complex (1a) also in 3D A549 and DU145 spheroidal culture. In addition, compared to classic adherent culture, spheroids can provide a microenvironment that more closely mimics the cellular interactions observed in tumor tissues. The therapeutic potential of synthesized compounds on 3D spheroids was detected by fluorescence staining of live and dead cells (Figure 9). For untreated 3D spheroid with normal morphology and structure, mostly we observed live cells and a small amount of dead cells mainly in the superficial regions. In contrast, after spheroid treatment by complex, we observed a significant increase in dead cells after spheroid treatment by complex.

3. Conclusions

The present work demonstrates the synthesis, physicochemical characterization, and anticancer activity *in vitro* of $[\text{Ir}(\eta^5\text{-Cp}^*)\text{Cl}_2\text{Pcfx-Cu}(\text{phen})]$ (IrPcfxCu (1)), $[\text{Ir}(\eta^5\text{-Cp}^*)\text{Cl}_2\text{Pnfx-Cu}(\text{phen})]$ (IrPnfxCu (2)), $[\text{Ir}(\eta^5\text{-Cp}^*)\text{Cl}_2\text{Plfx-Cu}(\text{phen})]$ (IrPlfxCu (3)), and $[\text{Ir}(\eta^5\text{-Cp}^*)\text{Cl}_2\text{Psfx-Cu}(\text{phen})]$ (IrPsfxCu (4)) complexes. All inorganic compounds were characterized by ESI-MS spectrometry, selected spectroscopic methods (*i.e.*, IR, fluorescence, and EPR), cyclic voltammetry, and variable temperature magnetic susceptibility measurements. Three of four complexes were structurally identified by single-crystal X-ray diffraction analysis. The coordination geometry of the iridium(III) ion in all Ir(III)–Cu(II) complexes adopts the half-sandwich pseudo-octahedral “three-leg piano-stool” geometry. The cyclopentadienyl fragment served as the top of the stool and the three leg sites were occupied by phosphorous from phosphine ligand and two chloride anions. Cu(II) ion in all Ir(III)–Cu(II) complexes is coordinated *via* nitrogen atoms (from phenanthroline ligand) and IrP(FQ) complexes (where FQ denotes fluoroquinolone) *via* deprotonated carboxylate and pyridone oxygen atoms forming a distorted square-pyramidal coordination geometry in the case of IrPcfxCu (1) and IrPnfxCu (3) complexes. Importantly, the crystal structure of $[\text{Ir}(\eta^5\text{-Cp}^*)\text{Cl}_2\text{Plfx-Cu}(\text{phen})]$ features the 1D metal–organic polymer and the analysis of packing in 3 reveals that the coordination geometry around Cu(II) ion is distorted octahedral. Furthermore, investigation of the elucidation of the behaviour of the Ir(III)–Cu(II) compounds allowed us to formulate the following general conclusions: (i) All complexes exhibit intense emission in solution; (ii) Redox activity of all complexes was

confirmed by cyclic voltamperometry; (iii) All complexes are characterized by weak magnetic properties. Surprisingly, one of the studied systems $[\text{Ir}(\eta^5\text{-Cp}^*)\text{Cl}_2\text{Pnfx-Cu(phen)}]$ exhibits a slow magnetic relaxation under the moderate DC magnetic field, which is extremely rare in the case of Cu(II) complexes; (iv) The heteronuclear Ir(III)/Cu(II) complexes displayed higher cytotoxicity than Cisplatin against all cell lines (A549, MCF7, DU145) except for the WM2664 cell line. (v) After encapsulation of complex 1 in liposomal formulation, a 10- fold cytotoxicity decrease toward the DU145 cell line was observed. (vi) Liposomes loaded with $[\text{Ir}(\eta^5\text{-Cp}^*)\text{Cl}_2\text{Pcfx- Cu(phen)}]$ effectively accumulate inside human lung adenocarcinoma and human prostate carcinoma cells with colocalization in nuclei. (vii) A precise cytometric analysis revealed a predominance of apoptosis over the other types of cell death. (viii) Complexes are able to significantly increase ROS generation. (ix) Efficient anticancer action in 3D multicellular tumor spheroids DU145 was demonstrated. All these data show the unique properties of the Ir(III)–Cu(II) complexes presented here and their huge potential in various medical treatments. Redox, luminescence, and magnetically active complexes with anticancer effectiveness (preliminarily proved *in vitro*) can be proposed for magnetic resonance imaging (MRI), targeted delivery *via* magnetic field control, targeted destruction of tumor tissue through hyperthermia or reactive oxygen species (phototherapy). We believe that Ir(III)– Cu(II) compounds are promising agents to further more detailed investigations as anticancer drugs.

4. Experimental Section

All data can be found in the supporting information

References

- [1] Sharma, P. C.; Goyal, R.; Sharma, A.; Sharma, D.; Saini, N.; Rajak, H.; Sharma, S.; Thakur, V. K. Insights on fluoroquinolones in cancer therapy: chemistry and recent developments. *Mater. Today Chem.* 2020, 17, No. 100296.
- [2] Sung, H.; Ferlay, J.; Siegel, R. L.; Laversanne, M.; Soerjomataram, I.; Jemal, A.; Bray, F. Global Cancer Statistics 2020: GLOBOCAN Estimates of Incidence and Mortality Worldwide for 36 Cancers in 185 Countries. *CA_Cancer J. Clin.* 2021, 71, 209–249.
- [3] Xu, Z.; Yang, Y.; Jia, X.; Guo, L.; Ge, X.; Zhong, G.; Chen, S.; Liu, Z. Novel cyclometalated iridium(III) phosphine-imine (PAN) complexes: highly efficient anticancer and anti-lung metastasis agents in vivo. *Inorg. Chem. Front.* 2020, 7, 1273–1283.
- [4] Kołoczek, P.; Skorska-Stania, A.; Cierniak, A.; Sebastian, V.; Komarnicka, U. K.; Płotek, M.; Kyzioł, A. Polymeric micelle-mediated delivery of half-sandwich ruthenium(II) complexes with phosphanes derived from fluoroloquinolones for lung adenocarcinoma treatment. *Eur. J. Pharm. Biopharm.* 2018, 128, 69–81.
- [5] Van Niekerk, A.; Chellan, P.; Mapolie, S. F. Heterometallic Multinuclear Complexes as Anti-Cancer Agents-An Overview of Recent Developments. *Eur. J. Inorg. Chem.* 2019, 2019, 3432–3455.
- [6] Mirzadeh, N.; Reddy, T. S.; Priver, S. H.; Bhargava, S. K. Synthesis, anti-proliferative and apoptosis-inducing studies of palladacycles containing a diphosphine and a Sn,As-based chelate ligand. *Dalton Trans.* 2019, 48, 5183–5192.
- [7] Wenzel, M.; Bigaeva, E.; Richard, P.; Le Gendre, P.; Picquet, M.; Casini, A.; Bodio, E. New heteronuclear gold(I) platinum(II) complexes with cytotoxic properties: are two metals better than one? *J. Inorg. Biochem.* 2014, 141, 10–16.
- [8] Farrell, N. P. Multi-platinum anti-cancer agents. Substitutioninert compounds for tumor selectivity and new targets. *Chem. Soc. Rev.* 2015, 44, 8773–8785.
- [9] Lopes, J.; Alves, D.; Morais, T. S.; Costa, P. J.; Piedade, M. F. M.; Marques, F.; Villa de Brito, M. J.; Garcia, M. H. New copper(I) and heteronuclear copper(I)-ruthenium(II) complexes: Synthesis, structural characterization and cytotoxicity. *J. Inorg. Biochem.* 2017, 169, 68–78.
- [10] Manzotti, C.; Pratesi, G.; Menta, E.; Di Domenico, R.; Cavalletti, E.; Fiebig, H. H.; Kelland, L. R.; Farrell, N.; Polizzi, D.; Supino, R.; Pezzoni, G.; Zunino, F. BBR 3464: a novel triplatinum complex, exhibiting a preclinical profile of antitumor efficacy different from cisplatin. *Clin. Cancer Res.* 2000, 6, 2626–2634.
- [11] Tripathy, S. K.; De, U.; Dehury, N.; Pal, S.; Kim, H. S.; Patra, S. Dinuclear $[(p\text{-cym})\text{RuCl}]_2(\mu\text{-phpy})(\text{PF}_6)_2$ and heterodinuclear $[(\text{ppy})_2\text{Ir}(\mu\text{-phpy})\text{Ru}(p\text{-cym})\text{Cl})(\text{PF}_6)_2$ complexes: synthesis, structure and anticancer activity. *Dalton Trans.* 2014, 43, 14546–14549.
- [12] Zhu, G.; Ma, L. Preparation Thereof and Therapeutic Use Thereof. US9650402B2, 2017.
- [13] Wehbe, M.; Leung, A. W. Y.; Abrams, M. J.; Orvig, C.; Bally, M. B. A Perspective – can copper complexes be developed as a novel class of therapeutics? *Dalton Trans.* 2017, 46, 10758–10773.
- [14] Sessoli, R.; Gatteschi, D.; Caneschi, A.; Novak, M. A. Magnetic bistability in a metal-ion cluster. *Nature* 1993, 365, 141–143.
- [15] Nava, A.; Rigamonti, L.; Zangrando, E.; Sessoli, R.; Wernsdorfer, W.; Cornia, A. Redox-Controlled Exchange Bias in a Supramolecular Chain of Fe₄ Single-Molecule Magnets. *Angew. Chem., Int. Ed.* 2015, 54, 8777–8782.
- [16] Ako, A. M.; Mereacre, V.; Lan, Y.; Wernsdorfer, W.; Clerac, R.; Anson, C. E.; Powell, A. K. An Undecanuclear Fe^{III} Single-Molecule Magnet. *Inorg. Chem.* 2010, 49, 1–3.

- [17] Ako, A. M.; Hewitt, I. J.; Mereacre, V.; Clerac, R.; Wernsdorfer, W.; Anson, C. E.; Powell, A. K. A ferromagnetically coupled mn(19) aggregate with a record $S = 83/2$ ground spin state. *Angew. Chem., Int. Ed.* 2006, 45, 4926–4930.
- [18] Moore, E. A.; Janes, R. *Metal–Ligand Bonding*; Royal Society of Chemistry, 2007.
- [19] Korchagin, D. V.; Ivakhnenko, E. P.; Demidov, O. P.; Akimov, A. V.; Morgunov, R. B.; Starikov, A. G.; Palii, A. V.; Minkin, V. I.; Aldoshin, S. M. Field supported slow magnetic relaxation in a quasideimensional copper(ii) complex with a pentaheterocyclictriphenodioxazine. *New J. Chem.* 2021, 45, 21912–21918.
- [20] Han, J.; Xi, L.; Huang, X.; Li, L. Magnetic Relaxation in a Dysprosium–Copper Heterometallic Cluster Involving Nitronyl Nitroxide Biradicals. *Cryst. Growth Des.* 2021, 21, 7186–7193.
- [21] Boča, R.; Rajnak, C.; Titiš, J.; Valigura, D. Field Supported Slow Magnetic Relaxation in a Mononuclear Cu(II) Complex. *Inorg. Chem.* 2017, 56, 1478–1482.
- [22] Hayashi, K.; Nakamura, M.; Sakamoto, W.; Yogo, Y.; Miki, H.; Ozaki, S.; Abe, M.; Matsumoto, T.; Ishimura, K. Superparamagnetic Nanoparticle Clusters for Cancer Theranostics Combining Magnetic Resonance Imaging and Hyperthermia Treatment. *Theranostics.* 2013, 3, 366–376.
- [23] Patil, R. M.; Thorat, N. D.; Shete, P. B.; Bedge, P. A.; Gavde, S.; Joshi, M. G.; Tofail, S. A. M.; Bohara, R. A. Comprehensive cytotoxicity studies of superparamagnetic iron oxide nanoparticles. *Biochem. Biophys. Rep.* 2018, 13, 63–72.
- [24] Bohara, R. A.; Thorat, N. D.; Chaurasia, A. K.; Pawar, S. H. Cancer cell extinction through a magnetic fluid hyperthermia treatment produced by superparamagnetic Co–Zn ferrite nanoparticles. *RSC Adv.* 2015, 5, 47225–47234.
- [25] He, X.; Liu, X.; Tang, Y.; Du, J.; Tian, M.; Xu, Z.; Liu, X.; Liu, Z. Half-sandwich Iridium(III) complexes with triphenylaminesubstituted dipyrindine frameworks and bioactivity applications. *Dyes Pigm.* 2019, 160, 217–226.
- [26] Du, Q.; Yang, Y.; Guo, L.; Tian, M.; Ge, X.; Tian, Z.; Zhao, L.; Xu, Z.; Li, J.; Liu, Z. Fluorescent half-sandwich phosphine-sulfonate iridium(III) and ruthenium(II) complexes as potential lysosometargeted anticancer agents. *Dyes Pigm.* 2019, 162, 821–830.
- [27] Koziel, S.; Komarnicka, U. K.; Ziołkowska, A.; Skorska-Stania, A.; Pucelik, B.; Płotek, M.; Sebastian, V.; Bieńko, A.; Stochel, G.; Kyzioł, A. Anticancer potency of novel organometallic Ir(III) complexes with phosphine derivatives of fluoroquinolones encapsulated in polymeric micelles. *Inorg. Chem. Front.* 2020, 7, 3386–3401.
- [28] Su, W.; Wang, X.; Lei, X.; Xiao, Q.; Huang, S.; Li, P. Synthesis, characterization, cytotoxic activity of half-sandwich rhodium(III), and iridium(III) complexes with curcuminoids. *J. Organomet. Chem.* 2017, 833, 54–60.
- [29] Millett, A. J.; Habtemariam, A.; Romero-Canelon, I.; Clarkson, G. J.; Sadler, P. J. Contrasting Anticancer Activity of Half-Sandwich Iridium(III) Complexes Bearing Functionally Diverse 2-Phenylpyridine Ligands. *Organometallics* 2015, 34, 2683–2694.
- [30] Lapasam, A.; Hussain, O.; Phillips, R. M.; Kaminsky, W. R.; Kollipara, M. R. Synthesis, Characterization and Chemosensitivity Studies of Half-Sandwich Ruthenium, Rhodium and Iridium Complexes Containing $\kappa 1(S)$ and $\kappa 2(N,S)$ Aroylthiourea Ligands. *J. Organomet. Chem.* 2019, 880, 272.
- [31] Liu, Z.; Sadler, P. J. Organoiridium Complexes: Anticancer Agents and Catalysts. *Acc. Chem. Res.* 2014, 47, 1174–1185. (32) Wilbuer, A.; Vlecken, D. H.; Schmitz, D. J.; Kraling, K.; Harms, K.; Bagowski, C. P.; Meggers, E. Iridium Complex with Antiangiogenic Properties. *Angew. Chem., Int. Ed.* 2010, 49, 3839–3842.
- [33] Tian, Z.; Yang, Y.; Guo, L.; Zhong, G.; Li, J.; Liu, Z. Dualfunctional cyclometalated iridium imine NHC complexes: highly potent anticancer and antimetastatic agents. *Inorg. Chem. Front.* 2018, 5, 3106–3112.

- [34] Qu, W.; Zuo, W.; Li, N.; Hou, Y.; Song, Z.; Gou, G.; Yang, J. Design of multifunctional liposome-quantum dot hybrid nanocarriers and their biomedical application. *J. Drug Target.* 2017, 25, 661–672.
- [35] Sercombe, L.; Veerati, T.; Moheimani, F.; Wu, S. Y.; Sood, A. K.; Hua, S. Advances and Challenges of Liposome Assisted Drug Delivery. *Front. Pharmacol.* 2015, 6, No. 286.
- [36] Pattni, B. S.; Chupin, V. V.; Torchilin, V. R. P. New Developments in Liposomal Drug Delivery. *Chem. Rev.* 2015, 115, 10938–10966.
- [37] Petrauskas, A. A.; Kolovanov, E. ACD/LogP method description, Perspect. *Drug Discovery Des.* 2000, 19, 99–116.
- [38] Bykowska, A.; Starosta, R.; Komarnicka, U. K.; Ciunik, Z.; Kyzioł, A.; Guz-Regner, K.; Bugła-Płoskońska, G.; Jeżowska-Bojczuk, M. Phosphine derivatives of ciprofloxacin and norfloxacin, a new class of potential therapeutic agents. *New J. Chem.* 2014, 38, 1062–1071.
- [39] Komarnicka, U. K.; Starosta, R.; Kyzioł, A.; Płotek, M.; Puchalska, M.; Jeżowska-Bojczuk, M. New copper(II) complexes bearing lomefloxacin motif: Spectroscopic properties, in vitro cytotoxicity and interactions with DNA and human serum albumin. *J. Inorg. Biochem.* 2016, 165, 25–35.
- [40] Komarnicka, U. K.; Starosta, R.; Kyzioł, A.; Jeżowska-Bojczuk, M. Copper(I) complexes with phosphine derived from sparfloxacin. Part I – structures, spectroscopic properties and cytotoxicity. *Dalton Trans.* 2015, 44, 12688–12699.
- [41] Kyzioł, A.; Cierniak, A.; Gubernator, J.; Markowski, A.; Jeżowska-Bojczuk, M.; Komarnicka, U. K. Copper(I) complexes with phosphine derived from sparfloxacin. Part III: multifaceted cell death and preliminary study of liposomal formulation of selected copper(I) complexes. *Dalton Trans.* 2018, 47, 1981–1992.
- [42] Bykowska, A.; Komarnicka, U. K.; Jeżowska-Bojczuk, M.; Kyzioł, A. CuI and CuII complexes with phosphine derivatives of fluoroquinolone antibiotics - A comparative study on the cytotoxic mode of action. *J. Inorg. Biochem.* 2018, 181, 1–10.
- [43] Efthimiadou, E. K.; Katsaros, N.; Karaliota, A.; Psomas, G. Mononuclear copper(II) complexes with quinolones and nitrogendonor heterocyclic ligands: Synthesis, characterization, biological activity and interaction with DNA. *Inorg. Chim. Acta* 2007, 360, 4093–4102.
- [44] Efthimiadou, E. K.; Thomadaki, H.; Sanakis, Y.; Raptopoulou, C. P.; Katsaros, N.; Scorilas, A.; Karaliota, A.; Psomas, G. Structure and biological activities of metal complexes of flumequine. *J. Inorg. Biochem.* 2007, 101, 64.
- [45] Uivarosi, V. Metal Complexes of Quinolone Antibiotics and Their Applications: An Update. *Molecules* 2013, 18, 11153–11197.
- [46] Zaky, M.; El-Sayed, M. Y.; El-Megharbel, S. M.; Taleb, S. A.; Refat, M. S. Complexes of nalidixic acid with some vital metal ions: Synthesis, chemical structure elucidation, and antimicrobial evaluation. *Russ. J. Gen. Chem.* 2013, 83, 2488–2501.
- [47] Jeffery, J. C.; Mather, J. P.; Otter, C. A.; Thornton, P.; Ward, M. D. Synthesis of the potentially pentadentate ligand 6,6'-bis(2-hydroxyphenyl)-2,2'': 6'',2''- terpyridine (H2L) and the crystal structure and magnetic properties of $\{Cu(HL)\}_2[PF_6]_2 \cdot 5MeCN$. *J. Chem. Soc., Dalton Trans.* 1995, 5, 819–824.
- [48] Garribba, E.; Micera, G.; Sanna, D.; Strnna-Erre, L. The Cu(II)-2,2'-bipyridine system revisited. *Inorg. Chim. Acta* 2000, 299, 253–261.
- [49] Chilton, N. F.; Anderson, R. P.; Turner, L. D.; Soncini, A.; Murray, K. S. PHI: A Powerful New Program for the Analysis of Anisotropic Monomeric and Exchange-Coupled Polynuclear d- and f- Block Complexes. *J. Comput. Chem.* 2013, 34, 1164–1175.
- [50] Mlakar, M.; Cuculić, V.; Frka, S.; Gašparović, B. Copperphospholipid interaction at cell membrane model hydrophobic surfaces. *Bioelectrochemistry* 2018, 120, 10–17.

[51] Hazarika, P.; Bezbaruah, B.; Das, P.; Medhi, O. K.; Medhi, C. A model study on the stacking interaction of phenanthroline ligand with nucleic acid base pairs: An ab initio, MP2 and DFT studies. *J. Inorg. Biochem.* 2011, *2*, 153–158.

[52] Wang, Z.; Bilegsaikhan, A.; Jerozal, R. T.; Pitt, T. A.; Milner, P. J. Evaluating the Robustness of Metal-Organic Frameworks for Synthetic Chemistry. *ACS Appl. Mater. Interfaces* 2021, *13*, 17517– 17531.

[53] Yang, V. W. The Cell Cycle. In *Physiology of the Gastrointestinal Tract*, 5th ed.; Elsevier, 2012; pp 451–543.

Supporting Information

Compounds under study

1, $[\text{Ir}(\eta^5\text{-Cp}^*)\text{Cl}_2\text{Pcfx-Cu(phen)}](\text{NO}_3)\cdot 1.75(\text{CH}_3\text{OH})\cdot 0.75(\text{H}_2\text{O})$,

$(\text{C}_{51}\text{H}_{52}\text{Cl}_2\text{CuFIrN}_6\text{O}_6\text{P})\cdot(\text{NO}_3)\cdot 1.75(\text{CH}_4\text{O})\cdot 0.75(\text{H}_2\text{O})$ ($M = 1353.19\text{ g mol}^{-1}$), CCDC 2175515

2, $[\text{Ir}(\eta^5\text{-Cp}^*)\text{Cl}_2\text{Pnfx-Cu(phen)}](\text{NO}_3)\cdot 1.75(\text{CH}_3\text{OH})\cdot 0.75(\text{H}_2\text{O})$, $\text{C}_{52}\text{H}_{53}\text{Cl}_2\text{CuFIrN}_5\text{O}_4\text{P}\cdot(\text{NO}_3)\cdot 2.75(\text{H}_2\text{O})$ ($M = 1300.15\text{ g mol}^{-1}$), CCDC 2175516

3, $[\text{Ir}(\eta^5\text{-Cp}^*)\text{Cl}_2\text{Plfx-Cu(phen)}](\text{NO}_3)\cdot 1.3(\text{H}_2\text{O})\cdot 1.95(\text{CH}_3\text{OH})$,

$\text{C}_{52}\text{H}_{53.5}\text{Cl}_2\text{CuF}_2\text{IrN}_5\text{O}_{3.5}\text{P}\cdot(\text{NO}_3)\cdot 1.3(\text{H}_2\text{O})\cdot 1.95(\text{CH}_4\text{O})$ ($M = 1348.02\text{ g mol}^{-1}$), CCDC 2175517

4, $[\text{Ir}(\eta^5\text{-Cp}^*)\text{Cl}_2\text{Psfx-Cu(phen)}]$, $\text{C}_{20}\text{H}_{16}\text{N}_{10}\text{Co}$ ($M = 1231.69\text{ g mol}^{-1}$)

Parameters	$\text{IrPNrCu}(\text{NO}_3)\cdot 1.75(\text{CH}_4\text{O})\cdot 0.75(\text{H}_2\text{O})$	$\text{IrPCpCu}(\text{NO}_3)\cdot 2.75(\text{H}_2\text{O})$	$\text{IrPLmCu}(\text{NO}_3)\cdot 1.3(\text{H}_2\text{O})\cdot 1.95(\text{CH}_4\text{O})$
Moiety Formula	$(\text{C}_{51}\text{H}_{52}\text{Cl}_2\text{CuFIrN}_6\text{O}_6\text{P})\cdot(\text{NO}_3)\cdot 1.75(\text{CH}_4\text{O})\cdot 0.75(\text{H}_2\text{O})$	$\text{C}_{52}\text{H}_{53}\text{Cl}_2\text{CuFIrN}_5\text{O}_4\text{P}\cdot(\text{NO}_3)\cdot 2.75(\text{H}_2\text{O})$	$\text{C}_{52}\text{H}_{53.5}\text{Cl}_2\text{CuF}_2\text{IrN}_5\text{O}_{3.5}\text{P}\cdot(\text{NO}_3)\cdot 1.3(\text{H}_2\text{O})\cdot 1.95(\text{CH}_4\text{O})$
Formula weight ($\text{g}\cdot\text{mol}^{-1}$)	1353.19	1300.15	1348.02
Crystal description	blue	pale green	green
Crystal size (mm)	$0.26 \times 0.12 \times 0.04$	$0.25 \times 0.10 \times 0.05$	$0.28 \times 0.11 \times 0.06$
Temperature (K)	293	100	100
Type of radiation	Cu K α	Cu K α	Cu K α
Crystal system	Triclinic	Triclinic	Orthorhombic
Space group	<i>P</i> -1	<i>P</i> -1	<i>Pbcn</i>
a (Å)	10.801 (2)	10.531 (3)	48.765 (5)
b (Å)	13.114 (3)	15.039 (4)	15.889 (2)
c (Å)	20.180 (5)	18.734 (5)	14.660 (3)
α (°)	100.01 (2)	66.38 (3)	
β (°)	99.95 (2)	82.87 (3)	
γ (°)	91.82 (2)	78.35 (2)	
Volume (Å ³)	2766.9 (11)	2659.4 (14)	11359 (3)
Z	2	8	8
Density calc. (mg/m^3)	1.624	1.624	1.577
Absorptioncoeff. (mm^{-1})	6.81	7.028	6.63
F(000)	1364	1309	5445
$\theta_{\text{min}} - \theta_{\text{max}}$ (°)	4.2–66.9	3.2–74.2	3.9 – 67.5
hkl ange	12 ← h ← - 12 15 ← k ← - 14 23 ← l ← - 24	13 ← h ← - 13 17 ← k ← - 18 21 ← l ← - 23	58 ← h ← - 58 16 ← k ← - 19 17 ← l ← - 17
Reflections collected	33507	43007	63264
Independent reflections	9814	10849	10196
R_{int}	0.037	0.034	0.053
Completeness to θ_{full} (%)	99.5	99.7	99.8
Absorptioncorrectiontype	analytical	gaussian	gaussian
T_{max} and T_{min}	0.773, 0.389	1.000, 0.320	1.000, 0.304
Data/restraints/parameters	9814/6/786	10849/0/877	10196/36/855
Goodness of fit F^2	1.240	1.039	1.127
R_1, wR_2 [$I > 2\sigma(I)$]	0.0442, 0.1082	0.0508, 0.1250	0.0630, 0.1677
R_1, wR_2 (all data)	0.0455, 0.109	0.0601, 0.132	0.0665,
Largest diff. peak and hole ($\text{e}\cdot\text{Å}^{-3}$)	0.99, -0.89	2.03, -3.49	2.29, -2.31

Tab. S1 Crystallographic experimental details

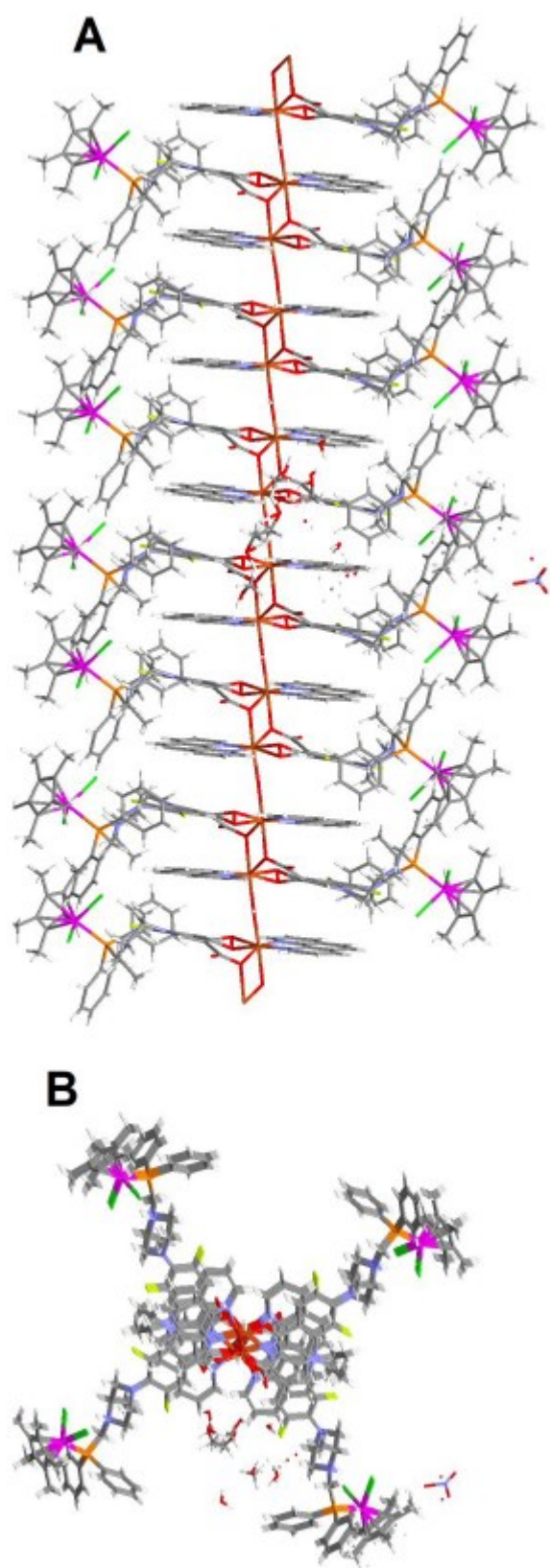


Fig. S1 A perspective view (A and B) of the 1D polymer chain in the crystal structure of **3**.

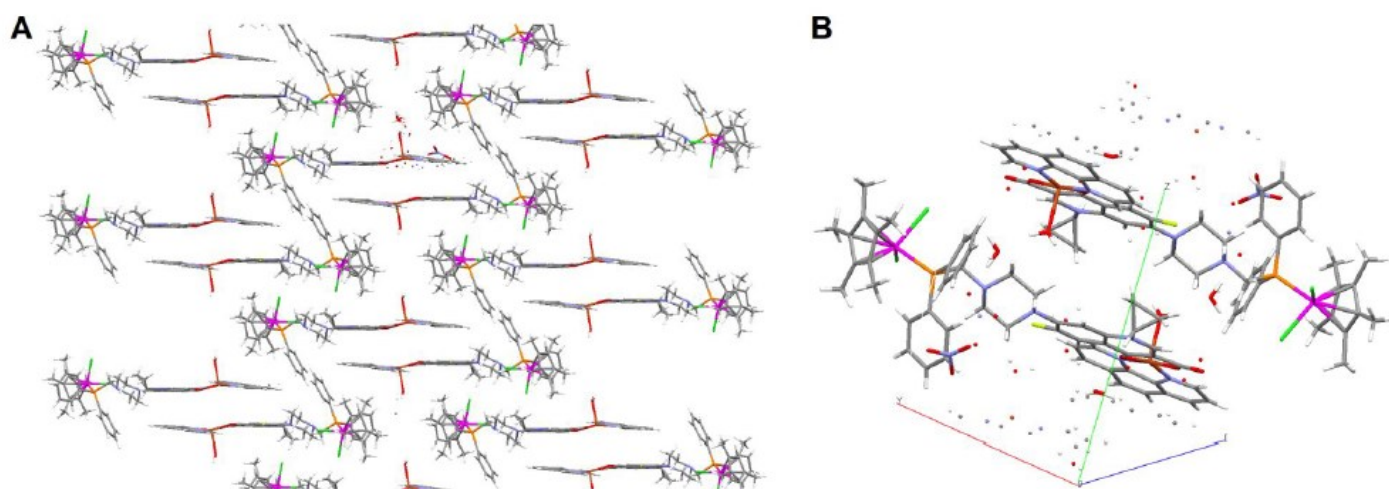


Fig. S2 A perspective view of the complex IrPCu showing (A) π -stacking interaction between the fluoroquinolone rings (B) packing diagram.

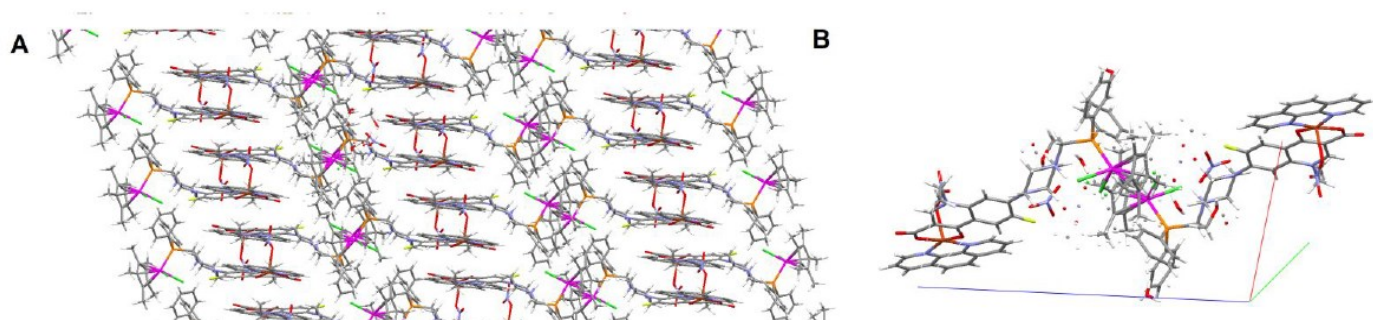


Fig. S3 A perspective view of the complex IrPNrCu showing (A) π -stacking interaction between the fluoroquinolone rings (B) packing diagram.

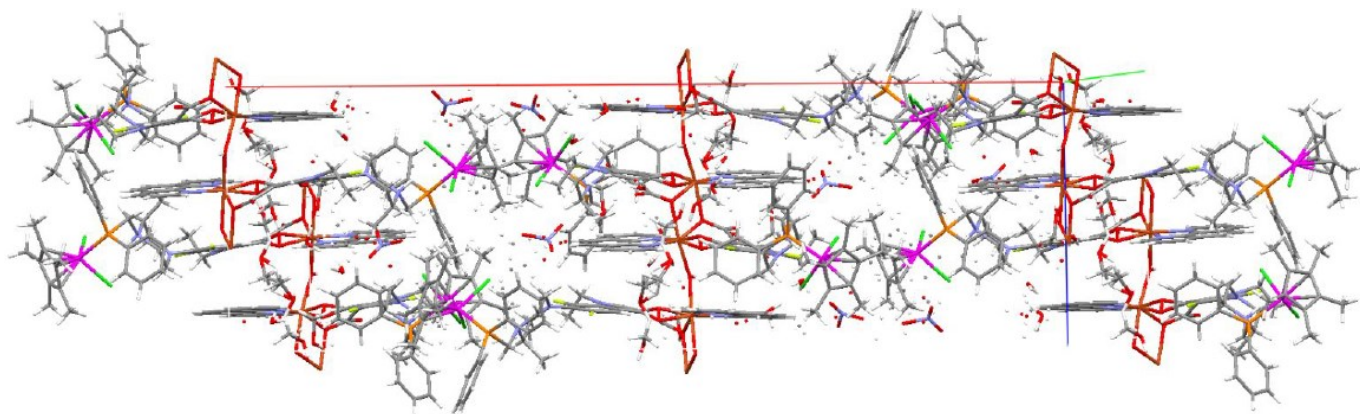


Fig. S4 Packing diagram of complex IrPLmCu

Additionally, the binuclear unit is stabilized by π -stacking interactions between phenanthroline and lomefloxacin fragments.

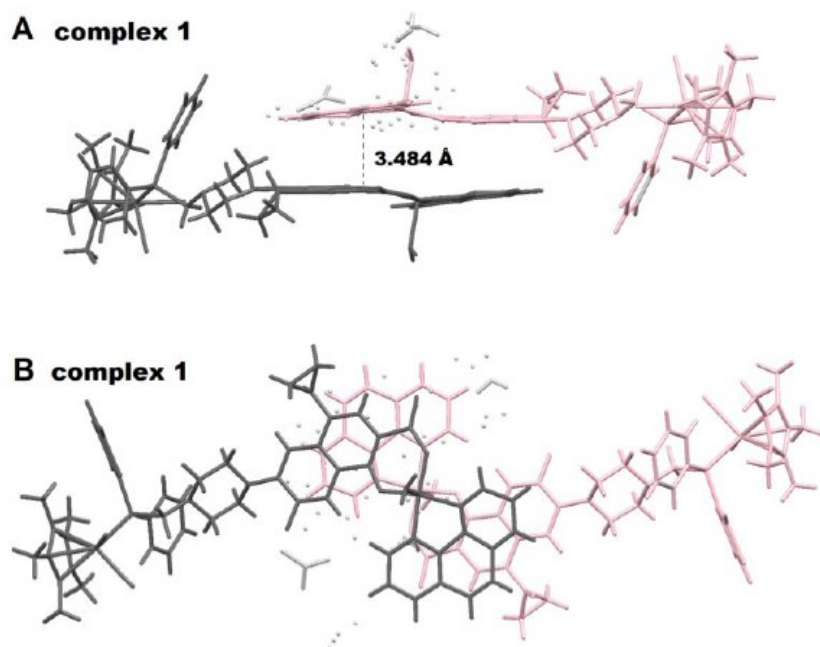


Fig. S5 Packing diagram of complex 1 showing (A) π -stacking interaction between the fluoroquinolone rings (B) offset pattern of the π - π stacking in complex 1.

Interactions between two independent fused-ring moieties: the fluoroquinolone fragment rings and the phen ligands can be found as well in cases of 1 and 2. As it could be expected, these interactions led to interesting molecular packing of the inorganic compounds stabilized by π -stacking interactions (Fig. S5, S6). The distances from the two centroids of ciprofloxacin (complex 1) or norfloxacin (complex 2) to the phen plane are 3.484 and 3.375 Å, respectively.

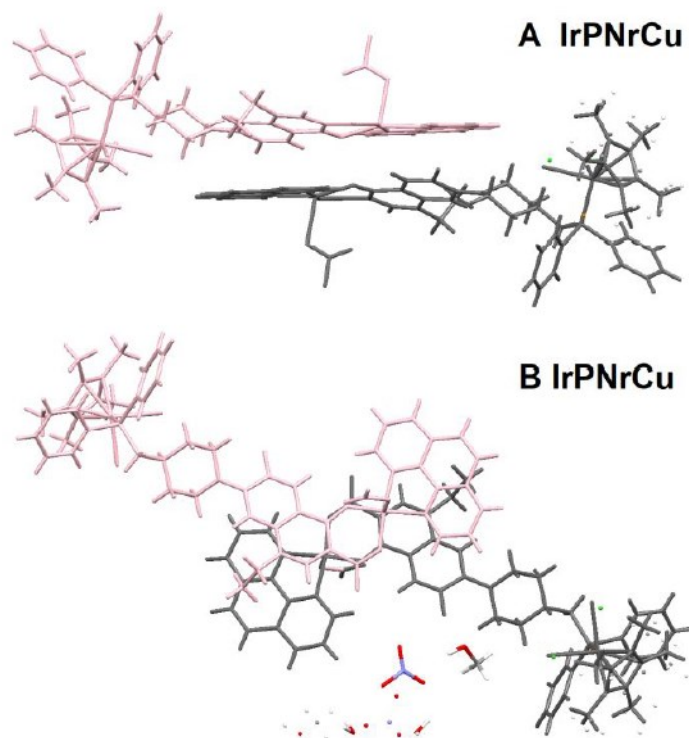


Fig. S6 Packing diagram of complex IrPNrCu showing (A) π -stacking interaction between the fluoroquinolone rings (B) offset pattern of the π - π stacking in complex IrPNrCu.

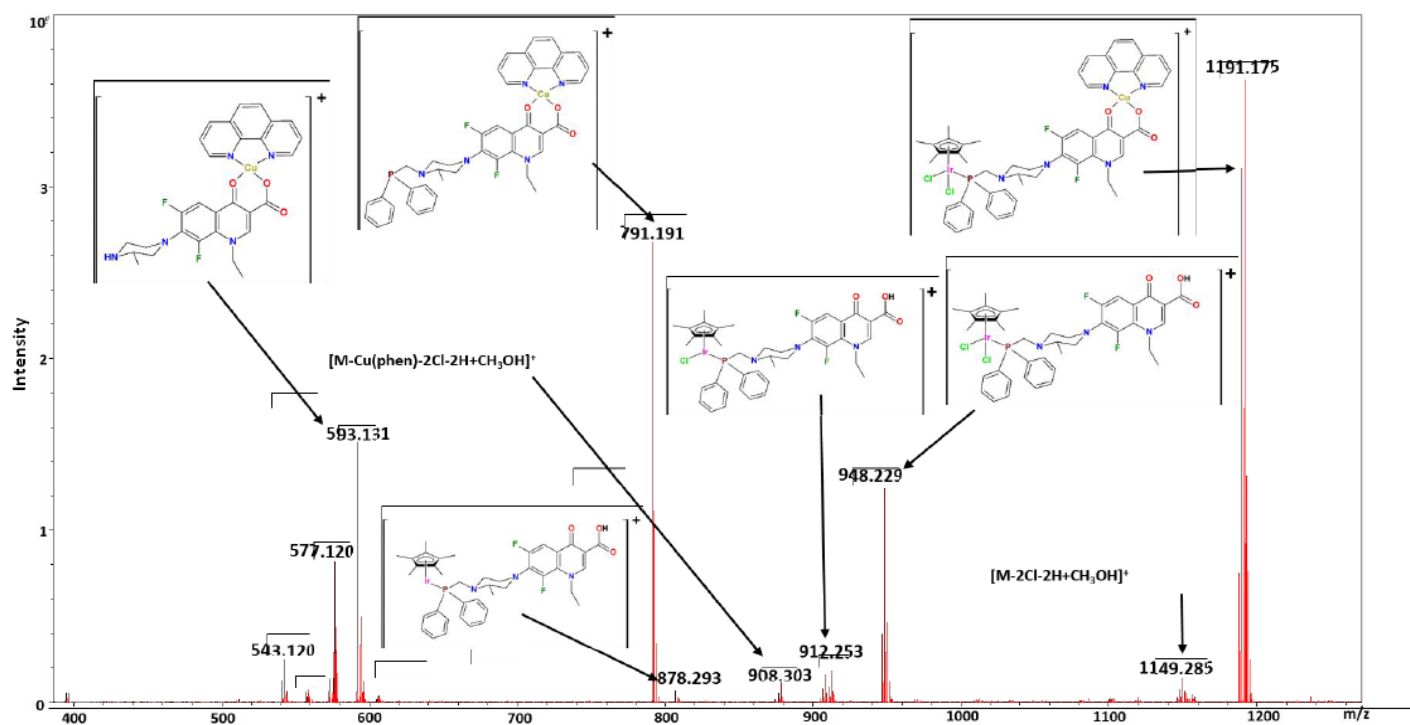


Fig. S7 A

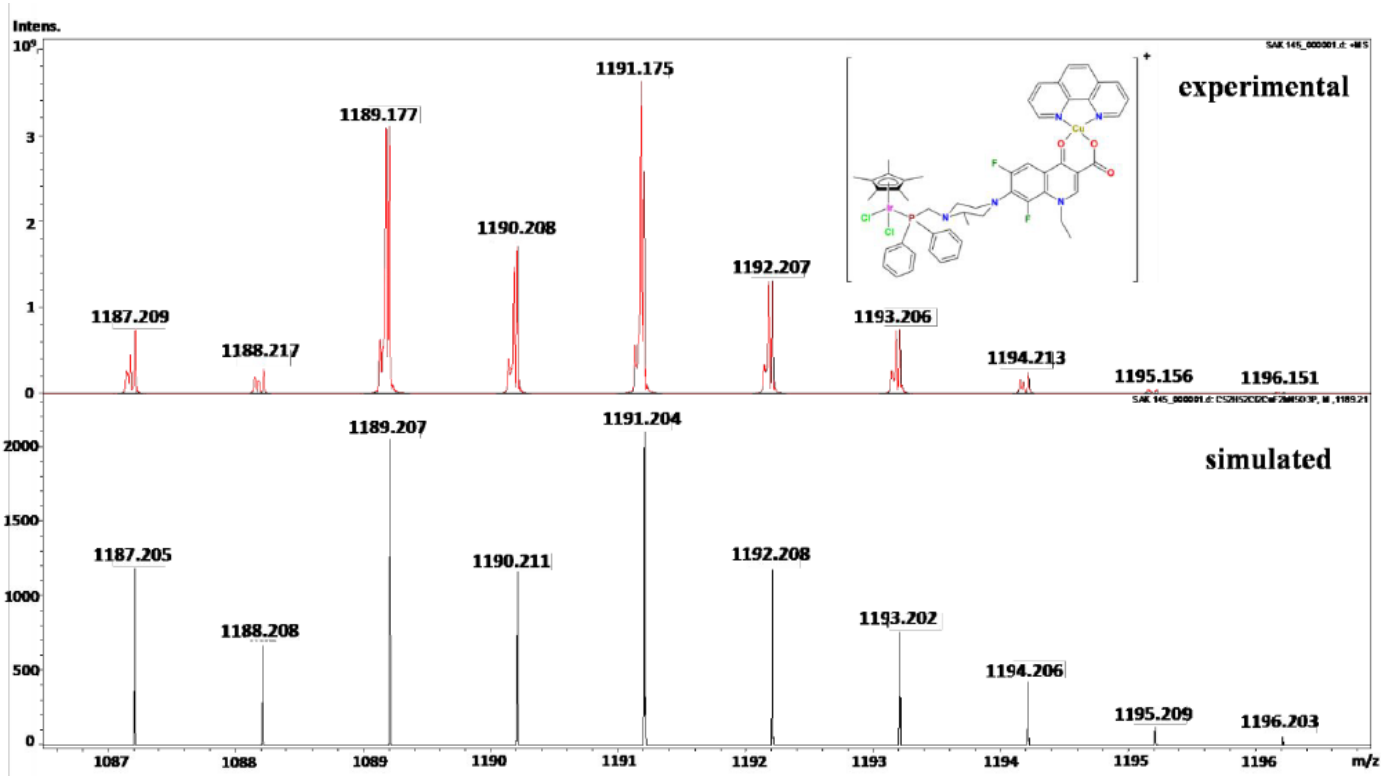


Fig. S7 B

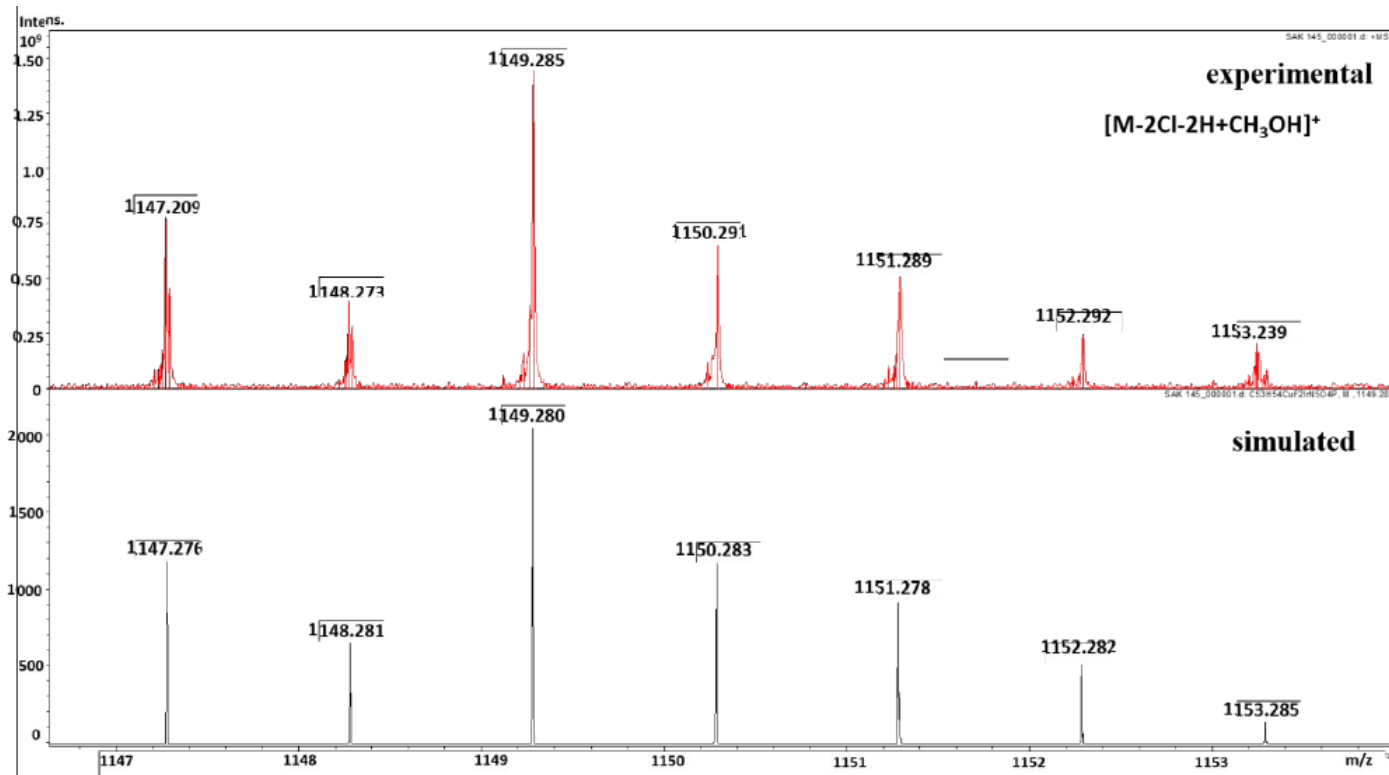


Fig. S7 C

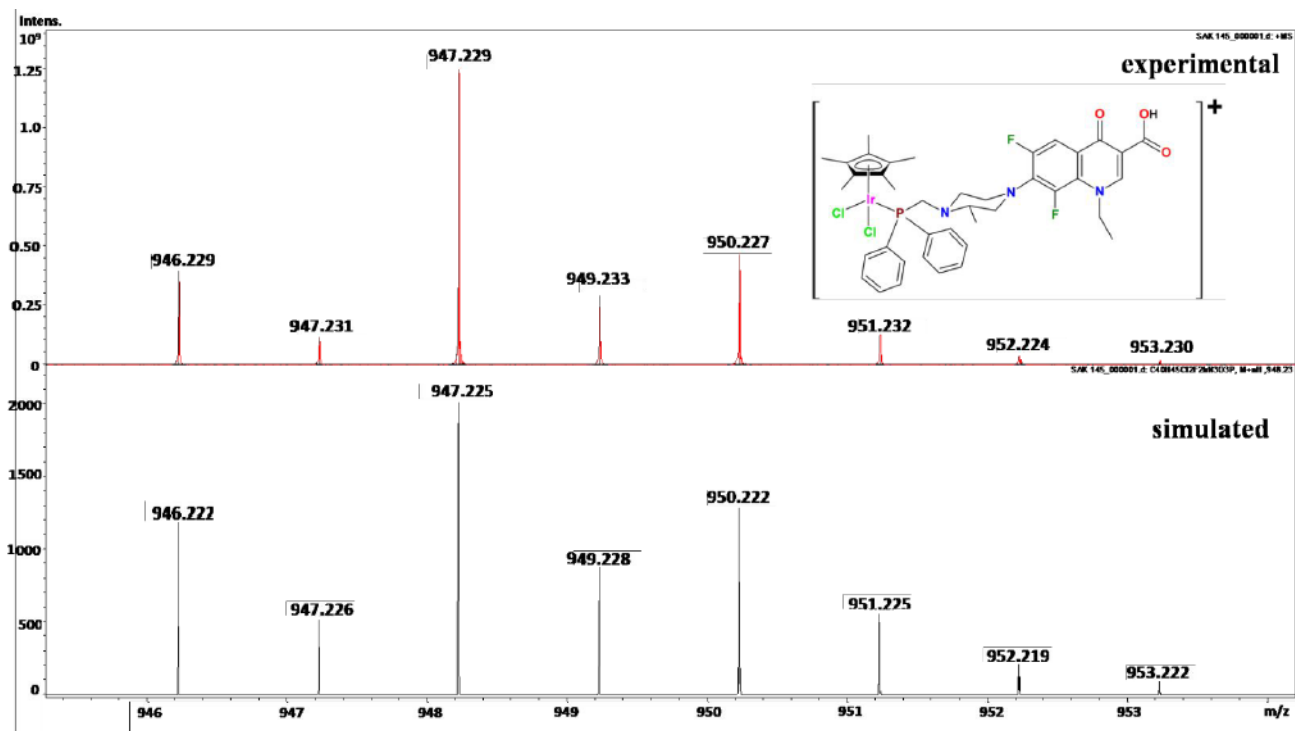


Fig. S7 D

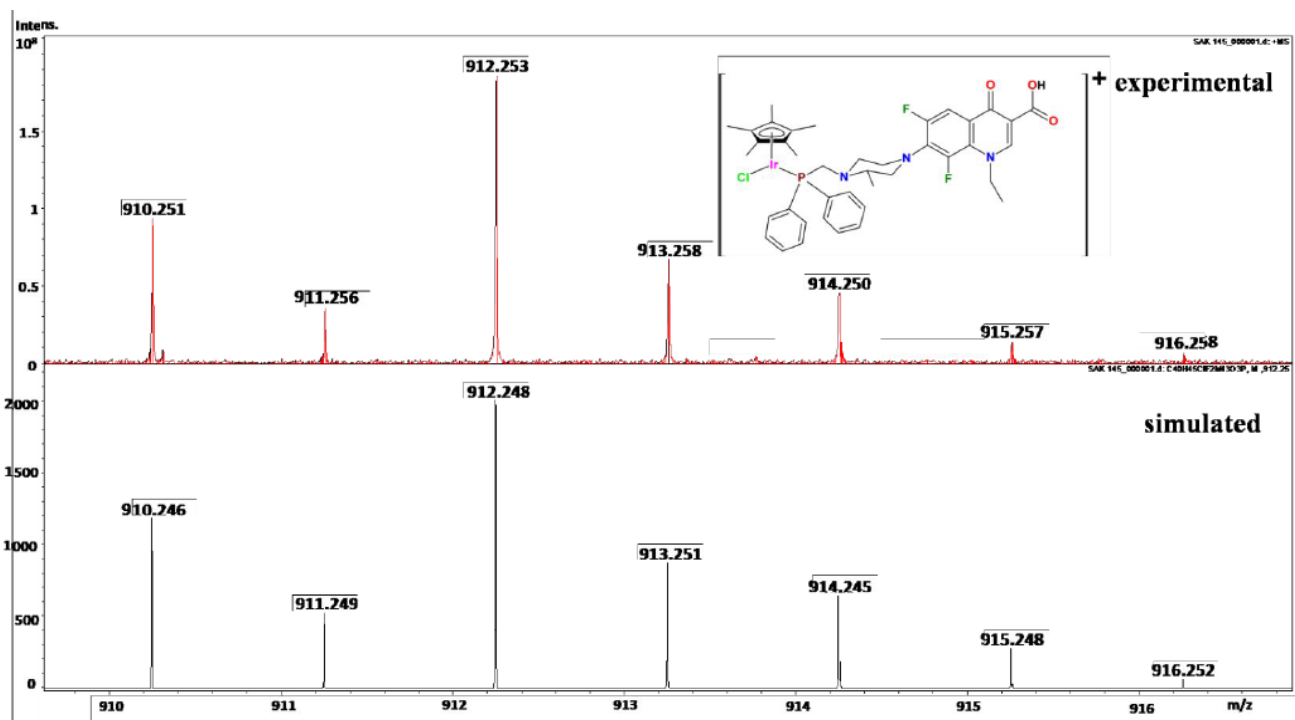


Fig. S7 E

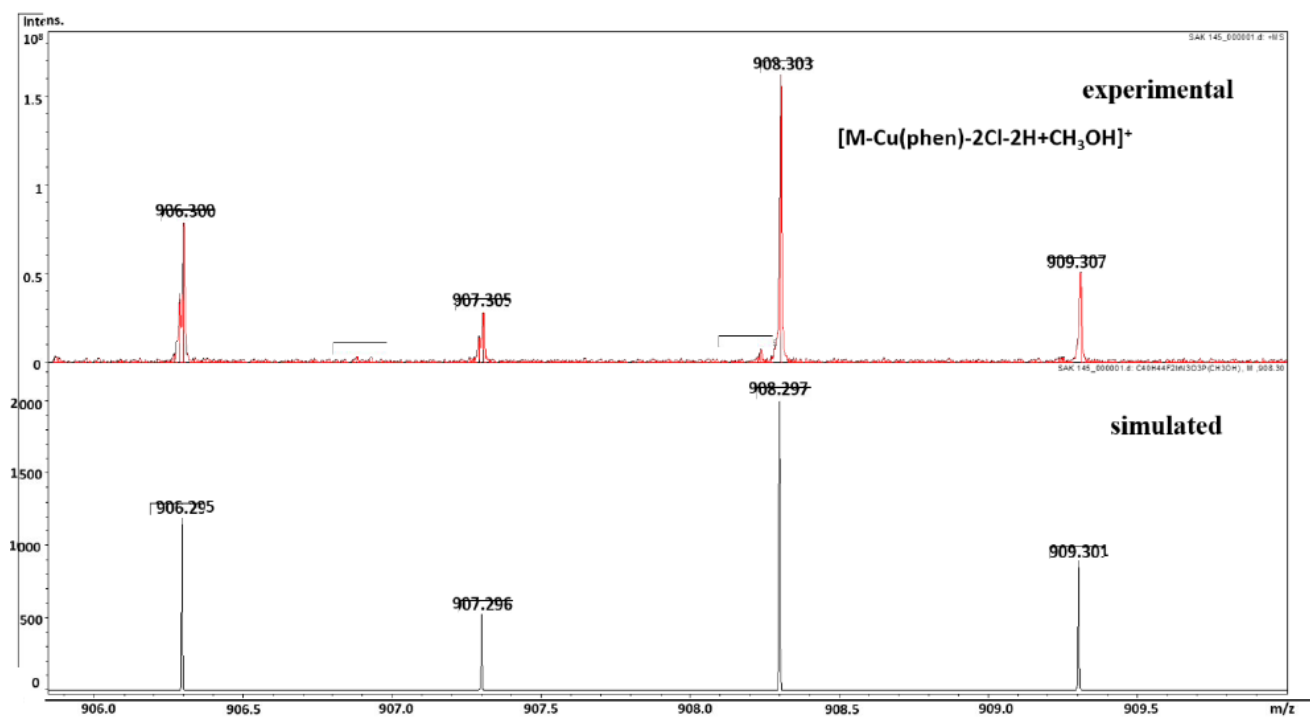


Fig. S7 F

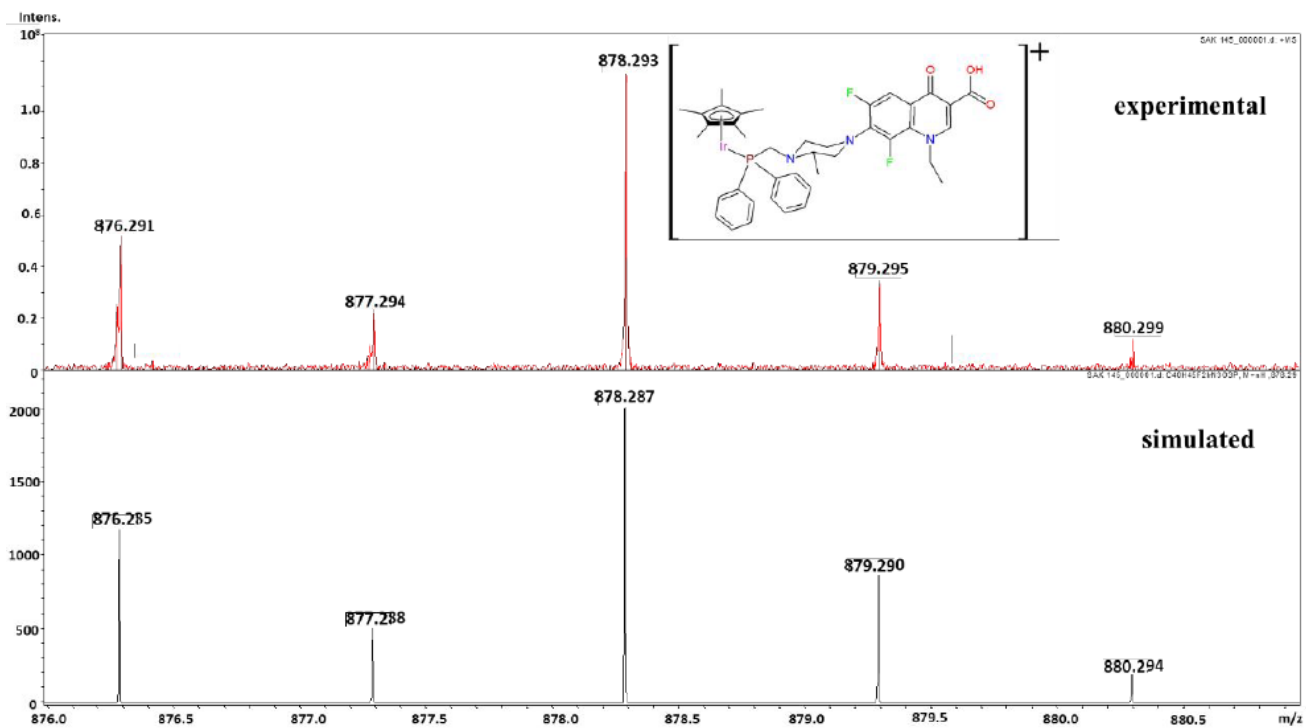


Fig. S7 G

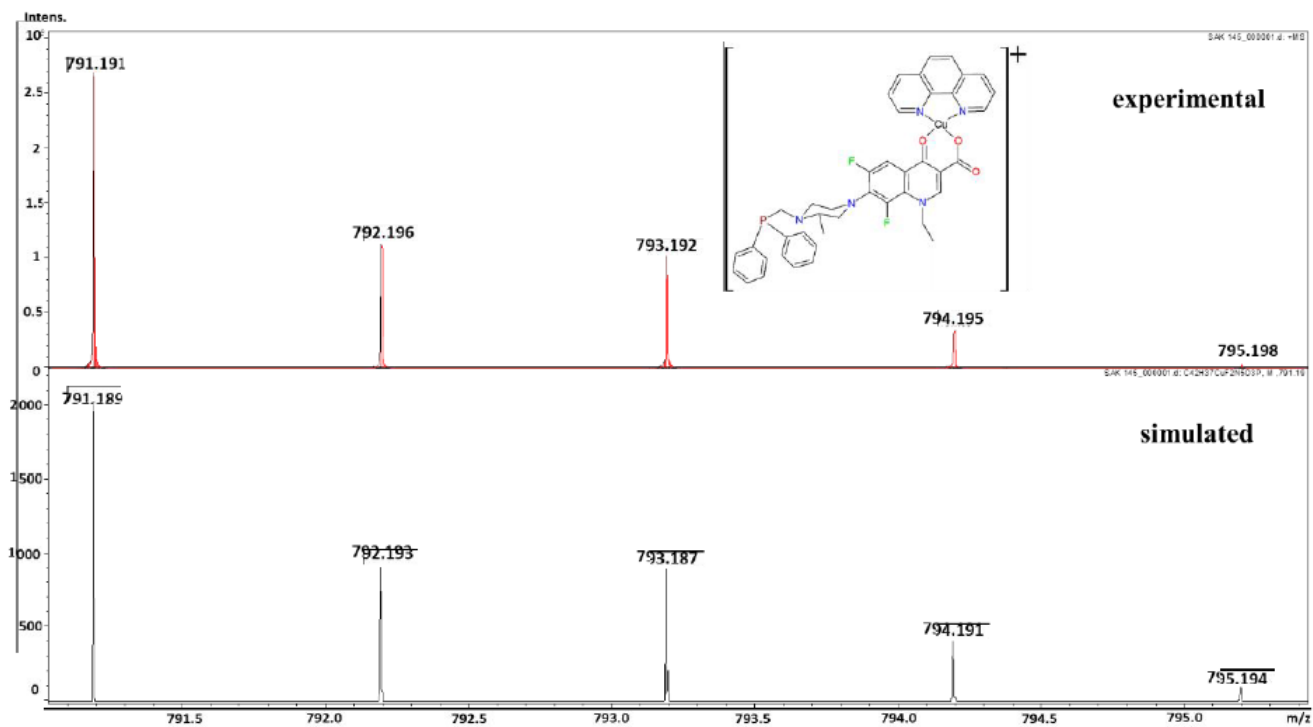


Fig. S7 H

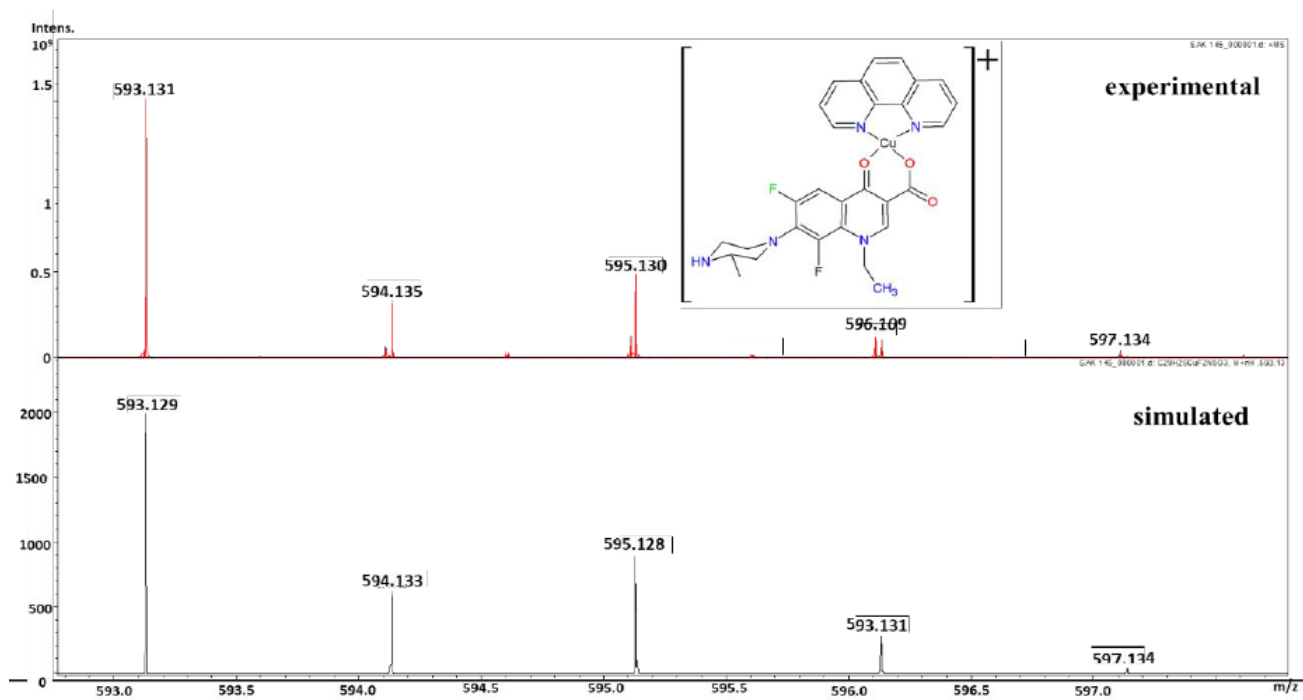


Fig. S7 I

Fig. S7 (a) ESI mass spectrum of IrPLmCu(phen). ESI(+)/MS in CH₃OH, m/z: 1191.175 [IrPLmCu(phen)]⁺ ; 1149.285 [IrPLmCu(phen)-HCl-Cl+CH₂OH]⁺ ; 948.229 [IrPLmCu(phen)-Cu(phen)+H]⁺ ; 912.253 [IrPLmCu(phen)- Cu(phen)-Cl]⁺ ; 908.303 [IrPLmCu(phen)-Cu(phen)-2Cl+CH₂OH]⁺ ; 878.293 [IrPLmCu(phen)-Cu(phen)-2Cl+H]⁺ ; 791.191 [IrPLmCu(phen)-IrCl₂]⁺ ; 593.131 [IrPLmCu(phen)-IrCl₂-PPh₂CH₂]⁺ (b) experimental and simulated spectra of [IrPLmCu(phen)+H]⁺ (c) experimental and simulated spectra of [IrPLmCu(phen)-2Cl-2H+CH₃OH]⁺ (d) experimental and simulated spectra of [IrPLmCu(phen)-Cu(phen)]⁺ (e) experimental and simulated spectra of [IrPLmCu(phen)- Cu(phen)-Cl]⁺ (f) experimental and simulated spectra of [IrPLmCu(phen)-Cu(phen)-2Cl-H+CH₃OH]⁺ (g) experimental and simulated spectra of [IrPLmCu(phen)-Cu(phen)-2Cl+H]⁺ (h) experimental and simulated spectra of [IrPLmCu(phen)-IrCl₂]⁺ (i) experimental and simulated spectra of [IrPLmCu(phen)IrCl₂PPh₂CH₂]⁺

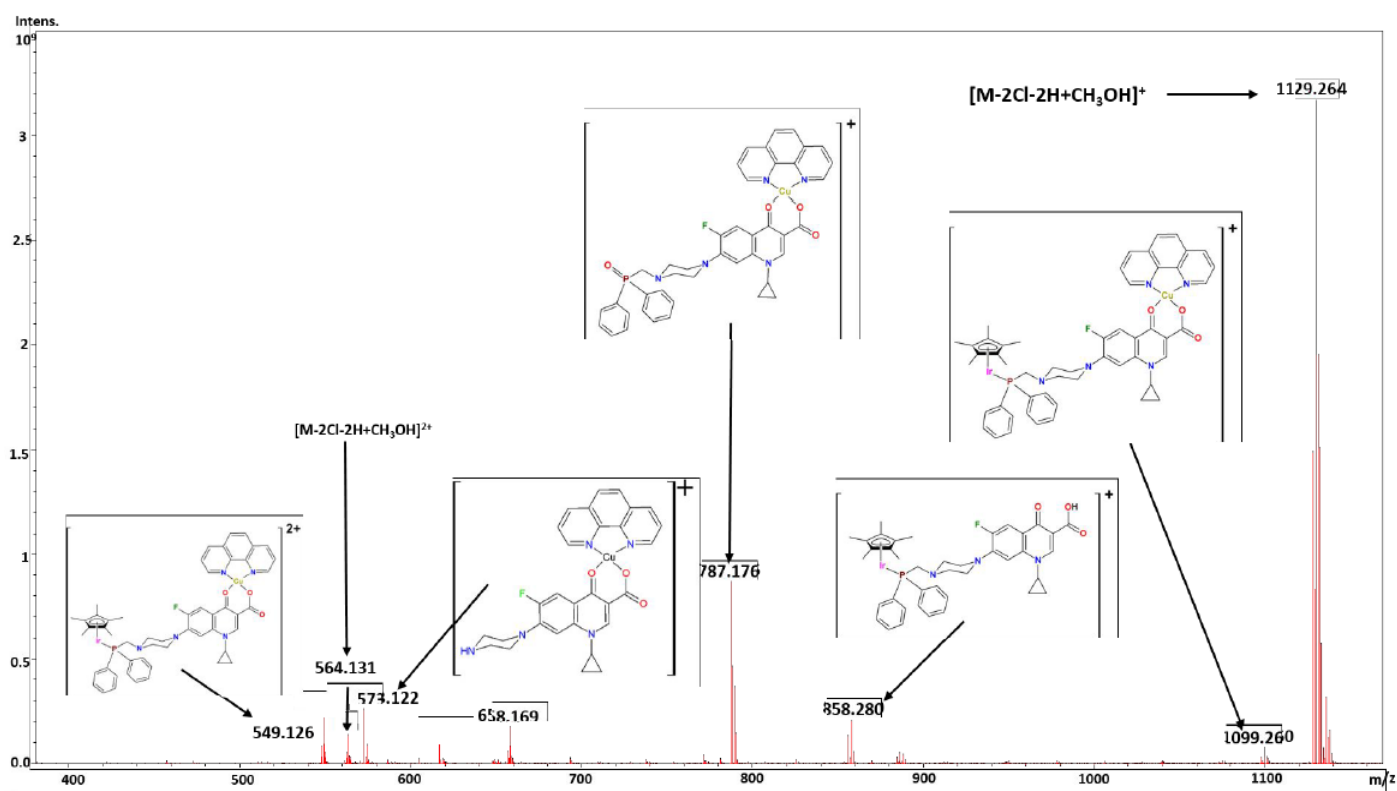


Fig. S8 A

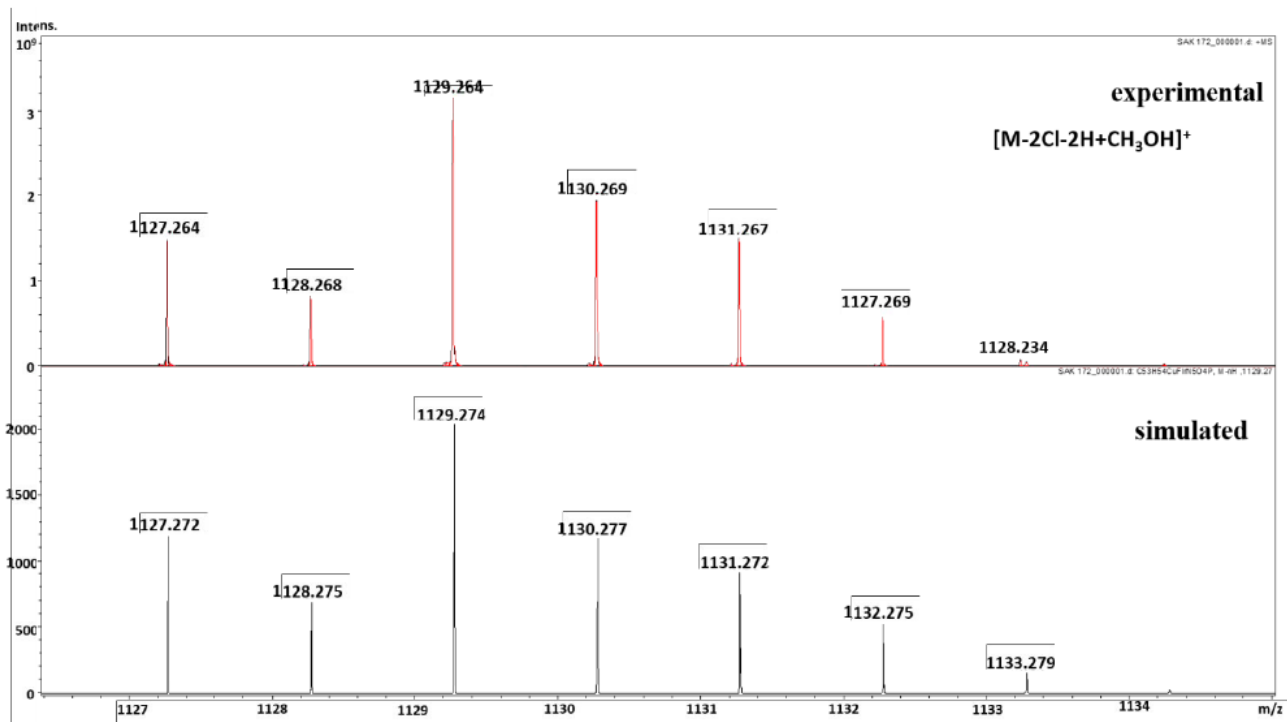


Fig. S8 B

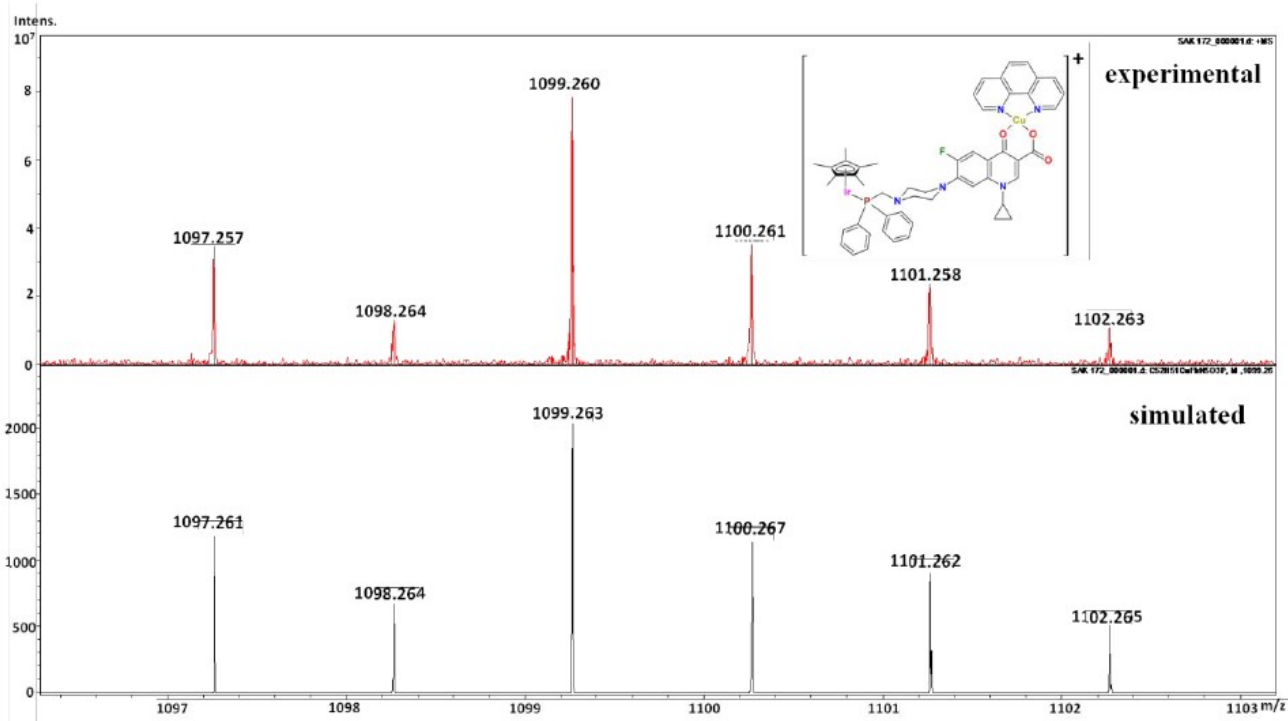


Fig. S8 C

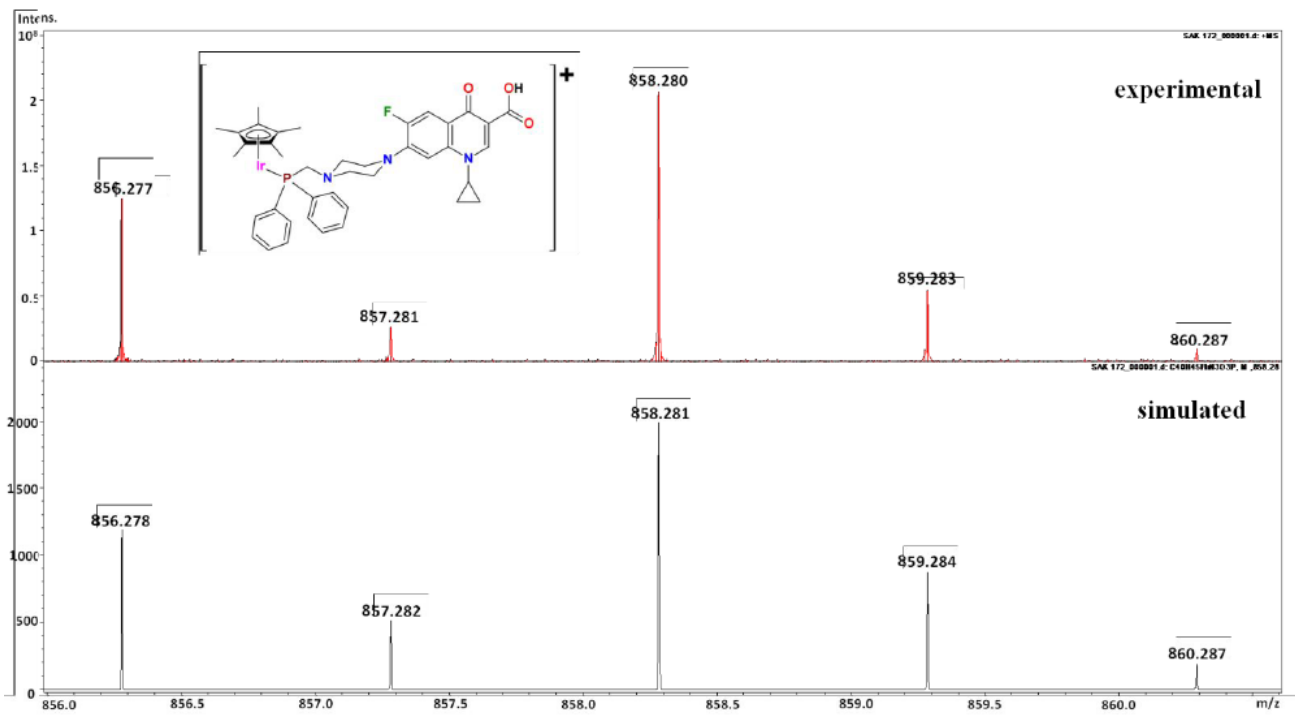


Fig. S8 D

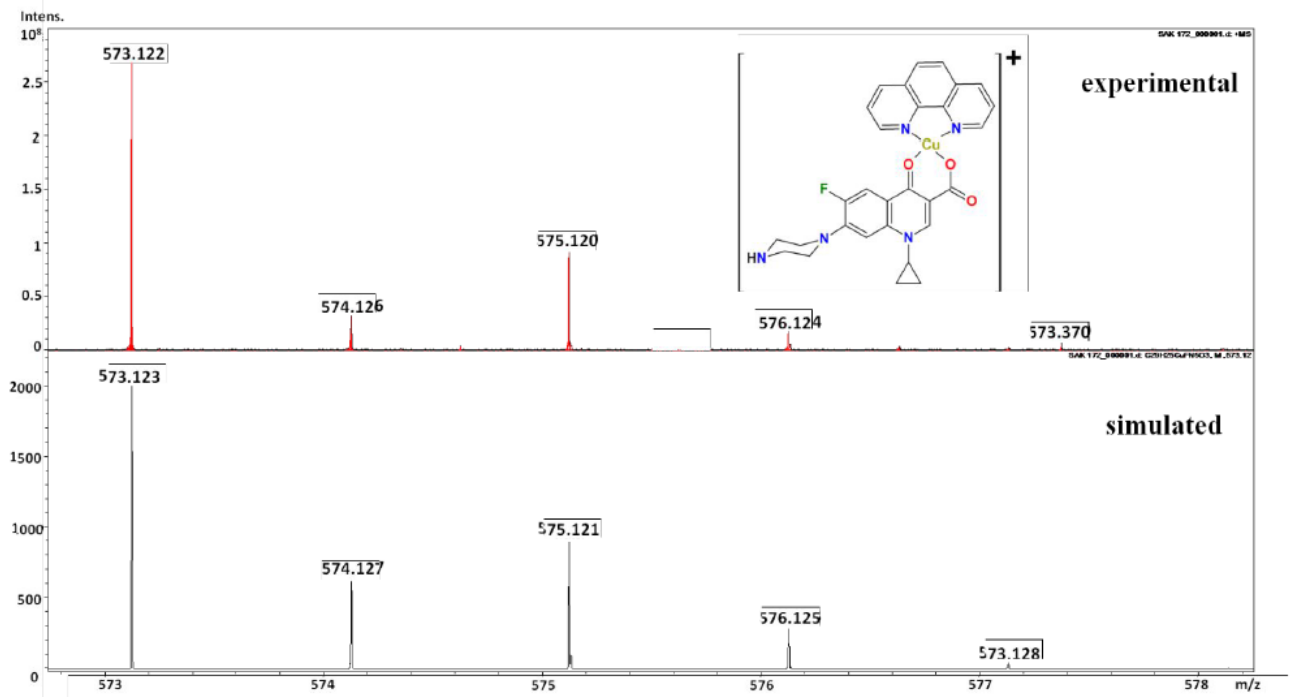


Fig. S8 E

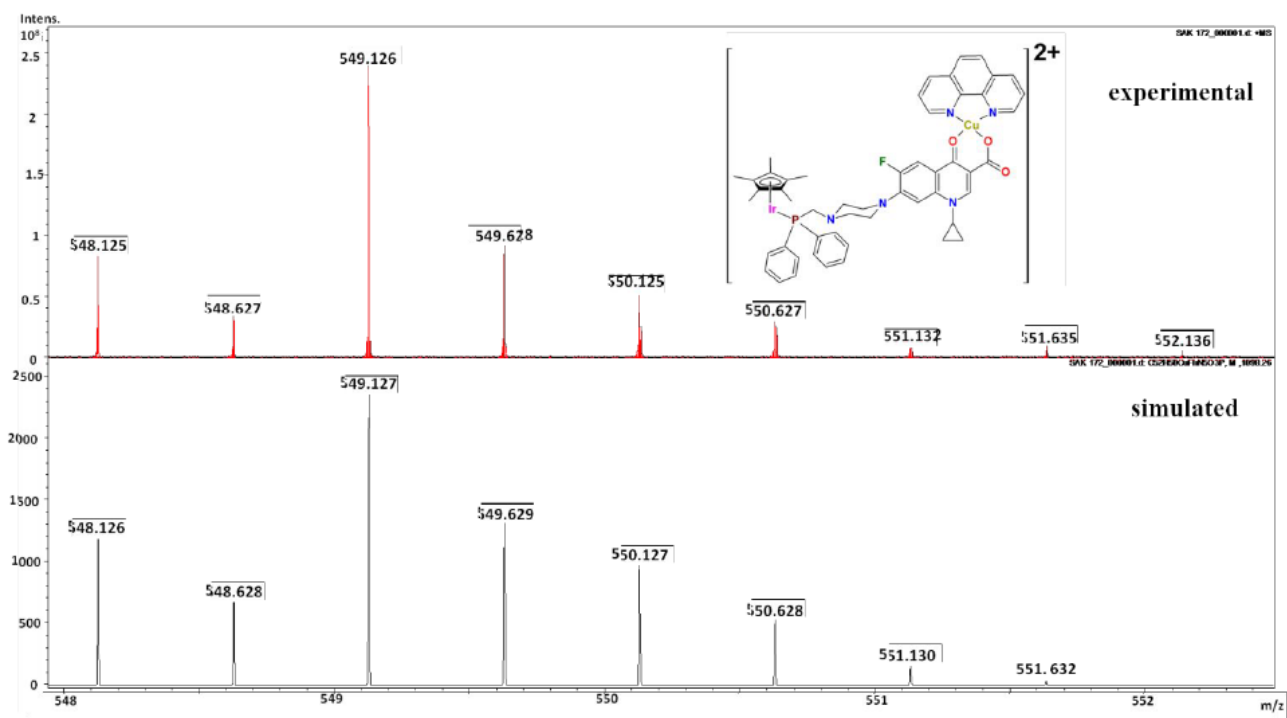


Fig. S8 F

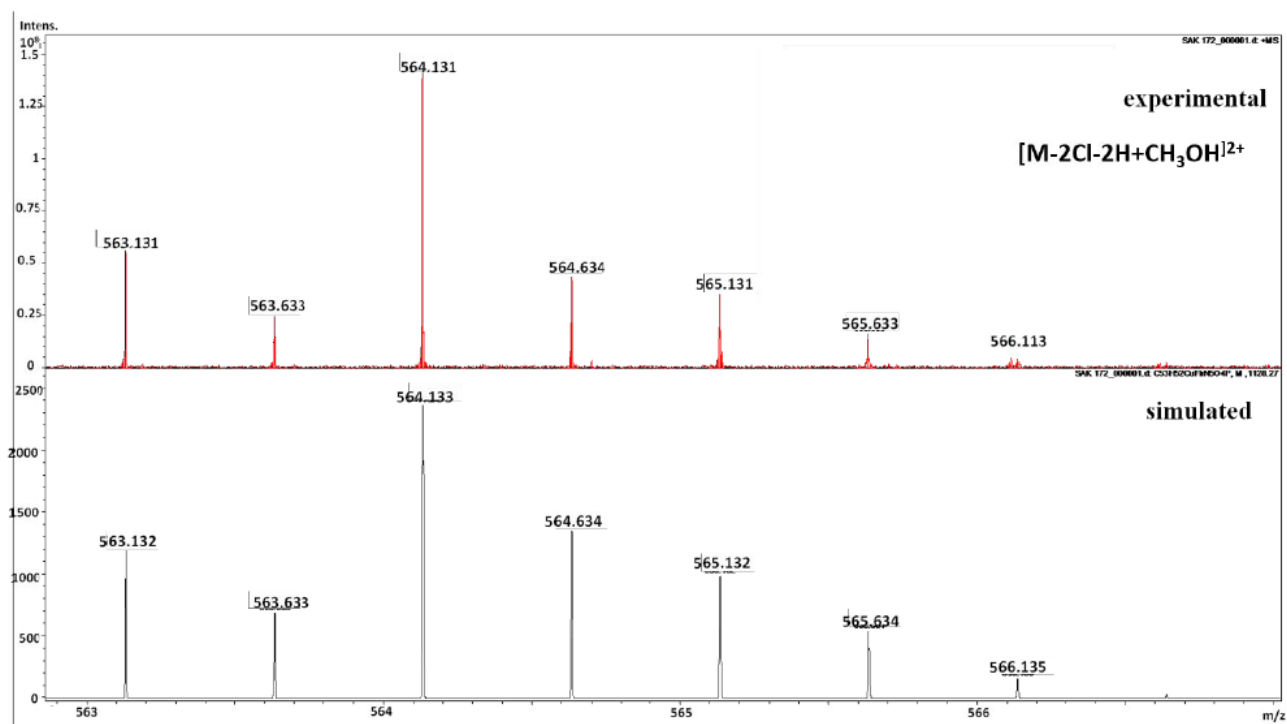


Fig. S8 G

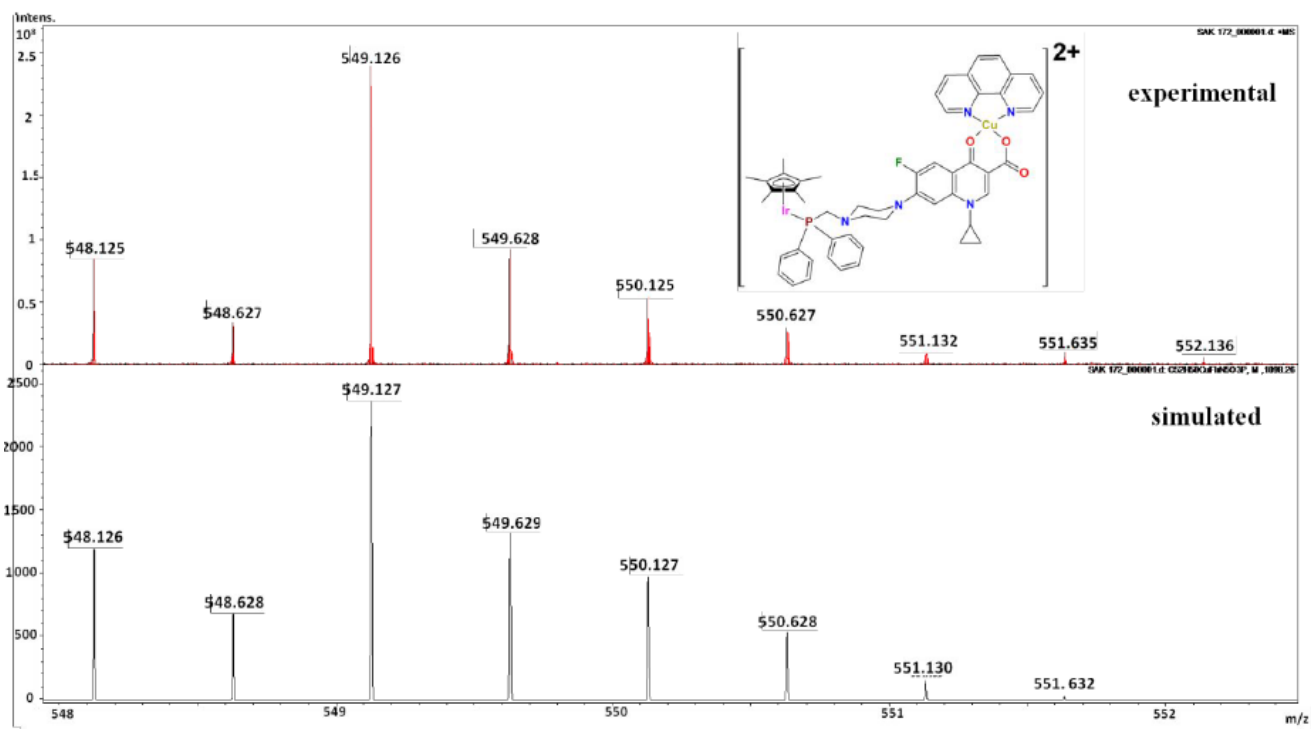


Fig. S8 H

Figure S8 (a) ESI mass spectrum of IrPCpCu(phen). ESI(+)*MS* in CH₃OH, *m/z*: 1129.264 [M-HCl-Cl+CH₂OH]⁺ ; 1099.260 [M-2Cl]⁺ ; 858.280 [M-2Cl-Cu(phen)+H]⁺ ; 787.176 [M-IrCpCl₂+O]⁺ ; 573.122 [M-IrCpCl₂-PPhCH₂]⁺ ; 564.131 [M-2HCl+CH₂OH]²⁺; 549.126 [M-HCl-Cl]²⁺ (b) experimental and simulated spectra of [M-HCl+CH₂OH]⁺ (c) experimental and simulated spectra of [M-2Cl]⁺ (d) experimental and simulated spectra of [M-2ClCu(phen)+H]⁺ (e) experimental and simulated spectra of [M-IrCpCl₂+O]⁺ (f) experimental and simulated spectra of [M-IrCpCl₂-PPhCH₂]⁺ (g) experimental and simulated spectra of [M-2HCl+CH₂OH]²⁺ (h) experimental and simulated spectra of [M-HCl-Cl]²⁺

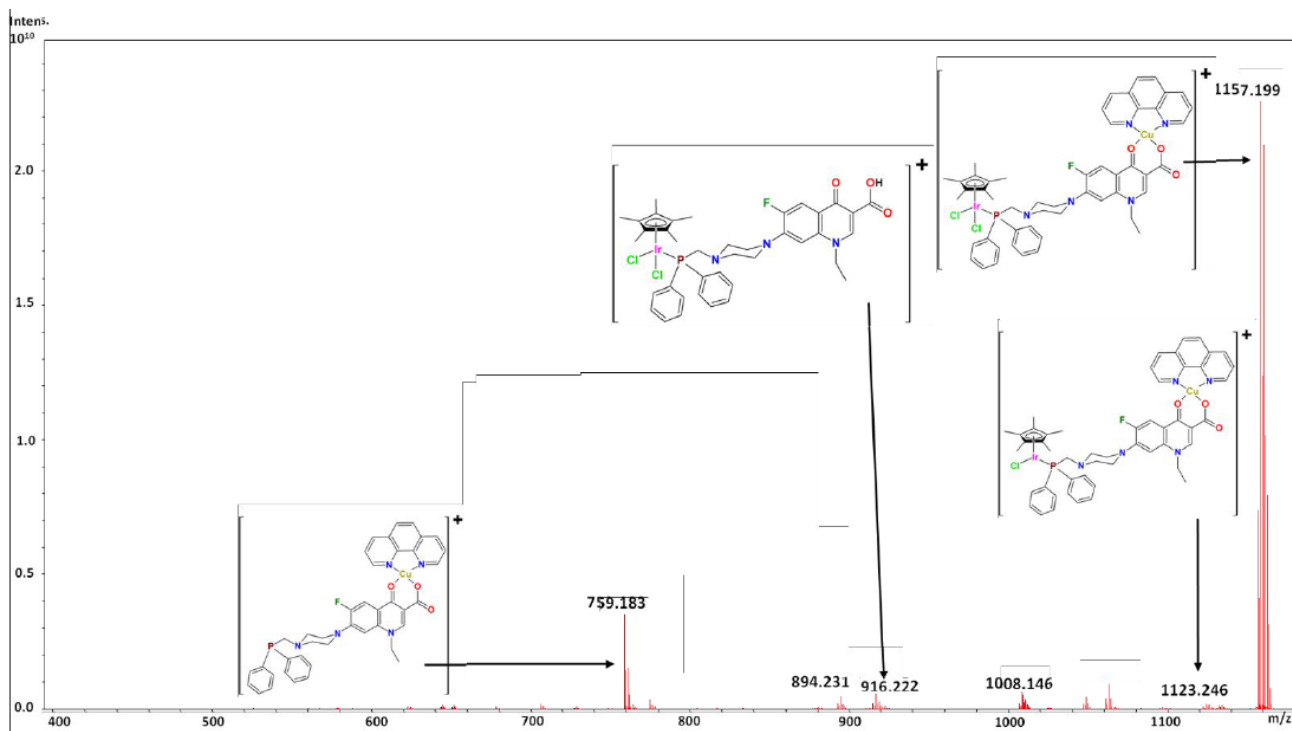


Fig. S9 A

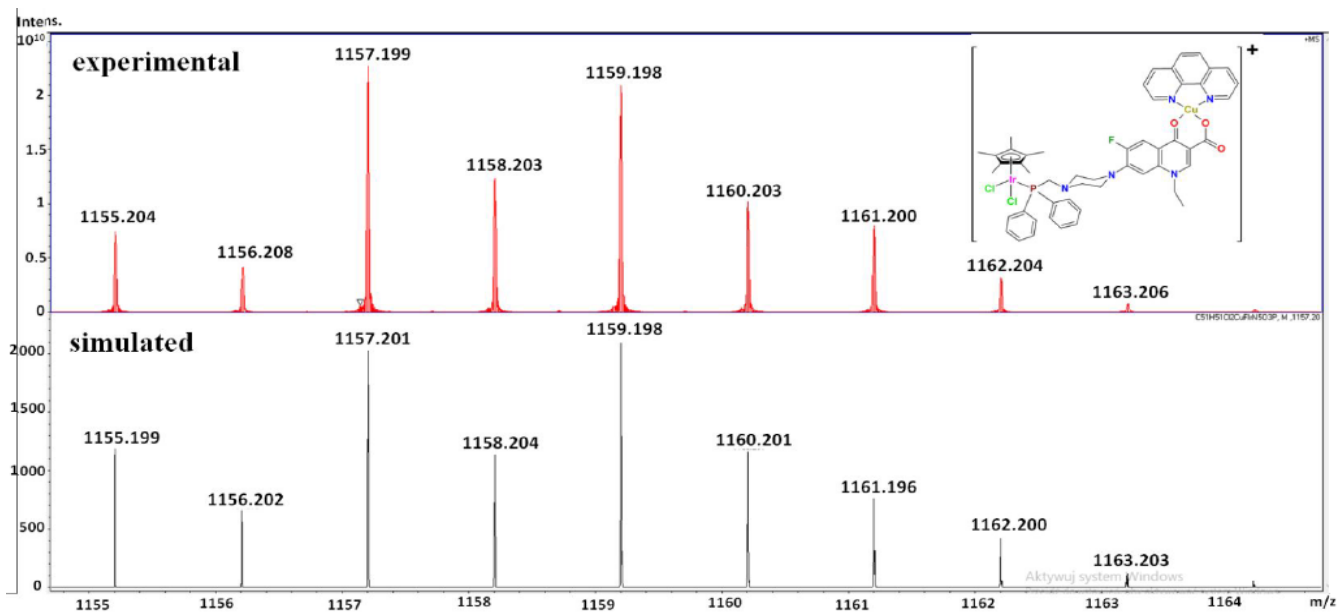


Fig. S9 B

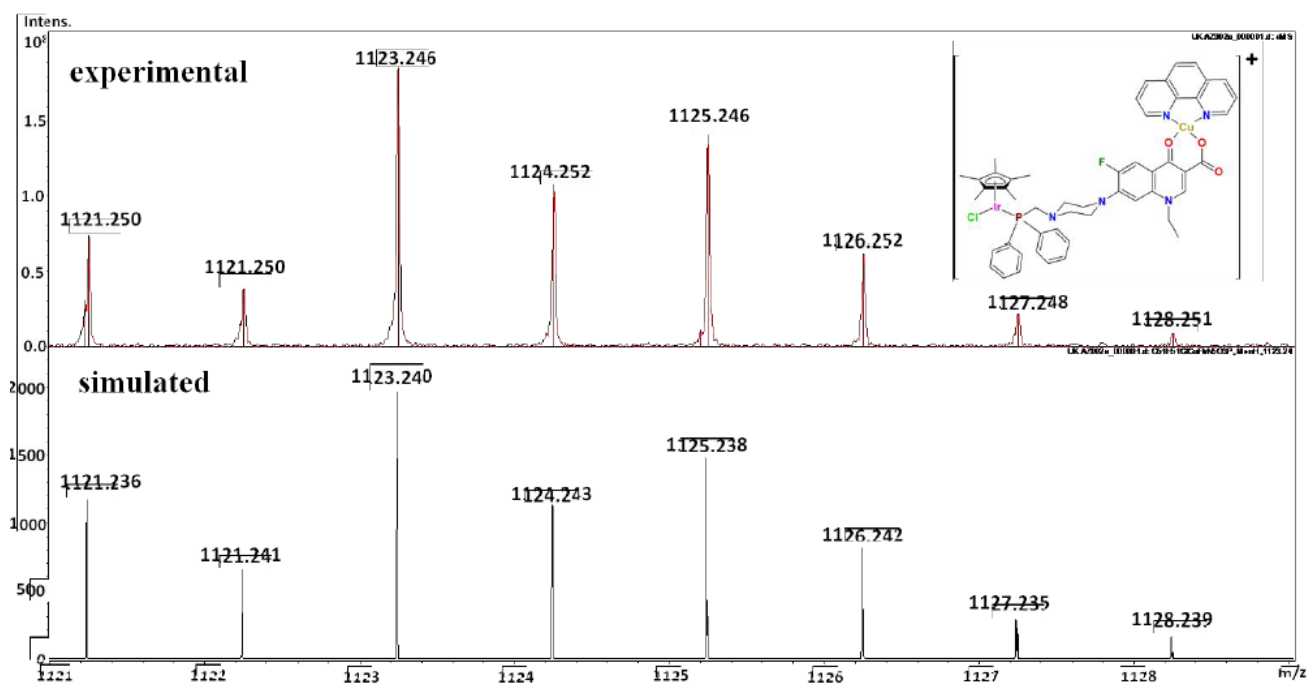


Fig. S9 C

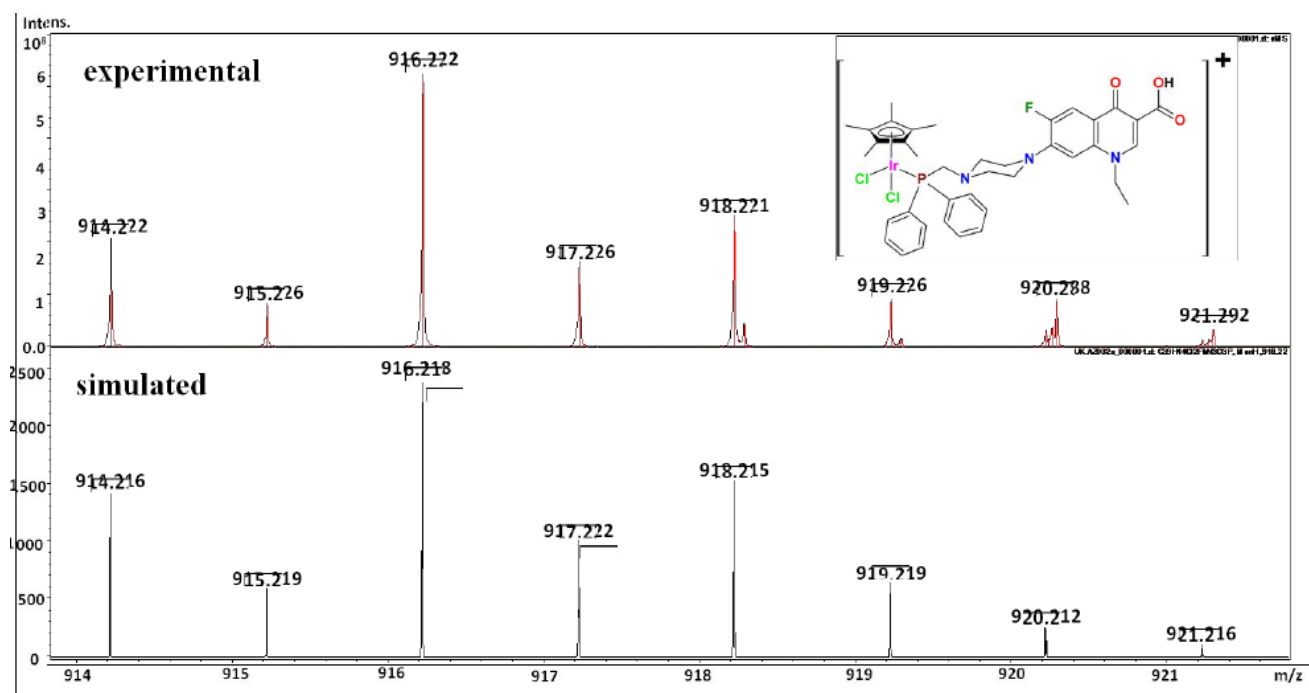


Fig. S9 D

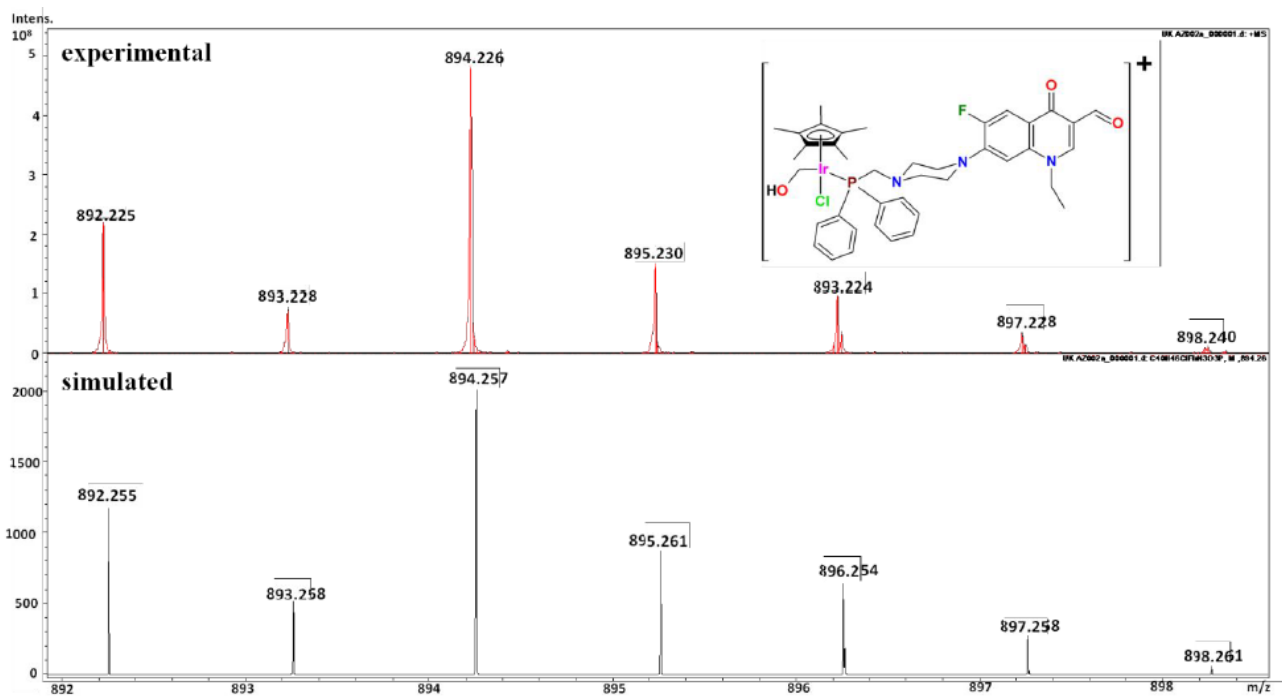


Fig. S9 E

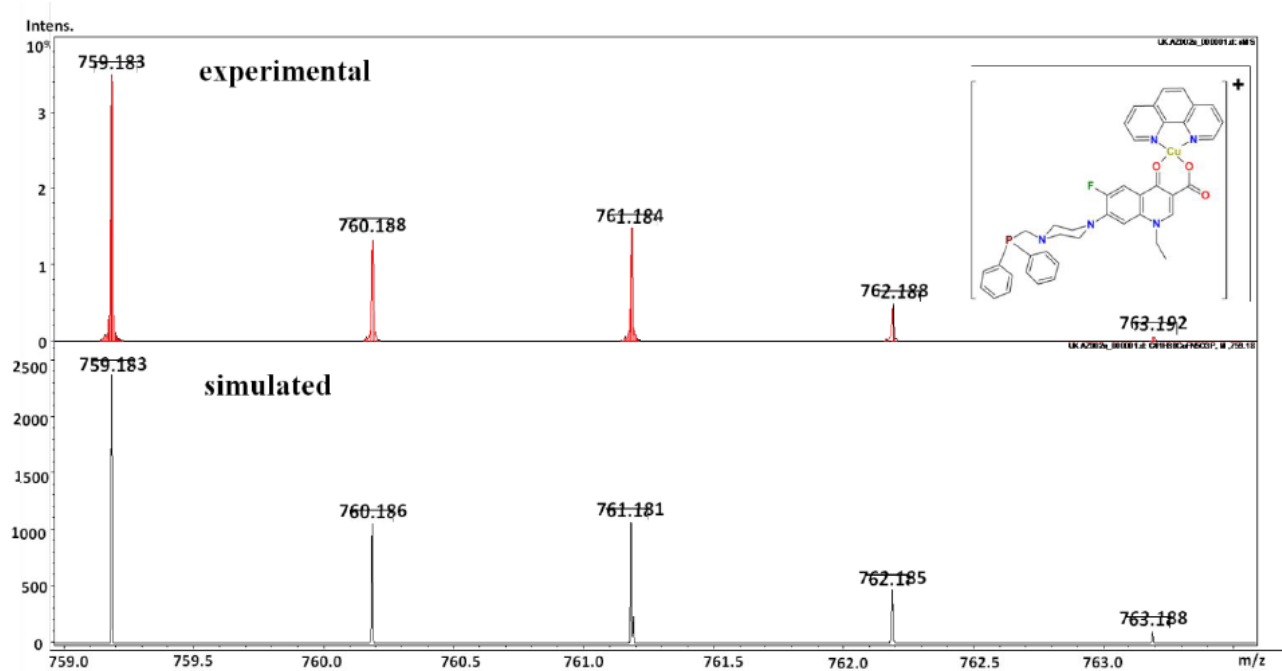


Fig. S9 F

Fig. S9 (a) ESI mass spectrum of IrPNrCu(phen). ESI(+)*MS* in CH₃OH, *m/z*: 1157.199 [M]⁺; 1123.246 [M-Cl+H]⁺; 916.222 [M-Cu(phen)+H]⁺; 894.226 [M-HCl-OH+CH₂OH]⁺; 759.183 [M-IrCpCl₂]⁺; (b) experimental and simulated spectra of [M]⁺; (c) experimental and simulated spectra of [M-Cl+H]⁺ (d) experimental and simulated spectra of [MCu(phen)+H]⁺ (e) experimental and simulated spectra of [M-HCl-OH+CH₂OH]⁺ (f) experimental and simulated spectra of [M-IrCpCl₂]⁺

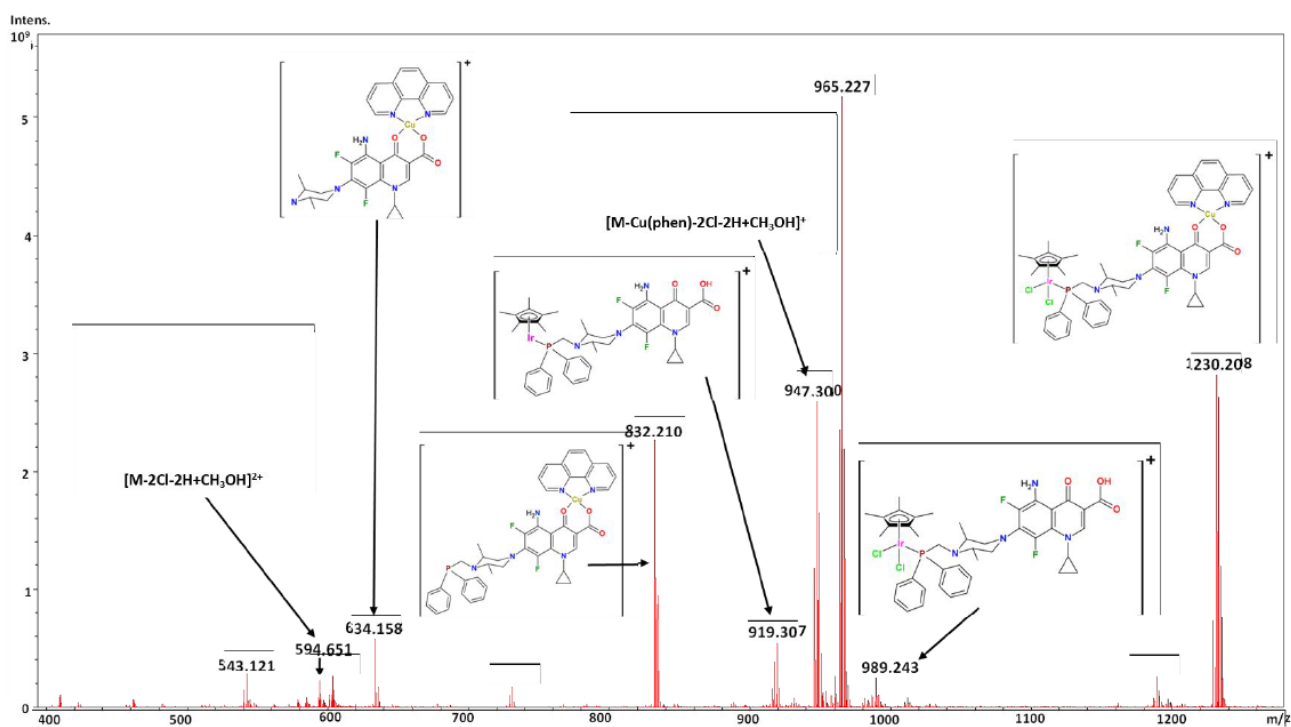


Fig. S10 A

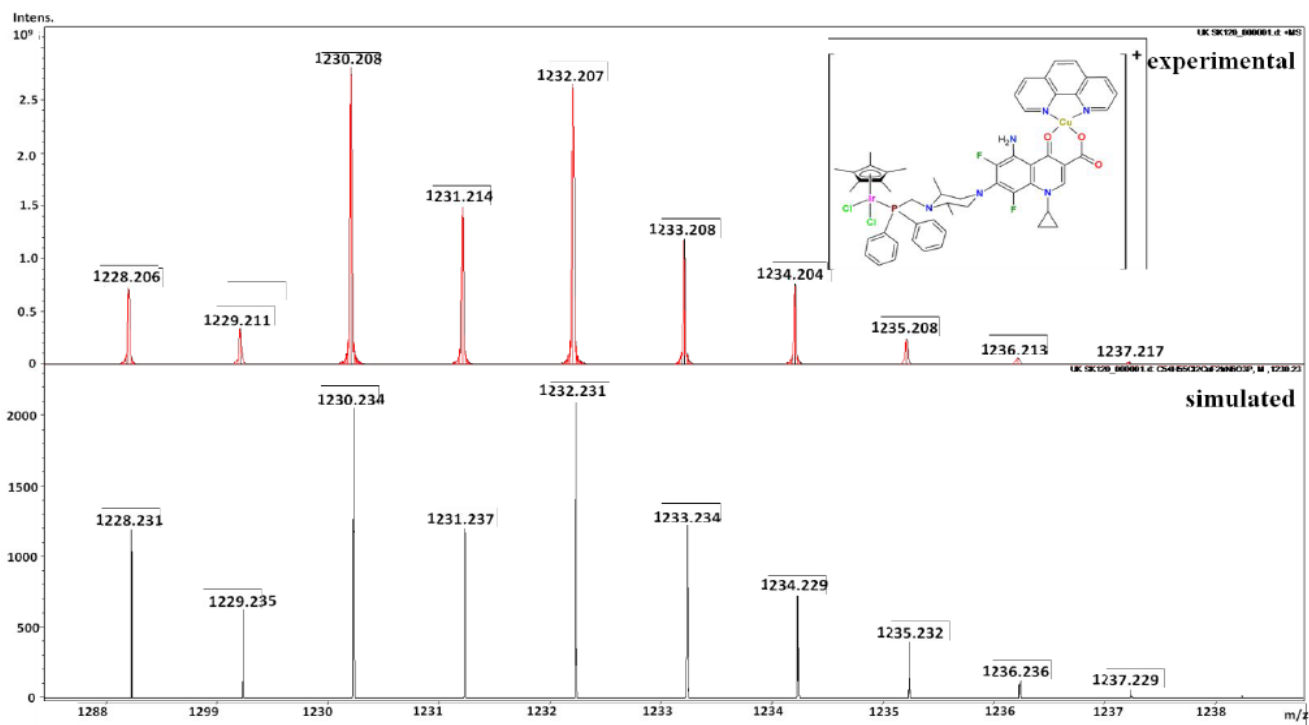


Fig. S10 B

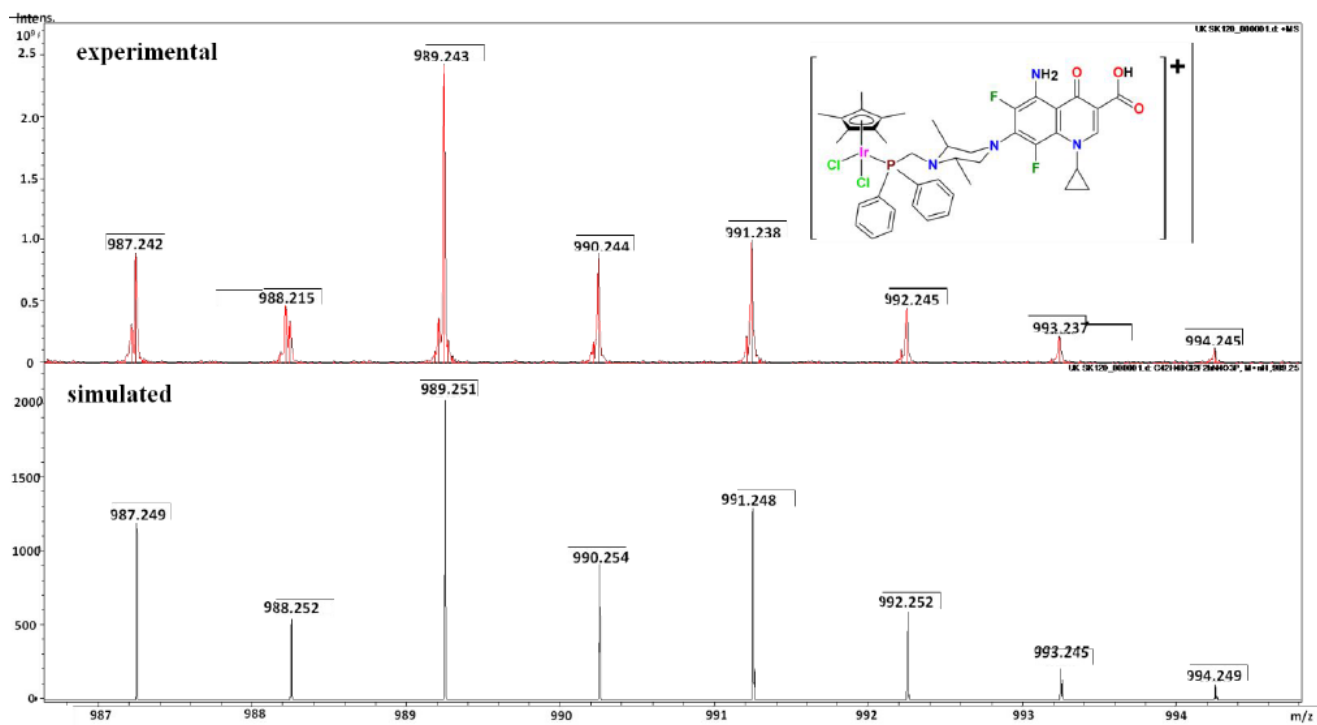


Fig. S10 C

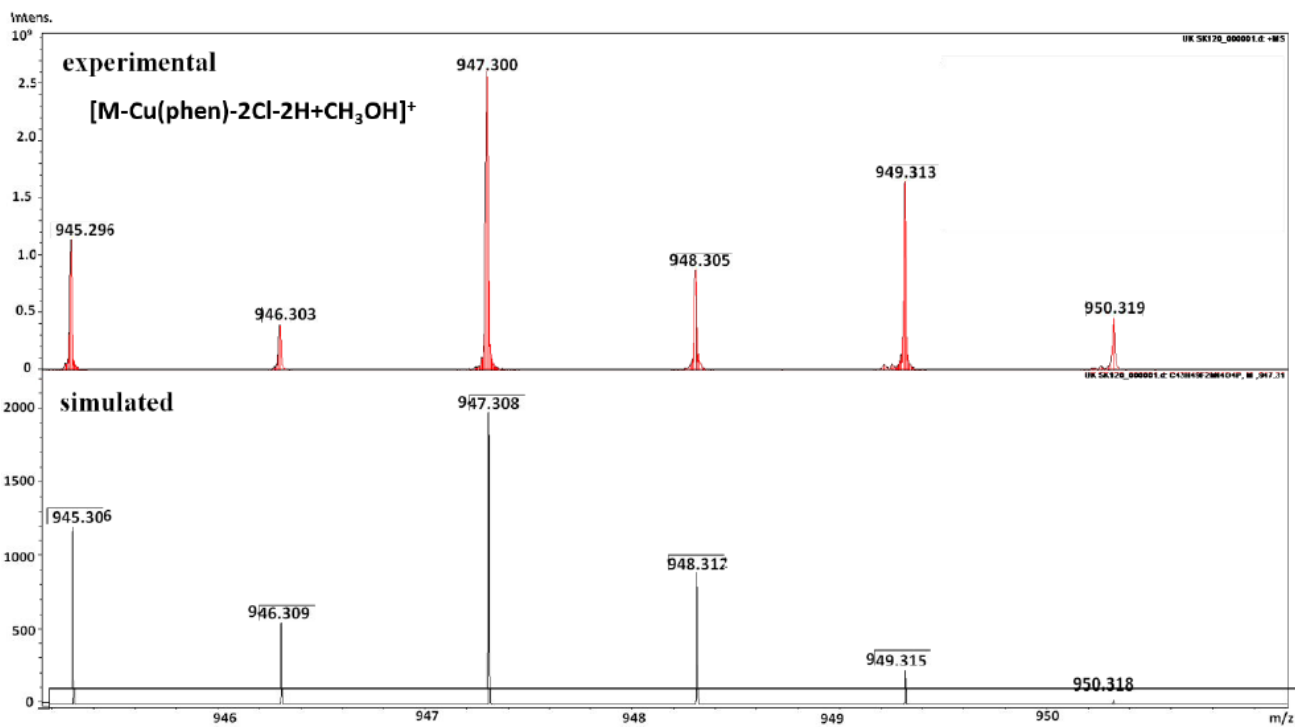


Fig. S10 D

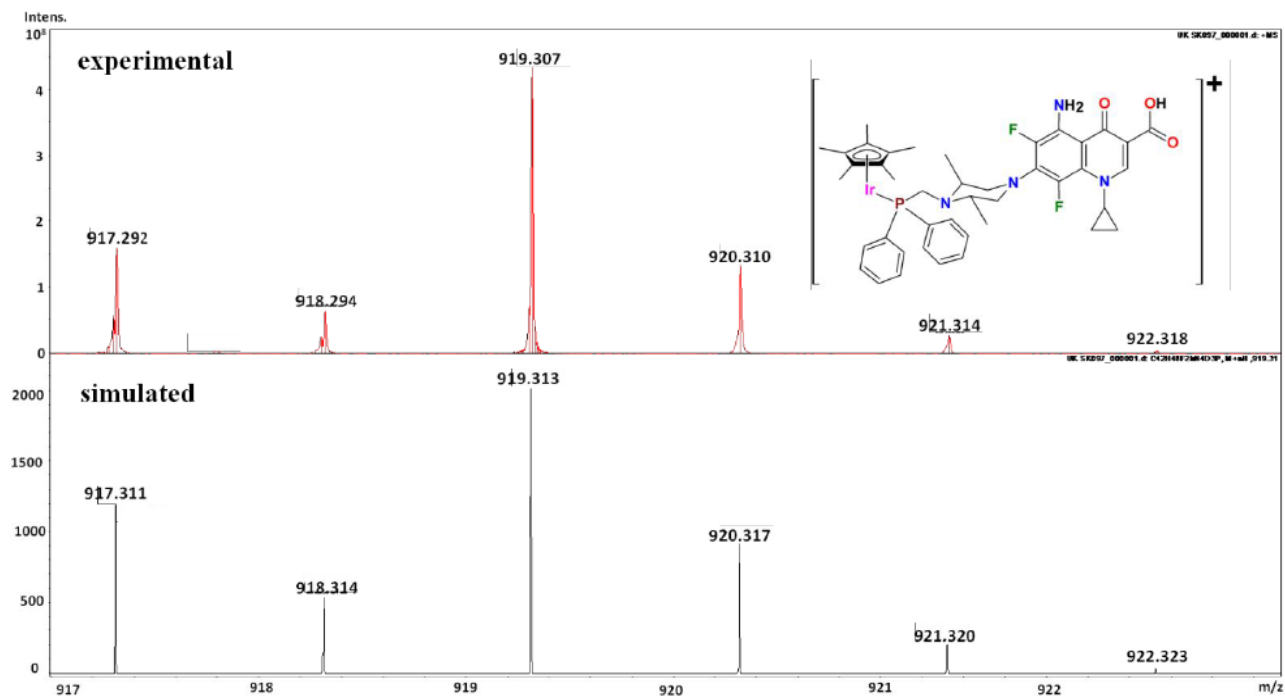


Fig. S10 E

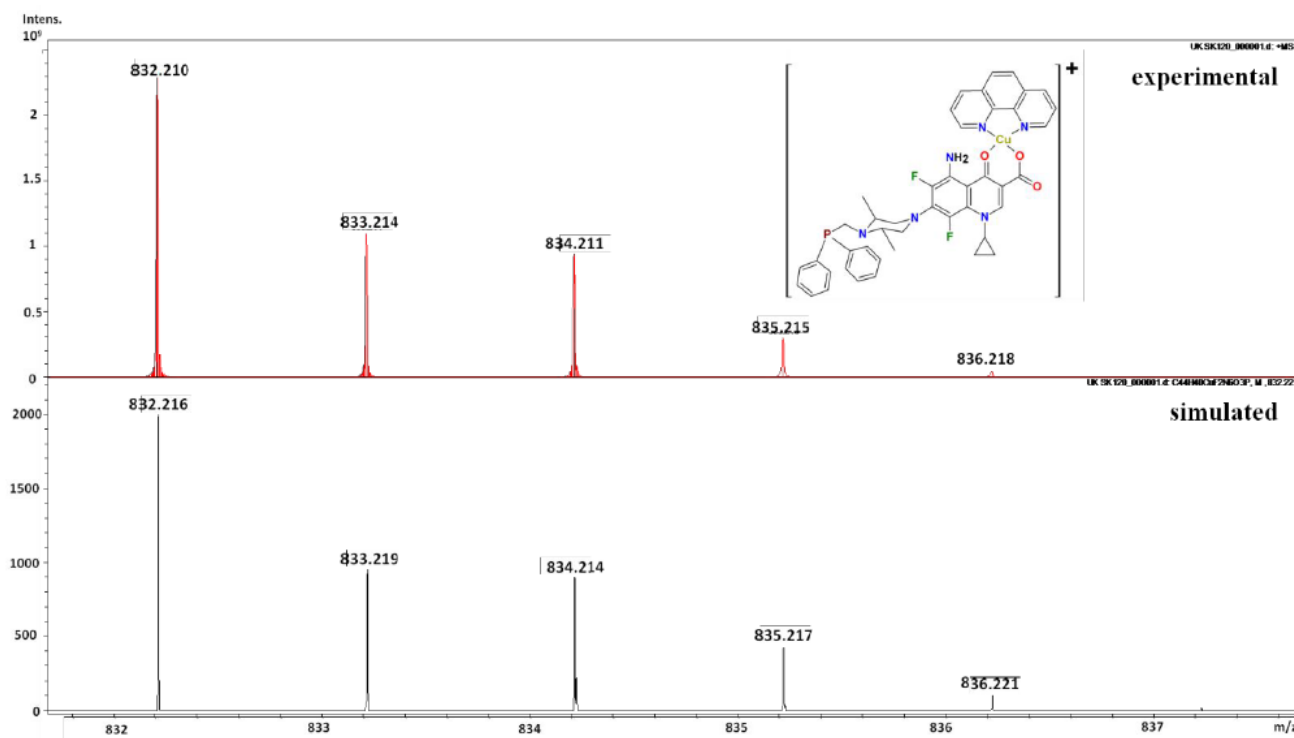


Fig. S10 F

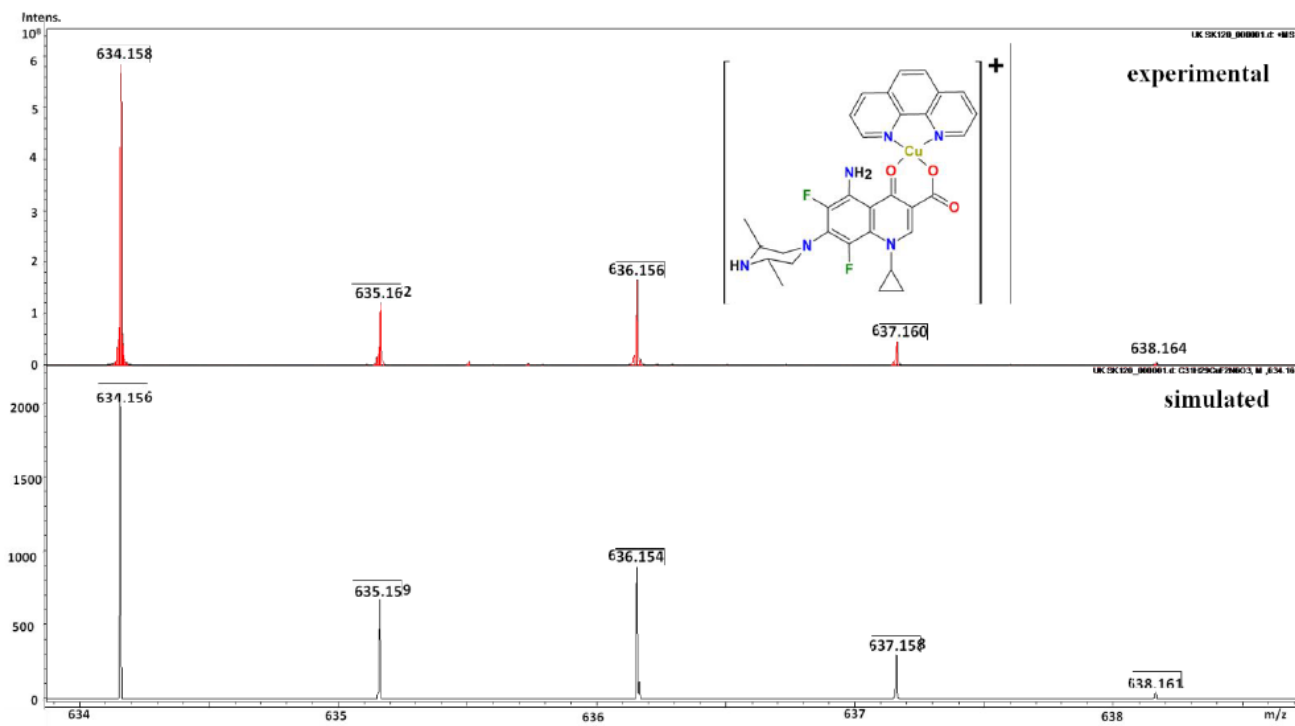


Fig. S10 G

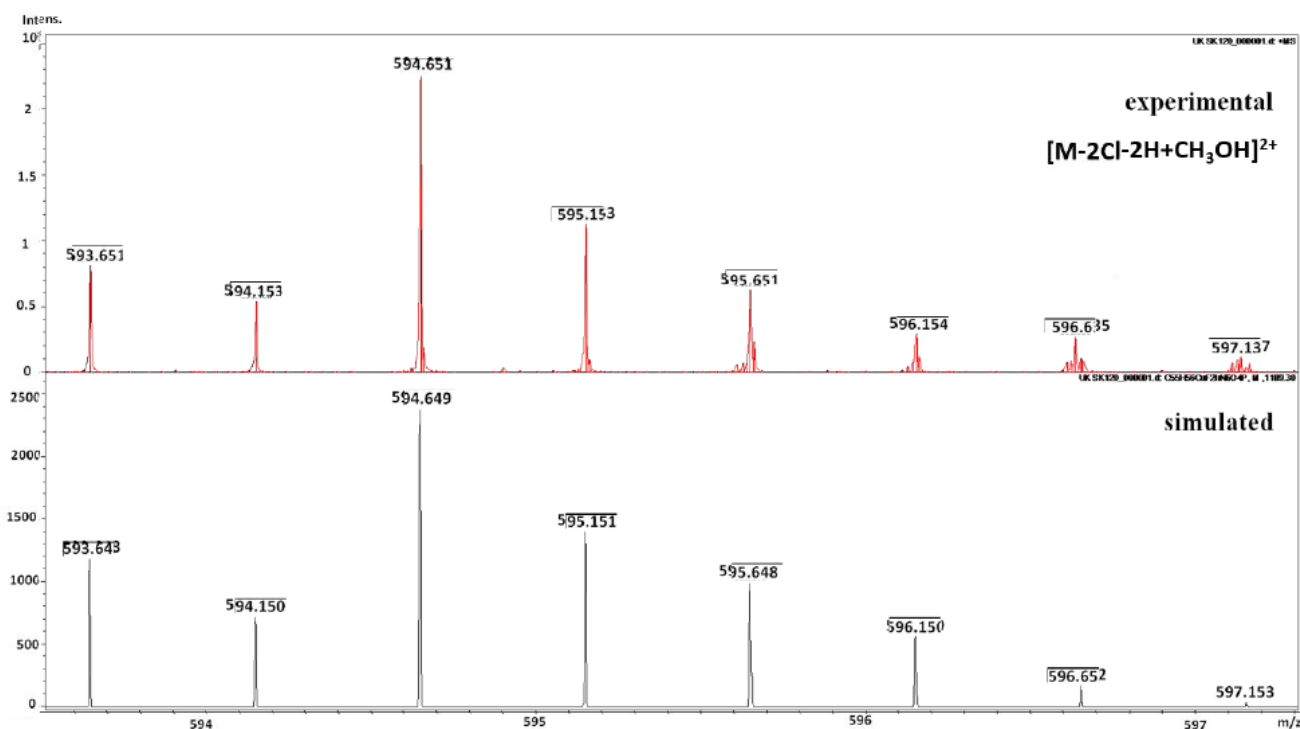


Fig. S10 H

(a) ESI mass spectrum of IrPSfCu(phen). ESI(+)-MS in CH₃OH, m/z : 1230.208 [M]⁺; 989.243 [MCu(phen)+H]⁺; 947.300 [M-Cu(phen)-2HCl+CH₂OH]⁺; 919.320 [M-Cu(phen)-2Cl+H]⁺; 832.210 [M-IrCpCl₂]⁺; 634.158 [M-IrCpCl₂-PPhCH₂]⁺; 594.651 [M-2HCl+CH₂OH]²⁺ (b) experimental and simulated spectra of [M]⁺ (c) experimental and simulated spectra of [M-Cu(phen)+H]⁺ (d) experimental and simulated spectra of [M-Cu(phen)-2HCl+CH₂OH]⁺ (e) experimental and simulated spectra of [M-Cu(phen)-2Cl+H]⁺ (f) experimental and simulated spectra of [M-IrCpCl₂]⁺ (g) experimental and simulated spectra of [M-IrCpCl₂-PPhCH₂]⁺ (h) experimental and simulated spectra of [M-2HCl+CH₂OH]²⁺

Infrared Spectroscopy

The FT-IR spectra of the four novel iridium(III)-copper(II) complexes in the far infrared region are shown in Fig. S10a, b for MIR region; and Fig. 10c shows FT-IR spectra of the starting reagent, Cu(phen)(NO₃)₂. The characteristic ν(C-H) stretching vibrations generate in the spectral range of 3057-2853 cm⁻¹ the medium peaks in the FT-ATR spectra of discussed complexes.

In the free ligands a strong band near 1720 cm⁻¹ is assigned to the ν(C=O) stretching vibrations of their carboxylic group (-COOH),¹ which is very weak or not observed in ATR spectra of these complexes. Besides, in the FT-IR spectra of the novel complexes are observed two characteristic bands attributed to the

antisymmetric and symmetric stretching vibrations of $\nu(\text{COO}^-)$, which can be the marker of the coordination model. The bands with medium intensity around 1630 cm^{-1} and 1335 cm^{-1} are assigned to the $\nu_{\text{as}}(\text{COO}^-)$ and $\nu_{\text{s}}(\text{COO}^-)$ stretching vibrations, respectively (Tab. 3).

Complex	$\nu_{\text{as}}(\text{COO}^-)$ [cm^{-1}]	$\nu_{\text{s}}(\text{COO}^-)$ [cm^{-1}]	$\Delta\nu$ [cm^{-1}]	$\nu(\text{C=O})$ [cm^{-1}] pyridine group	$\nu(\text{C=N})$ [cm^{-1}]	$\nu(\text{Cu-O})$ [cm^{-1}]	$\nu(\text{Cu-N})$ [cm^{-1}]
1	1618	1333	285	1583	1517	520	543
1*	1630	1334	296	1587	1519	524	548
2	1627	1308	319	1584	1519	501	554
2*	1632	1335	297	1587	1520	523	ov
3	1619	1321	298	1585	1520	512	523
3*	1633	1327	306	1588	1522	512	540
4	1630	1292	338	1576	1519	ov	ov
4*	1632	1293	339	1583	1520	ov	ov

Abbreviations: ν - stretching vibrations, ν_{as} - antisymmetric stretching vibrations, ν_{s} -symmetric stretching vibrations, ov- overlapped band; * in MeOH.

Tab. 3 The characteristic discussed bands in FT-IR spectra of complexes **1-4**.

We have determined the model of binding the used ligands to Cu^{2+} by showing Δ parameter ($\Delta = (\nu_{\text{as}}(\text{COO}^-) - \nu_{\text{s}}(\text{COO}^-))$). In the studied complexes Δ parameters are in the range of $285\text{--}339\text{ cm}^{-1}$, which indicates the monodentate (unidentate) coordination of the carboxylate group in **1-4**, because Δ is larger than in ionic compounds.² Nevertheless, the strong bands observed at 1624 cm^{-1} , 1628 cm^{-1} , 1612 cm^{-1} and at 1645 cm^{-1} in the FT-IR spectra of $\text{Ph}_2\text{PCH}_2\text{cfx}$, $\text{Ph}_2\text{PCH}_2\text{nfx}$, $\text{Ph}_2\text{PCH}_2\text{lfx}$, $\text{Ph}_2\text{PCH}_2\text{sfx}$ phosphine ligands are assigned to $\nu(\text{C=O})_{\text{py}}$ stretching vibrations, respectively. These peaks are shifted to lower frequencies in the range of $1558\text{--}1568\text{ cm}^{-1}$ for the FT-IR spectra of studied iridium-copper complexes indicating decrease in the stretching force constant of the C=O bond as consequence of the coordination of the oxygen atom to the Cu^{2+} ions. In the FT-IR spectrum of free phen (1,10-phenanthroline) ligand a characteristic band around 1586 cm^{-1} is due to $\nu(\text{C=N})$ stretching vibrations and is shifted to a lower frequency in FT-IR spectra of **1-4** ($\nu = 69\text{--}64\text{ cm}^{-1}$). This shift indicates the coordination of the pyridine nitrogen atoms of the phenyl group to the copper ions (from nitrogen atom to the empty d-orbital of the metal ion) in a bidentate model.²

Actually, the FT-IR spectroscopy can be used as a good analytical tool to follow the coordination of organic ligands with metal ions,³ which we confirm by analysis in FIR spectral region of the studied complexes **1-4**. The coordination marker bands: $\nu(\text{Cu-O})$ and $\nu(\text{Cu-N})$ are found in the FT-IR spectra of these complexes, *i.e.* at 520 , and 543 cm^{-1} for complex **1**, at 554 cm^{-1} and 501 cm^{-1} for complex **2**, respectively. These bands are absent in the spectra of free $\text{Ph}_2\text{PCH}_2\text{cfx}$, $\text{Ph}_2\text{PCH}_2\text{nfx}$, $\text{Ph}_2\text{PCH}_2\text{lfx}$, $\text{Ph}_2\text{PCH}_2\text{sfx}$ ligands and phen.

Nevertheless, dissolving the obtained complexes in methanol hardly changes their structures, which can be seen in the comparison of the spectra in the solid state with methanol solutions (Fig. S10a,b).

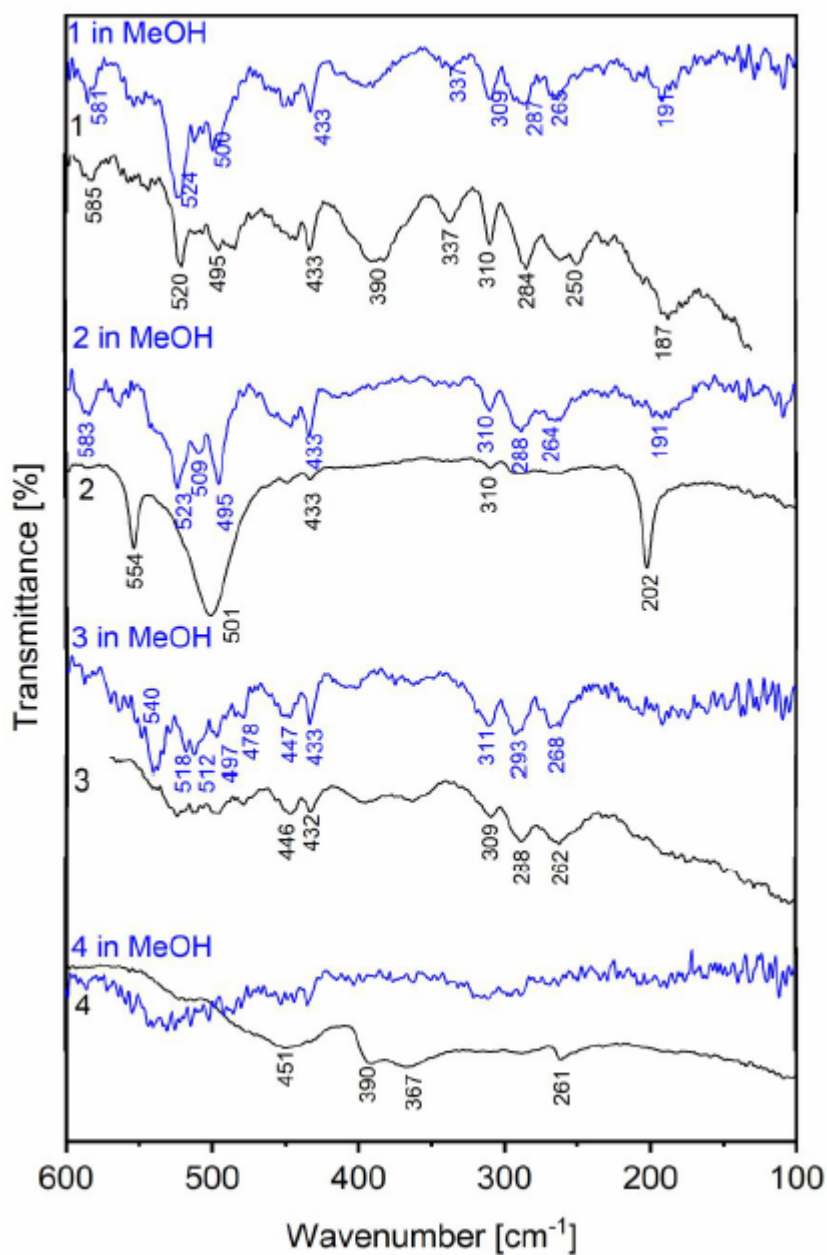


Fig. S11 A The FT-FIR spectra of complexes 1-4.

[1] Nakamoto, K. Infrared and Raman Spectra of Inorganic and Coordination Compounds, Part B. *J. Wiley & Sons Inc.* New York, **2009**

[2] Socrates, G. Infrared and Raman characteristic group frequencies: tables and charts. *J. Wiley & Sons*, **2004**

[3] Yadav, S.; Singh, R. V. Ferrocenyl-substituted Schiff base complexes of boron: Synthesis, structural, physicochemical and biochemical aspects. *Spectrochim Acta A Mol Biomol Spectrosc* **2011**, *78*, 298-306

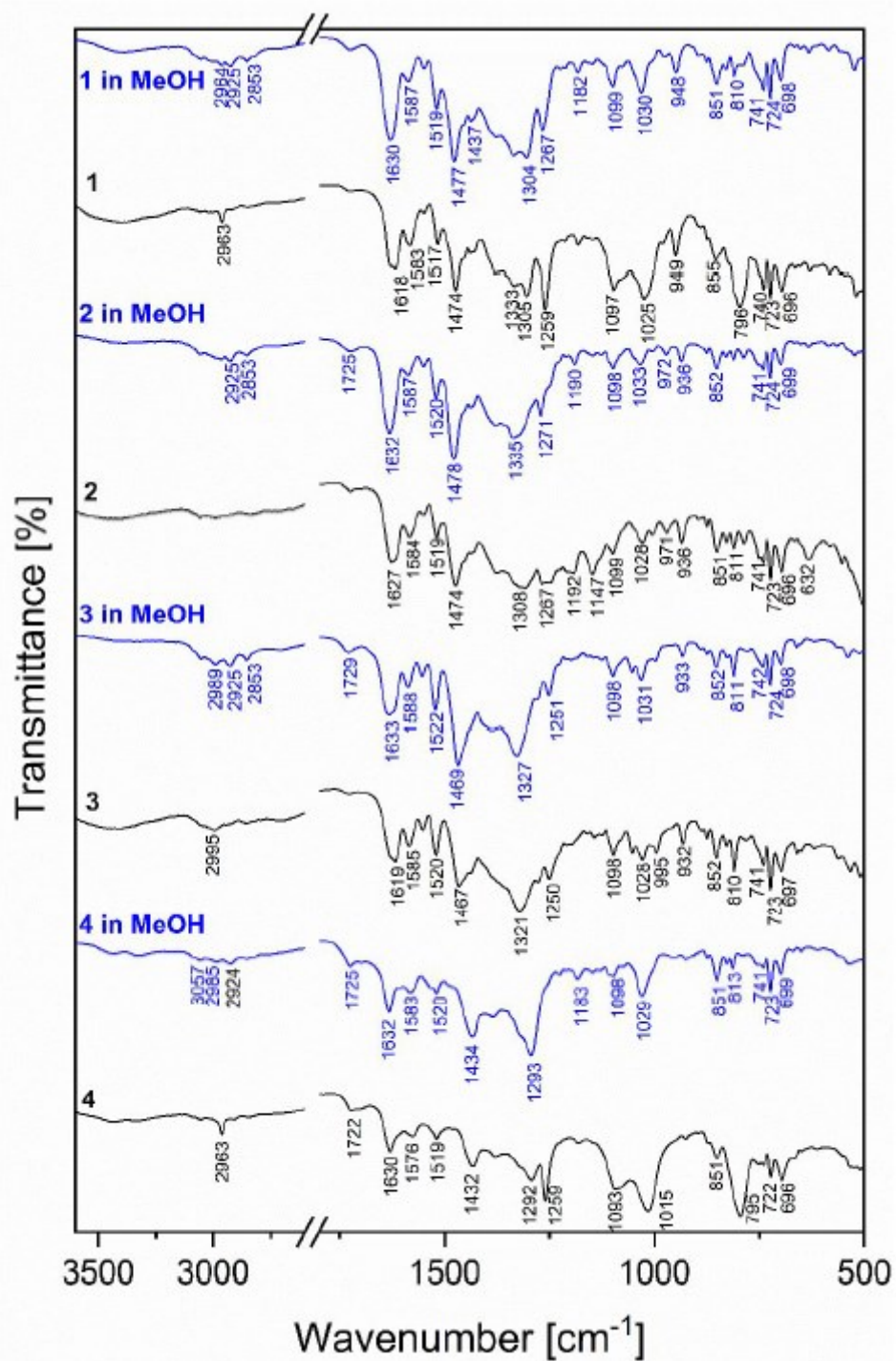


Fig. S11 B The FT-IR spectra of complexes 1-4 in the MIR spectral region.

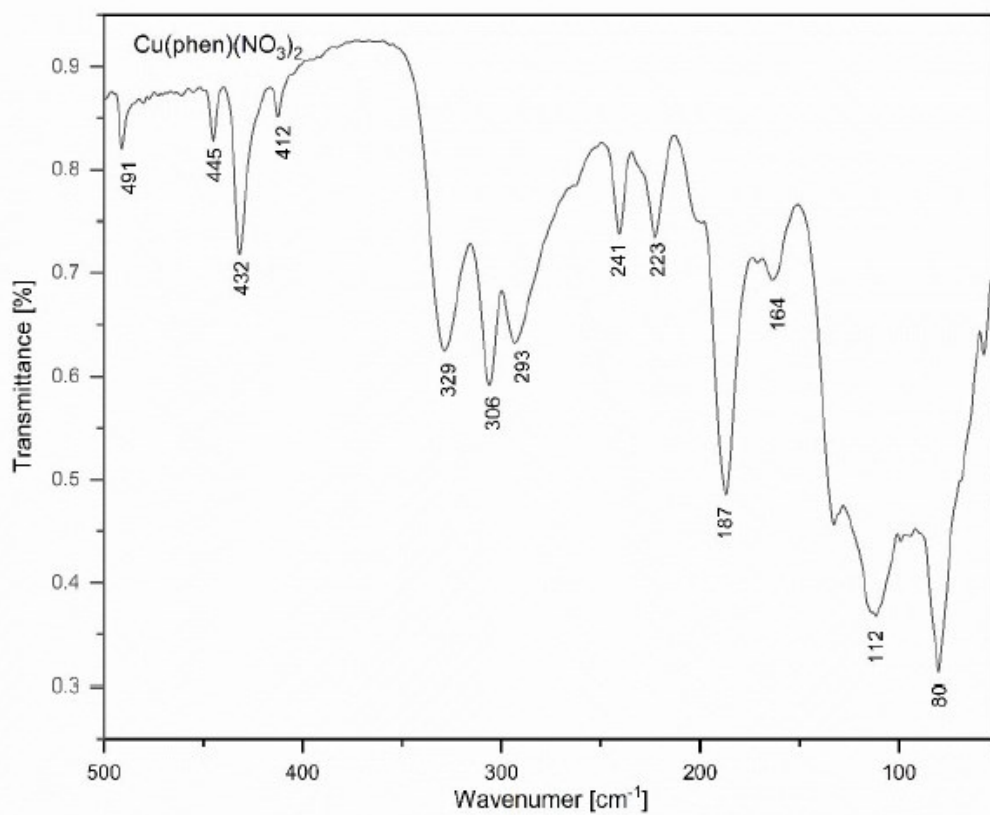
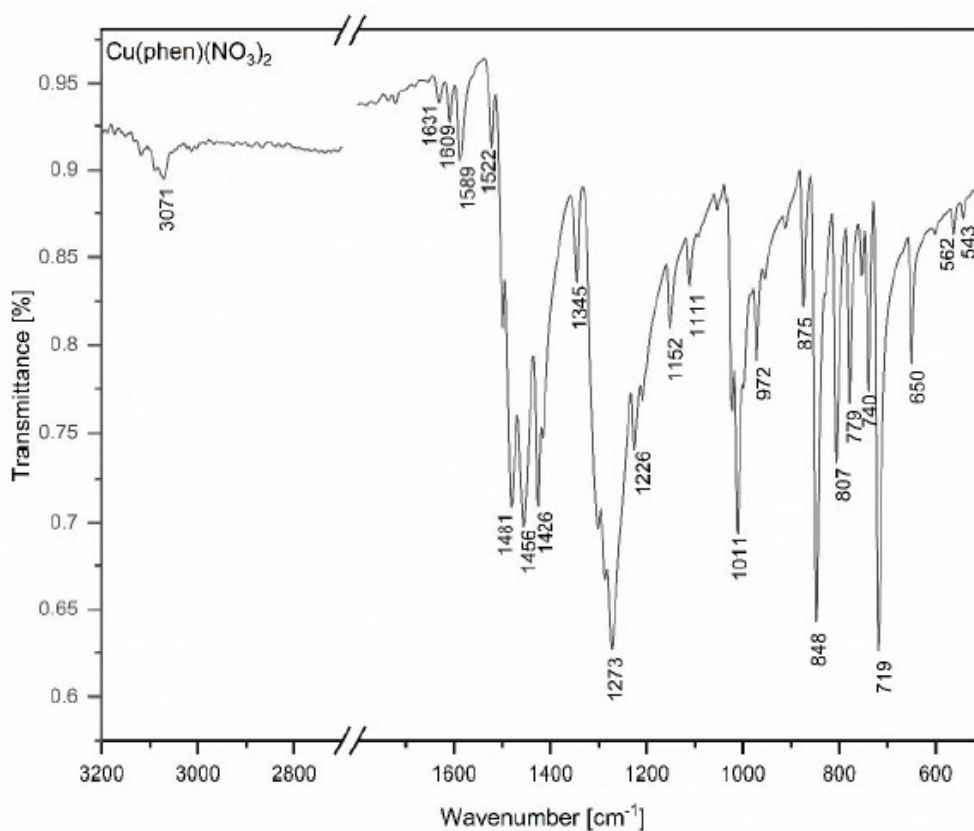


Fig. S11 C The FT-IR spectra of $\text{Cu(phen)(NO}_3)_2$ in the MIR and FIR spectral regions

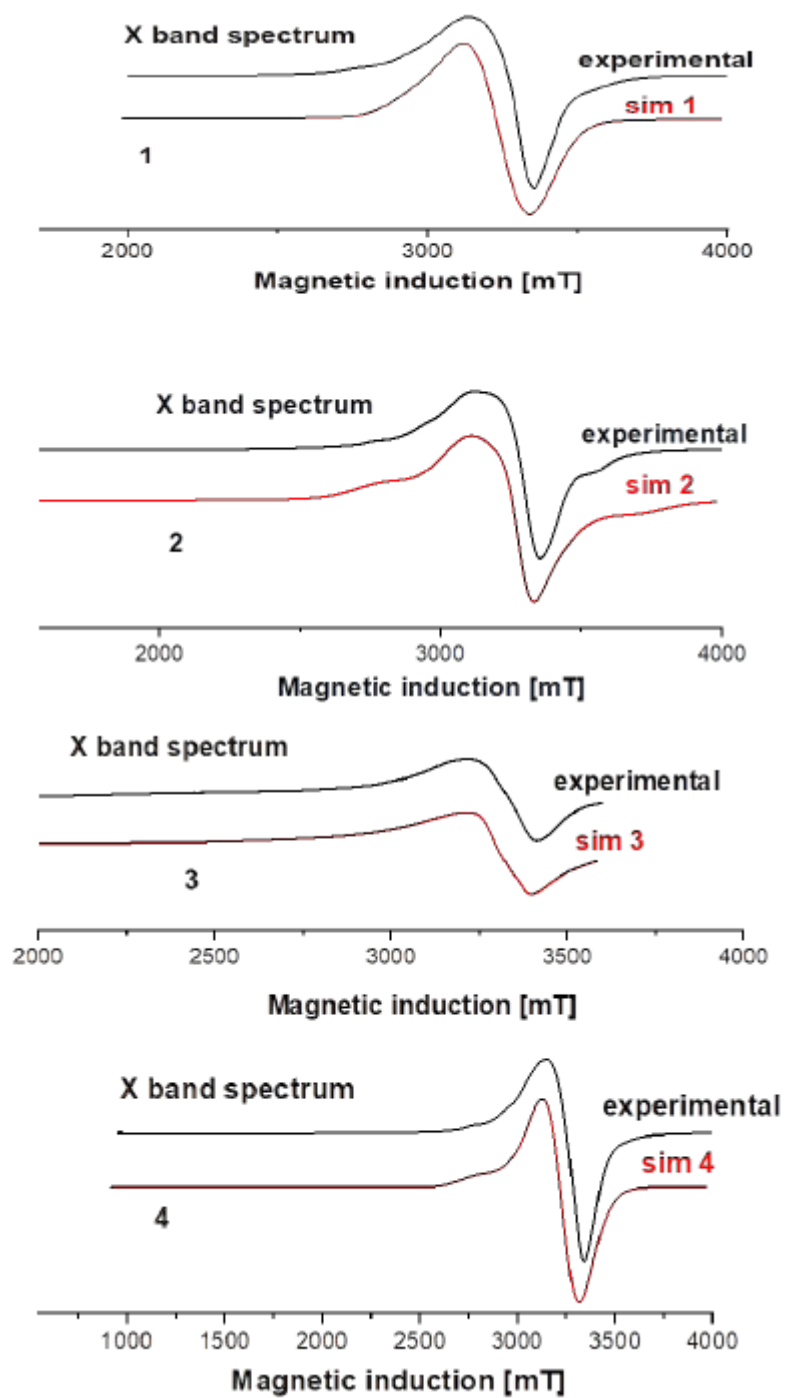


Fig. S12 The X-band EPR spectra of **1 - 4** at 77 K together with the spectrum calculated by computer simulation of the experimental spectra with spin Hamiltonian parameters given in the text.

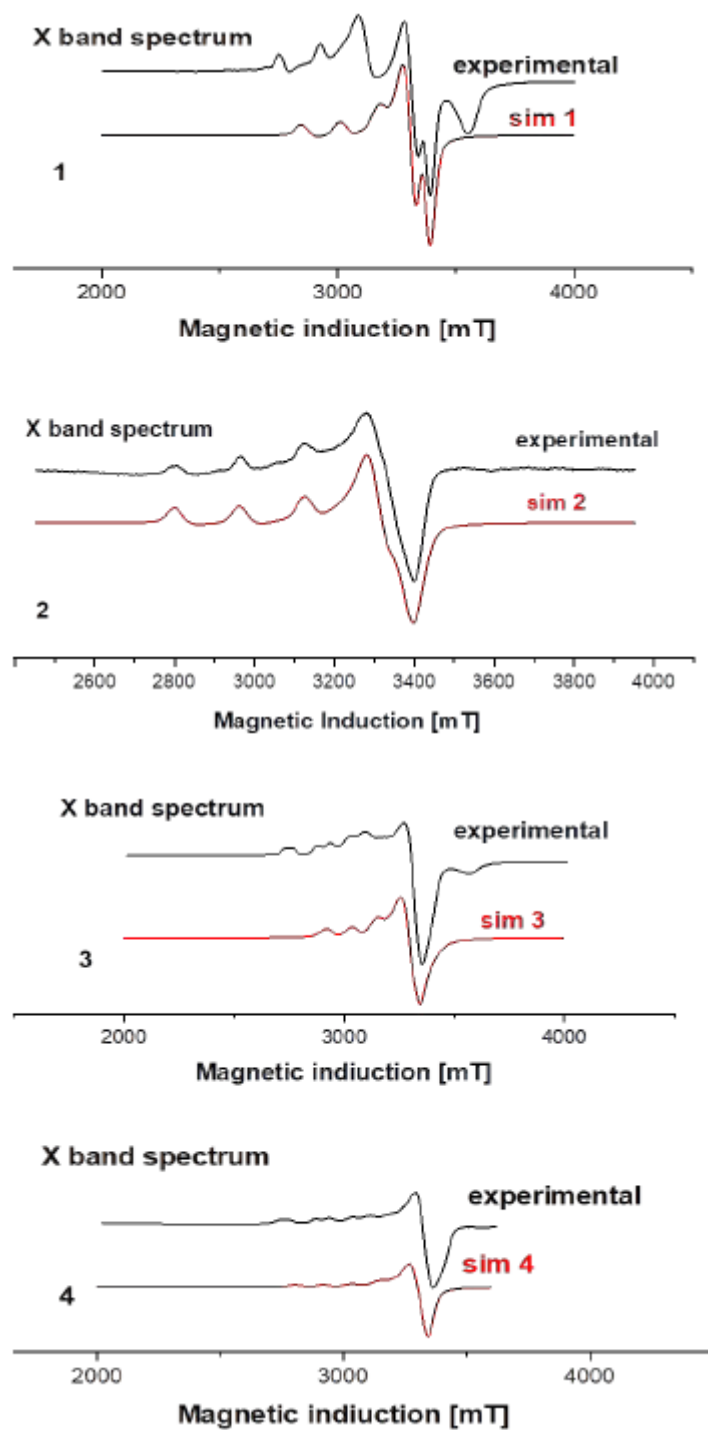


Fig. S13 EPR frozen solution spectra (at 77 K) of compounds **1** - **4**; in DMSO solvent together with the theoretical spectrum calculated using the parameters given in the text.

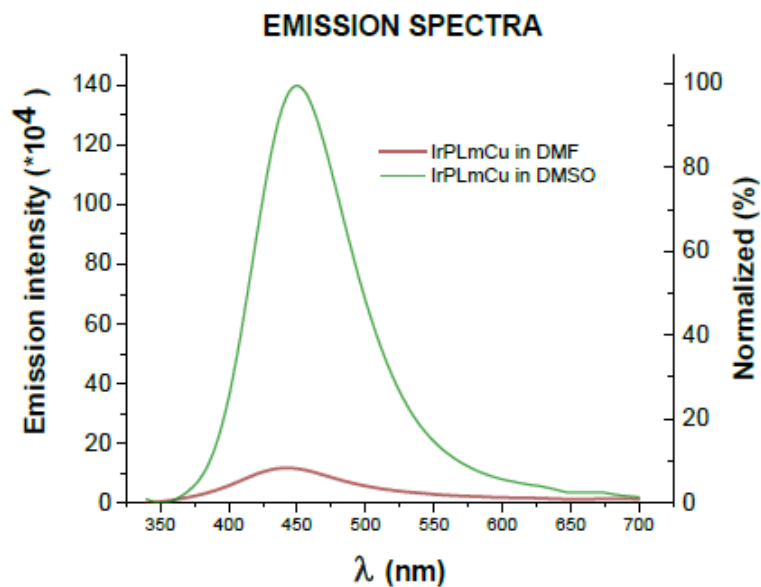


Fig. S14 Emission spectra obtained for IrPLmCu(Phen) and RuPLmCu(Phen) both in DMF and DMSO solution.

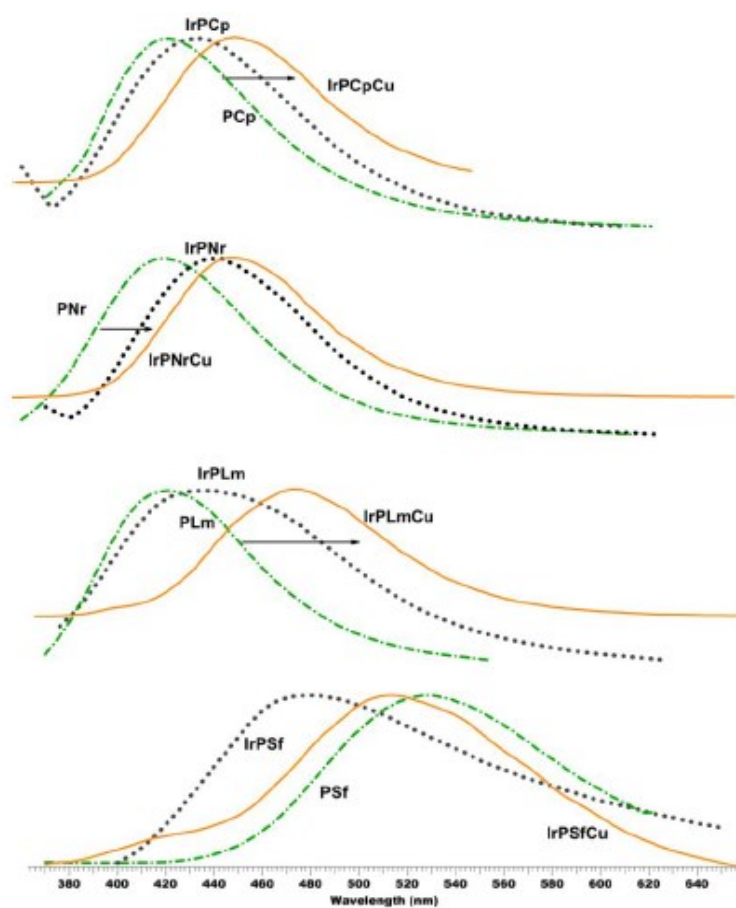


Fig. S15 Normalized emission spectra for heteronuclear Ir(III)/Cu(II) complexes, homonuclear Ir(III) complexes and the corresponding phosphine ligands; $\lambda_{exc} = 340$ nm, 298 K.

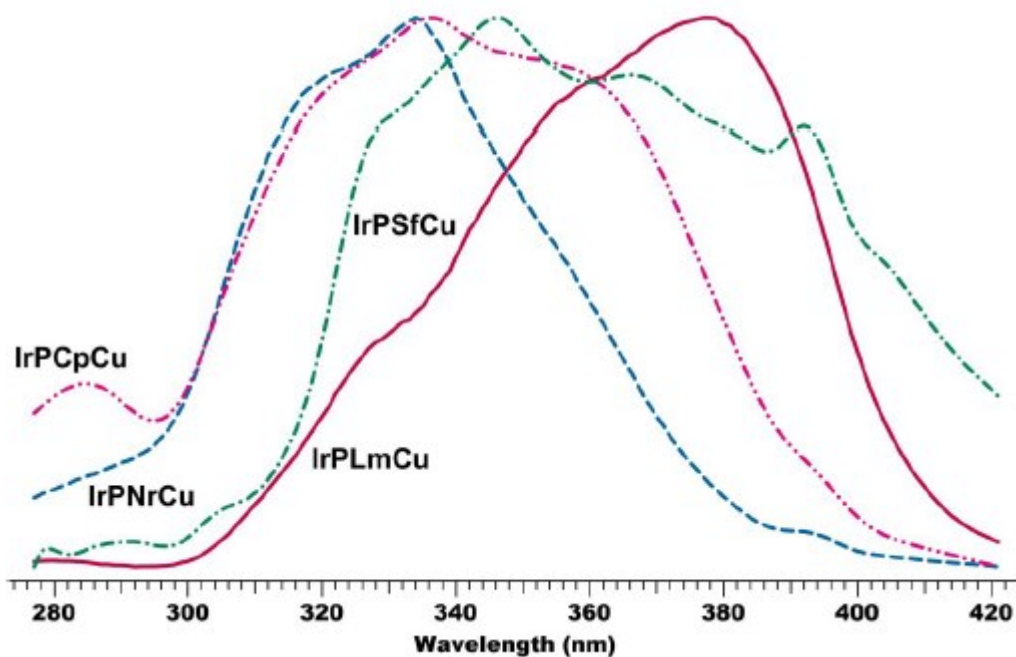
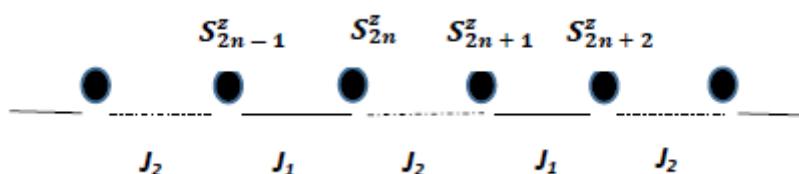


Fig. S16 Excitation spectra of IrPCpCu, IrPNrCu, IrPLmCu and IrPSfCu

Magneto-structural studies

DC measurements

To fit and interpret the magnetic susceptibility data of examined complexes, first it is necessary to find all possible magnetic pathways. As mentioned in the structural discussion, complexes **3** can be viewed as a monometallic chain in which the neighboring Cu(II) ions are bridged either by carboxylate groups of phosphino-fluoroquinolone ligands or OH⁻ linkers with Cu...Cu separation of 3.470 Å and 4.193 Å, respectively. Considering above the susceptibility data was analysed using a Hamiltonian [eq. 1] for an alternating Ising chain shows in scheme S1: (52)



Scheme S1 Alternating Ising chain.

$$H = \sum_{n=1}^{N/2} \left[-2J_1 S_{2n-1}^z S_{2n}^z - 2J_2 S_{2n}^z S_{2n+1}^z - g\beta H (S_{2n-1}^z - S_{2n}^z) \right], \quad \text{eq. 1}$$

where S_{2n}^z denotes the z – component of the 2ⁿ-th spin in a linear chain, J_1 and J_2 are.

The zero-field susceptibility of alternating antiferromagnetic Ising chain is:

$$\chi = \frac{Ng^2\beta^2}{4kT} \left[\frac{e^{K_1+K_2}}{\cosh(K_1-K_2)} \right], \quad \text{eq. 2}$$

Where

$$K_1 = \frac{J_1}{2kT}, K_2 = \frac{J_2}{2kT}$$

The best agreement with the experimental magnetic data for **3** was obtained with $J_1 = -0.82 \text{ cm}^{-1}$, $J_2 = -0.29 \text{ cm}^{-1}$, $g_{av}(\text{Cu}) = 2.09$ and $\text{TIP} = 66 \cdot 10^{-6} \text{ cm}^3 \text{ mol}^{-1}$, $R = \frac{\sum[(\chi T)_{\text{exp}} - (\chi T)_{\text{calc}}]^2}{\sum[(\chi T)_{\text{exp}}]^2} = 2.42 \cdot 10^{-5}$ (solid blue line in Figure 7A). The calculated curve matches the magnetic data well. The obtained result suggests that the stronger antiferromagnetic exchange interaction is mediated through the doubly oxygen bridge of carboxylate group (the higher J value, shorter Cu...Cu contact) which correspond to the magneto-structural correlations presented in the literature.^{53,54} For dimers with planar or near-planar cores $[\text{Cu}_2(\mu_2\text{-O})_2]^{2+}$ the exchange coupling constant (J) depends on the value of the Cu - O - Cu (ϕ) angle and the Cu-O bridge distance (R) especially expressed by the ϕ / R ratio, and from more complicated factors such as geometry around paramagnetic centers.⁵⁵⁻⁵⁷ Thus for $\phi > 97.5^\circ$ the interaction is predicted to be antiferromagnetic ($S = 0$ ground state) and for $\phi < 97.5^\circ$ the ground state is equal 1 ($S = 1$) and interaction should be ferromagnetic. The small magnitude of this interaction may be due to the asymmetry of the oxide bridge (two different R values, one much shorter 2.058 Å and the other much longer 2.220 Å) causing distortion of the OH geometry and an unusually long distance Cu...Cu.

Complexes **1**, **2** and **4** can be considered as mononuclear species which create supramolecular one dimensional polymeric architecture through π -stacking interactions and system of hydrogen bonds between the water molecule and oxygen atoms from carbonyl groups with shortest Cu ... Cu contact 4.196 (1), 4.904 (2) Å. The intermolecular interactions in all monomeric complexes was calculated using the well-known PHI program⁵¹ which allows the simultaneous fitting of $\chi T(T)$ and $M(H)$ dependencies. The TIP was also included into the fitting procedure. The least squares fit of the experimental data by this expressions leads to the following results: $g_{av}(\text{Cu}) = 2.09$, $zJ' = -0.09 \text{ cm}^{-1}$, $\text{TIP} = 138 \times 10^{-6}$ for **1** (red lines in Fig. 7A) and $g_{av}(\text{Cu}) = 2.11$, $zJ' = 0.15 \text{ cm}^{-1}$, $\text{TIP} = 192 \times 10^{-6}$ for **2** (green lines in Fig. 7A) and $g_{av}(\text{Cu}) = 2.14$, $zJ' = 0.28 \text{ cm}^{-1}$, $\text{TIP} = 226 \times 10^{-6}$ for **4** (black lines in Fig. 7A). The discrepancy factor is 2.09×10^{-5} (**1**), 6.93×10^{-6} (**2**) and 3.57×10^{-6} (**4**). These data indicate that a weak exchange interaction between nearest copper atoms in the crystal lattices can exist of antiferromagnetic in **1** and ferromagnetic in **2** and **4** nature. The temperature independent paramagnetic term is bigger than usually found. Although the origins of the observed phenomenon are unclear, it was verified by repeated measurements.

AC susceptibility measurements

New information was obtained from the AC susceptibility measurements. They were performed first at low temperature $T = 2.0$ K for a set of representative frequencies of the alternating field ($f = 1.1, 11, 111,$ and 1111 Hz) by ramping the magnetic field from zero to BDC = 1 T with the working amplitude BAC = $0.3 \mu\text{T}$. There was no absorption signal (out-of-phase susceptibility component χ'') at the zero-field owing to a fast magnetic tunneling. With the increasing external field, this component raised, and only for complex **2** passed through a maximum between 0.1 and 0.2 T at the highest frequencies (Figure S16). This behavior indicates that **2** can exhibit the field induced slow magnetic relaxation.

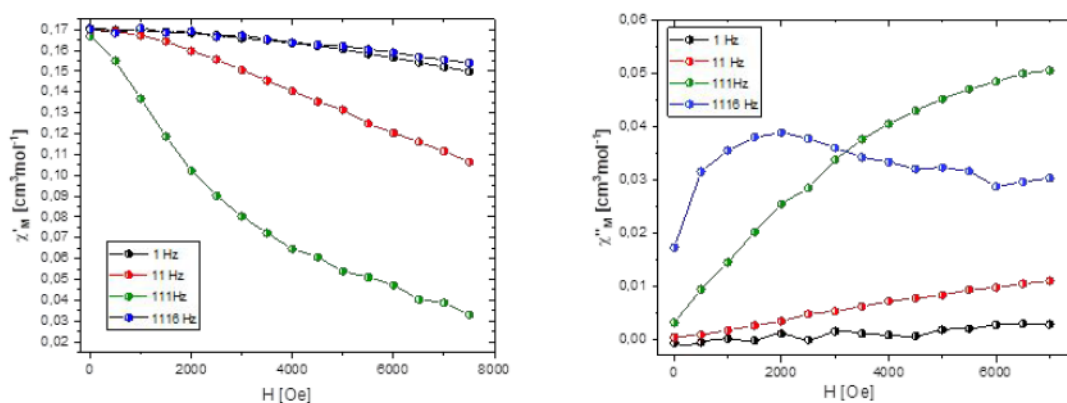


Fig. S17 Field dependencies of the AC susceptibility components for **2** at $T = 2.0$ K for a set of frequencies of the AC field. Lines are a guide for the eye.

Subsequent experiments were done at a fixed external magnetic field BDC = 0.1 T (the maximum of the high-frequency signal) changing the frequency between $f = 0.1$ to 1500 Hz for a set of temperatures between $T = 1.8$ and 12 K (Figure S17). The in-phase ($\chi' M'$) and out-of-phase ($\chi' M''$) components exhibit small frequency dependences with the application of an external field of 0.2 T, indicative the possibility of a slow relaxation of magnetization, although the maxima in $\chi' M''$ are missing. Using this data we cannot suggest SMM or SIM behavior. However, the relaxation process for Cu(II) ions is very rare due to the absence of a barrier to spin reversal: the axial zero-field splitting parameter D is undefined. However, some $S = 1/2$ spin systems such V(IV), low-spin Mn(IV), Ni(I, III), only three example of Cu(II), Os(V), Ir(IV), Fe(III) and Ru(III) complexes show a slow magnetic relaxation (SMR) that is supported by the external magnetic field.⁵⁸⁻⁶² The presence of a relaxation process in complex **2** can be a result of geometry around Cu(II) ions. Though the D parameter cannot be assigned to mononuclear copper(II) complexes, these are well-known as anisotropic systems showing at least two distinct $g_z \neq g_x$ values well seen in the EPR spectra of an axial type. Thus, even in the absence of the zero-field splitting, there exists a magnetic anisotropy. Additionally, the rest complexes not exhibit a relaxation process. This may be due to the presence of higher square-

pyramidal geometry distortion in **2** ($\tau' = 0.26$), which should lead to a greater difference between g_x and g_y and thus greater anisotropy of g tensor than those for **1**, **3** and **4**.

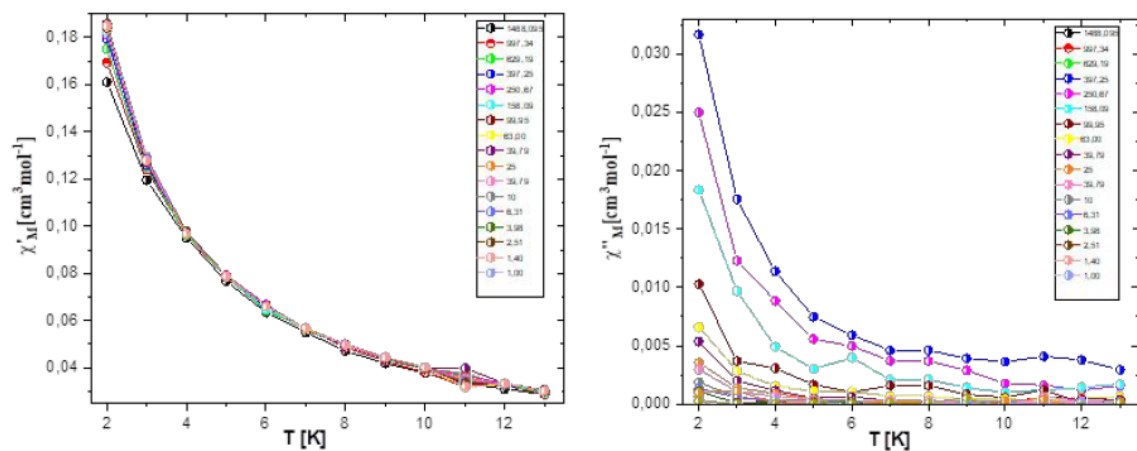


Fig. S18 Temperature dependence of (a) the in-phase and (b) out-of-phase molar susceptibility of **2**.

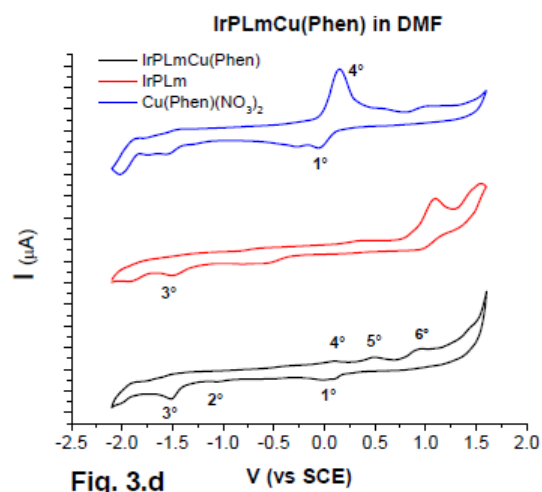
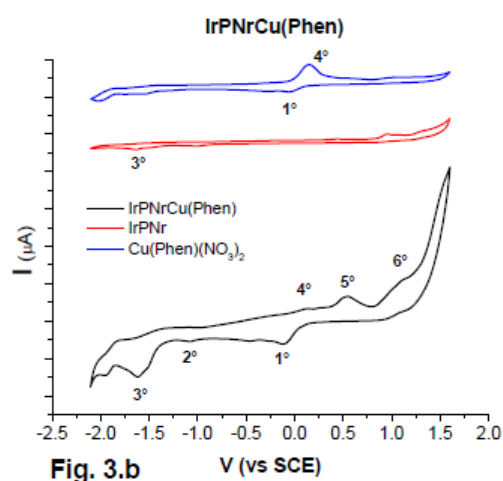
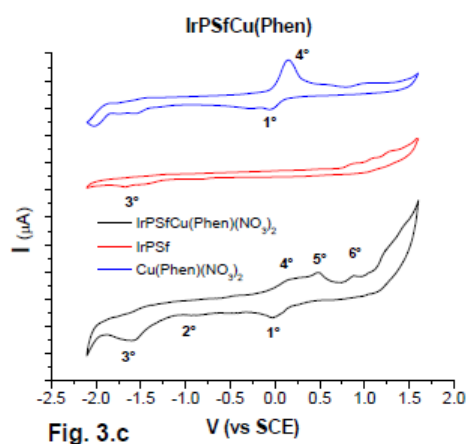
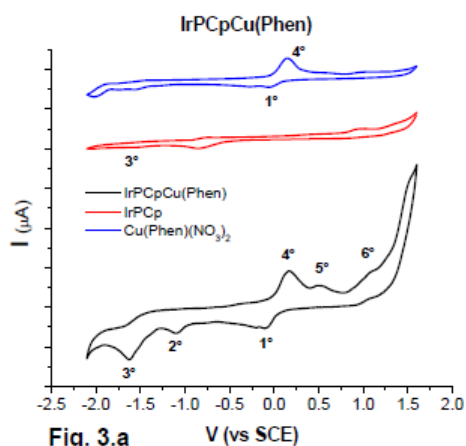


Fig. S19 Cyclic voltammetry of the mononuclear fragments of Iridium complexes in DMF (50mV/s from -2.1 to +1.6 vs SCE, 0.1M TBAPF₆ as supporting electrolyte).

Ligands		Homonuclear Ir ^{III} complexes		Heteronuclear Ir ^{III} -Cu ^{II} complexes	
PCp	5.81	IrPCp	7.73	IrPCpCu	3.47
PSf	6.35	IrPSf	7.44	IrPSfCu	3.83
PLm	6.86	IrPLm	7.51	IrPLmCu	3.92
PNr	5.97	IrPNr	7.26	IrPNrCu	3.55

Tab. S3 Calculated log P values for ligands using program ACD/log P¹ and complexes using program ALOGPS 2.150.(1-3)

Formulation	Diameter [nm] (TEM, ImageJ)	Hydrodynamic diameter [nm] (DLS)	Zeta potential [mV] (pH =)
L	135.8 ± 21.0 nm	146.8 ± 13.6, PDI = 0.01	-30.2 ± 2.7 mV
1a	83.7 ± 18.4 nm	108.8 ± 24.7, PDI = 0.05	-42.3 ± 6.2 mV

Tab. S4 Hydrodynamic diameter and Zeta potential determined by DLS technique as well as loading content and encapsulation efficiency determined by ICP-MS technique for selected liposome formulations.

Experimental methods

General procedures

All starting reagents (iridium and ruthenium), 2nd (Hcfx, Hnfx, Hlfx) and 3rd (Hsfx) generation fluoroquinolones (>98%), phosphines, [Cu(phen)(NO₃)₂], [Ir(η⁵-Cp*)Cl₂]₂ and solvents were purchased from Sigma Aldrich and used without further purifications. All solvents were deaerated prior to use. Anhydrous Dimethylsulphoxide (DMSO) (34869-1L CAS: 67-68-5 ≥99.7%) and dimethylformamide (227056-1L CAS: 68-12-2 ≥99.8%) were purchased from Sigma Aldrich.

Tetrabutylammoniumhexafluorophosphate (TBAPF₆) was obtained from Alfa Aesar (CAS: 3109-63 5 98%). Electrodes for cyclic voltammetry were a platinum wire counter electrode (Matech Ø0.5mm 99.9%) a SCE reference (303/SCG/6) and glassy carbon disk working electrode from Amel Electrochemistry (303/SCG/6). Mononuclear complexes (IrPsfx, IrPlfx, IrPnfx and IrPcfx) (26) and aminomethyl(diphenyl)phosphines (Psfx, (67) Plfx, (38) Pnfx (37) and Pcfx (68)) were synthesized as described previously.

Characterization of organometallic iridium(III) complexes

X-Ray quality crystals were obtained by slow evaporation mother liquor. SCXRD measurements for 1 and 3, were performed on a Rigaku Oxford Diffraction XtaLAB Synergy-R DW diffractometer equipped with a HyPix ARC 150° Hybrid Photon Counting (HPC) detector using CuKα (λ = 1.54184 Å). For structure 2 a Xcalibur Gemini Ultra diffractometer equipped with Ruby CCD detector using CuKα (λ = 1.54184 Å) was employed. All measurements were performed at 100 K. Data were processed using the CrystAlisPro software. The structures were solved by intrinsic phasing with SHELXT (2015 release) and refined by fullmatrix least-squares methods based F 2 using SHELXL. For all structures, H atoms bound to C atoms were placed in the geometrically idealized positions and treated in riding mode, with C-H = 0.95 Å and Uiso(H) = 1.2Ueq(C) for C-H groups, and C-H = 0.98 Å and Uiso(H) = 1.5Ueq(C) for CH₃ groups. The N- and O-bonded hydrogen

atoms which were at initial stage of refinement located from difference maps and then constrained with AFIX 13 and AFIX 3 command, respectively. Crystallographic data of the structures have been deposited at the Cambridge Crystallographic Data Centre with CCDC reference numbers :

2175515 [Ir(η^5 -Cp*)Cl₂Pf_x-Cu(phen)](NO₃)·1.3(H₂O)·1.95(CH₃OH);

2175516 [Ir(η^5 -Cp*)Cl₂Pn_fx Cu(phen)](NO₃)·1.75(CH₃OH)·0.75(H₂O);

2175517 ([Ir(η^5 -Cp*)Cl₂Pc_fx-Cu(phen)](NO₃)·1.75(CH₃OH)·0.75(H₂O).

Elemental analyses (C, H and N) were carried out with a Vario Micro Cube–Elementar. Mass spectra were recorded with a Bruker MicrOTOF-Q II spectrometer with an ESI ion source under the following conditions: nebulizer pressure: 0.4 bar, dry gas: 4.0 L*min⁻¹ heated to 180 °C. Data were recorded in the positive ion mode, while profile spectra were recorded in the mass range 50–3000 m/z; end plate offset –500 V; capillary voltage 4500 V; mass resolving power of the instrument was over 18 000. Mass calibration was done using the cluster method with a mixture of 10 mM sodium formate and isopropanol (1 : 1, v/v) before the run. In order to record the spectra the compounds were dissolved in chloroform. Electronic absorption spectroscopy was carried out with an UV-Vis spectrophotometer (Agilent Technologies, Cary300 UV-Vis).

Steady state luminescence spectra were acquired with an Edinburgh Instruments FS920 spectrofluorimeter equipped with a R928 phototube detector. The spectroscopic energy E₀₀ was obtained from the crossing of the normalized absorption and emission spectra. FT-IR spectra of complexes were recorded using a BrukerVertex 70V vacuum spectrometer equipped with a diamond ATR cell with resolution of 2 cm⁻¹ in the middle-infrared (4000-500 cm⁻¹) and far-infrared (600–100 cm⁻¹) regions at room temperature as solid state and methanolic solutions (c = 0.80%) as well. The spectral data were collected and further elaborated using Bruker OPUS software.

Direct current (DC) magnetic measurements in the temperature range 1.8-300 K (BDC = 0.1 T) and variable field (0-5 T) (at low temperature) were performed using a Quantum Design SQUID-based MPMSXL-5-type magnetometer. Corrections were based on subtracting the sample holder signal and contribution χ_D estimated from the Pascal constants.⁶⁹ Variable-temperature (2–7 K) alternating current (AC) magnetic susceptibility measurements under different applied static fields in the range of BDC = 0–1.0 T were carried out with Quantum Design Physical Property Measurement System (PPMS). Magnetic measurements were carried out by crushing the crystals and restraining the sample in order to prevent any displacement due to its magnetic anisotropy.

Electron paramagnetic resonance (EPR) spectra were measured using a Bruker ELEXYS E 500 Spectrometer equipped with NMR teslameter and frequency counter at X-band. The experimental spectra were simulated with use of computer programs (S=1/2) written by Dr. Andrew Ozarowski from NHMFL, University of

Florida. The solid compounds dissolved in water and a few drops of DMSO were added to the samples to ensure good glass formation at liquid nitrogen temperature.

Synthesis of heterometallic iridium-copper complexes

The Ir(III)/Cu(II) complexes **1–4** were prepared according to following general synthetic procedure: a solution of the [Cu(phen)(NO₃)₂] (1 equiv) in methanol (5 mL) was slowly added to a stirred solution of mononuclear complexes Ir(III) (1 equiv) in the same solvent (20 mL) and the mixture was stirred at room temperature in the dark. After 24 h of stirring dark-green (complexes 1-3) / -brown (complex 4) solid has been formed. The solid was filtered off, washed a few times with mixture of water and methanol (V:V = 5:1) and dried under vacuum. Green/brown solid was recrystallized from CH₃OH (T=28°C) to give microcrystals in each case (but only complexes 1-3 were suitable for x-ray analysis).

Data for [Ir(η^5 -Cp*)Cl₂Pcfx-Cu(phen)] (1)

Yield: 84%, Molar mass: 1300.196%g/mol. Anal. Calcd for C₅₂H₅₃Cl₂CuFIrN₅O₄P·(NO₃)·2.75(H₂O): C, 48.04; H, 4.54; N, 6.46%. Found: C, 48.05; H, 4.55; N, 6.47%.

ESI(+)-MS in CH₃OH, m/z: 1129.264 (theor.: 1129.274) (100%) [IrPCpCu-H₂Cl-Cl₂H+CH₂OH]⁺; 1099.260 (theor.: 1099.263) (3%) [IrPCpCu-2Cl]⁺; 858.280 (theor. 858.281) (6%) [IrPCpCu-2Cl-Cu(phen)+H]⁺; 787.176 (theor.: 787.178) (27%) [IrPCpCu-IrCl₂+O]⁺; 573.122 (theor.: 573.123) (9%) [IrPCpCu-IrCl₂-PPH₂CH₂]⁺; 564.131 (theor.: 564.133) (5%) [IrPCpCu-2H-2Cl+CH₃OH]²⁺; 549.126 (theor.: 549.127) (6%) [IrPCpCu-HCl-Cl]²⁺

Data for [Ir(η^5 -Cp*)Cl₂Pnfx-Cu(phen)] (2)

Yield: 89%, Molar mass: 1353.226%g/mol. Anal. Calcd for (C₅₁H₅₂Cl₂CuFIrN₆O₆P)·(NO₃)·1.75(CH₄O)·0.75(H₂O): C, 46.82; H, 4.51; N, 7.25%. Found: C, 46.83; H, 4.52; N, 7.27%.

ESI(+)-MS in CH₃OH, m/z: 1157.199 (theor.: 1157.201) (100%) [IrPNrCu+H]⁺; 1123.246 (theor.: 1123.240) (1%) [IrPNrCu-Cl+H]⁺; 916.222 (theor.: 916.218) (4%) [IrPNrCu-Cu+H]⁺; 759.183 (theor.: 759.183) (17%) [IrPNrCu-IrCl₂]⁺

Data for [Ir(η^5 -Cp*)Cl₂Plfx-Cu(phen)] (3)

Yield: 88%, Molar mass: 1357.29%g/mol. Anal. Calcd for

$C_{52}H_{52}Cl_2CuF_2N_5O_3PIr \cdot (NO_3) \cdot 1.3(H_2O) \cdot 1.95(CH_4O)$: C, 48.26; H, 4.81; N, 6.19%. Found: C, 48.28; H, 4.82; N, 6.20%.

ESI(+)MS in CH_3OH , m/z: 1191.175 (theor.: 1191.204) (100%) $[IrPLmCu+H]^+$; 1149.285 (theor.: 1149.280) (5%) $[IrPLmCu-H_2Cl-2HCl+CH_3OH]^+$; 948.229 (theor.: 948.225) (38%) $[IrPLmCu-Cu]^+$; 912.253 (theor.: 912.248) (5%) $[IrPLmCu-Cu(phen)-Cl]^+$; 908.303 (theor.: 908.297) (4%) $[IrPLmCu-Cu(phen)-2Cl-2H+CH_3OH]^+$; 878.293 (theor.: 878.287) (3%) $[IrPLmCu-Cu(phen)-2Cl+H]^+$; 791.191 (theor.: 791.187) (76%) $[IrPLmCu-IrCl_2]^+$; 593.131 (theor.: 593.129) (43%) $[IrPLmCu-IrCl_2-PPh_2CH_2]^+$

Data for $[Ir(\eta^5-Cp^*)Cl_2Psfx-Cu(phen)]$ (4)

Yield: 78%, Molar mass: 1231.69%g/mol. Anal. Calcd for $C_{54}H_{55}Cl_2CuF_2N_6O_{-3}PIr$: C, 52.66; H, 4.50; N, 6.82%. Found: C, 52.65; H, 4.49; N, 6.81%.

S52

ESI(+)MS in CH_3OH , m/z: 1230.208 (theor.: 1230.234) (58%) $[IrPSfCu+H]^+$; 989.243(theor.: 989.251) (4%) $[IrPSfCu-Cu(phen)+H]^+$; 947.300(theor.: 947.308) (52%) $[IrPSfCu-Cu(phen)-2H-2Cl+CH_3OH]^+$; 919.307(theor.: 919.313) (12%) $[IrPSfCu-Cu(phen)-2Cl+H]^+$; 832.210 (theor.: 832.216) (48%) $[IrPSfCu-IrCpCl_2]^+$; 634.158 (theor.: 832.156) (12%) $[IrPSfCu-IrCpCl_2-PPhCH_2]^+$; 594.651 (theor.: 594.649) (4%) $[IrPSfCu-2H-2Cl+CH_3OH]^{2+}$

Electrochemical characterization

Cyclic voltammetry was carried out with an Autolab PGSTAT302N potentiostat-galvanostat. A single compartment cell of the type GC/SCE/Pt containing a deoxygenated supporting electrolyte made of 0.1 M TBAPF₆ in DMF was used. Typically, an analytic concentration of 0.5 mM was adopted. Voltammetric cycles were performed at 50mV/s, scanning from open circuit to negative potentials and backwards.

Preparation of liposomes

Cholesterol (100 mg) and phosphatidylcholine (200 mg) were dissolved in dichloromethane (4.5 ml). After mixing 150 μ l of the solution was transferred to each Eppendorf tube (30 pieces, 1.5 ml). The solvent was blown out by nitrogen during rotating. This way liposome film was formed on the walls of tube. Each Eppendorf tube contained 10 mg of liposome. The complexes (2, 1, 0.5, 0.25 and 0.125 mg) were dissolved in dichloromethane (300 μ l) and added to Eppendorf tube with liposome solution (10 mg in 150 μ l of CH_2Cl_2). The solutions were homogenized in ultrasonic bath (10 min) and then blown out by nitrogen.

Water (1 ml) was poured on the film and Eppendorf tube was homogenized in ultrasonic bath to form light brown or light green liposome suspension. The samples were shaken and heated on Thermomixer comfort for 15 min at 60°C.

TEM characterization of liposomes

Liposomes morphology was analyzed by using a FEI™ Tecnai T20 Microscope operated at 200 kV. The size was determined from the enlarged TEM micrographs, using commercially available software ImageJ, counting at least 50 particles in different images.

DLS characterization of liposomes

The average hydrodynamic diameter and electrokinetic potential were determined by the dynamic light scattering (MADLS; Zetasizer Ultra, Malvern). Measurements were performed in PBS (pH = 7.4) at room temperature.

Cell cultures

MCF7 cell line (human breast adenocarcinoma, morphology: epithelial-like, ATCC: HTB-22), A549 cell line (human lung adenocarcinoma, morphology: epithelial, ATCC: CCL-185) and HaCaT (human keratinocyte) were cultured in Dulbecco's Modified Eagle's Medium (DMEM, Corning) with phenol red, supplemented with 10% fetal bovine serum (FBS) and with 1% streptomycin/penicillin. WM266 4 cell line (human skin (metastasis), morphology: epithelial, ATCC CRL-1676) were cultured in EMEM (EBSS) + 2mM Glutamine + 1% Non-Essential Amino Acids (NEAA) + 1% Sodium Pyruvate (NaP) + 10% Foetal Bovine Serum (FBS). DU-145 cell line (human prostate carcinoma) and HEK293T cell line (human embryonic kidney) were cultured in minimum essential medium (MEM, Corning) with only 10% fetal bovine serum (FBS). Cultures were incubated at 37 °C under a humidified atmosphere containing 5% CO₂. Cells were passaged using a solution containing 0.05% trypsin and 0.5 mM EDTA. All media and other ingredients were purchased from ALAB, Poland.

Cytotoxic activity

Since most of the studied compounds are insoluble in aqueous media, therefore they needed to be predissolved in DMSO for biological tests. Cytotoxicity was assessed by MTT assay performed according to the protocols described previously. (70) In brief, 1×10⁴ cells per well, seeded in 96 well flat-bottom microtiter plate, were incubated with the tested complexes (1, 2, 3 and 4) at various concentrations for 24 h. After that time, solutions of compounds were washed out, cells were washed three times with PBS and fresh medium was applied. Each compound concentration was tested in five replicates and repeated at least three times. Determined values of IC₅₀ (concentration of a drug required to inhibit the growth of 50%

of the cells) are given as mean +S.D. (Standard Deviation). Furthermore, post-treatment survival assessment of the treated cells was analyzed under a fluorescence inverted microscope (Olympus IC51, Japan) with an excitation filter 470/20 nm. For this, cells were stained with two versatile fluorescence dyes: fluorescein diacetate (FDA, 5 mg/mL) and propidium iodide (PI, 5 mg/mL) in standard conditions in the dark for 20 min. Before visualization dyes were removed and cells were washed with PBS twice. IC₅₀ values were determined, after 72 h, from the plots of cell viability in the presence of various concentrations of each compound by matching dose–response curves.

Cellular uptake

A549 and Du-145 cells at a density of 2×10^6 cells per 2 mL were seeded on 6 well plates and were incubated with **1a** and **1b** (2mL) for 24 h (37 °C, 5% CO₂). Additional wells were incubated with medium alone as a negative control. Then, compound solutions were removed; the cells were washed twice with PBS buffer, and trypsinized. Measurement of the concentration of iridium ions was carried out using a mass spectrometer (ELAN 6100 PerkinElmer) with inductively coupled plasma (ICP-MS). For analysis, the collected cells were mineralized in 1 mL of 65% HNO₃ at 60°C for 1 h. The iridium content under each condition is expressed as ng mg⁻¹ protein. The protein content was assessed with Bradford Protein Assay (Thermo Scientific™).⁷¹ The experiment was repeated at least 3 times and results are presented as mean value +S.D.

Confocal laser scanning microscopy

The intracellular uptake of **1a** was studied in the A549 and DU145 cancer cells according to the previously applied protocol.⁴ In brief, before imaging, A549 and Du145 cells were seeded on microscopic slides at a density of 1×10^5 cells. Cells were kept for 24 h at 37°C in a 95% atmospheric air and 5% CO₂ humidified atmosphere. After being washed with fresh medium, the cells were incubated in the dark with 1 μM solution of **1a** prepared growth medium for 2 h. Next, cells were stained with phalloidin-atto488 (Sigma Aldrich) to visualize the cytoskeleton and then incubated for 10 min with Hoechst 33342 for nuclear staining. After this incubation, at 37 °C, in the dark, the cells were washed with HBSS two times, and the slide was transferred to the microscope stage and cells were visualized under a confocal microscope Zeiss LSM 880 (Carl Zeiss, Jena, Germany) with a 63× oil immersion objective. Images were analyzed by Zeiss ZEN Software.

Cell death analysis by flow cytometry

Annexin V Apoptosis Detection Kit FITC (Invitrogen) and Propidium Iodide (Thermo Fischer Scientific, Waltham, Massachusetts, USA) were used to distinguish cell death (apoptotic and necrotic cells) induced by studied compounds quantitatively due to the previously described protocol.⁵ In brief, the studied

compounds **1a** and **1b** (in a broad range of concentration ranging between 100 and 0.01 μM) were incubated for 24 h with A549 and HaCaT cells (seeded at density 5×10^5 cells/mL) in 12 well plates. After this time, the compound solutions were removed, and the cells were washed twice with PBS buffer (phosphate buffered saline, pH = 7.4). Trypsin was added to the cells and then they were left for 10 min at 37 °C in a humidified atmosphere containing 5% CO₂. The cells were collected, centrifuged, and separated from the supernatant, then washed twice with 0.5 ml PBS buffer (buffer phosphate saline NaCl, KCl, Na₂HPO₄, KH₂PO₄) and suspended in Binding Buffer. Fifteen minutes before measuring, cells were stained with Annexin V-FITC and PI and incubated in the dark. Viable and dead (early apoptotic, late apoptotic, and necrotic) cells were detected using the BD Accuri flow cytometer (BD Biosciences). The experiment was repeated at least 3 times.

Cell cycle analysis

The A549, Du145 and HaCaT cells (3×10^5 /well) were seeded in 12 well plates and treated with various concentrations of **1a**, **1b** and cisplatin (CDDP) for 24 h. Synchronization of A549, Du145 and HaCaT cell cultures was performed by serum starvation protocol. Serum starvation is widely used for synchronizing donor cells by arresting them in the G₀/G₁ phase of the cell cycle.⁶ Cell cultures were seeded and incubated in a growth medium with 20% FBS overnight to synchronize the cell cultures. Then the cultures were rinsed by PBS and changed to serum-free medium. After serum starvation for 18 h, the cells were passaged and released into the cell cycle by the addition of serum. Then cells were treated with **1a**, **1b** and CDDP for 24 h. For FACS analysis, cell samples were harvested with trypsinization and stained with propidium iodide (20 $\mu\text{g}/\text{mL}$). Cell cycle phase distributions were analyzed by flow cytometry (BD Bioscience). Experiments were repeated at least three times.

Three-dimensional culturing *in vitro*

For hanging drop formation, the lid from a tissue culture dish was removed and 5×10^5 A549 or DU-145 cells in 10 μl drops were placed on the bottom of the lid. In each case, the cell suspension was homogeneous and did not contain aggregates, since it determines the size and uniformity of spheroids. Then, the lid was inverted onto the PBS-filled bottom chamber and incubated at 37 °C/ 5% CO₂/ 95% humidity. The sphere growth was monitored daily and incubated until either cell sheets or aggregates were formed. Once sheets were formed, they were transferred to 96 well plates coated with Geltrex matrix and incubated with a completed growth medium until spheroids were created. Using optimal growth conditions, a period of 4–7 days was found to be optimal for spheroid assembly. The direct effect of drug toxicity was examined on spheroids derived from both A549 and Du-145 cell lines. For cytotoxicity assessment, spheroids were grown and were monitored for 5–7 days. After this time, the spheres were treated with the tested liposomal formulation of **1** (**1a**) at increasing doses ($0.1 \times \text{IC}_{50}$, IC_{50} , and $10 \times \text{IC}_{50}$, IC_{50} determined for the

corresponding Pluronic P-123 nanoformulations), and the plates were further incubated at 37 °C. Forty-eight hours after treatment, the spheroids were stained with 4',6-diamidino-2-phenylindole (DAPI), calcein AM (CAM), and propidium iodide (PI) to estimate the live/dead cells population for one hour, washed and visualized using a confocal microscope Zeiss LSM 880 (Carl Zeiss, Jena, Germany) with a 10× oil immersion objective. Images were analyzed by Zeiss ZEN Software.⁷

References

- [1] Petrauskas, A. A.; Kolovanov, E. ACD/Log P method description, *Perspect, Drug Discovery Des.*, **2000**, 19, 99–116
- [2] Tetko, V.; Gasteiger, J.; Todeschini, R.; Mauri, A.; Livingstone, D.; Ertl, P.; Palyulin, V. A.; Radchenko, E. V.; Zefirov, N. S.; Makarenko, A. S.; Tanchuk, V. Y.; Prokopenko, V. V. Virtual computational chemistry laboratory-design and description. *J. Comput.-Aided Mol. Des.*, **2005**, 19, 453-463
- [3] VCCLAB, Virtual Computational Chemistry Laboratory – Design and Description, Virtual Computational Chemistry Laboratory, <http://www.vcclab.org>, **2005**
- [4] Kyzioł, A.; Cierniak, A.; Gubernator, J.; Markowski, A.; Jeżowska-Bojczuk, M.; Komarnicka, U. K. Copper(i) complexes with phosphine derived from sparfloxacin. Part III: multifaceted cell death and preliminary study of liposomal formulation of selected copper(i) complexes, *Dalton Trans.*, 2018, 47, 1981-1992
- [5] Komarnicka, U. K.; Pucelik, B.; Wojtala, D.; Lesiów, M. K.; Stochel, G.; Kyzioł, A. Evaluation of anticancer activity in vitro of a stable copper(I) complex with phosphine-peptide conjugate, *Sci Rep.*, 2021, 11, 23943
- [6] Chen, M.; Huang, J.; Yang, X.; Liu, B.; Zhang, W.; Huang, L.; Deng, F.; Ma, J.; Bai, Y.; Lu, R.; Huang, B.; Gao, Q.; Zhuo, Y.; Ge, J. Serum starvation induced cell cycle synchronization facilitates human somatic cells reprogramming, *PLoS One*, 2012, 7, e28203
- [7] Pucelik, B.; Arnaut, L. G.; Stochel, G.; Dabrowski, J. M. Design of Pluronic-based formulation for enhanced redaporfin-photodynamic therapy against pigmented melanoma, *ACS Appl. Mater. Interfaces*, 2016, 8, 22039

List of publications and patents:

- [1] **Article** "Electronic Properties of Electron-Deficient Zn(II) Porphyrins for HBr Splitting" ; *Applied Sciences* (2019) doi.org/10.3390/app9132739
- [2] **Article** "Syngas Evolution from CO₂ Electroreduction by Porous Au Nanostructures" *ACS Appl. Energy Mater.* 2020, 3, 5, 4658–4668
<https://doi.org/10.1021/acsaem.0c00301>
- [3] **Article** Two out of Three Musketeers Fight against Cancer: Synthesis, Physicochemical, and Biological Properties of Phosphino Cu^I, Ru^{II}, Ir^{III} Complexes. *Pharmaceuticals* **2022**, 15, 169.
<https://doi.org/10.3390/ph15020169>
- [4] **Article** Electrocatalytic hydrogen evolution using hybrid electrodes based on single-walled carbon nanohorns and cobalt(II) polypyridine complexes *J. Mater. Chem. A*, 2021, 9, 20032–20039
<https://doi.org/10.1039/D1TA03645A>
- [5] **Article** Self-Assembled Multinuclear Complexes for Cobalt(II/III) Mediated Sensitized Solar Cells. *Appl. Sci.* **2021**, 11, 2769. <https://doi.org/10.3390/app11062769>
- [6] **Article** Indium-modified copper nanocubes for syngas production by aqueous CO₂ electroreduction, *Dalton Trans.*, **2022**, 51, 10787–10798 <https://doi.org/10.1039/D2DT00779G>
- [7] **Article** Liposomal binuclear Ir(III)-Cu(II) coordination compounds with phosphino-fluoroquinolone conjugates for human prostate carcinoma treatment, *Inorg. Chem.* **2022**, 61, 48, 19261–19273 <https://doi.org/10.1021/acs.inorgchem.2c03015>
- [8] **Patent** "Procedimento per la formazione e la rigenerazione di un catodo in rame di una cella elettrochimica e cella elettrochimica per la produzione di prodotti industriali" 09/08/2019 ref. 31.L1086.12.IT.1 Italian patent
- [9] **PCT International Application Published under the Patent cooperation Treaty** : Process for Forming and regenerating a copper cathode for an electrochemical cell and electrochemical cell for the production of industrial products. I.P.N: WO 2021/028779 A1---- converted into **European patent** n. EP 4010513 15/06/2022

Most of the research activity was funded thanks to:





Università
degli Studi
di Ferrara

Sezioni

Dottorati di ricerca

Il tuo indirizzo e-mail

nrtlsn@unife.it

Oggetto:

Dichiarazione di conformità della tesi di dottorato

Io sottoscritto Dott. (Cognome e Nome)

Nioretini Alessandro

Nato a:

Arzignano

Provincia:

Vicenza

Il giorno:

30/03/1992

Avendo frequentato il Dottorato di Ricerca in:

Scienze Chimiche

Ciclo di Dottorato

35

Titolo della tesi:

Electroreduction of carbon dioxide over nanostructured metallic cathodes: a route towards artificial photosynthesis

Titolo della tesi (traduzione):

Elettroriduzione dell'anidride carbonica su catodi metallici nanostrutturati: una via verso la fotosintesi artificiale

Tutore: Prof. (Cognome e Nome)

Caramori Stefano

Settore Scientifico Disciplinare (S.S.D.)

CHIM/03

Parole chiave della tesi (max 10):

CO2 electroreduction Syngas electrochemistry electrocatalysis

Consapevole, dichiara

CONSAPEVOLE: (1) del fatto che in caso di dichiarazioni mendaci, oltre alle sanzioni previste dal codice penale e dalle Leggi speciali per l'ipotesi di falsità in atti ed uso di atti falsi, decade fin dall'inizio e senza necessità di alcuna formalità dai benefici conseguenti al provvedimento emanato sulla base di tali dichiarazioni; (2) dell'obbligo per l'Università di provvedere al deposito di legge delle tesi di dottorato al fine di assicurarne la conservazione e la consultabilità da parte di terzi; (3) della procedura adottata dall'Università di Ferrara ove si richiede che la tesi sia consegnata dal dottorando

in 1 originale cartaceo e 1 in formato PDF/A caricata sulla procedura informatica Esse3 secondo le istruzioni pubblicate sul sito: <http://www.unife.it/studenti/dottorato> alla voce ESAME FINALE – disposizioni e modulistica; (4) del fatto che l'Università, sulla base dei dati forniti, archiverà e renderà consultabile in rete il testo completo della tesi di dottorato di cui alla presente dichiarazione attraverso la pubblicazione ad accesso aperto nell'Archivio Istituzionale dei Prodotti della Ricerca IRIS-UNIFE (www.iris.unife.it) oltre che attraverso i Cataloghi delle Biblioteche Nazionali Centrali di Roma e Firenze; DICHIARO SOTTO LA MIA RESPONSABILITA': (1) che la copia della tesi depositata presso l'Università di Ferrara in formato cartaceo è del tutto identica a quella caricata in formato PDF/A sulla procedura informatica Esse3, a quelle da inviare ai Commissari di esame finale e alla copia che produrrò in seduta d'esame finale. Di conseguenza va esclusa qualsiasi responsabilità dell'Ateneo stesso per quanto riguarda eventuali errori, imprecisioni o omissioni nei contenuti della tesi; (2) di prendere atto che la tesi in formato cartaceo è l'unica alla quale farà riferimento l'Università per rilasciare, a mia richiesta, la dichiarazione di conformità di eventuali copie; (3) che il contenuto e l'organizzazione della tesi è opera originale da me realizzata e non compromette in alcun modo i diritti di terzi, ivi compresi quelli relativi alla sicurezza dei dati personali; che pertanto l'Università è in ogni caso esente da responsabilità di qualsivoglia natura civile, amministrativa o penale e sarà da me tenuta indenne da qualsiasi richiesta o rivendicazione da parte di terzi; (4) che la tesi di dottorato non è il risultato di attività rientranti nella normativa sulla proprietà industriale, non è stata prodotta nell'ambito di progetti finanziati da soggetti pubblici o privati con vincoli alla divulgazione dei risultati, non è oggetto di eventuali registrazioni di tipo brevettale o di tutela. PER ACCETTAZIONE DI QUANTO SOPRA RIPORTATO

Dichiarazione per embargo

12 mesi

Richiesta motivata embargo

4. Privacy

Liberatoria consultazione dati Eprints

Consapevole del fatto che attraverso l'Archivio Istituzionale ad accesso aperto dei Prodotti della Ricerca IRIS-UNIFE (www.iris.unife.it) saranno comunque accessibili i metadati relativi alla tesi (titolo, autore, abstract, ecc.)

Firma del dottorando

Ferrara, li 02/02/2023 Firma del Dottorando Alessandro Niorettini 

Firma del Tutore

Visto: Il Tutore Si approva Firma del Tutore Stefano Caramori 